Theses and Dissertations   Student Graduate Works

9-7-2007

Phenomenological Model for Infrared Emissions from High-Explosive Detonation Fireballs

Kevin C. Gross

Follow this and additional works at: https://scholar.afit.edu/etd

Part of the Nuclear Commons

PHENOMENOLOGICAL MODEL FOR INFRARED EMISSIONS FROM HIGH-EXPLOSIVE DETONATION FIREBALLS

DISSERTATION

Kevin C. Gross, Civillian

AFIT/DS/ENP/07-03

DEPARTMENT OF THE AIR FORCE
AIR UNIVERSITY

AIR FORCE INSTITUTE OF TECHNOLOGY

Wright-Patterson Air Force Base, Ohio

APPROVED FOR PUBLIC RELEASE; DISTRIBUTION UNLIMITED

AFIT/DS/ENP/07-03

PHENOMENOLOGICAL MODEL FOR INFRARED EMISSIONS
FROM HIGH-EXPLOSIVE DETONATION FIREBALLS

DISSERTATION

Presented to the Faculty

Department of Engineering Physics

Graduate School of Engineering and Management

Air Force Institute of Technology

Air University

Air Education and Training Command

In Partial Fulfillment of the Requirements for the

Degree of Doctor of Philosophy

Kevin C. Gross, B.S., M.S.

Civilian

September 2007

PHENOMENOLOGICAL MODEL FOR INFRARED EMISSIONS
FROM HIGH-EXPLOSIVE DETONATION FIREBALLS

Kevin C. Gross, B.S., M.S.

Civilian

Approved:

//signed//		30 Aug 2007
Glen P. Perram (Chairman)		Date
//signed//		29 Aug 2007
Meir Pachter (Dean's Representative)		Date
//signed//		31 Aug 2007
Stephen Cain (Member)		Date
//signed//		06 Sep 2007
James Engel (Member)		Date
//signed//		29 Aug 2007
Ronald F. Tuttle (Member)		Date

Accepted:

//signed//		07 Sep 2007
M. U. Thomas		Date
Dean, Graduate School of		
Engineering and Management		

Abstract

Prior to this work, a phenomenological description of mid-wave infrared (MWIR) emissions from high-explosive (HE) detonation fireballs did not exist, hampering efforts to classify the type and size of HEs from their electro-optical signatures. In recent field tests, temporally-resolved infrared spectra ($0.05 \leq \Delta t \leq 0.12$ s, $2 \leq \Delta\tilde{\nu} \leq 8$ cm^{-1}) were collected via a Fourier-transform spectrometer (FTS) from the detonation fireballs of two types of conventional military munitions (CMM) as well as uncased TNT and four types of enhanced novel explosives (ENEs). The FTS data is not appreciably corrupted by artifacts due to scene changes resulting from the fast transient events. The CMM spectra are dominated by continuum emission, and a single-temperature Planckian distribution, modified for atmospheric attenuation, captures most of the variation in the data. Fitted CMM temperatures are well described by an exponential decay to ambient at an approximate rate of 0.8 s^{-1}. A two-temperature fit to CMM spectra improved results, suggesting variations in the temperature field are important. Some evidence of selective emission is identified by systematic patterns in the fit residuals. The behavior of these systematic residuals affords a distinction between the two types of CMMs studied.

The uncased TNT and ENE spectra appear strongly influenced by both continuum and selective emission. For the purpose of dimensionality reduction, a physics-based spectral model is developed consisting of seven parameters—fireball size, temperature, particulate absorption coefficient, and gas concentrations for H_2O, CO_2, CO, and HCl. Fitting this model to the observed MWIR spectra affords a compact, high-fidelity representation with physically-constrained features that correlate with both the type and weight of the HE. For example, the hydrogen-to-carbon ratio ($\mathcal{R}$) estimated from the fitted concentrations separates the TNT and ENE events. Spectrally-determined $\mathcal{R}$ values are somewhat consistent with stoichiometric expectations. Comparing average values of $\mathcal{R}$ for the uncased explosives with the limiting thermodynamic value (in parentheses): TNT 1.13 (0.79); ENE0B 9.2 (21.3); ENE1 4.9 (6.7); ENE2A 4.6 (5.8); ENE2B 6.5 (6.7). Treating all ENEs as a single class and assuming $\mathcal{R}$ obeys a normal distribution, Bayesian discrimination revealed a

decision boundary of $\mathcal{R} = 1.67$ with a mean probability of error less than 0.3%. For a detection probability of ENE of 99%, the associated false-alarm rate was less than 10^{-4}%. The Fisher ratio for the two classes was 17.4. Temperature decay rates k_T correlate with charge weight W, following a power-law dependence $k_T \propto W^b$ with $-0.52 \leq b \leq -0.25$ depending on explosive type. Initial TNT fireball temperatures agree with optical pyrometry studies. Radiative emission is an important component of the cooling process and the optical properties of the fireball may be a factor in the observed weight dependence of k_T. Initial emissivities are between 0.6–1.0, and rapidly decay due to a decrease in the particle absorption coefficient κ_p. It may be possible that the κ_p decay is evidence of soot oxidation, and the temporal behavior of κ_p from several TNT fireballs correlates with recently published temperature-dependent soot oxidation kinetics.

Acknowledgements

First, I am deeply indebted to my wife and three children for gracefully enduring this lengthy process and providing the needed support throughout. Without them, the stresses and difficulties encountered during this extended effort would have seemed much greater. Next, I extend my gratitude to Glen Perram who provided excellent guidance when needed and appropriate distance when lessons were better learned the hard way. From him I learned a variety of good things, many related to this work, others about broader aspects of science, and still others about life in general. Ronald Tuttle is to be thanked for both his academic advice and necessary support to see this project to its completion. The remaining committee members—Jim Engel, Stephen Cain, and Meir Pachter—also deserve recognition for their thoughtful contributions which improved the quality of this work. Thanks are extended to Greg Smith (technician) and Mark Houle (bureaucratic ninja) for their help in the planning, execution, and successful completion of several field tests. Of course friendships forged along the way made for a more enjoyable expericence: thanks (in no particular order) Bryan Steward, Trevor Warren, Mike Hawks, Andy Dills, Carl Druffner, Randy Bostick, Matt Lange, Chad Hollingsworth, and others for many good times! And to all the friends I used to have before the simultaneous embarkation upon a doctorate and fatherhood, my apologies for loosing touch.

Kevin Gross

Table of Contents

List of Figures

List of Tables

List of Symbols

List of Abbreviations

Phenomenological Model for Infrared Emissions from High-Explosive Detonation Fireballs

I. Introduction

Consider the following scenario: A suspicious package is found in a public place. The local bomb squad is dispatched since, in an abundance of caution, the package is presumed to contain an explosive device. The immediate concern is the public's safety. Once the scene is properly evacuated, the bomb squad sends in a robot to fetch the suspicious item. It is carefully transported to a safe, open location where it can be neutralized via a controlled detonation. At this point, it is often learned that the suspicious item was nothing more than an accidentally dropped bag or package. With the heightened sensitivity to frequent acts of terrorism across the world, packages found in odd, public locations can be forgivably mistaken for more sinister objects. But sometimes they are. In such cases, the controlled detonation of the suspicious package results in a fiery spectacle, a detonation fireball fueled by the unknown explosive material inside. This package was placed with the intention of harming a lot of people. Now it is time to look for the perpetrator.

In both large and small cities across the country, bomb squads are dispatched several times a year to neutralize suspicious packages. More often than not, the packages never posed a real threat to public safety. But when actual explosive devices are found, it is important to learn as much as possible about the weapon. Details about the weapon provide clues needed to apprehend the criminal. However, safety concerns typically prevent a thorough forensic analysis of the device prior to the controlled detonation. After the device is neutralized, officers from the crime lab will collect clues about its composition and construction. For example, the size of the debris field is measured since it correlates with the size and shape of the explosive charge. Residue samples are collected and can be sent to a laboratory for gas chromatography and mass spectrometry analysis. This GCMS technique can provide important information about the composition of the explosive material. However, this procedure takes time, and clues about the device that would help focus the initial investigation are not immediately available.

Determining the type and size of the high explosive (HE) used in the device is important for several reasons. Not only do these variables define the HEs damage potential, knowledge of these variables—even after the fact—provides important clues about the perpetrator and his level of sophistication. For example, some explosive materials are readily available (e.g., ammonium nitrate in the form of fertilizer) whereas others are much harder to obtain (e.g., the military-grade explosive HMX). If evidence is found that the device contained HMX, the authorities would likely consider it the work of a sophisticated terrorist with access to DoD weapons facilities or with an extensive chemistry background and access to precursor materials. Similarly, if evidence was found that the explosive was aluminized, the investigation might focus on the limited number of producers and distributors of powdered aluminum. Knowing how big the original explosive was is also key. The larger the device, the more likely clues (in the form of store receipts or parcel shipment logs) can be found regarding the acquisition of the individual components. Finally, information about the explosive device offers key details needed to build an accurate profile of the perpretratior. Was it the work of an amateur or did he have training in the construction of explosives? Are its materials and construction similar to those used in other solved or unsolved crimes? Answers to such questions influence the profile and improve database searches for related cases and/or repeat offenders.

As just suggested, knowledge about the composition and size of a HE device employed in a crime provides key information that can lead to the apprehension of the perpetrator. And the more quickly this information becomes available, the more quickly the investigation can be appropriately focused. What if the type and size of the explosive material could be ascertained via remote sensors while the device is being neutralized via detonation? This capability could provide a rapid assessment of these key characteristics, and do so in a manner which maximizes the safety of the investigators. The purpose of this research effort is to develop the requisite fireball emissions phenomenology needed to determine if spectra collected from the neutralization detonation can be used to characterize the underlying explosive material. The extraction of phenomenological parameters from these measured spectra will be used to guide the search for the appropriate discriminating features in fireball emissions signatures. Of course, the capability to "fingerprint" HEs from their electro-optical (EO) signatures may be useful in ways beyond the forensic scenario just presented.

For example, EO emissions from fireballs may improve battle space characterization by providing increased situational awareness. It is possible that counter-terrorism and homeland security efforts may benefit from this capability as well.

The detonation of a high explosive results in a luminous fireball. Infrared spectral emissions from the fireball may reveal key HE characteristics since most absorption and emission features in this wavelength regime are associated with molecular species. Knowledge of the amounts and temporal behavior of these detonation by-products—for example, water and carbon dioxide in the case of hydrocarbon exposives— may be used to infer the type of material used. For example, the quantity of H_2O and CO_2 liberated upon detonation will be influenced by the stoichiometry of the explosive material. Furthermore, the evolution of these by-products with time is driven by the kinetic pathways governing the oxidative decomposition of the starting material, and their temporal signature may provide additional clues about the starting material. Visible spectra of the HE fireball could be used to determine if the HE was metalized (e.g. aluminum particles) by the presence (or absence) of characteristic metal-oxide emissions in this electromagnetic region. Explosive size might be best estimated using imagery, and may be inferred from other measured characteristics of the fireball.

The successful exploitation of emissive signatures from HE detonation fireballs requires an understanding of the underlying phenomenology, an understanding which has not been explored and presented until now. Currently, the conversion of reaction exothermicity to infrared and visible emissions in HE detonations is poorly documented. Not surprisingly, no simple model describing the infrared emissions from a HE detonation fireballs has been previously reported. The problem here is not that the underlying physics are unknown; rather, the relevant pieces of physics have not been brought to bear on this particular problem. Which components of the complex phenomena of a reacting fireball dominate the emissive characteristics? What information content is contained in the emissive signature? Can a HE emissive signature be reduced to a small set of characteristic descriptors which enable its distinction from other HEs types? With the dearth of information regarding spectral emissions from HEs, these are questions which had no obvious answers at the beginning of this project. Answers to these questions are necessary for this research effort, namely the

extraction of key features from fireball emissions. Key features are the quantitative, reproducible, physically-meaningful bits of information contained in the emissions pattern. Ideally, they will be invariant to variables which cannot be controlled (e.g., atmospheric conditions) and should be distinct for different types of events. Using these key features, classification algorithms will provide a probabilistic answer to the question of "what type and how big was that high explosive?" To set the stage for answering this question, a summary of relevant background material is presented and contrasted with the approach taken in this research effort.

1.1 Background

The detonation of a high explosive (HE) is essentially a combustion reaction under extreme conditions. One unit of the solid or liquid explosive is rapidly converted to several units of gaseous by-products in a violent, highly exothermic reaction. Under suitable conditions–for example, confining the combustion process to a small volume–the rapid increase in pressure resulting from the simultaneous increase in number density and temperature produces a shock wave. The shock wave, in turn, continues to drive this extreme combustion reaction in the remaining HE material [38]. Several microseconds later, the shock front leaves the explosive and continues outward inflicting substantial damage on the nearby surroundings. The shock wave leaves behind a luminous fireball, typically fuel-rich as many HEs are under-oxidized. Turbulence facilitates mixing with atmospheric oxygen thereby continuing the oxidation of these detonation by-products. In some systems, this afterburning is more energetic than the initial detonation reaction. However, being unconfined, the afterburning system is probably more like a typical combustion system compared with the extremes of the preceding detonation. The instrumentation described in the next chapter used to study the luminous fireball will primarily sense the afterburning and subsequent cooling stages; the initial detonation occurs too rapidly to be sensed by the spectrometers and effectively sets the initial conditions for the fireball signature.

There has been much work devoted to understanding the detonation [22, 38] and shock phenomena [65, 66, 72, 96, 105, 110] in high explosives. Simple empirical relationships have been found for many common explosives which relate molecular properties such as structure and density to experimentally determined detonation velocities and pressures [22]. Approximate values for the net energy release, temperature and final volume after a detonation can be estimated using thermodynamic data [16] and the ideal gas law.

4

More sophisticated approaches incorporate thermodynamic equilibrium constants and equations of state tailored to the non-ideal detonation environment. CHEETAH is a computer package which implements this thermodynamical approach and is used in the development and performance characterization of explosives [42]. Fundamentally, however, the detonation represents a difficult hydrodynamics problem that is coupled to a reactive chemical system, and important time-dependent features of this dynamic system cannot be understood from a purely thermodynamical approach. Mader [72] summarizes several decades worth of work that has been applied to the understanding of HE detonations primarily through numerical thermohydrodynamic simulations. Here, the evolving flow field is handled by hydrodynamics equations while the chemistry is still handled by thermodynamic relationships.

In recent decades, experimental work has produced elementary reaction rates for the dominant pathways found in various combustion mechanisms [6, 44, 67]. The National Institute of Standards and Technology (NIST) Chemical Kinetics Database [84] tabulates Arrhenius rate expressions for more than eleven-thousand bimolecular reactions. Several specialized collections of rate coefficients are made available for combustion mechanisms for specific fuels, for example methane [11] or propene [54] combustion. As computational power has steadily improved, modern multi-phase reactive-flow hydrodynamic codes such as FLUENT now treat the chemical components via kinetic (as opposed to thermodynamic) equations as discussed in Ref. [18]. While the computations take on the order of weeks to months to perform, they have been successfully applied to diverse systems including combustion engines [33, 89] and scramjet motors [80]. Upon establishing the flow field, the results of these computational fluid dynamics (CFD) calculations can be post-processed with radiative transfer packages such as the Standardized Infrared Radiation Model (SIRRM) [41] or the Fast Line-of-sight Imagery for Target and Exhaust Signatures (FLITES) [23, 24] to predict the spectral distribution of radiant energy emitted from the system. In principle, this CFD approach appears well-suited to the prediction of HE detonation fireball spectra, perhaps enabling HE characterization via matching observed data with a synthetic spectral library. However, it will be argued in the next section that this approach is hampered by several technical problems and, while a worthwhile approach to understanding HE detonations, is not the most suitable tool for the HE characterization problem.

Various laser-based spectroscopic techniques have aided the understanding and characterization of controlled combustion processes [5, 63, 64]. For example, coherent anti-Stokes Raman spectroscopy (CARS) is used to monitor gas temperatures and concentrations in typical combustion flames [103, 104] as well as laboratory-scale rocket plumes [47]. Cavity ring-down spectroscopy [12, 109] is an extremely sensitive technique allowing low-concentration reactive intermediates such as $^1CH_2$ [74] and the radical CH [27] to be measured. Laser-induced breakdown spectroscopy (LIBS) is an atomic emission technique used to study the elemental composition of combustion flames [37, 51], and enables the estimation of the temperature [71] and the fuel-air ratio [36]. Laser-induced fluorescence spectroscopy (and planar LIF or PLIF) is a widely-used and high-sensitivity technique for detecting particular chemical species, measuring temperature, and tracking the fuel-air ratio [64, 76, 83, 95, 102]. Furthermore, because it is based on fluorescence (instead of absorption), PLIF can reveal the spatial dependence of this information as well as other measures dependent on the flow field [25, 73, 101]. Finally, laser-induced incandescence (LII) is a spectral technique typically used to study the time-dependent temperature and size distributions of soot in combustion sources [78, 97].

For the study of detonation fireballs from high-explosives weighing 10–1000 kg, safety, cost, and technical issues preclude the use of most active spectroscopic techniques. Instead, passive techniques which remotely record the emission from the fireball must be used[1]. To the extent that the afterburning fireball behaves like a typical combustion system, it is expected that it can be studied using Fourier-transform spectroscopy[2] (FTS), as has been done in the study of other combustion sources. For example, FTS has been used to characterize emissions from methane-air combustion flames [99], measure concentrations from hot flue gases at power plants [19], track chlorinated hydrocarbons found in incinerator exhaust [52], and monitor emissions from advanced powertrains [1] including turbine aircraft engines [3, 53, 92] in order to improve performance and minimize pollution. FTS has even been used by NIST to quantify combustion by-product concentrations for the development of a standard database for which various CFD codes can be benchmarked [107]. Note that

---

[1]In active spectroscopy, a radiation source (e.g. a tunable laser) is passed through the system so its transmittance profile can be directly measured. In passive (emissive) spectroscopy, the emitted radiance is measured directly, requiring a contrast between the background and source.

[2]Prism and grating-based spectroscopy are also applicable to the study of HE fireballs and other fast-transients. Since the spectral features most useful to the HE characterization problem were not known *a priori*, FTS was initially chosen over grating instruments for its ability to collect high-resolution spectra over a wide band pass. In more recent field tests, a visible grating spectrometer was also deployed but that data set was not analyzed as part of this dissertation.

in these studies, the emissive source is in a near steady-state which enables the collection of time-averaged, high SNR spectra. Unlike the spectroscopy of large HE detonation fireballs presented in this work, many of the sources just described were conducive to and studied by active spectroscopy.

Common to many of these combustion studies via spectroscopy is the method by which the spectra are interpreted using simple radiative transfer concepts in conjunction with a spectral database such as HITRAN [90]. Weiser [106] summarizes key components of the radiative transfer theory, and Fleckl *et. al.* [40] and Modest *et. al.* [82] provide evidence that this approach works at the high temperatures encountered in combustion systems. Where the current work differs is in bringing these methods to the analysis of a class of fast-transient events which heretofore have not been reported on in the literature. The afterburning and cooling fireball, depending on its size can last up to at most a few seconds. The rapidity with which this source changes prevents signal-averaging. Furthermore, lacking hardened, protected equipment, only emissive signatures from large HE fireballs can be collected, and a model for the fireball behavior is needed to interpret the collected spectra. To do so, a consideration of the radiative transfer in a fireball will be necessary.

Spectroscopy has been used in several studies of explosives prior to this work. Many efforts have focused on understanding aging effects on explosives or developing trace detection techniques [75]. Many common HE materials (TNT, RDX, HMX, etc.) have unique absorption cross-sections in the terahertz portion of the electromagnetic spectrum. Since THz frequencies can penetrate common dielectric materials (clothing, luggage bags, shoes, etc.), the spectroscopy and instrumentation are being rapidly developed for stand-off detection of common HEs [39, 70, 98, 111]. Reflectance FTS has been used to examine the extinguished (and formerly combusting) surfaces of common gun propellants to infer information about the underlying combustion mechanisms [93, 94]. Rapid-scan FTS techniques have been developed to uncover the mechanisms governing the thermal decomposition of high explosives such as RDX and HMX [58, 88]. In these studies, thermolysis of the HE was controlled so that combustion did not occur. Instead, thermal decomposition of the HE occurred over several seconds (~10–60 s) and at relatively low temperatures (~500–700 K) and pressures (~1000 psi). By contrast, in the detonation of a HE, decomposition occurs in the nano-

7

to micro-second timescale, temperatures may exceed two-thousand Kelvin, and pressures may be as large as 500,000 atm [42, 110].

Only recently have optical spectra of HE detonation fireballs been published in the literature, and the work of this research group accounts for most of these publications [4, 30, 32, 48, 86, 87]. However, Goroshin *et. al.* recently published visible spectra (400–800 nm) of fireballs resulting from the detonation of TNT, nitromethane (NM), and NM mixed with Al, Mg, or Zr powders [45]. The TNT, NM, NM + Al, and NM + Zr spectra exhibited strong continuum radiation and some selective emission lines from the metal and metal oxides were also assigned. The NM + Mg featured a number of selective emission lines, most of which were attributed to Mg and MgO. All spectra featured weak to moderate, unresolved Na emission doublet near 590 nm. The visible spectra were captured to enable the appropriate selection of bandpass filters for their three-color pyrometer. (Assuming a greybody radiator, temperature can be inferred via ratios of the observed radiance in different wavelength bands. Selective emission in a chosen band will corrupt this temperature measurement, and the visible spectra indicate those regions which must be avoided for successful temperature measurements via pyrometry.) No analysis of the fireball spectra was reported apart from assigning several of the metal and metal-oxide emission lines. Their fireball temperature estimates for TNT measured by optical pyrometry are compared with spectral estimates resulting from this work in Chapter IV.

Perhaps the most relevant related work was recently published by Weiser and Eisenreich. They describe an ideal experimental set-up for capturing time-resolved spectra of pyrotechnic events in the near infrared and visible regime [106]. Their paper also presents some moderate-resolution spectra from nitromethane and iso-octane pool fires as well as from exhaust plumes from various propellants. The pool fires and exhaust plumes are small scale and produced under controlled laboratory conditions. They provide a theoretical framework for interpreting the spectra similar to what is presented here; however, they employ a random band model and assume the optically-thin limit to simplify the analysis. The present work differs in several respects, of which a few technical differences are: (1) actual time-resolved spectra from full-scale, fast-transient HEs fireballs were collected in the field; (2) full line-by-line calculations are used to match the spectral resolution of the

instrument; (3) the optical depth varies from thick to thin, enabling the de-coupling of the fireball's geometric length and constituent concentrations by using calibrated spectral intensities.

In an effort to identify key features for the HE classification problem, a few former AFIT students collected temporally-resolved infrared emissions from HE fireballs during several field tests [29, 86]. Interpreting and extracting the information content contained within these observed spectra is the essential focus of this dissertation. In the spirit of reverse-engineering, the data guided the development of a simplified physical fireball emissions model. The model is successfully fit to the observed HE fireball spectra, collapsing the dimensionality down to a few physically-meaningful parameters. The model parameters are the fireball size, temperature, continuum absorption coefficient (for soot emissions), and four by-product concentrations (H_2O, CO_2, CO, HCl). Quantities derived from these fit parameters will be shown to be key features in that they strongly correlate with the type and size of the high explosive, a result suggesting that discrimination of HEs from electro-optical signals is possible. By virtue of fitting the data so well, the model also provides a method of studying fireball behavior, in particular the time-dependence of quantities such as temperature. Some initial inferences concerning the temporal phenomenology of HE fireballs are also presented in this document.

1.2 Alternate Approaches to the Classification Problem

Before beginning, it is worth commenting on two other approaches, denoted "Statistics" and "First Principles", which might be taken to solve the HE classification problem. In the end, pattern-recognition tools will be used to ascribe a likelihood that the inputted feature set maps to a particular type of HE. So in the Statistics approach, one might directly feed the observed data to the classification algorithms, bypassing the phenomenological modeling. Or recognizing that substantial dimensionality reduction is necessary (a single time-resolved data cube can contain a quarter-million data points), techniques such as principle component analysis might be used to achieve this instead of a physical model. The problem with such a non-phenomenological approach is that the remotely collected fireball spectra contain large amounts of both redundant and extraneous information. A phenomenological model eliminates much of the redundancy and

naturally partitions the information into useful and extraneous categories. For example, the fireball model presented in this work separates the spectral features associated with atmospheric attenuation from the spectral features associated with the fireball emissions. It is difficult for a neural network to "learn" only the differences in the data resulting from real fireball features when significant extraneous differences are present in the observed data used to train it. Arbitrary dimensionality reduction achieved by, for example, taking the first n principle components from a data cube will not, in general, decouple the extraneous and useful bits of information.

In the First Principles approach, one might attempt to predict the spectral signature that would be emitted from a HE fireball. A spectral library of HE signatures could be developed, enabling measured signatures to be associated with a HE via spectral matching algorithms. Reactive-flow (RF) computational fluid dynamics (CFD) represents perhaps the best-suited method of generating a spectral library. In practice, this is an extremely difficult and very demanding task. Chung points out [18, pp 725] that the following processes of "kinetics, laminar and turbulent hydrodynamics, thermal conductivity, viscosity, molecular diffusion, thermochemistry, radiation, nucleation, surface effects, evaporation, condensation, etc." must be well understood to adequately perform such calculations. Barlow, summarizing the current capabilities of CFD in 2007, states the following [5]:

> Direct numerical simulation (DNS) of the fully coupled equations of fluid motion, molecular transport, and chemical reaction can today be applied only to canonical reacting flows with idealized boundary conditions and to the simplest of laboratory-scale turbulent flames. While such simulations are excellent tools for fundamental research on specific turbulent combustion phenomena, the leading-edge cases already require hundreds of millions of computational cells and millions of computer processor hours. Therefore, calculations of practical combustion devices must rely on a range of simplifying assumptions and computational models, which must in turn have solid experimental and theoretical foundations if they are to be accurate, predictive, and robust.

Fortunate for the combustion community, an enormous amount of experimental and theoretical work has been performed, providing the required foundations to employ simplifications which enable CFD to be practically applied to various combustion scenarios. However, this is not the case for HE detonation fireballs with little published work on the afterburning combustion process. Using CFD with SIRRM or FLITES to predict HE spectral signatures would require significant validation. In fact, the act of performing the radiative transfer in

post-processing stage may introduce large errors in both the establishment of the flow field as well as the spectral radiant emission. In most RF-CFD codes, the radiative energy loss is treated in an approximate way since coupling a full solution to the radiative transfer component results in a computationally intractable problem. Typically, only after the flow field is established are accurate radiative transport calculations performed. As a result of this simplification, important turbulent-radiation interactions (TRI) are ignored. Deshmukh *et. al.* point out that excluding TRI in CFD calculations (which, when included, accounted for 96% of the CPU time in their study) can lead to significant errors, including underestimations of radiative flux by 30–50% [28]. In the context of modeling electro-optical signatures, the radiative transfer component *is* the most important part of this problem, and it is difficult to estimate the utility of post-processed spectra from CFD flow-fields without a substantial validation effort.

Other technical complications in CFD involve the use of experimental reaction rates. While reaction rates for key elementary combustion reactions are now available, they are typically measured under non-turbulent conditions. Turbulence affects the rates in ways that have not been fully characterized, limiting their usefulness in and reducing the accuracy of CFD calculations [18]. Additionally, for most HEs full reaction mechanisms starting with the unreacted explosive and terminating with its fully-oxidized state are non-existant. Fortunately, the initial decomposition via detonation to simple gases and solid particulate matter can be handled using thermodynamic codes such as CHEETAH [42]. However, Weiser makes the case [106] that the use of equilibrium-based codes and other factors currently limit the ability of CFD calculations to accurately predict emission spectra from combustion systems. While Beckstead *et. al.* suggest kinetic modeling of solid propellants (of which some are also explosives) is not yet predictive due to insufficient knowledge about the initial decomposition reactions, they provide a review [8] of the theoretical aspects and progress made toward these predictions and suggest that soon such predictions will become reliable.

In principle, the techniques of RF-CFD might be able to synthesize a HE fireball spectrum for comparison with real data. Such work should be pursued as it would be complementary to and offer relevant insight for the phenomenological approach described in this document. However, several technical obstacles prevent RF-CFD from being used to reliably synthesize HE fireball spectra. Furthermore, unlike the simple physical

model developed in this work, RF-CFD models cannot be used to extract information from a real HE fireball spectrum, and as a consequence of its inherent high-dimensionality, do not provide an intuitive description of the dominant features found therein. It is possible, however, that the phenomenological understanding gained in this research effort may indicate which processes can be simplified (and which cannot) so that CFD can be more accurately applied to the generation of HE fireball signatures.

1.3 Document Preview

Dimensionality reduction and feature extraction are crucial first steps to solving the HE characterization problem, and neither a first-principles nor purely statistical approach appear to be suitable approaches to the solution. The key contribution of this dissertation is the development and validation of a phenomenological approach to dimensionality reduction that yields key features for HE characterization. An overview of the emissions data collected by a Fourier-transform spectrometer (FTS) and leading to the development of this model is presented in Chapter II. Ancillary yet important issues to be discussed include sensor calibration, the effects of atmospheric absorption, and scene-change artifacts due to observation of a dynamic scene by FTS. In Chapter III, previous efforts by the author [48, 49] to describe conventional military munitions emissions are summarized for completeness. Chapter IV provides the physical basis for the fireball model along with an interpretation of results obtained by fitting it to a few fireball spectra. Fits to a large number of distinct HE emission spectra were performed, and Chapter V presents the behavior of the fit parameters to examine how information about the size and type of the HE can be extracted. This chapter also sets the stage for better understanding fireball phenomena by offering a physical interpretation of the time-dependent behavior of the temperature and particulate absorption coefficient. Finally, conclusions are presented in Chapter VI along with a roadmap for future efforts. Several appendices are also included to provide important yet ancillary bits of information.

II. Experimental data

Over the past decade, the remote sensing group at AFIT has collaborated with various ground-truth teams in deploying a variety of sensors to characterize transient events. These joint efforts have focused on collecting electro-optical emissions from short-lived combustion events, for example detonation fireballs and muzzle flashes from small arms fire. AFIT's key contributions to these efforts include the introduction of new instrumentation for signature collection and, most importantly, the development of phenomenological models for signature interpretation and subsequent exploitation.

For each field campaign, the ground truth team typically deploys a collection of spectrometers, radiometers, and imagers spanning the visible and infrared regime for signature collection and event characterization. Conventional munition signatures were collected during the Radiant Brass exercises and tank muzzle-flash emissions were characterized in the Iron Rose tests. Recent attention has been focused on gathering signatures from improvised explosive devices (IEDs) currently deployed against US and Coalition forces by rogue organizations. Several field tests were convened to specifically address the IED threat. In particular, two campaigns (Brilliant Flash I and II) were executed to collect electro-optical signatures to assess the feasibility distinguishing engineered explosives (e.g., TNT) from IEDs constructed from readily available materials. More recently, the Bronze Scorpio exercises characterized the emissive properties of artillery shells detonated in various configurations to simulate the munitions-based IEDs encountered by US and coalition forces in Iraq. Finally, AFITs remote sensing lab recently designed and executed two tests which quantified the flash-suppressing characteristics of a novel gunpowder when fired from small-arms weaponry. Table 1 summarizes several recent field tests involving AFITs remote sensing laboratory.

The field tests just described were costly, dangerous, and designed to provide a rough characterization of the types of transient events typically encountered in the battlespace. The purpose of this research effort is to move beyond rough charaterizations of the data and towards a simple physical description of event phenomenology. This task is difficult as the constraints on and original scope of the field campaigns resulted in data sets which span many degrees of freedom with limited or no repetitions. For example, in Brilliant Flash II, there was only one detonation of each explosive in the 1000 kg weight class. Thus, when considering

Table 1: Summary of recent field tests in which electro-optical signatures were collected to enable the characterization of several types of transient events. The author was involved in the last three field tests: he was responsible for the AFIT team in Bronze Scorpio, and he served as the primary investigator in both Muzzle Flash I and II.

Field Test	Description	Events	Variables[a]	Instruments[b]
Radiant Brass III A 2-5 Aug 1999	Aircraft-delivered CMMs	33	12 (2 HEs, 3 weights, 4 approach vectors)	Bomem MR-154 FTS (Δv = 7.71 cm^{-1}, Δt = 0.049 s, 1.6-20 μm) 4-channel radiometer (InSb, 200 Hz, various filters) AGEMA MWIR FPA (5 Hz)
Radiant Brass III B 26-29 Oct 1999	Statically-detonated CMMs	23	4 (3 HEs, 3 weights, 2 detonation methods)	Bomem MR-154 FTS (Δv = 7.71 cm^{-1}, Δt = 0.049 s, 1.6-20 μm) 4-channel radiometer (InSb, 200 Hz, various filters) AGEMA MWIR FPA (5 Hz)
Brilliant Flash I 8-17 Jul 2002	ENEs (IEDs from readily available materials)	51	9 (3 HEs, 3 weights)	Bomem MR-154 FTS (Δv = 1.83 cm^{-1}, Δt = 0.123 s, 1.6-20 μm) Bomem MR-354 FTS (Δv, Δt unknown) 4-channel radiometer (InSb, 200 Hz, various filters) Cincinnati Electronics IRRIS FPA (256x256 InSb, 40 Hz) Indigo AlphaNIR FPA (320x256 InGaAs, 30 Hz, 0.9-1.7 μm) Canon XL-1 3-chip video (720x480 Si, 60 Hz interlaced)
Brilliant Flash II 2-13 Jun 2003	ENEs	44	9 (3 HEs, 3 weights)	Bomem MR-154 FTS (Δv = 1.83 cm^{-1}, Δt = 0.123 s, 1.6-20 μm) Bomem MR-354 FTS (Δv = 1.83 cm^{-1}, Δt = 0.029 s, 2-5 μm) 4-channel radiometer (InSb, 200 Hz, various filters) Cincinnati Electronics IRRIS FPA (256x256 InSb, 40 Hz) Indigo AlphaNIR FPA (320x256 InGaAs, 30 Hz, 0.9-1.7 μm)
Bronze Scorpio	Munitions-based IEDs	62	11 (3 HEs, 2 weights, 2 detonation methods)	Bomem MR-154 FTS (Δv = 1.83 cm^{-1}, Δt = 0.123 s, 1.6-20 μm) Bomem MR-254 FTS (Δv = 1.83 cm^{-1}, Δt = 0.029 s, 0.9-5.5 μm) Bomem MR-354 FTS (Δv = 1.83 cm^{-1}, Δt = 0.029 s, 2-5 μm) 4-channel radiometer (InSb, 200 Hz, various filters) Cincinnati Electronics IRRIS FPA (256x256 InSb, 40 Hz) Indigo AlphaNIR FPA (320x256 InGaAs, 30 Hz, 0.9-1.7 μm) Phantom high-speed color camera (800x600 Si windoable, 4.8-150 kHz)
Muzzle Flash I	Small-arms fire	140	4 (2 propellants, 2 bullets)	Bomem MR-154 FTS (Δv = 1.83 cm^{-1}, Δt = 0.123 s, 1.6-20 μm) Bomem MR-254 FTS (Δv = 1.83 cm^{-1}, Δt = 0.029 s, 0.9-5.5 μm) Indigo AlphaNIR FPA (320x256 InGaAs, 30 Hz) Phantom high-speed color camera (800x600 Si windoable, 4.8-150 kHz)
Muzzle Flash II	Small-arms fire	90	2 (2 propellants)	Indigo AlphaNIR FPA (320x256 InGaAs, 30 Hz) 3-channel radiometer (2 Si Vis/NIR, 1 InAs - MWIR, 100 kHz)

[a] Not all possible combinations of variables were explored in each test

[b] Instrument data unavailable is displayed in grey

the results presented in subsequent chapters, it is important to remember that they are supported by limited quantities of experimental data.

Despite the challenges imposed by the nature of available data, this research effort focuses on discovering the phenomenology of high-explosive detonation fireball emissions for the purpose of developing a simple physical model capable of representing those emissions. Motivating the need for a fireball model is the desire to infer properties of the high-explosive from its electro-optical emissions following detonation. The approach taken might be described as a reverse-engineering problem since we've started with the observed data and from that tried to infer the dominant physical processes giving rise to the phenomena. Time-resolved infrared spectroscopy is the tool by which the phenomenology will be studied. Specifically, spectra collected by a Fourier-transform spectrometer (FTS) during the Radiant Brass III and Brilliant Flash II exercises are the data from which a model of fireball emissions is developed in this dissertation. For each of these two tests, a summary of the instrumentation and signature collection methodology relevant to this work will be provided and will be followed by a brief presentation of some representative data. Detailed descriptions of the tests and thorough explorations of the data can be found in the appropriate references [4, 29, 86]. Preceding this, however, will be a necessary digression into the calibration and use of FTS for measuring transient event signatures.

2.1 Spectro-radiometry via Fourier-transform interferometry

Fourier-transform spectroscopy is a mature discipline based on interferometry, and this technique enjoys several benefits over other forms of spectroscopy including the throughput (Jacquinot) and multiplex (Fellget) advantages [10]. These and other favorable attributes of FTS have lead to its adoption in a multitude of fields requiring spectral information in the infrared. As a result, FTS is a technology that is continually being improved and it is now possible to acquire ruggedized, high-speed interferometers for use in non-laboratory environments, including outer space [9]. However, the transient nature of HE fireballs and the rough environment in which they are studied pushes FTS near the limits of its ability to collect useful data.

15

Table 2: Definitions, symbols, and units associated with several radiometric quantities. When the terms involving radiant energy (L, I, and F) are expressed as a function of $\tilde{\nu}$, the result is a distribution function valid over the infinitesimal range $[\tilde{\nu}, \tilde{\nu} + d\tilde{\nu}]$ and cm^{-1} is appended to the units in the denominator.

Symbol	Name	Units	Definition
A	area	cm^2	projected area of source
R	length	cm	distance between source and collection optic
θ	linear angle	rad	angle between source and collection optic
Ω	solid angle	sr	$d\Omega = \frac{dA}{R^2}$
ϕ	flux	W	radiant energy reaching collection optic per unit time
L	radiance	$\frac{W}{cm^2\,sr}$	$L = \frac{\partial^2 \phi}{\partial A \cos\theta \, \partial\Omega}$
I	intensity	$\frac{W}{sr}$	$I = \frac{\partial\phi}{\partial\Omega} = \int_A L \cos\theta \, dA$
F	irradiance	$\frac{W}{cm^2}$	$F = \frac{\partial\phi}{\partial A_d}$, A_d = area of collection optic
$B_{\tilde{\nu}}$	Planck distribution	$\frac{W}{cm^2\,sr\,cm^{-1}}$	$B_{\tilde{\nu}} \, d\tilde{\nu} = \frac{2\,h\,c^2\,\tilde{\nu}^3}{\exp(h\,c\,\tilde{\nu}/k_B T) - 1} \, d\tilde{\nu}$

After discussing the basic calibration procedure, a brief theoretical discussion of FTS will be presented to unveil potential problems when collecting spectra of transient phenomena.

2.1.1 Calibration. Radiometric terminology follows the SI convention as presented in Dereniak and Boreman's Infrared Detectors and Systems [26]. An important exception to the SI system is the preference of using centimeters for length and wavenumbers $\tilde{\nu}$ (cm^{-1}) to describe spectral quantities. The wavenumber $\tilde{\nu}$ is the reciprocal of wavelength λ (expressed in cm) and is proportional to a photon's frequency ν and the energy of a transition ΔE via the relationship $\tilde{\nu} \equiv \frac{1}{\lambda} = \frac{\nu}{c_0} = \frac{\Delta E}{h\,c_0}$. Here, c_0 is the speed of light in a vacuum and h is Planck's constant. Table 2 defines the basic radiometric units and related terminology used in this work.

A blackbody with circular aperture of area A_{bb} was placed at a distance R_{bb} from the FTS. The multiple temperatures of the blackbody T_i are much larger than the ambient temperature to ensure ample contrast between the calibration source and background. With $R_{bb} \gg \sqrt{A_{bb}}$ and noting that a blackbody source is Lambertian, the resultant irradiance distribution F at the entrance optic can be expressed as

$$F_i(\tilde{\nu}) \simeq \frac{A_{bb}}{R_{bb}^2} B(\tilde{\nu}, T_i) \tag{1}$$

16

where B is Planck's distribution corresponding to the source temperature T_i. In wavenumbers, Planck's distribution is specified as

$$B_{\tilde{\nu}} = \frac{c_1 \tilde{\nu}^3}{\exp\left(c_2 \tilde{\nu}/T\right) - 1} \tag{2}$$

where $c_1 = 2\,h\,c_0^2$, $c_2 = h\,c_0/k_B$, and k_B is the Boltzmann constant.

At each wavenumber, the spectrometer responses $V_i(\tilde{\nu})$ were linearly mapped to the entrance optic irradiances $F_i(\tilde{\nu})$ using a gain (a_1) and offset (a_0) term determined by a least squares fit to i equations

$$V_i(\tilde{\nu}) = a_1(\tilde{\nu})\, G\, T_{atm}(\tilde{\nu})\, F_i(\tilde{\nu}) + a_0(\tilde{\nu}) \tag{3}$$

The gain term accounts for multiplicative effects such as the quantum efficiency of the detector and instrument throughput. The offset term accounts for additive terms such as instrument self-emission and background radiance. The scale factor G accounts for the combined effects of the instruments' pre-amplifier gain setting and the presence of attenuating filters (wire mesh or neutral density), both of which may change[1] to accomodate the wide dynamic range encountered during a field test. The effect of atmospheric attenuation over the distance R_{bb} is estimated by T_{atm} using available meteorological data. In principle, separating atmospheric attenuation from detector response is necessary since the distance between the event of interest is different from R_{bb}.

During the field tests, the FTS was triggered several seconds prior to the detonation event. The raw spectra were converted to intensity using the following method. First, the individual raw background spectra were averaged together to provide an estimate of a_0. Although calibration provides a_0, the background radiance observed during calibration is often substantially different from the background radiance observed during the event collection. The entrance optic flux was computed from

$$F_{obs}(\tilde{\nu}) = \frac{V_{obs}(\tilde{\nu}) - a_0(\tilde{\nu})}{G\, T_{atm}(\tilde{\nu})\, a_1(\tilde{\nu})} \tag{4}$$

---

[1] Ideally, a calibration would be performed for each unique combination of pre-amplifier gain and attenuating filters. A compressed test schedule precluded this possibility for the field tests described in this document. Instead, the manufacturer's gain factor specifications were used and multiplicative effects for the various attenuating filters were experimentally determined.

In principle, the part of a_0 representing background radiance needs to be scaled to account for the fraction of the FOV consumed by the source[2]. The calibration procedure described here does not permit this as the separation of instrument self-emission cannot be distinguished from background radiance. In practice, however, this detail is irrelevant because (1) the choice of optics typically results in source areas much smaller than the total FOV and (2) for most detonation fireball spectra, $V_{obs}(\tilde{\nu}) \gg a_0(\tilde{\nu})$. These details do become important as the fireball approaches the ambient temperature, but these late-time spectra are excluded from analysis because the signal-to-noise ratio (SNR) is poor. For convenience, the measured irradiance is converted to apparent intensity I_{obs} by the distance to the event R, i.e.

$$I_{obs}(\tilde{\nu}) \simeq R^2 F_{obs}(\tilde{\nu}) = T_{atm}(\tilde{\nu}) I_{src}(\tilde{\nu}) \tag{5}$$

where I_{src} is the source intensity and T_{atm} now accounts for atmospheric attenuation over R. The conversion from irradiance to intensity assumes that the source is a Lambertian radiator, the source diameter is much smaller than its distance from the spectrometer, and the source under-fills the instrument's FOV.

To solidify the preceding discussion, Figure 1 presents the raw spectral voltage from an early 50 kg TNT fireball collected during Brilliant Flash 2. Also shown is the average of the background spectra acquired prior to the detonation. The instrument is configured to accommodate the peak intensity of the detonation fireball, and as a result, the combination of low gain and attenuating meshes limits the background emission to a tiny fraction of the total spectral voltage. It is also worth noting that the InSb detector does not have a filter to limit photons with frequencies higher than the Nyquist limit ($\sim 7900\,\mathrm{cm}^{-1}$ for the HeNe laser). Above background voltages are measured near this limit, and as a result, aliasing may be a problem at high wavenumbers. To mitigate this effect, the wavenumber axis was truncated at $7100\,\mathrm{cm}^{-1}$. A plot of the InSb detector response function (i.e., the gain term a_1) as estimated via a calibration is provided in Figure 2. Four temperatures (900, 950, 1000, and 1200 C) were used to estimate the InSb response in terms of photon energies. The peak response occurs near $1865\,\mathrm{cm}^{-1}$ (5.36 μm). Response falls off rapidly at longer wavelengths (detector

---

[2]If the source is opaque, the background behind it does not contribute. If the source is seim-transparent, the photons from the background are likely altered as they propagate throught it.
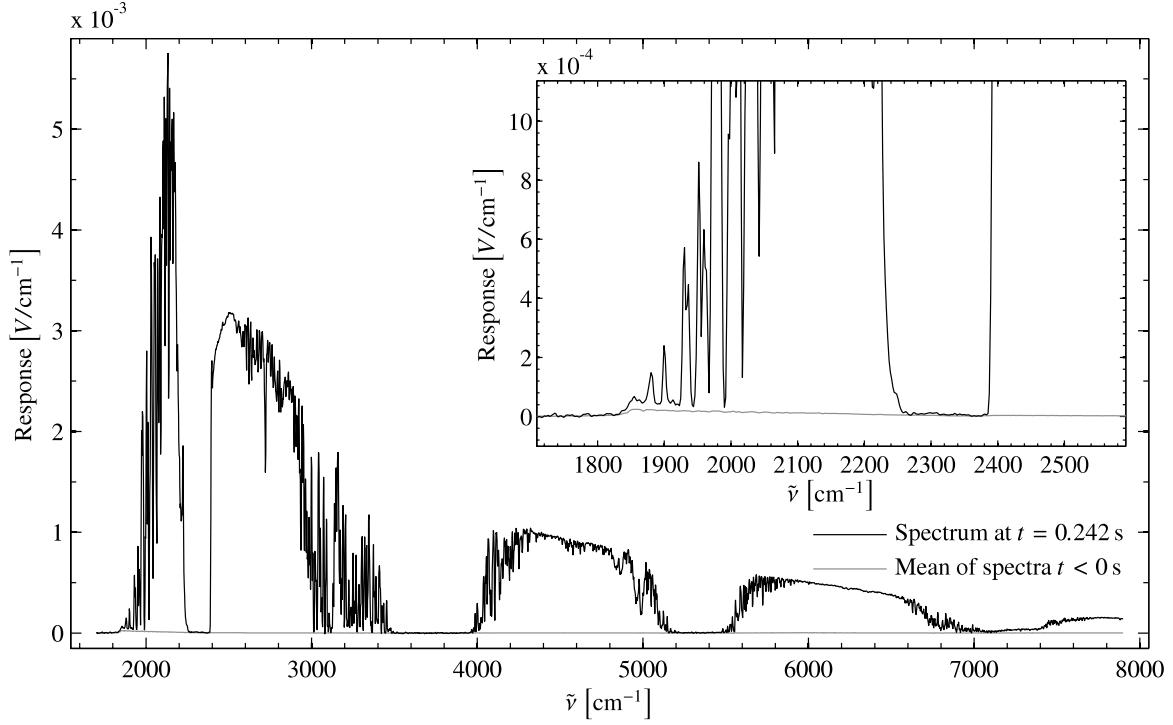
Figure 1: Raw spectral voltage (black) corresponding to a 50 kg TNT detonation fireball. For comparison, the average of the 38 background ($t < 0$) spectra is displayed in grey.

cut-off) and gradually at shorter wavelengths. Note that if the effects of atmospheric transmittance are not properly accounted for, the apparent detector response will be underestimated in regions where significant absorption occurs.

2.1.2 Interferogram processing. In most applications, a properly calibrated FTS will result in useable spectra with the conversion from an interferogram being automatically handled in software. An implicit assumption in this process is that the source is not varying during the acquisition of the interferogram. Detonation fireballs are by nature transient, and it is necessary to briefly examine the process of converting an interferogram to a spectrum to understand possible problems associated with scene-change artifacts, i.e. errors introduced into the spectrum because of a non-static source. In the following analysis, the continuous Fourier transform will be used. Note, however, that the interferograms are converted to spectra using the discrete Fourier transform.
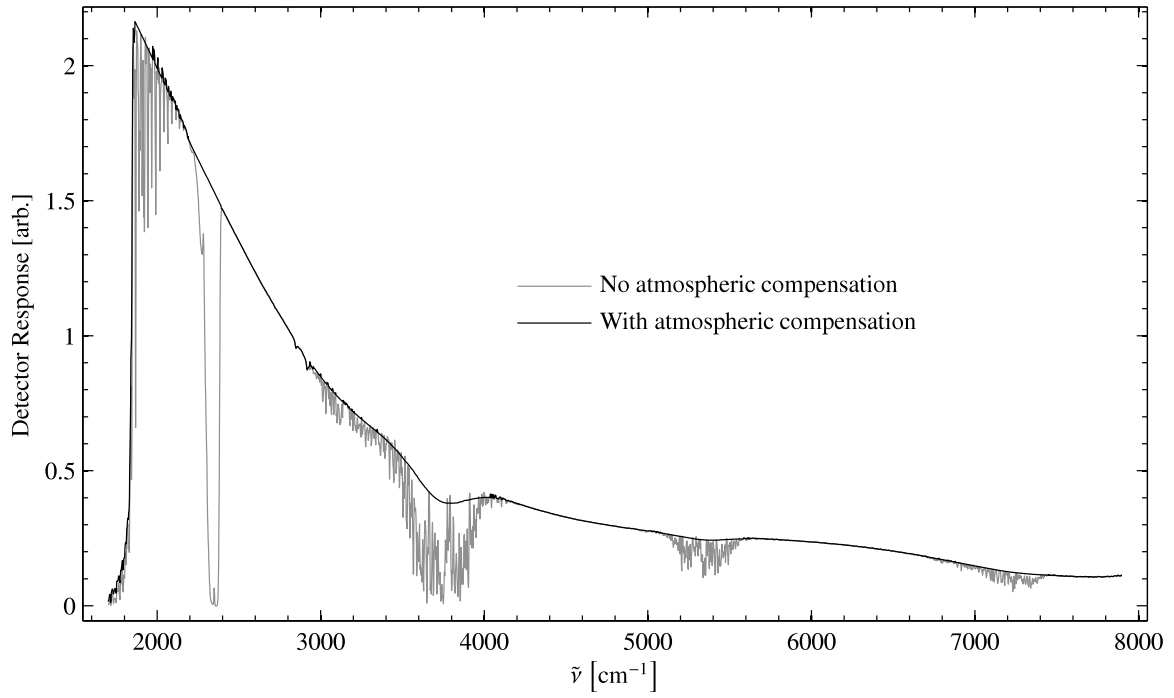
Figure 2: Typical detector response profile (gain a_1) for the InSb detector in the Bomem MR-154 FTS. The arbitrary units are energy-based (not photon-based). The grey curve represents the apparent detector response when viewing a blackbody through a several feet of atmosphere and not compensating for transmittance effects. Accounting for the atmospheric attenuation results in a better estimate of the detector response curve, which is shown in black.

An interferogram y is related to the source spectrum Y by

$$y(\delta) = \int_0^\infty Y(\tilde{v}) \cos\left(2\pi\tilde{v}\delta - \Theta(\tilde{v})\right) \, d\tilde{v} \tag{6}$$

where δ is the optical path difference (cm) between the interfering light beams and Θ is a frequency-dependent phase term accounting for optical, electronic, and sampling effects [46]. For example, imprecise sampling of the point at which perfect constructive interference occurs (i.e., zero path difference or ZPD) would result in a linear phase shift (i.e. a ramp in phase space). Electronic filters are typically responsible for imparting a frequency dependence in this phase term. For instruments that record double-sided interferograms ($-\delta_{max} \leq \delta \leq \delta_{max}$ where δ_{max} is the maximum optical path difference), Θ introduces asymmetry. Noise will also impart asymmetry in the interferogram. The spectrum can be recovered via the Fourier transform

$$Y(\tilde{v}) = \int_{-\infty}^\infty y(\delta) \, e^{2\pi\, i\, \tilde{v}\, \delta} d\delta \tag{7}$$

The true spectrum Y will be distributed across the real and imaginary axes in the complex plane. Phase correction is necessary to rotate the signal into the real plane, leaving noise equitably distributed among both planes.

The simplest method of phase correction is performed by computing complex calibration coefficients (a_1 and a_0). Assuming sources of phase remain constant between calibration and event acquisition, the phase will be accounted for in the complex representation of a_1 and a_0. In a controlled laboratory environment, this assumption is valid. However, vibrations and sudden jolts are common occurrences in the harsh environment encountered during field tests. Such effects were found to alter the instrument's sampling grid which resulted in a new Θ that differed from the phase function present during calibration. To account for this, all interferograms (including calibration) were phase-corrected using the Mertz algorithm [77] as described by Griffiths and de Haseth [46], and only the real components of a_1 and a_0 were used map raw signals back to irradiances.

2.1.2.1 Scene-change artifacts. For a transient event, the change in Y with time may dominate all other sources of asymmetry in the collection of an interferogram. This will impart artifacts in both the real and imaginary components which in general cannot be fixed by phase correction techniques. The nature of these scene-change artifacts (SCAs) was recently investigated by Kick [62]. In his work, he considered a source which smoothly varied between three instantaneous spectra. At the start of the double-sided interferometric collection, the spectrum is Y_1; at ZPD, the spectrum is Y_2; and at the end of the collection, the spectrum is Y_3. For all points in between, the spectrum is described by the unique quadratic polynomial passing through these three points in time. Assuming an ideal interferometer, the following expression for the measured spectrum Y_M was derived

$$Y_M(\tilde{\nu}) = Y_2 - \frac{1}{(4\,\pi\,\delta_{max})^2}\frac{\partial^2\,(2Y_1 - 4Y_2 + 2Y_3)}{\partial\tilde{\nu}^2} + i\,\frac{1}{4\,\pi\,\delta_{max}}\frac{\partial\,(Y_3 - Y_1)}{\partial\tilde{\nu}} \tag{8}$$

where δ_{max} refers to the largest optical path difference in the interferogram and $i = \sqrt{-1}$.

For a scene which changes linearly in time, $Y_2 = (Y_1 + Y_3)/2$ and the second derivative in the real part of Equation 8 will vanish. In other words, the imaginary component will bear evidence of SCAs, but the real part will faithfully represent the instantaneous spectrum Y_2. Only when the scene changes quadratically in time will artifacts impact the real component. Despite this quadratic behavior, the real part is modified by a second-order correction and may be approximated by the instantaneous source spectrum Y_2. Kick demonstrated that at moderate resolution (worse than $0.5\,\text{cm}^{-1}$), the measured spectrum was virtually identical to Y_2 even under extremely non-linear spectral changes during the measurement time. Kick was not studying high-explosive detonations, however, and nothing has been presented which enables an estimation of the magnitude of the correction to the real part in Equation 8. Furthermore, he used the continuous Fourier transform to simulate the effects of SCAs. Real instruments employ the discrete Fourier transform, and it is possible that under some conditions real SCAs will differ from those simulated by the continuous transform. Nonetheless, the counter-intuitive conclusion that SCAs have little practical impact on the real part of the measured spectrum will be supported by analysis in Chapter IV.

2.2   Radiant Brass

Several campaigns under the Radiant Brass (RB) moniker were performed during the late 1990s to characterize infrared emissions from the detonation of conventional military munitions. AFIT collaborated with Wyle Laboratories in the testing performed at the Fallon Range Training Complex in Nevada over the periods 2-5 August 1999 (phase 3A) and 25-29 October 1999 (phase 3B). What follows is a quick overview of the RB3 tests; consult Orson's masters thesis [86] for a more thorough discussion. For RB3A, an F/A-18 aircraft was used to deliver 33 general purpose bombs using three different approach vectors, namely 65, 155 or $355°$ with respect to the instrumentation line-of-sight. 23 of the same types of munitions were statically detonated during RB3B. The HE was either Tritonal or H-6, and was enclosed in an iron shell. Tritonal is a mixture of 80% TNT and 20% aluminum. H-6 is comprised of RDX (~45%), TNT (30%), aluminum (21%) and a binding wax (4%). Three different weapon sizes were studied and are generically labeled small (S), medium (M), or large (L). The specific high explosive is generically labeled by A or B. Analysis of 18 events (13 AS and 5 BL) collected during RB3B is the subject of Chapter III.

AFIT deployed an ABB-Bomem MR-154 Fourier-transform spectrometer, a dual-channel interferometer, to collect moderate-resolution spectra in the midwave infrared (MWIR). The instrument was configured with InSb (1.6–5.6 μm) and HgCdTe (2.0–20 μm) detectors and was typically operated at a nominal spectral resolution of $16\,\text{cm}^{-1}$ ($\Delta\tilde{\nu} = 7.71\,\text{cm}^{-1}$) with a collection frequency of 21 Hz. A few detonation spectra were collected at $4\,\text{cm}^{-1}$ resolution ($\Delta\tilde{\nu} = 1.93\,\text{cm}^{-1}$) which reduced the acquisition rate to roughly 8 Hz. Data from the HgCdTe detector were noisy and not studied. The instrument was coupled to a 76 mrad full field-of-view (FFOV) telescope. Detonations occurred between 3.2–4.9 km away from the instruments on a variety of earth surfaces including clay craters, hard sand, and rock. An illustration of the test geometry and event locations is provided in Figure 3. An Electro Optics LS1050 blackbody placed 76 in. from the FTS was used for calibration. Double-sided interferograms were collected (2048 pts @ $16\,\text{cm}^{-1}$, 8192 pts @ $4\,\text{cm}^{-1}$) and individually phase corrected via the Mertz algorithm [77] using 384 points on each side of the centerburst. Co-adding of interferograms was not performed given the transient nature of the events being studied.

39.910

39.905

39.900

39.895

39.890

39.885

39.880

39.875

39.870

■ Instrument Suite

Clay Craters

2 km radius

BL Events

Sand Dune

AS Events

Hard Sand

Lone Rock

Rock/Rubble

4 km radius

Latitude (degrees N)

118.39   118.38   118.37   118.36   118.35   118.34   118.33

Longitude (degrees W)
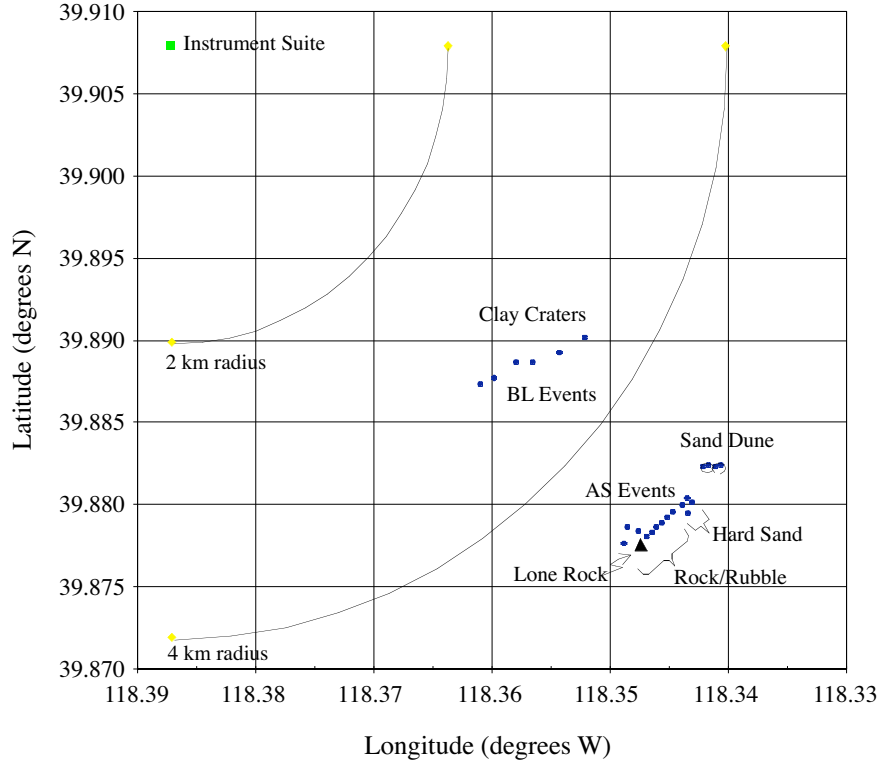
Figure 3:   Test geometry for the Radiant Brass phase 3B field exercise.

Wyle Laboratories deployed a 4-channel, 200 Hz radiometer using InSb detectors. A different bandpass filter was used in front of each detector to limit its responsivity to a narrow portion of the midwave infrared. An Agema (now FLIR Systems) 900 THV camera featuring both an InSb and an HgCdTe focal-plane array (FPA) (each 272x136 pixels) provided MWIR imagery at 8 Hz. Orson's initial comparisons of FTS data integrated over the appropriate bandpass filter transmissions suggested good radiometric agreement with the Wyle radiometers [86]. Unfortunately, Wyle's radiometer and imagery data were unavailable for this work, and a more thorough comparison of instrument data could not be performed.

2.2.1 RB3 data summary.   A typical data cube collected by the MR-154 of a statically detonated AS bomb is presented in Figure 4. The intensity briefly grows with time and is followed by a smooth decay to background. The rate of this decay is strongly dependent on frequency. This is particularly evident in Figure 5 which compares two spectra from this data cube. After about 1 s, the intensity is near $0 \, \mathrm{W/sr/cm^{-1}}$ at $6000 \, \mathrm{cm^{-1}}$; at $2000 \, \mathrm{cm^{-1}}$, the intensity has only decayed to roughly 1/5 of its peak value in the same time.
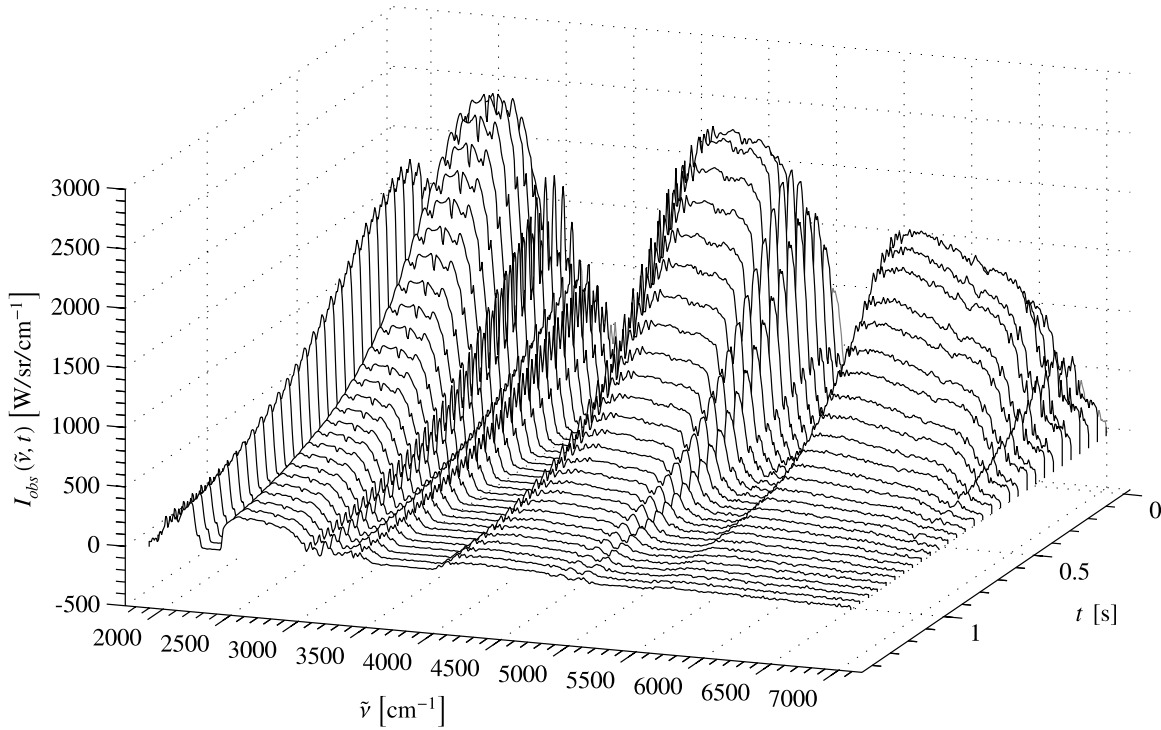
Figure 4: Waterfall plot of apparent intensity from a type AS conventional munition detonation. The nominal spectral and temporal resolutions are $16\,\mathrm{cm}^{-1}$ and $21\,\mathrm{Hz}$, respectively.

The estimated atmospheric transmittance profile is also provided in Figure 5 and it is clear that nearly all of the spectrally sharp features in the intensity profiles correspond to absorption features in the transmittance function. (Most of the absorption features are due to trace atmospheric gases such as H_2O and CO_2.) It follows that the fireball source spectrum in the MWIR is a fairly smooth, slowly-varying function of frequency. A rudimentary analysis of the data by Orson suggested that the broadband source behavior could be crudely fit[3] to a single-temperature Planckian distribution [86, 87]. Improvements to this analysis by the author were reported in the literature [48, 49]. Chapter III summarizes these efforts, and it will be shown that the spectral and temporal behavior of these conventional munition fireballs are reasonably described by a single-temperature greybody radiator which cools in time.

The imaginary component of the spectrum at $t = 0.10\,\mathrm{s}$ is also provided in Figure 5 to assess the potential impact of scene-change artifacts. The imaginary component was multiplied by 5 to make its structure more evident. In the absence of SCAs, the imaginary component provides a "snapshot" of the noise level

---

[3]Effects of atmospheric attenuation were not accounted for in Orson's analysis.
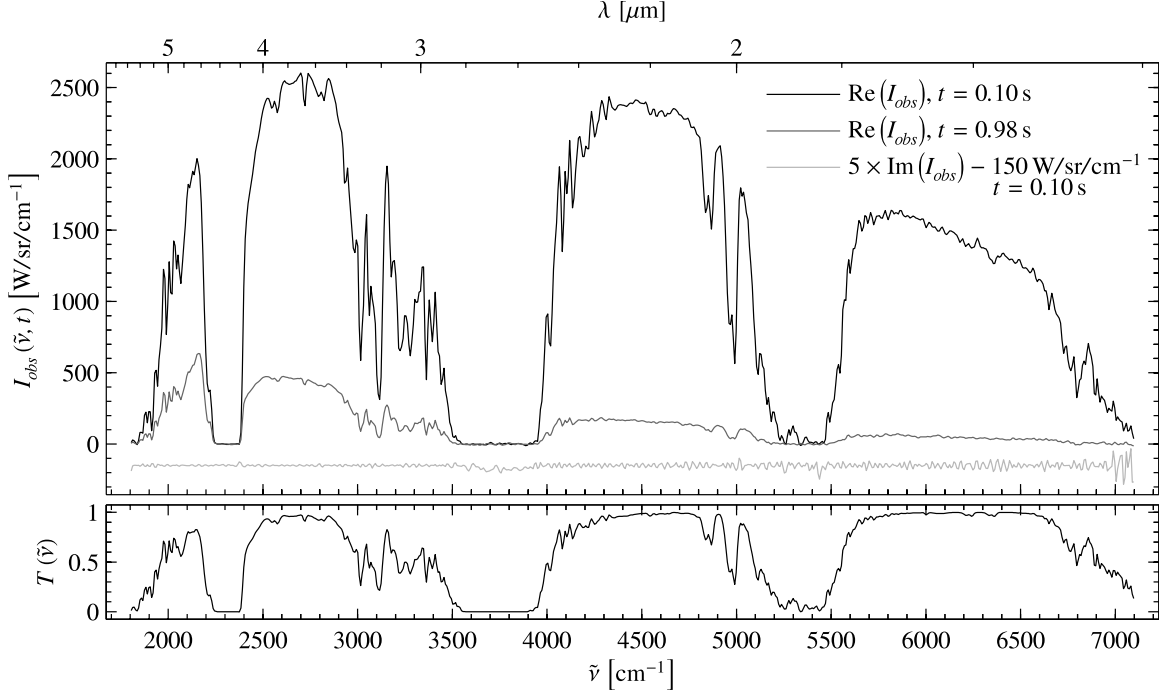
Figure 5: *Top panel*: Apparent spectral intensity of a type AS bomb at $t = 0.1\,\text{s}$ and $t = 0.98\,\text{s}$. *Bottom panel*: The estimated transmittance profile computed from meterological data collected near the time of this detonation event.

of the instrument. Examination of the imaginary component does not reveal any obvious structure that is distinguishable from white noise. This does not rule out the presence of SCAs, but rather suggests that the impact of SCAs on this spectrum is indistinguishable from other noise sources. In the next section, evidence of SCAs will be visible in the imaginary spectrum.

2.3 Brilliant Flash

The Brilliant Flash (BF) field tests were convened to characterize electro-optical emissions from detonated IEDs constructed from readily-available components. The IEDs studied in the BF tests were termed enhanced novel explosives (ENEs) as they were formulated with "booster" ingredients that enhance afterburning and sustain the overpressure duration. Special emphasis was placed on finding characteristics which distinguish these ENEs from conventional engineered explosives such as tri-nitro-toluene (TNT). The first campaign (BF1) occurred over the period 9-15 July 2002 at the Air Force Research Laboratory test range at Tyndall AFB. The second campaign (BF2) occurred during the period 2-13 June 2003 at the Utah Test and

Training Range (UTTR). The AFIT team collaborated with ATK/MRC, the lead ground-truth team, during both field exercises.

The spectrometer configuration during BF1 resulted in many fireballs which over-filled the instrument's field-of-view (FOV) and precluded conversion to apparent intensity. The phenomenological model of fireballs developed in Chapter IV requires intensity data to decouple the effects of size (projected area) and radiance. As a result, the spectra collected during BF1 were not studied in this work and details of the test will not be discussed.

The plan for BF2 was to collect signatures from TNT and three types of ENEs. All ENEs have some baseline ingredients in common. The addition of two distinct "booster" ingredients and the use of different relative amounts of the baseline ingredients resulting in HEs labeled by ENE1 and ENE2. Midway through the test, changes were made to the ENE mixtures resulting in a total of 5 distinct HEs labeled ENE0A, ENE0B, ENE1, ENE2A, ENE2B. The HEs were either 10, 50, 100, or 1000 kg in size and a block of C-4 (10% by weight) was used to initiate the detonation. The effective stoichiometric composition of the ENEs, accounting for the C-4 detonator, is provided in Table 3. Included in the table is each explosive's oxygen ratio, a measure of the available oxygen in the HE relative to the oxygen needed to fully oxidize the HE atomic constituents. The explosives considered in this work contain in various proportions C, H, N, O, and Al; for short they will be referred to as CHNOAl explosives. The fully-oxidized byproducts of CHNOAl explosives are CO_2, H_2O, and Al_2O_3; nitrogen is converted to N_2 as it is thermodynamically favored over various oxygenated nitrogen compounds. A total of 44 high explosives were detonated during the test, and the event matrix in Table 4 presents the distribution of events according to weight and type.

The suite of instruments was located on an elevated knoll approximately 3.26 km from the detonation zone as illustrated in Figure 6. The ABB-Bomem MR-154 was configured with the InSb and HgCdTe detectors and successfully collected 40 of the 44 events at 4 cm^{-1} resolution at 8 Hz. Double-sided interferograms consisting of 8192 points were collected. Phase correction was performed with 384 points on each side of the centerburst using the Mertz algorithm. The FTS was coupled to a 28 mrad telescope providing a circular field-of-view with a diameter of approximately 90 m at the target. Several Electro Optics blackbodies

Table 3:   Relative amounts of the atomic constituents found in the different explosives used in the Brilliant Flash II field test. The amounts account for the presence of C-4 used to detonate the explosive. Oxygen ratio denotes the amount of O_2 available in the HE relative to the amount needed for full oxidation (e.g. $C \rightarrow CO_2$, $2H \rightarrow H_2O$, and $2Al \rightarrow Al_2O_3$).

HE	C	H	N	O	Al	Oxygen Ratio
TNT	1.00	0.79	0.48	0.89	0.00	0.370
ENE0A	1.00	24.02	12.36	17.90	4.08	0.889
ENE0B	1.00	21.26	10.99	15.83	6.12	0.726
ENE1	1.00	6.74	2.62	4.26	3.76	0.388
ENE2A	1.00	5.84	2.49	4.05	3.57	0.394
ENE2B	1.00	6.71	2.93	4.71	2.92	0.484

Table 4:   Number of detonation events successfully collected by the MR-154 during Brilliant Flash II categorized by the type and size of the high explosive. Quantities in the parenthesis denote the total number of high explosives detonated during the test.

HE	10 kg	50 kg	100 kg	1000 kg
TNT	4 (4)	4 (5)	2 (3)	1 (1)
ENE0A	1 (1)	0 (0)	0 (0)	0 (0)
ENE0B	0 (0)	4 (4)	2 (2)	0 (0)
ENE1	1 (1)	3 (4)	3 (3)	1 (1)
ENE2A	1 (1)	3 (4)	2 (2)	1 (1)
ENE2B	0 (0)	4 (4)	1 (1)	1 (1)
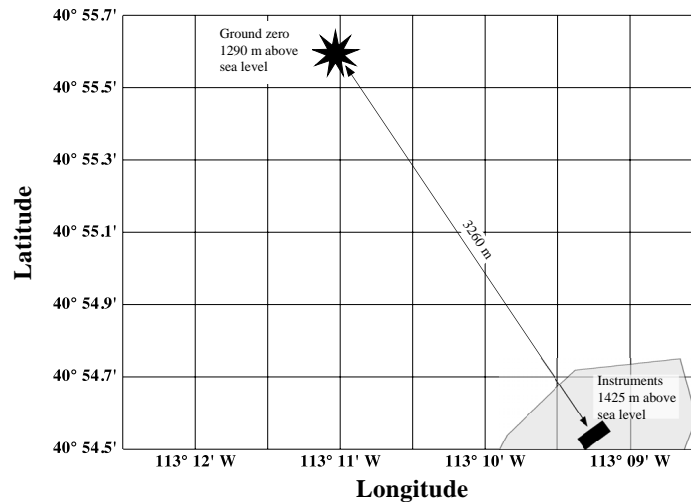
Figure 6:   Brilliant Flash II test geometry indicating the coordinates of the instrument suite and the detonation site.

with temperatures between 900–1000 K were used to calibrate the spectrometer as described in Dills' test report [31]. The MR-154 was approximately 15 m away from the calibration source. At this distance, the blackbody aperture–which is on the order of an inch–was a small fraction of the instrument's field-of-view. In the MWIR, the blackbody temperatures provided ample contrast from the 300 K background scene despite the small aperture size. However, in the long wave infrared, there was not sufficient contrast as the background radiance dominated the signal, and the HgCdTe spectra could not be reliably calibrated in the 500–1200 cm^{-1} region. The HgCdTe data awaits a proper post-calibration and is not considered in this work. The apparent intensity of the fireballs spanned a wide dynamic range and scaled with the weight of the high explosive. To maximize SNR, the MR-154 configuration was taylored to the expected photon levels using a combination of wire mesh filters and different electronic gain settings. These settings were transcribed in a notebook as the instrument software could not automatically track the gain level or the presence of mesh filters. In some cases, insufficient signal attenuation resulted in a few saturated interferograms early in the collection sequence. The corresponding corrupted spectra were excluded from analysis.

AFIT deployed several other instruments to UTTR which are briefly described. A Princeton Instruments 0.25 m grating spectrometer was used to collect visible spectra. Infrared imagery was collected by an Indigo Systems Alpha NIR camera, featuring an InGaAs (0.9–1.7 μm) FPA framing at 30 Hz. A Canon XL-1 3-chip video camera provided audio-visual documentation of the test and was also used for quantitative analysis of fireball size. A thorough analysis of the imagery can be found in Dills' publications [29, 30, 32]. The ATK/MRC team deployed a 4-channel, 200 Hz radiometer[4]; each channel featured a different bandpass filter. They also used an ABB-Bomem MR-354 FTS, an interferometer featuring acquisition rates and input optics superceding those of the MR-154. The MR-354 collected spectra at 4 cm^{-1} resolution at a rate of 34 Hz. The MR-354 lacked a cold reference and used a different InSb detector, and as a result, the instrument SNR was poor compared with the MR-154. Furthermore, the effective spectral range was limited to 2000–4500 cm^{-1}. A collection of meterological instruments were employed to monitor temperature, pressure, and atmospheric water vapor and enabled good estimates of atmospheric transmittance profiles in the infrared.

---

[4]The radiometer actually sampled at 2 kHz; however, the resulting time profiles were noisy and were downsampled to 200 Hz to improve the SNR.
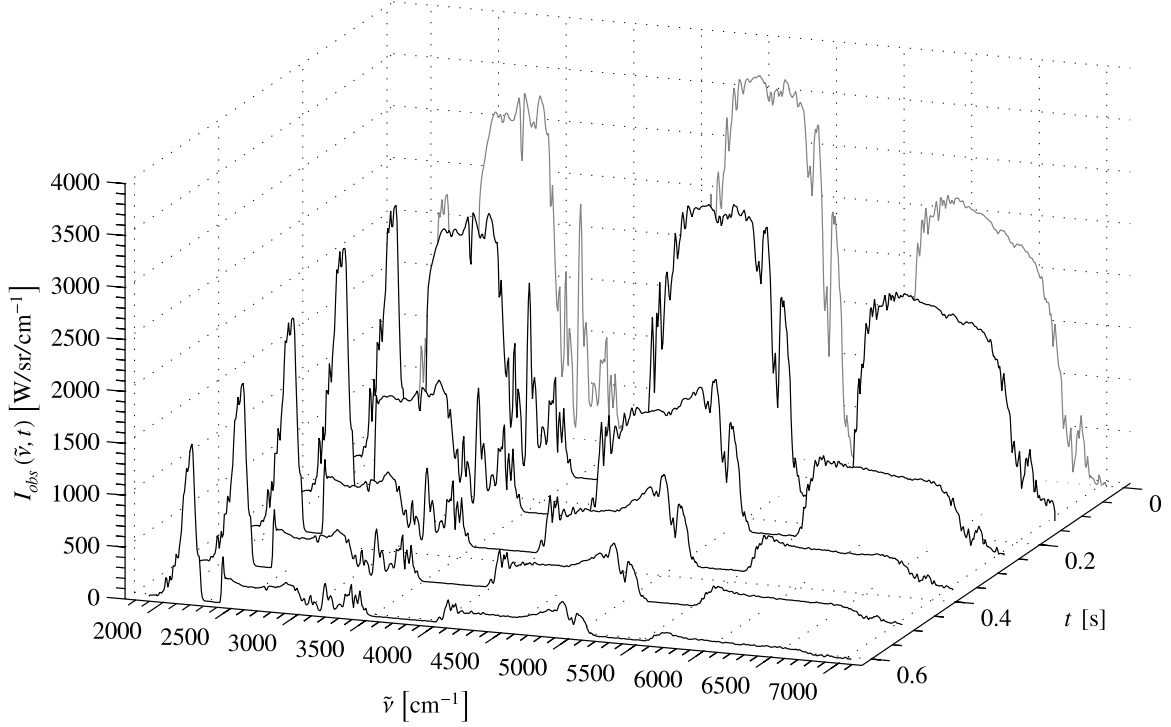
Figure 7: Waterfall plot of apparent intensity from the detonation of 50 kg of TNT. The spectral resolution has been degraded to $16\,\mathrm{cm}^{-1}$ to improve visibility of the gross structure. The temporal resolution is approximately 8 Hz. The centerburst of the interferogram corresponding to the grey spectrum saturated the detector so the absolute intensity is uncertain.

2.3.1 BF2 data summary. The data cube collected by the MR-154 of a 50 kg TNT detonation is provided in Figure 7. The spectral resolution has been degraded to a resolution of $16\,\mathrm{cm}^{-1}$ to improve visibility. Initially, the spectrum is similar to those of conventional munitions. However, the general shape of the spectrum quickly becomes more complex than the conventional munitions examined during RB3. In the MWIR, the duration of emissions from a TNT or ENE detonation is between 0.5–4 s, with emissions from larger explosives being brighter and lasting longer than smaller ones. During that time, the measured flux spans about three orders of magnitude with a decay that is approximately exponential. For a given HE weight, the ENE fireballs were brighter than the TNT fireballs.

A view of the spectrum at full resolution is displayed in Figure 8 along with the corresponding atmospheric transmittance profile. Many absorption features are present in the observed fireball spectrum and correspond to attenuation by trace atmospheric gases, most notably water and carbon dioxide. Water vapor is responsible for the majority of the absorption features although carbon dioxide (CO_2) and methane (CH_4)

30
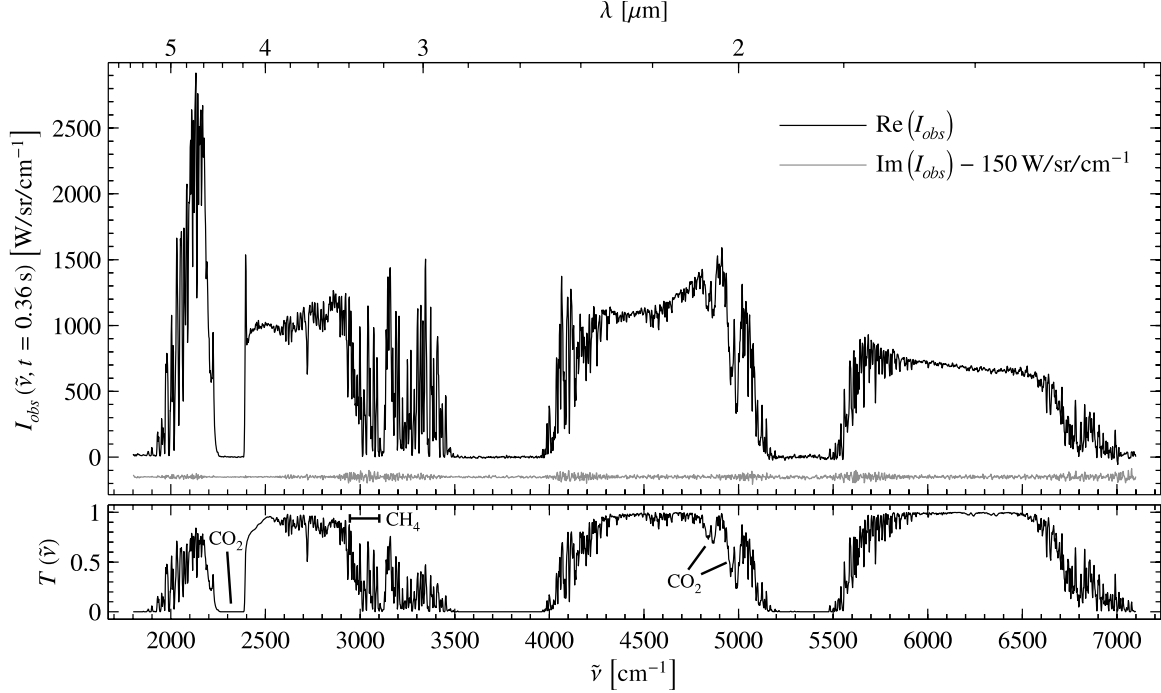
Figure 8: *Top panel*: Apparent spectral intensity from the detonation of $50\,\mathrm{kg}$ of TNT at $t = 0.36\,\mathrm{s}$. The imaginary component of the spectrum has been offset and is shown in grey. *Bottom panel*: The estimated transmittance profile computed from meterological data collected near the time of this detonation event. Most of the absorption features are due to water vapor; a few regions are noted in which attenuation is the result of other trace gases.

strongly attenuate in the indicated regions. Water and carbon dioxide are the fully-oxidized byproducts of hydrocarbon combustion, and the corresponding atmospheric absorption bands indicate spectral regions in which emissions from these products would be expected. The high temperature of the fireball enables the population of ro-vibrational states not accessable at atmospheric temperatures which leads to emission "in the wings" of the strong H_2O and CO_2 absorption bands. It will be shown in Chapter IV that the observed emission patterns are consistent with this interpretation. The simple Planckian fireball model will be extended to incorporate these hot-gas emissions and the continuum emission will be described by small particulate emitters. This improved model fits the observed spectra well and provides physical features which distinguish the TNT fireballs from the various ENE fireballs.

Examination of the imaginary component of the spectrum in Figure 8 suggests evidence of SCAs given the presence of systematic structure above white noise levels in specific spectral regions. White noise levels can be estimated by examining the spectral regions with no signal due to total atmospheric attenuation. The

structure in the imaginary component corresponds to regions in which the slope of the atmospheric transmittance function is large. This is consistent with Kick's analysis given that the contribution from T_{atm} will influence the derivatives appearing in Equation 8. The presence of SCAs in the imaginary component, if visible at all, were discernible only in the first few spectra. After that, the signal had decayed to a level at which SCAs could not be distinguished from instrument noise.

The impact of SCAs on the real part of fireball spectra cannot be strictly known. However, during the BF2 test a faster FTS (MR-354, 34 Hz) collected spectra of the same events at the same spectral resolution, and a comparison of nearly coincident spectra from both instruments enables an order-of-magnitude estimate of SCAs. A 50 kg TNT event was randomly chosen and the fireball spectra collected closest in time ($t \simeq 0.20$ s, $\Delta t \simeq 0.01$ s)[5] by the instruments are compared in Figure 9. To mitigate the effects of radiometric errors, each spectrum was normalized. For reference the 3σ error level of the noisier MR-354 is provided where σ is the standard deviation about the mean static background spectra acquired prior to detonation. The difference between the two spectra is small compared with the total intensity and is comparable to the 3σ level of the MR-354. Assuming the MR-354 is unaffected by SCAs, this difference provides an upper-bound on the effect of SCAs on the real component of the MR-154 spectrum. It is likely that other factors, for example the slight difference in time between the two spectra, also contribute to this difference. Note that if SCAs were strongly affecting the MR-154 spectrum, a discernable systematic change in the high-frequency "noise" in the spectral region of 2900–3500 cm^{-1} might be expected on the basis of a large second derivative of the atmospheric transmittance function (chain rule applied to Equation 8) in that region. Encouragingly, this does not appear to be the case. Rather, the difference between the MR-154 and MR-354 spectra exhibits mostly broadband variations with wavenumber and the magnitude of the high-frequency "noise" component appears to trend nicley with the 3σ profile from the MR-354. Additional analysis in Chapter IV will demonstrate more convincingly that SCAs have no practical impact on the real part of the spectrum.

---

[5]The difference in time is less than the temporal resolution of the MR-354. An examination of the interferograms was performed to establish precisely when the detonation occurred during the mirror travel. This resulted in an offset applied to each time vector as reported from each instrument.
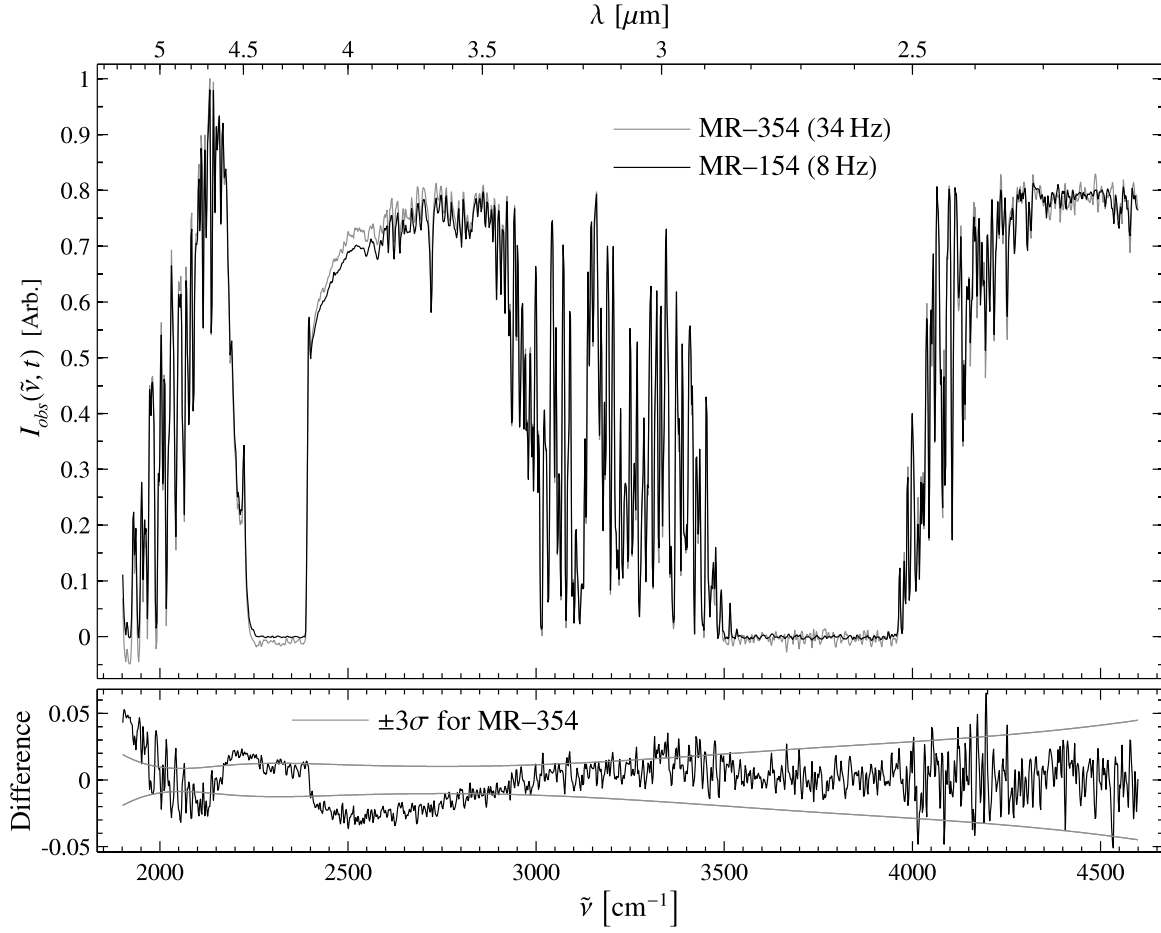
Figure 9: Top: Comparison of 50 kg TNT fireball spectra collected by the MR-154 (black, $t = 0.21$ s) and MR-354 (grey, $t = 0.20$ s). Each spectrum was normalized to minimize radiometric differences. Bottom: Difference between the two spectra (black) and the $\pm 3\sigma$ curve for the MR-354, where σ is the standard deviation of the normalized background spectra.

Radiometric agreement between ATK/MRC's radiometer suite and MR-354 was typically good and fairly consistent. And in some cases, agreement between AFITs MR-154 and ATK/MRC's instruments was good as well. Figure 11 presents a case in which the agreement between the two spectrometers and a radiometer is excellent. The spectrometer data was integrated over the filter bandpass used in the radiometer. The inset plot illustrates the filter transmittance as well as the atmospheric transmission profile in that region. Unfortunately, the agreement between the MR-154 and the ATK/MRC's instrumentation was not always this good, and in some cases peak intensities differed by as much as a factor of 4. Figure 11 summarizes the relative differences in time-integrated intensity over 2–5 μm for the two spectrometers[6]. For 28 events, the integrated intensities agreed to within 50%, but relative differencse as large as 125% were found among the remaining 9 co-observed events. Because of the favorable agreement between the radiometers and MR-354, the data collected by those instruments were considered the best estimates for absolute apparent intensity. For each data set, a single multiplicative scale factor was determined for the MR-154 which enabled the best match to apparent intensities recorded by the ATK/MRC instruments.

---

[6]For both instruments, each spectrum in time was integrated over 2–5 μm. The resulting intensity profile was then integrated over the duration of the event in time. Periods of time were excluded in which either of the instruments' data was corrupt due to detector saturation.
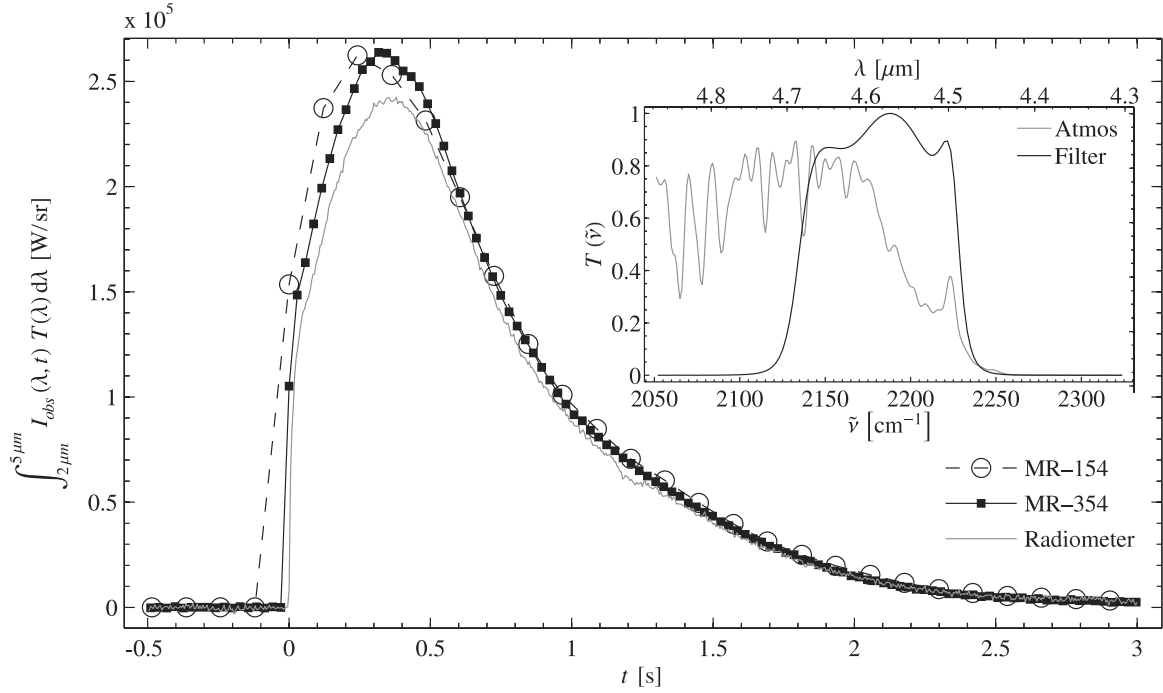
Figure 10: Comparison of absolute intensities collected by a radiometer, the MR-354 and the MR-154 for the detonation of 100 kg of ENE1. The inset plot indicates the transmittance T of the bandpass filter (black) used by the radiometer and over which the spectral data was integrated. Also provided in the inset plot is the atmospheric transmittance profile (grey) in that spectral region.
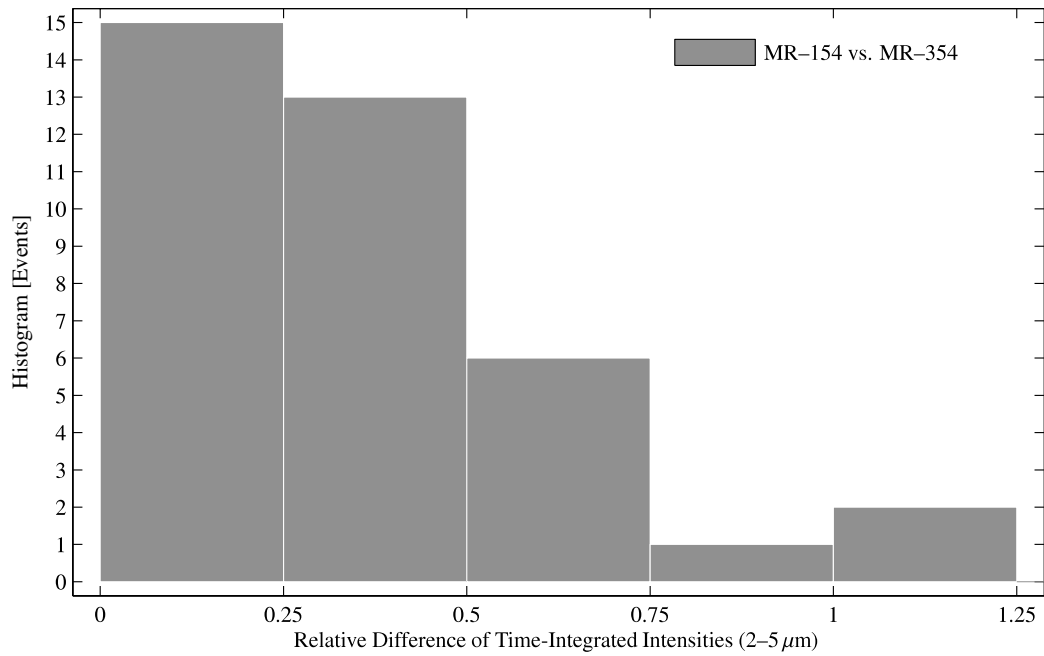
Figure 11: Relative difference of time-integrated intensities measured by the MR-154 and MR-354 in the form of a histogram.

III. Greybody Fireball Model

In this chapter, it will be demonstrated that the general behavior of MWIR emissions from conventional munition detonation fireballs can be described by a single-temperature Planckian distribution. This presentation represents a brief summary of work previously reported by the author [49], which was built upon the efforts of previous AFIT students [4, 86, 87]. A short discussion of multi-temperature Planckian fits to conventional munition detonation spectra will also be provided. The data examined in this chapter comes from the Radiant Brass III-B field test.

3.1 Single-Temperature Model

As discussed in the previous chapter, the spectra of conventional military munitions (CMM) are characterized by broadband emission. Perhaps the simplest possible description of the CMM emissions comes from assuming a homogeneous fireball in thermodynamic equilibrium, radiating as a greybody. In this case, the expected intensity as a function of wavenumber and time can be expressed as

$$I_{obs}(\tilde{\nu}, t) = T(\tilde{\nu})\, \varepsilon A(t)\, B(\tilde{\nu}, \mathrm{T}(t)) \tag{9}$$

where T represents the effects of atmospheric attenuation, ε is the frequency-independent emissivity, A is the area of the fireball as projected into the observation plane, and B is the Planckian distribution at temperature T. In a non-imaged spectrum, ε and A cannot be determined independently, so the results will be discussed in terms of the emissive area εA. Atmospheric data (pressure, temperature, and wet-bulb temperature) were collected on-site and fed to the radiative transfer code LBLRTM [21] to compute the atmospheric transmittance profile T. (The atmospheric data was not available at the beginning of this project. This lead to the development of a general-purpose method for inverting the atmospheric state from the data itself. This method is presented in Appendix A.)

The results of fitting Equation 9 to the initial spectrum of an AS (type A small) CMM fireball are presented in Figure 12. The optimum fit parameters for this spectrum were T $= 1732(8)$ K and $\varepsilon A = 173(3) \times 10^4\, \mathrm{cm}^2$. The quantity in parentheses represents the statistical uncertainty in the fit parameter as
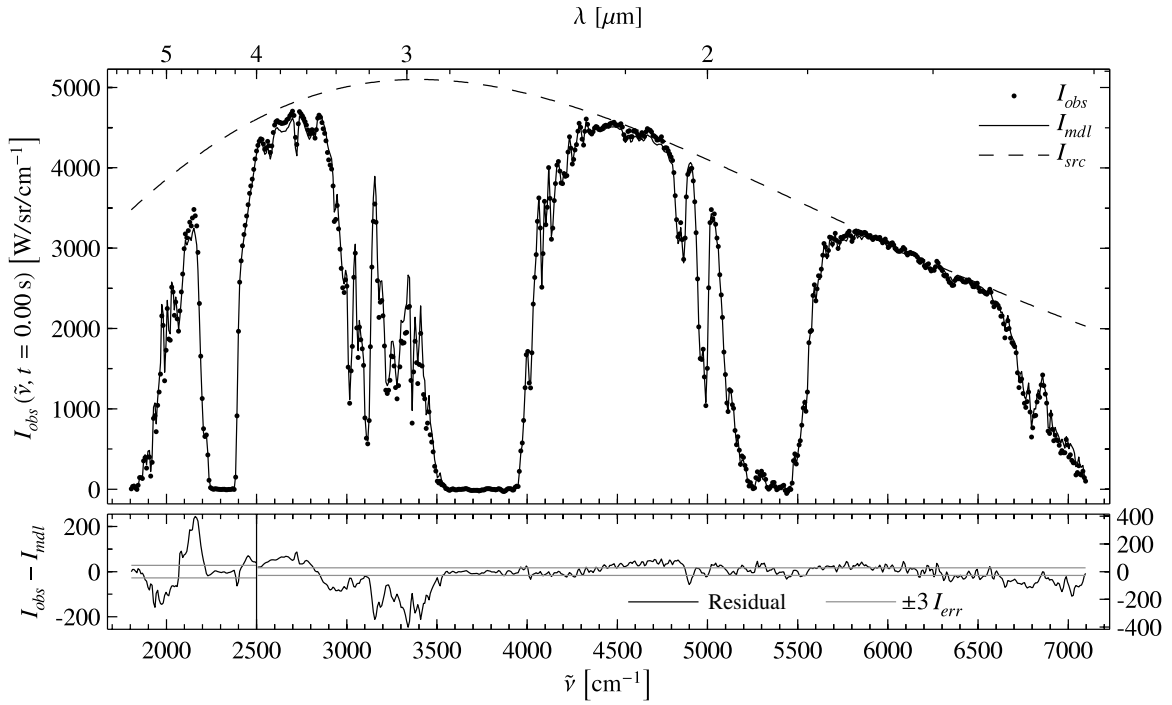
Figure 12: *Top panel*: Initial observed fireball spectrum (·) from the detonation of an AS CMM compared with the best fit model (solid line). The estimated at-source Planckian intensity distribution is also provided (dashed line). *Bottom panel*: Fit residuals ($I_{obs} - I_{mdl}$, black) compared with I_{err} (grey), which is an estimate of the instrument noise level. The left ordinate is used for $\tilde{\nu} < 2500\,\mathrm{cm}^{-1}$ and the right ordinate corresponds to $\tilde{\nu} \geq 2500\,\mathrm{cm}^{-1}$.
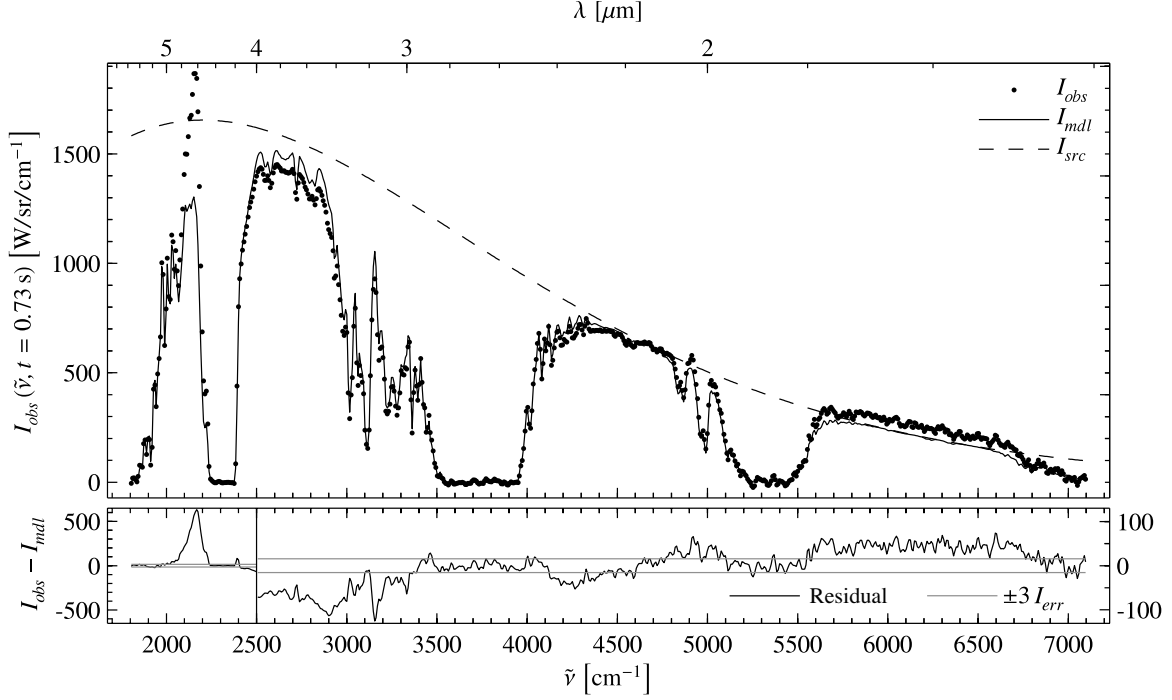
Figure 13: *Top panel*: Observed fireball spectrum at $t = 0.73$ s ($\cdot$) from the detonation of an AS CMM compared with the best fit model (solid line). The estimated at-source Planckian intensity distribution is also provided (dashed line). *Bottom panel*: Fit residuals ($I_{obs} - I_{mdl}$, black) compared with I_{err} (grey), which is an estimate of the instrument noise level. The left ordinate is used for $\tilde{\nu} < 2500\,\text{cm}^{-1}$ and the right ordinate corresponds to $\tilde{\nu} \geq 2500\,\text{cm}^{-1}$.

measured by the 95% confidence interval. The fit quality is good, although some systematic error is evident in the fit residuals ($I_{obs} - I_{mdl}$) between 1900–2200 and 3000–3500 cm^{-1}. For comparison, ± 3 sigma bounds are provided. These bounds are computed from a notional estimate of the instrument noise level I_{err}, where $I_{err} = \text{RMS}(\text{im}(I_{obs}(\tilde{\nu}))$ and RMS denotes the root-mean-squared (RMS) value. Note that two ordinate scales are provided—one for $\tilde{\nu} < 2500\,\text{cm}^{-1}$ and the other for $\tilde{\nu} \geq 2500\,\text{cm}^{-1}$—to improve visibility of the residuals. For this spectrum, the RMS value of the residuals was 85 W/sr/cm^{-1}. In regions where SNR > 5 and $T_{atm}(\tilde{\nu}) > 0.05$, the RMS relative error was 9.1%. In the median, the relative error was 1.7% in magnitude, suggesting excellent fit quality over most of the spectral region. Subsequent relative errors will be reported for spectral regions satisfying the SNR and T requirements just stated. The standard error (SE) of the fit is 9.2, i.e. the residuals are on average ~9 times greater than the estimated noise level I_{err}.

Performing the same Planckian fit at a later time ($t = 0.73$ s) results in poorer agreement with the data as seen Figure 13. There appears to be evidence of a strong selective emission feature near 2100 cm^{-1}

38

as indicated by the large, narrow, and positive residual in this spectral region. It is likely due in part to emission from hot CO or CO_2, both of which are capable of emitting in this region due to nearby fundamental vibrational modes. Additionally, CO_2 would be expected to have various overtone and combination bands populated as a result of the high fireball temperature. Inclusion of selective emitters in the fireball model will be the topic of Chapter IV. Systematic errors smaller in magnitude span the rest of the collection bandpass. Despite these obvious systematic errors, the gross behavior of the observed spectrum is captured by the Planckian fit. The total intensity had decreased by the observation time and the RMS residual value was $76 \, \text{W/sr/cm}^{-1}$. The standard error increased to 14.7, as did the RMS and median magnitude relative errors which were 14% and 8.6%. The fitted temperature and emissive area were $T = 1218(18) \, \text{K}$ and $\varepsilon A = 206(14) \times 10^4 \, \text{cm}^2$. Of course, these values are biased estimates given the presence of systematic errors; however, they likely serve as decent approximations to the average fireball temperature and emissive area. It will be shown in § 3.4 that inclusion of a second Planckian term dramatically improves the fit to this spectrum, suggesting that some of the systematic error can be explained in terms of temperature variation across the fireball.

3.2   Fit Parameter Temporal Dynamics

The temporal behavior of the fit parameters for the AS CMM discussed above are presented in Figure 14. Temperature smoothly and monotonically decayed with time, suggesting that the cooling processes dominated any exothermic chemistry that might have been occurring at the same time. The temperature curve is reasonably described by an exponential decay with an initial temperature of 1788(24) K and a decay rate of $0.76(0.2) \, \text{s}^{-1}$. However, an exponential curve does not capture all the variation in $T(t)$. A more complete phenomenological description of temperature dynamics will be postponed until Chapter V. The εA curve is more interesting, particularly in the beginning. Assuming ε constant, the fireball initially expands rapidly before assuming a slower, more constant growth rate. Of course, this initial behavior could also be the result of a rapid decrease in emissivity with time. The emissive area dynamics await confirmation with MWIR imagery. While the temperature is typically accurate to within a few percent, the uncertainty in εA is 3–6 times
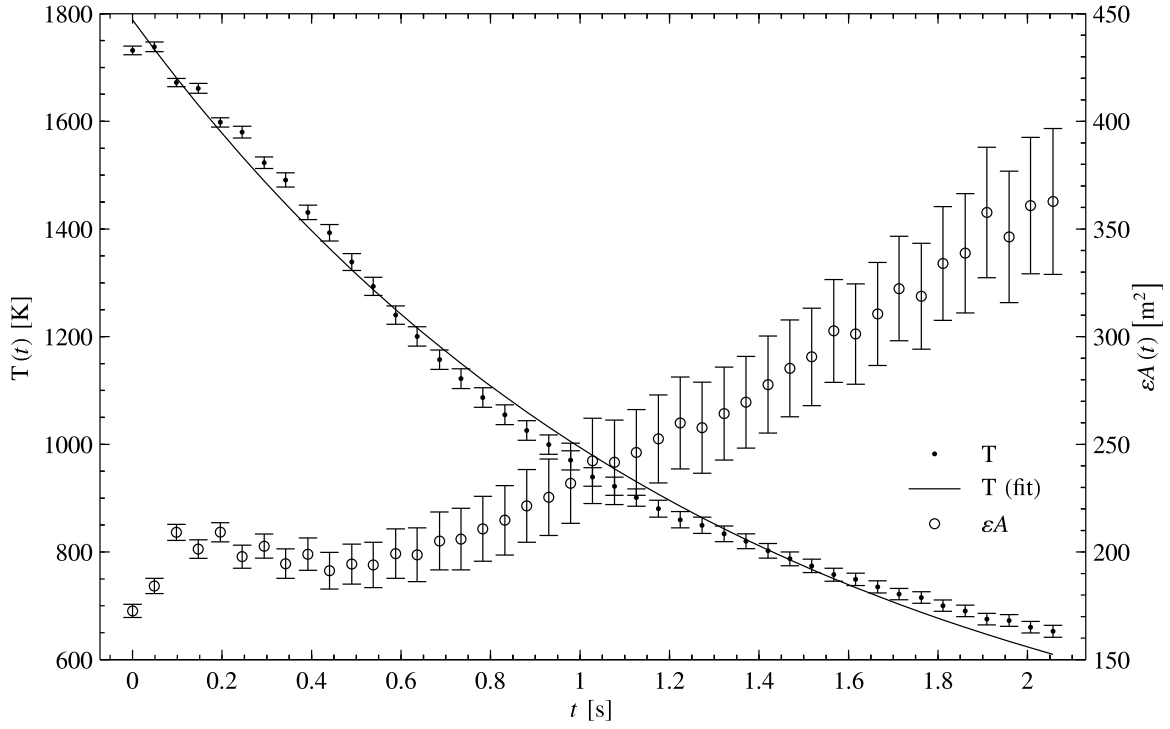
Figure 14: Spectral estimates of temperature (·) and emissive area (○) plotted as functions of time for a small, type A CMM detonation fireball. The T-axis is on the left and the εA-axis is on the right. Vertical error bars represent the statistical uncertainty (95% confidence interval) in the fit parameter. The solid black curve represents an exponential fit to the temperature curve.
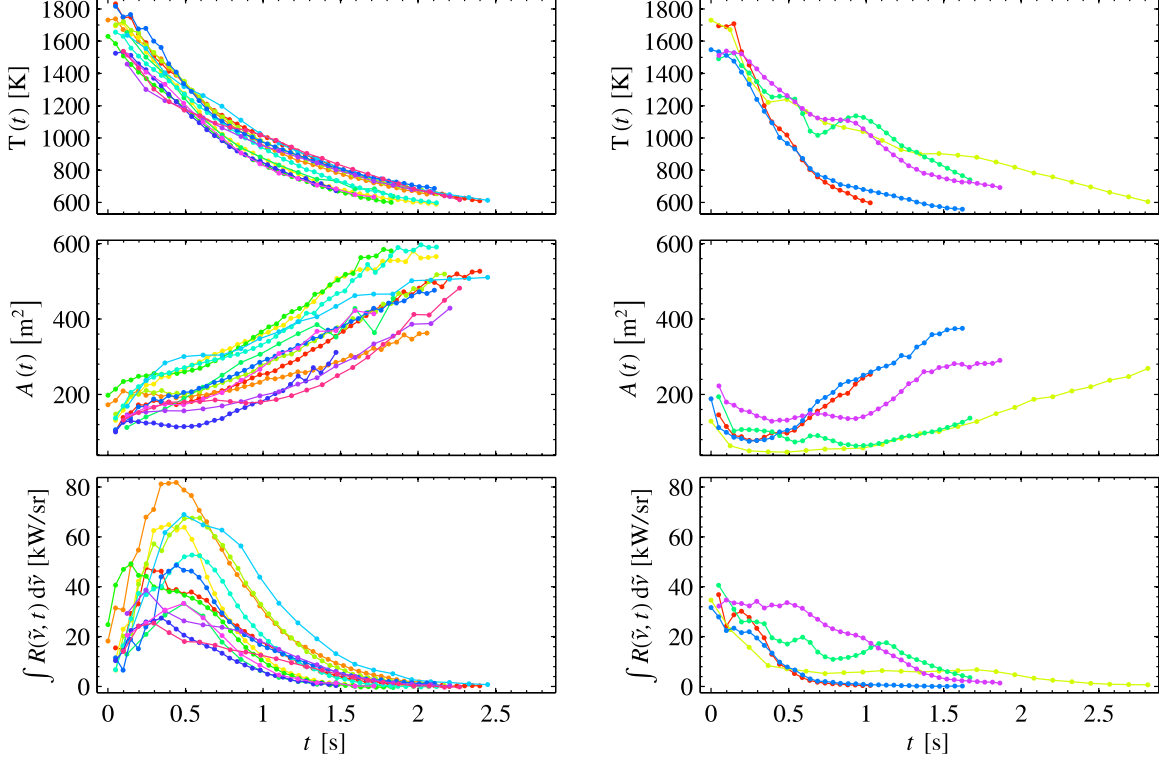
Figure 15: Extracted features from CMM detonation fireballs–Type A small are on the left and type B large are on the right. *Top panels*: Temperature versus time. *Middle panels*: emissive area versus time. *Bottom panels*: Spectrally-integrated ($2000 \leq \tilde{v} \leq 2200\,\mathrm{cm}^{-1}$) fit residual versus time. Various colors (or various grey levels if printed) are used to enhance visibility of individual profiles.

larger. This is a consequence of the Planckian distribution. For example, a 5% uncertainty in a temperature of 1500 K results in a 30% uncertainty in the peak height of the blackbody radiance curve. The increase with time in fit parameter uncertainty is primarily governed by the decreasing signal-to-noise ratio.

3.3 Extracted Features from Fireball Model

To assess the reproducibility and possible utility of the model parameters to the munitions classification problem, Equation 9 was fit to all CMM spectra collected during the RB3B field test. Two types of CMMs were detonated—13 small, type A and 5 large, type B—and the extracted fit parameters are provided in Figure 15. The AS munitions featured temperature profiles which were more reproducible than the BL profiles. The AS temperature curves were all monotonically decreasing in an approximately exponential fashion. Initial temperatures were between 1680–1830 K. Fits to an exponential curve revealed decay rates between

0.58–0.91 s^{-1} with a mean and standard deviation of 0.78 and 0.12 s^{-1}. Three of the five initial temperatures for the BL munitions were slightly less than 1600 K and the others were near 1700 K. Some BL temperature curves displayed secondary maxima and most were poorly represented by an exponential decay. The rate at which the BL fireballs cooled exhibited substantial variability.

Time-resolved emissive area curves were fairly reproducible for both the AS and BL munitions fireballs. Initially, εA increased in time for the AS fireballs, whereas εA initially decreased for the BL fireballs. The magnitudes of the emissive areas for BL were often smaller than those obtained for the AS events, a counter-intuitive result. This is likely the result of partial shielding of the BL fireballs resulting from their detonation in a clay crater. Presumably, the crater partially obscured a portion of the fireball, thereby reducing the apparent intensity received by the FTS. The AS events were detonated on either rock or hard sand and were in full view. The long-term behavior of εA for both CMM types is a gradual increase, which may be the result of an expanding fireball.

A third feature was extracted from the spectra in an effort to indirectly capture the apparent selective emission near 2100 cm^{-1} provisionally attributed to CO_2. To do so, the fit residual $I_{obs}(\tilde{\nu}, t) - I_{mdl}(\tilde{\nu}, t)$ was integrated over the spectral range $2000 \leq \tilde{\nu} \leq 2200$ cm^{-1}, i.e.

$$\Delta I(t) = \int_{2000\,\text{cm}^{-1}}^{2200\,\text{cm}^{-1}} (I_{obs}(\tilde{\nu}, t) - I_{mdl}(\tilde{\nu}, t))\ \mathrm{d}\tilde{\nu} \tag{10}$$

The results of this are provided in the bottom panel of Figure 15. In general, the AS fireballs feature a fairly repeatable $\Delta I(t)$ profile in which an initial rise is followed by a slightly more gradual decay. The "selective emission" typically lasts between 1.5–2 s. In contrast, $\Delta I(t)$ curves for most BL fireballs are characterized by an immediate and nearly continual decay to 0 W/sr. On average, the peak hight and area under the $\Delta I(t)$ curve was larger for the AS fireballs. If this residual is connected with CO_2, the difference in behavior of $\Delta I(t)$ may reflect a difference in the kinetics of its production, and may serve as a key feature for distinguishing type-A and type-B explosives in terms of fundamental differences at the chemical level.

42

3.4 Two-Temperature Model

The most obvious systematic error is the large positive residuals near $2100\,\mathrm{cm^{-1}}$ and is due to the neglect of selective emitters in this simple model of fireball emissions. However, a more subtle systematic trend in the residuals was observed across much of the observation bandpass. This can be seen in Figure 13 as a small negative residual between $2500\text{–}3500\,\mathrm{cm^{-1}}$ and as a small positive residual between $5500\text{–}6750\,\mathrm{cm^{-1}}$. It is possible that this is the result of a non-uniform temperature field. To begin assessing this possibility, the following two-temperature Planckian distribution was fit to this spectrum:

$$I_{mdl}(\tilde{v}, t) = T(\tilde{v})\left((\varepsilon A)_1 B(\tilde{v}, T_1) + (\varepsilon A)_2 B(\tilde{v}, T_2)\right) \tag{11}$$

Here, the emissive areas $(\varepsilon A)_i$ and corresponding temperatures T_i are fit parameters. This functional form imposes a view that the fireball is comprised of two distinct possibly non-contiguous areas, each with a distinct temperature and possibly with a distinct emissivity. This picture of a fireball is nearly as unrealistic as the perfectly homogeneous, single-temperature one described by Equation 9; however, it introduces additional freedom to account for, in an approximate way, the effects of a nonuniform temperature field within the fireball.

Fitting Equation 11 to the same spectrum as presented in Figure 13 resulted in a substantial improvement, the results of which are displayed in Figure 16. Data points between $2075 \leq \tilde{v} \leq 2250\,\mathrm{cm^{-1}}$ were omitted during fitting to prevent biasing by the selective emission in this region[1]. The standard error of the fit is 5.1, and the RMS and median magnitude relative errors are 6.2% and 2.6%, respectively. These fit statistics were based on the exclusion of a small portion of low-SNR data as previously described.

The fit residuals at $\tilde{v} > 2500\,\mathrm{cm^{-1}}$ are now only slightly above the estimated instrument noise level. Interestingly, there are three regions—3400, 4000, and $4900\,\mathrm{cm^{-1}}$—in which the observed spectrum is slightly larger than the modeled data. These regions are where selective emission from water (3400 and $4000\,\mathrm{cm^{-1}}$)

---

[1] Ignoring data points between 2075 and $2250\,\mathrm{cm^{-1}}$ did not strongly affect the single-temperature fits, and the improved fit results are almost entirely due to the inclusion of a second distribution.
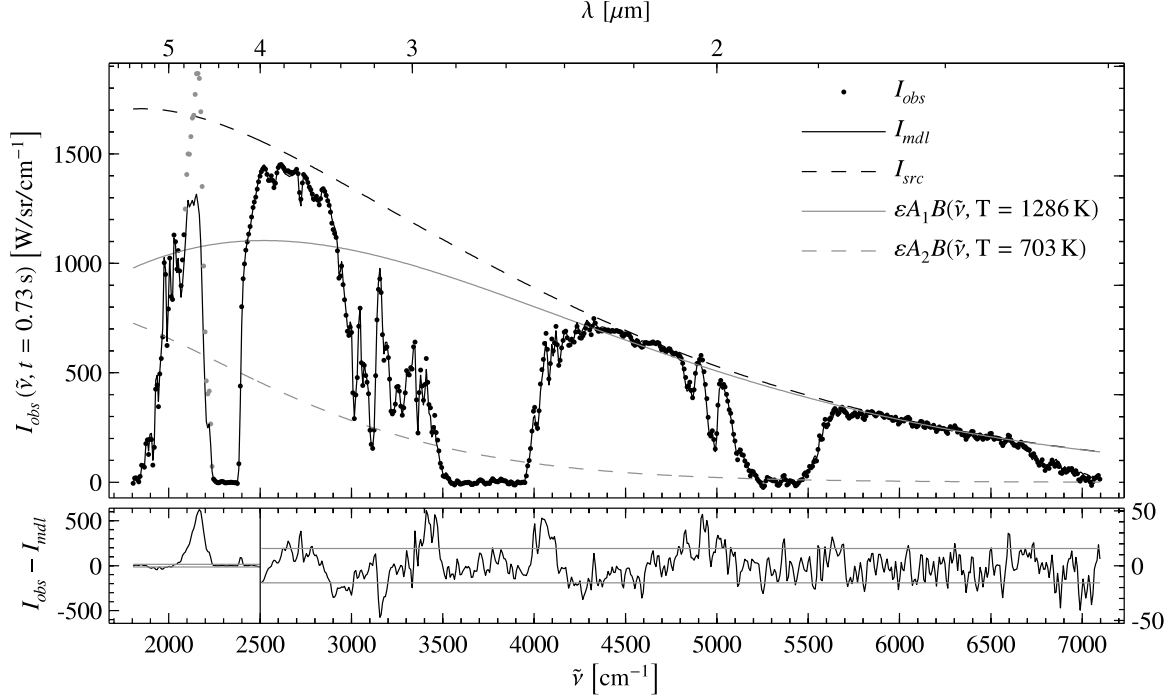
Figure 16: *Top panel*: Observed fireball spectrum at $t = 0.73$ s ($\cdot$) from the detonation of an AS CMM compared with the best fit, two-temperature model (solid black line). The grey points were excluded from the fit. The estimated at-source Planckian intensity distribution is also provided (dashed black line). The individual Planckian basis functions at fitted temperatures $T_1 = 1286$ K and $T_2 = 703$ K and weighted by fitted emissive areas are also shown as the solid and dashed grey lines. *Bottom panel*: Fit residuals ($I_{obs} - I_{mdl}$, black) compared with I_{err} (grey), which is an estimate of the instrument noise level. The left ordinate is used for $\tilde{\nu} < 2500$ cm^{-1} and the right ordinate corresponds to $\tilde{\nu} \geq 2500$ cm^{-1}.

and carbon dioxide ($4900\,\mathrm{cm}^{-1}$) might be expected[2]. It will be seen in Chapter IV that a different class of explosives emit strongly in these regions and can be explained on the basis of selective emission from H_2O and CO_2. At the longer wavelength region of the spectrum, the fit residuals are again seen to be large between 2000–$2200\,\mathrm{cm}^{-1}$. This is not surprising given the likely presence of selective emission; furthermore, many of these points were omitted from the fitting. It is interesting to note that there is a large positive residual on the long-wavelength side of the CO_2 absorption feature as well as a small positive residual on the short-wavelength side. This is consistent with emission from CO_2[3].

Performing this analysis for all the spectra from this AS fireball yielded the time-resolved fit parameters presented in Figure 17. Emissive areas $(\varepsilon A)_1$ corresponding to the higher temperature were smaller than the corresponding values obtained from the single-temperature fits. Oscillation in the magnitude of both $(\varepsilon A)_1$ and its uncertainty were observed. The source of this peculiar behavior is unknown. The emissive area $(\varepsilon A)_2$ corresponding to the lower temperature was initially the same as $(\varepsilon A)_1$ and steadily grew to a size about four times larger than $(\varepsilon A)_1$. The oscillatory behavior was not observed in the ratio, indicating that the effect on $(\varepsilon A)_1$ was balanced by the opposite effect on $(\varepsilon A)_2$. In general the uncertainties in the emissive areas were much larger than those from the single-temperature fits.

The larger of the fitted temperatures T_1 were slightly higher in the two-temperature fits. The same oscillatory behavior was observed in T_1, although in a more subdued fashion. T_1 was as much as 16% larger than the single-temperature results, but on average only larger by about 8%. The smaller of the fitted temperatures T_2 was typically between 600–$800\,\mathrm{K}$. Initially, the need for a second temperature was not supported by the data, and this was indicated by the large parameter uncertainties at early times.

---

[2]The small positive residuals above the instrument noise level could be emission "in the wings" of the corresponding absorption bands by water and carbon dioxide.

[3]The R-branch of the ro-vibrational band begins to head back towards longer wavelengths with increasing rotational quanta. This occurs near $2400\,\mathrm{cm}^{-1}$, and in the event that a hot CO_2 source is viewed through a long path of cold CO_2, the asymmetry in the "red-wing blue-wing" emission pattern is expected.
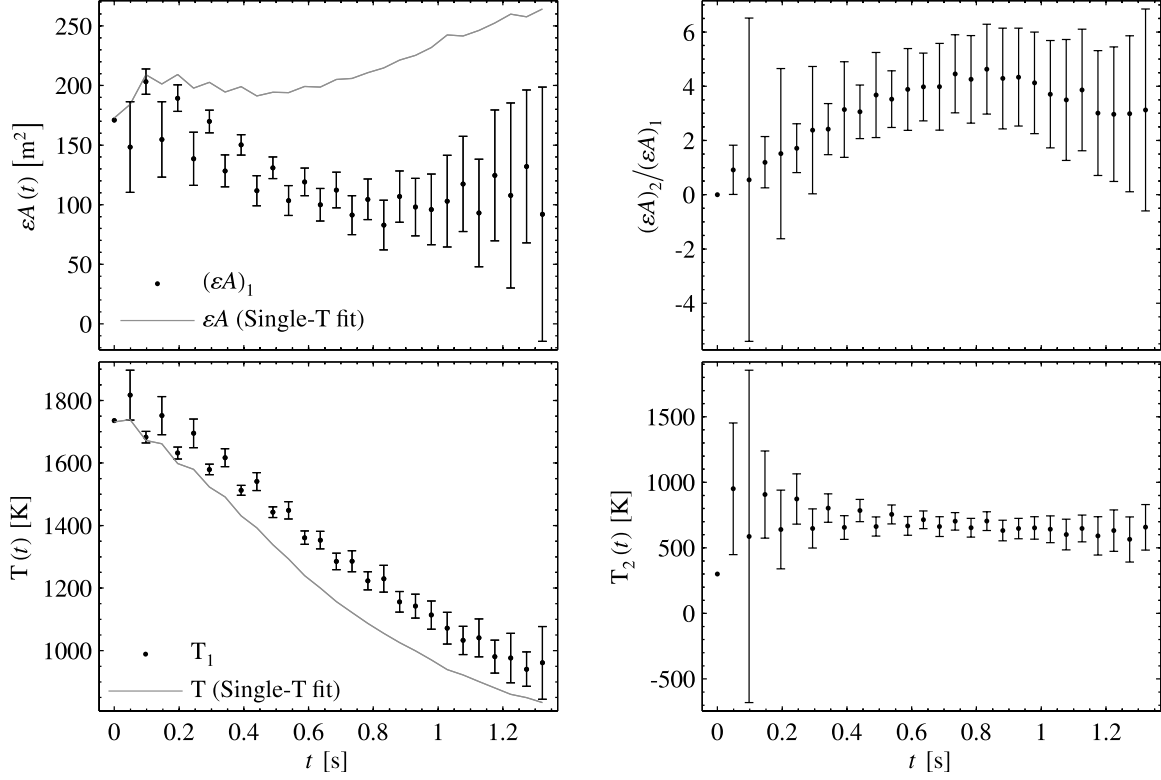
Figure 17: *Top-left panel*: Spectral estimates of the emissive area term (·) corresponding to the larger fitted temperature. This is compared with the emissive area from the single-temperature fit (grey line). *Top-right panel*: Ratio of the emissive area terms from the two-temperature fits. *Bottom-left panel*: Spectral estimates of the larger temperature (·) from the two-temperature fits compared with results from the single-temperature fits. *Bottom-right panel*: Spectral estimates of the smaller temperature. In each panel, vertical error bars represent the statistical uncertainty in the displayed quantities.

3.5 Conclusions

In general, the MWIR emissions collected from two types of conventional military munitions detonations revealed spectra which were qualitatively very similar. Spectra from both types of fireballs were dominated by continuum emission with some evidence of possible selective emission near $2100\,\mathrm{cm}^{-1}$. Despite these qualitative similarities, fitting the spectra to a single-temperature Planckian distribution afforded a dimensionality reduction which preserved much of the original fidelity. In general, CMM fireballs can be considered greybody radiators which cool from 1600–1800 K to ambient within 3–4 s. The AS temperature curves were nearly exponential with a decay rate near $0.78\,\mathrm{s}^{-1}$. The BL temperature curves were not as simply described and occasionally featured secondary maxima.

Early temporal behavior of the emissive area indicates differences in fireball behavior. The εA curves initially increased for the AS events, yet initially decreased for the BL events. Future tests should include MWIR imagery so that the emissivity behavior can be separated from the fireball area. Such a distinction is important to an improved phenomenological understanding as temporal changes in emissivity are likely connected to chemical processes (e.g., soot oxidation) whereas area changes are linked to the underlying flow fields.

The systematic error near $2100\,\mathrm{cm}^{-1}$ observed in the spectral fits may be the result of selective emission. The temporal behavior of this feature clearly distinguishes the AS fireballs from the BL fireballs. The AS fireballs are characterized by a rise and subsequent decay in $\Delta I(t)$ whereas the BL fireballs feature a $\Delta I(t)$ profile which decays from the moment of observation.

The inclusion of a second Planckian distribution term enables a better fit to the observed spectra. The broadband fit errors are substantially reduced, leaving behind only a small amount of systematic error. In addition to the large residual near $2100\,\mathrm{cm}^{-1}$, smaller systematic patterns in the residuals emerge and reinforce the view that selective emission is needed to fully describe observed detonation fireball spectra. The following chapter will provide the radiative transfer framework needed to properly include these effects, although at the price of assuming only a single-temperature distribution. Once selective emission is included, the computational costs are increased by several orders of magnitude, and the inclusion of spatial variations in the

temperature field will be excluded. The Brilliant Flash II data set will be used to develop the improved fireball model as the observed spectra contain much stronger evidence of selective emission, and thus a much better test of an improved fireball model. Furthermore, the BF2 spectra appear less influenced by a spatially-varying temperature field.

IV. Selective Radiator Model

In the previous chapter, a single-temperature Planckian distribution reasonably described the intensity distributions of detonation fireballs of conventional military munitions, suggesting the dominant role that continuum emitters played in the fireball. Examination of the fit residuals indicated that a small amount of selective emission from water and carbon dioxide may have contributed to the spectrum as well. Spectra collected from uncased TNT and several types of IEDs during the Brilliant Flash II field test indicated a much stronger contribution from selective radiators. This first part of this chapter provides a physical basis for incorporating selective emission into a fireball emissions model. The derivation, which is based on a solution to the continuity equation of radiative transfer, is presented below as it entails several necessary simplifying assumptions which may seem questionable. The assumptions will not be rigorously justified; instead, they will be judged as useful approximations by comparing observed data to the model derived from them. The fireball model will be fit to some representative BF2 spectra demonstrating that a high-fidelity dimensionality reduction of infrared fireball emissions is possible, a crucial step towards robust discrimination of high explosives. The reduced dimensionality is obtained by a minimal set of parameters (size, temperature, particulate extinction, and four byproduct concentrations), and their temporal behavior will be briefly explored. The hydrogen-to-carbon ratio $\mathcal{R}$ as estimated from the relevant byproduct concentrations is found to correlate well with the thermodynamic values expected from explosive stoichiometry. Since this ratio will prove to be a useful feature for HE discrimination, a sensitivity study is performed assessing the impact of non-ideal collection parameters on estimates of $\mathcal{R}$.

4.1 Radiative Transfer

The transfer of radiation along a path is influenced by the intervening material. At any point along the direction of travel, the local properties of the participating material determine the amounts of photon extinction and augmentation. Photons can be absorbed and converted to other forms of energy or they can be scattered out of the line-of-sight (LOS). Photons can also be "born" due to both spontaneous and stimulated emission, and scattering can also result in photons being redirected into the LOS. Radiative Transfer is the methodology of accounting for these various phenomena, and the components necessary for the development

of a fireball model will be presented as adapted from Modest [81] and Chandrasekhar [15]. Several simplifying assumptions will then be introduced which will enable an approximate, analytic solution for fireball emissions.

The following differential equation governs the transfer of a pencil of radiation $L_{\tilde{\nu}}$ along a path $\vec{s} = s\,\hat{s}$ by accounting for the various extinction and augmentation phenomena:

$$\frac{1}{c}\frac{\partial L_{\tilde{\nu}}}{\partial t} + \hat{s} \cdot \vec{\nabla} L_{\tilde{\nu}} = \kappa_{\tilde{\nu}} B_{\tilde{\nu}} - (\kappa_{\tilde{\nu}} + \beta_{\tilde{\nu}})\, L_{\tilde{\nu}} + \frac{\beta_{\tilde{\nu}}}{4\pi} \int_{4\pi} L_{\tilde{\nu}}(\hat{s}_i)\, \Phi_{\tilde{\nu}}(\hat{s}_i, \hat{s})\, \mathrm{d}\Omega_i \qquad (12)$$

Here, c is the speed of light in the material (which for practical purposes is the speed of light in a vacuum), $\kappa_{\tilde{\nu}}$ is the absorption coefficient (cm^{-1}), $\beta_{\tilde{\nu}}$ is the scattering coefficient (cm^{-1}), and $\Phi_{\tilde{\nu}}$ is the scattering phase function. The differential terms on the left hand side represent the changes in radiance as a function of time and location. The right hand side accounts for the different phenomena leading to such changes. The first term accounts for spontaneous and stimulated emission from the participating material. The second term accounts for photons either absorbed or scattered out of the LOS. The phase function describes the probability that a ray from the direction $\hat{s}_i$ will be scattered into the LOS $\hat{s}$; the integral over the solid angle 4π sr accounts for all in-scattered photons. All quantities appearing in Equation 12 can vary with location in space, time, and wavenumber, and the radiance and phase function also depend on direction. Equation 12 accounts for all possible sources and sinks of photons and can be considered an equation of continuity, i.e. an expression for the conservation of energy. In practice, the differential term $\frac{1}{c}\frac{\partial L_{\tilde{\nu}}}{\partial t}$ can be neglected as the timescales associated with photons traversing a mean-free path in typical materials are much shorter than characteristic times associated with fluid dynamic phenomena [110, pp. 133].

Equation 12 implicitly assumes that the material is in local thermodynamic equilibrium (LTE) so that in a small volume surrounding the point $\hat{s}$, the distribution of energy states is governed by the Boltzmann

distribution and hence a local temperature exists. If this were not the case, the energy state distribution would need to be specified and the term $\kappa_{\tilde{\nu}} B_{\tilde{\nu}}$ would need to be modified[1].

The assumption of LTE—or at least quasi-equilibrium—is fundamental to solving radiative transfer problems. Zel'dovich [110, pp. 120] defines a state in quasi-equlibrium if certain energy modes equilibrate quickly (e.g., by collisions) and if the interaction between these and other energy modes is small. In this work, the assumption of LTE will be made to enable a solution of Equation 12. Note that the LTE assumption has been used to successfully treat stellar atmospheres [14] and shock-front luminosities [110, Ch. 9].

Dropping the time-dependent term, recognizing $\hat{\mathbf{s}} \cdot \vec{\nabla} L_{\tilde{\nu}} = \frac{dL_{\tilde{\nu}}}{ds}$, and introducing some new terms, Equation 12 can be compactly rewritten as

$$\frac{dL_{\tilde{\nu}}}{d\tau_{\tilde{\nu}}} + L_{\tilde{\nu}} = S_{\tilde{\nu}}(L_{\tilde{\nu}}, \hat{\mathbf{s}}) \tag{13}$$

where $\tau_{\tilde{\nu}}$ is the dimensionless optical depth given by

$$\tau_{\tilde{\nu}} = \int_0^s (\kappa_{\tilde{\nu}} + \beta_{\tilde{\nu}}) \, ds \tag{14}$$

The source term $S_{\tilde{\nu}}(L_{\tilde{\nu}}, \hat{\mathbf{s}})$ represents sources contributing photons to the LOS and is given by

$$S_{\tilde{\nu}}(L_{\tilde{\nu}}, \hat{\mathbf{s}}) = (1 - \omega_{\tilde{\nu}}) B_{\tilde{\nu}} + \frac{\omega_{\tilde{\nu}}}{4\pi} \int_{4\pi} L_{\tilde{\nu}}(\hat{\mathbf{s}}_i) \, \Phi_{\tilde{\nu}}(\hat{\mathbf{s}}_i, \hat{\mathbf{s}}) \, d\Omega_i \tag{15}$$

where the term $\omega_{\tilde{\nu}}$ is defined by the ratio of scattering and total extinction quantities, i.e.

$$\omega_{\tilde{\nu}} = \frac{\beta_{\tilde{\nu}}}{\kappa_{\tilde{\nu}} + \beta_{\tilde{\nu}}} \tag{16}$$

This term is commonly referred to as the material's single-scattering albedo.

---

[1] Gamache and Rothman treat this problem in general [43]. For a two-level system with energy levels labeled by i and j and an upper state populations n_i, the term $\kappa_{\tilde{\nu}} B_{\tilde{\nu}}$ would be replaced by $n_i A_{ij} hc\tilde{\nu}/4\pi$ [81, pp. 328], where A_{ij} is the Einstein A coefficient governing the rate of transition from i to j via spontaneous emission.

Solving the integro-differential equation (Eq. 13) is difficult in general due to the presence of scattering, and is the subject of many astrophysical texts, e.g. Chandrasekhar's *Radiative Transfer* [15]. For the purposes of deriving a simple, closed-form solution for fireball emissions, the effects of scattering will be ignored. Paraphrasing Modest [81], in most hydrocarbon combustion systems, the sizes of the gaseous and particulate (soot) byproducts are small enough (0.005–0.08 μm diameter for soot) that Rayleigh's scattering theory holds in the MWIR. From this, particulate scattering efficiencies can be derived and are approximately three orders-of-magnitude smaller than the corresponding absorption efficiencies. Furthermore, the particulates are sufficiently small enough that their temperature is the same as the surrounding gas. (If this were not the case, the condition of LTE would not hold.)

By ignoring scattering ($\beta_{\tilde{\nu}} = \omega_{\tilde{\nu}} = 0$), Equation 13 simplifies to

$$\frac{\mathrm{d}L_{\tilde{\nu}}}{\mathrm{d}\tau_{\tilde{\nu}}} + L_{\tilde{\nu}} = B_{\tilde{\nu}} \tag{17}$$

which can be solved by introducing the integrating factor $e^{\tau_{\tilde{\nu}}}$ and initial condition $L_{\tilde{\nu}}(0)$:

$$L_{\tilde{\nu}}(\tau_{\tilde{\nu}}) = L_{\tilde{\nu}}(0)\, e^{-\tau_{\tilde{\nu}}} + \int_0^{\tau_{\tilde{\nu}}} B_{\tilde{\nu}}(\tau_{\tilde{\nu}}')\, e^{-(\tau_{\tilde{\nu}} - \tau_{\tilde{\nu}}')}\, \mathrm{d}\tau_{\tilde{\nu}}' \tag{18}$$

$L_{\tilde{\nu}}(0)$ is the background radiance and its attenuation via absorption is modeled by $e^{-\tau_{\tilde{\nu}}}$. If there are no appreciable sources of photons after that, i.e. the integral is zero, then this is simply the exponential form of Beer's law. When the participating material can radiate, the terms within the integral account for both the production of photons at any given point along the LOS ($B_{\tilde{\nu}}\, \mathrm{d}\tau_{\tilde{\nu}}$) and their subsequent losses ($e^{-(\tau_{\tilde{\nu}} - \tau_{\tilde{\nu}}')}$) incurred along the remaining pathlength.

4.2 *Simplified Radiative Transfer for Fireball Spectroscopy*

The general solution to the radiative transfer equation for a non-scattering source in LTE is not suitable for modeling detonation fireball spectra without further simplifications. For example, the temperature and matter fields are not known *a priori*. Reactive-flow computational fluid dynamics calculations might enable

an estimate of the spatial variations of matter and temperature. However, such calculations consume enormous computational resources and require accurate reaction rates for the 100s of important reaction pathways. For many novel explosives, the kinetic pathways have not been studied. Furthermore, this approach is antithetical to this effort of developing a simple, efficient tool for quickly extracting information from fireball emissions.

To solve Equation 18 for detonation fireballs, the following simplifying assumptions will be made:

1. the fireball geometry is a cube[2] of length r

2. the temperature and matter fields are homogeneous within the fireball volume $V = r^3$

3. the FTS is at a large distance R from the fireball $(R \gg r)$

4. $L(0)$ is small and can be removed from observed data via background subtraction (recall Figure 1)

5. the atmosphere between the FTS and fireball is homogeneous

6. emission from the ~300 K atmosphere can be ignored

The first three assumptions lead to a simple, one-dimensional form for fireball radiance. The fourth assumption is based on experience with observed fireball spectra. The last two assumptions are justified as follows. Over the short horizontal path encountered in the field tests, the atmosphere can be reasonably treated as a uniform, well-mixed gas. And at terrestrial temperatures, the MWIR emission from the atmosphere is negligible compared with emissions from the fireball. Figure 18 illustrates the geometry of the simplified fireball and instrumentation in a Cartesian coordinate system.

Based on these assumptions, only the line-of-sight along x needs to be considered. The homogeneity allows the optical depth parameter to be expressed as $d\tau_{\tilde{\nu}} = -\kappa_{\tilde{\nu}} \, dx$ so that at the point r, Equation 18 can be solved:

$$L_{\tilde{\nu}}(r) = \left(1 - e^{-\kappa_{\tilde{\nu}} r}\right) B_{\tilde{\nu}}(\mathrm{T}) \tag{19}$$

---

[2]Radiative transfer for the (slightly) more appropriate spherical geometry is more complicated and is treated in Appendix B. Errors which result from the homogeneous assumption are expected to introduce more systematic error than errors associated with the choice of fireball geometry.
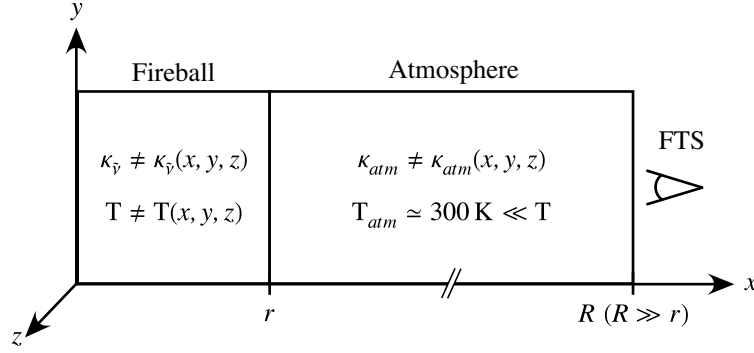
Figure 18: Depiction of the fireball and instrumentation geometry illustrating several of the assumptions introduced to enable a simple solution of the radiative transfer equation.

The exponential term in parenthesis is the fireball transmittance T, and Kirchoff's law enables the entire parenthetical term to be recognized as the fireball emissivity ε, i.e. $\varepsilon = 1 - T$. Equation 19 represents the source fireball radiance. To arrive at the apparent radiance at the FTS, the source radiance needs to be augmented by the transmittance of the atmosphere T_{atm}, i.e. $L_{\tilde{v}}(R) = T_{atm}(\tilde{v}) L_{\tilde{v}}(r)$. (Assumption 6 allowed the term representing atmospheric emission, $(1 - T_{atm}) B_{\tilde{v}}(T_{atm})$, to be ignored.) The projected area of the cube is used to convert apparent radiance to apparent intensity:

$$I_{\tilde{v}} = T_{atm}(\tilde{v}) \, r^2 \, \varepsilon(\tilde{v}) \, B_{\tilde{v}}(T) \tag{20}$$

4.3 Computation of Apparent Intensity

The absorption coefficient $\kappa_{\tilde{v}}$ is the sum of absorption cross-sections $\sigma_i(\tilde{v})$ weighted by the absorber concentrations ξ_i, i.e.

$$\kappa_{\tilde{v}} = \Sigma_i \, \xi_i \, \sigma_i(\tilde{v}) \tag{21}$$

Two forms of matter will be considered, namely gases and particulates. For particulates, an accurate description of $\sigma(\tilde{v})$ requires detailed knowledge of the size distribution and the material's complex index of refraction. Particulate absorption can be wavelength dependent, but it is difficult to estimate this functional dependence without knowledge of these properties. In many combustion systems the particulate matter is

treated as a grey [106] ($\sigma(\tilde{v}) = $ const.). This approach will be taken here and κ_p will serve as a model

parameter, noting that the effects of concentration and cross-section cannot be separated in the grey case.

The absorption cross-section for a gas is defined by $\sigma(\tilde{v}) = \sum_j S_j f(\tilde{v}_j - \tilde{v}; \vec{p}_j)$, where the absorption

line at wavenumber $\tilde{v}_j$ is characterized by a linestrength S_j and a normalized lineshape profile f, which is

itself described by a collection of lineshape parameters $\vec{p}_j$. Under LTE, S_j varies with temperature accord-

ing to the Boltzmann distribution. The lineshape parameters $\vec{p}_j$ describe the width of and pressure-induced

shifts in the line profile as functions of pressure and temperature. A Voight profile was used as pressure and

doppler effects will both contribute to the lineshape in the high-temperature fireball at atmospheric pressure.

Spectral databases such as HITRAN [90, 91] or GEISA [57] can be used to determine σ for various small

molecules at temperatures up to 600 K. The elevated temperatures encountered in combustion systems make

molecular states thermally accessible which are difficult to measure at low temperatures and which require

substantial effort to accurately predict using *ab initio* or extrapolation techniques. As a result, spectral param-

eters suitable for high-temperature simulations exist for only a few small molecules. Fortunately, parameters

for three prominant hydrocarbon combustion byproducts–H_2O, CO_2, and CO–have been tabulated in the

high-temperature (HITEMP) extension to HITRAN and the Carbon Dioxide Spectroscopic Databank [100]

(CDSD), and have been found suitable [40, 82] for temperatures up to 1500 K.

The Line-by-Line Radiative Transfer Model [21] (LBLRTM) was used with HITEMP and CDSD to

pre-compute molecular cross-sections for H_2O, CO_2, and CO at temperatures spanning 275–3000 K in 25 K

increments. Evidence for emission from HCl was later found in the data, and line parameters for this molecule

were taken from HITRAN since high-temperature parameters were unavailable. The wavenumber axis was

uniformly sampled with $\Delta\tilde{v} = 0.003\,\text{cm}^{-1}$ and covered 1500–7800 cm^{-1}. Cross-sections at an arbitrary

temperature were estimated via linear interpolation using the two nearest sampled temperatures. To facilitate

comparison with observed data, the monochromatic source spectrum of Equation 20 was multiplied by the

(monochromatic) atmospheric transmittance function $T_{atm}(\tilde{v})$ and convolved with the FTS instrument line

shape (ILS) giving the following model of intensity I_{mdl}

$$I_{mdl}(\tilde{\nu}) = \int_{-\infty}^{\infty} T_{atm}(\tilde{\nu}') \, I_{\tilde{\nu}'} \, \text{ILS}\left(\tilde{\nu} - \tilde{\nu}'\right) \, \mathrm{d}\tilde{\nu}' \qquad (22)$$

LBLRTM efficiently performed this convolution using a pair of Fourier transforms and the Hanning (cosine) apodization filter to match the output of the MR-154. A Levenberg-Marquardt nonlinear optimization routine was used to fit each observed fireball spectrum to Equation 22 by adjusting the fireball size r, temperature T, particulate absorption coefficient κ_p, and the gaseous concentrations ξ_i where i is one of H_2O, CO_2, CO, or HCl. For completeness, the functional form of the fireball model is explicitly expressed as

$$I_{mdl}(\tilde{\nu}; r, \text{T}, \kappa_p, \xi_i) = \text{ILS} \star T_{atm}(\tilde{\nu}) \, r^2 \left(1 - e^{-r\left(\kappa_p + \Sigma_i \xi_i \sigma_i(\tilde{\nu};\text{T})\right)}\right) B_{\tilde{\nu}}(\text{T}) \qquad (23)$$

where $\star$ denotes convolution and it is understood that all wavenumber-dependent terms are "monochromatic". T_{atm} is parameterized by several meteorological inputs, namely the local temperature and pressure, as well as the concentrations of several trace gases such as H_2O, CO_2, N_2O, and CH_4. Temperature, pressure and water vapor concentration will be taken from meteorological instruments on site during BF2 testing. The June 2004 average CO_2 concentration of $380\,\text{ppm}_\text{v}$ was taken from the La Jolla Pier monitoring station in California [60]. The remaining trace gases were estimated using current values from the IPCC report [56].

4.3.1 Model limitations. Equation 23 represents the simple model to which spectra will be fit for the primary purposes of dimensionality reduction and the extraction of key features. The best key features are ones that strongly correlate with real phenomena so that when the phenomena differ, the key features might be used to discriminate between them. Several drastic assumptions were made to arrive at Equation 23 and the resulting inbuilt systematic errors suggest caution in interpreting the physical meaning of the fit parameters. Nonetheless, it will be demonstrated that the spectral fit parameters are physically reasonable and where possible compare favorably with other data sources. This may suggest that the systematic biasing of fit parameters is not unacceptably large, and more importantly, that the correlations between the fit parameters

and the underlying phenomena are mostly preserved. Chapter V demonstrates that the features extracted from

the fireball spectra clearly distinguish the two different classes of HEs examined during BF2.

The functional form of Equation 23 also suggests a mathematical set of limitations. First, suppose poor

calibration resulted in an intensity scale off by some multiplicative value C. The size and concentration terms

will need to be corrected for this radiometric scaling factor via

$$r_t = r_m \sqrt{C}$$

$$\xi_t = \xi_m \big/ \sqrt{C} \tag{24}$$

$$\kappa_{p,t} = \kappa_{p,m} \big/ \sqrt{C}$$

where the subscript t and m denote the true and measured quantities, respectively. It is important to note that

a radiometric scaling error only affects the interpretation of the size and concentration-based parameters. It

does not affect the fit quality, nor does it change the estimated fireball temperature.

Another potential problem with Equation 23 occurs if the fireball is optically thin. In this case, the size

and concentration terms become highly correlated as evidenced by the following Taylor series expansion

$$1 - e^{-r\left(\kappa_p + \Sigma_i \xi_i \sigma_i(\tilde{\nu})\right)} \simeq r \ (\kappa_{\tilde{\nu}} + \Sigma_i \xi_i \sigma_i(\tilde{\nu})) \tag{25}$$

In fitting Equation 23 to spectra, the parameter correlation matrix was used to identify when this was a

problem. In practice, this was a minor issue as there was sufficient "optical thickness" at enough frequencies

so that higher-order terms in the expansion would be needed. These higher-order terms effectively decouple

size r from concentration ξ_i allowing both to be determined from well-calibrated spectral intensities.

Finally, in some fireballs, the optical depth can be large enough that the source spectrum appears like a

blackbody. All of the conventional munition fireballs collected during RB3 appeared like this. Initial spectra

collected during the BF2 tests also were highly Planckian. In the limit of large $\kappa_p\, r$, the fireball emissivity

tends to 1 and selective emission is not observed. The spectrum could also appear to be free from selective

emission in the event that $\kappa_p \gg \Sigma_i \xi_i \sigma_{\tilde{\nu}}$. Note that sufficient frequency-dependent selective emission is needed to reliably distinguish between the effects of emissivity and area. In the perfectly grey case where $\varepsilon \neq \varepsilon(\tilde{\nu})$, Equation 23 reduces to $I_{mdl} = (\varepsilon r^2) B_{\tilde{\nu}}(\text{T})$. In this case, *a priori* knowledge of ε is needed to compute the true projected area r^2.

4.4 Ideal Fireball

Presented in Figure 19 is a synthetic spectrum generated by Equation 23 for the following set of parameters: $r = 1000\,\text{cm}$, $\text{T} = 1800\,\text{K}$, $\kappa_p = 2 \times 10^{-4}\,\text{cm}^{-1}$, and $[\xi_{H_2O}, \xi_{CO_2}, \xi_{CO}, \xi_{HCl}] = [4.99, 10, 5, 0.01] \times 10^{17}\,\text{molec/cm}^3$. The apparent, source, and Planckian intensities are all provided at a spectral resolution of $4\,\text{cm}^{-1}$ to match BF2 experimental conditions. The Planckian intensity represents the source intensity if the emissivity were 1. Many of the spectral features from water and carbon dioxide emission are attenuated by the atmospheric transmittance profile. However, the large fireball temperature does permit substantial emission in the wings of the strong absorption bands of H_2O and CO_2. Below, the total fireball emissivity is also shown and compared with the particulate emissivity $\varepsilon_p = e^{-r\kappa_p}$, which is about 0.2. Across most of the MWIR, the emissivity is influenced by both particulate and selective emission. However, near $6100\,\text{cm}^{-1}$, the emission is dominated by the grey particulate matter.

Individual emissivity curves for each of the included gaseous byproducts are provided at instrumental resolution to indicate the shape and location of their contributions[3] to the overall spectrum. At $4\,\text{cm}^{-1}$ resolution, the water emissivity is dominated by a broadband variation with frequency. Some narrow emission features are present on top of this broadband structure. The CO_2 emissivity profile varies smoothly with frequency and lacks spectrally sharp features. This is a consequence of the large number of overlapping combination and resonance lines that are thermally accessible at high temperatures. This combined with CO_2's large molecular cross-section for many lines leads to emissivities of 1 in two bands under these conditions. CO substantially overlaps with CO_2 between 2000–$2200\,\text{cm}^{-1}$. The overtone transition near $4200\,\text{cm}^{-1}$ will be important in determining CO concentrations. The emission lines of HCl are resolved at $4\,\text{cm}^{-1}$ resolution.

---

[3]The total emissivity is not the product of individual emissivities, however. Instead, the total gas-phase emissivity is, to a good approximation, one minus the product of individual gaseous transmittance profiles, i.e. $\varepsilon = 1 - \prod_i T_i$.
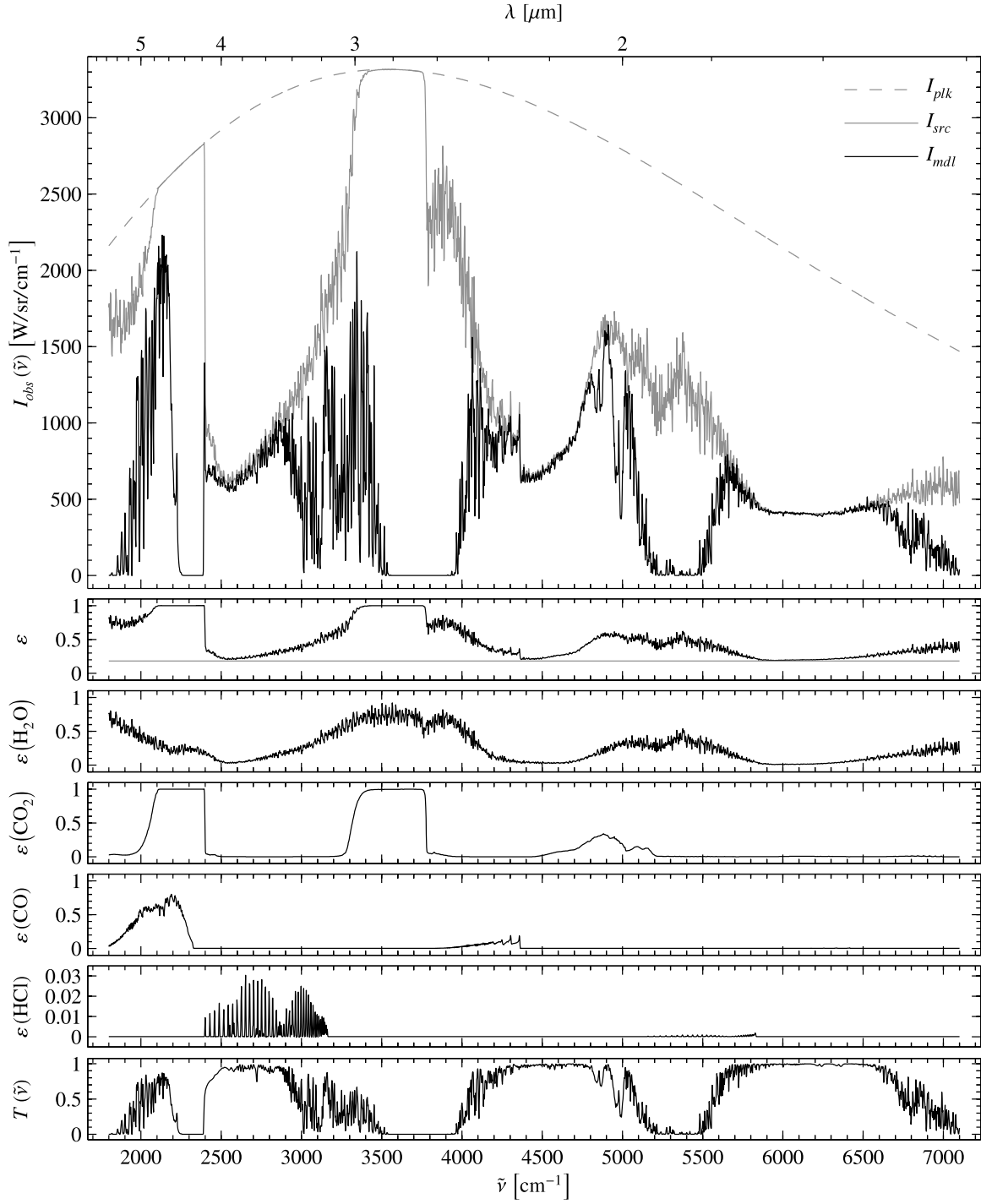
Figure 19: *Top panel*: Apparent (black) and source (solid grey) intensity for an ideal fireball. The source intensity for an ideal blackbody (Planckian) radiator of the same size is also provided (dashed grey). The next panel illustrates the total fireball emissivity (black) and the greybody contribution from particulates (grey). The next four panels provide in order the individual emissivities for H_2O, CO_2, CO, and HCl. The bottom panel presents the atmospheric transmittance profile over a 3.26 km pathlength for reference.
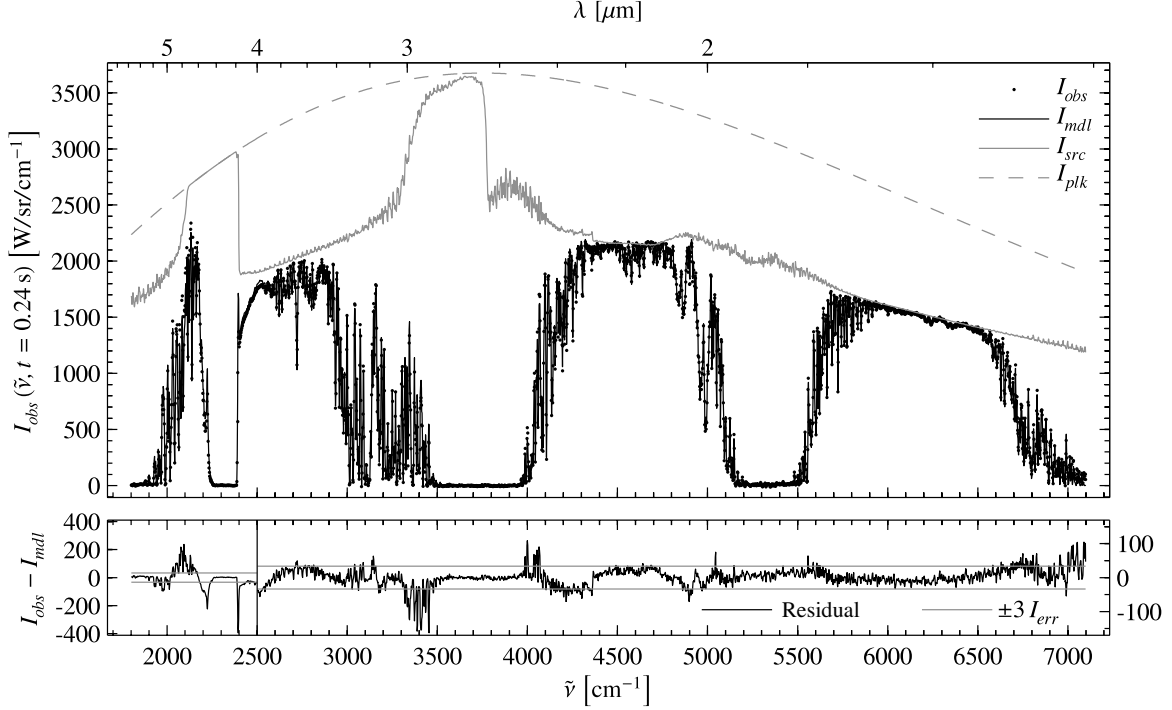
Figure 20: *Top panel*: Observed fireball spectrum (·) at $t = 0.24$ s from a 50 kg TNT detonation compared with the best fit model (solid black). The estimated at-source spectrum is provided (solid grey) along with the Planckian intensity distribution (dashed grey). *Bottom panel*: Fit residuals ($I_{obs} - I_{mdl}$, black) compared with I_{err} (grey), which is an estimate of the instrument noise level. The left ordinate is used for $\tilde{\nu} < 2500 \, \text{cm}^{-1}$ and the right ordinate corresponds to $\tilde{\nu} \geq 2500 \, \text{cm}^{-1}$.

Because the low-temperature HITRAN spectral linelist was used, an abrupt cutoff of the HCl lines is evident at $2400 \, \text{cm}^{-1}$. However, the cutoff is near the CO_2 atmospheric absorption band and will not strongly affect fitting Equation 23 to the observed data. For reference, the emission features of the individual gases can be compared with a typical atmospheric transmittance profile for the BF2 tests.

4.5 Analysis of 50 kg TNT Fireball Spectra

A 50 kg TNT spectrum at $t = 0.24$ s is compared with the best fit to Equation 23 in Figure 20. The source spectrum and Planckian intensity distribution are also provided. At this early time, the spectrum is dominated by the particulate emission and has much of the underlying Planckian shape. The fit residuals ($I_{obs} - I_{mdl}$) are provided and in many spectral regions are on the order of the instrument's noise level. Some regions exhibit systematic errors, particularly between 2000–2250 and 3300–3500 cm^{-1}. For comparison,

± 3 sigma bounds are provided. These bounds are computed from an estimate of the instrument noise level, where $I_{err} = \text{RMS} (\text{im}(I_{obs}(\tilde{\nu}))$ and RMS denotes the root-mean-squared (RMS) value. Note that two ordinate scales are provided—one for $\tilde{\nu} < 2500\,\text{cm}^{-1}$ and the other for $\tilde{\nu} \geq 2500\,\text{cm}^{-1}$—to improve visibility of the residuals. For this spectrum, the RMS value of the residuals was $35\,\text{W/sr/cm}^{-1}$. In regions where $\text{SNR} > 5$ and $T_{atm}(\tilde{\nu}) > 0.05$, the RMS relative error was 7.5%. In the median, the relative error was 1.3% in magnitude, suggesting excellent fit quality over most of the spectral region. Subsequent relative errors will be reported for spectral regions satisfying the SNR and T requirements just stated. The standard error (SE) of the fit is 3.1, i.e. the residuals are on average ~3 times greater than the noise level estimated by I_{err}.

At $t = 0.49\,\text{s}$, the spectrum shows evidence of much more selective emission, and the data and fit are compared in Figure 21 (a). Systematic errors are more prevalent in the fit residuals. The negative residual between 4100–$4400\,\text{cm}^{-1}$ indicates a large over-estimation of the carbon monoxide concentration. Likewise, the negative residuals near 3400 and $4900\,\text{cm}^{-1}$ correspond to over-estimated carbon dioxide concentration. The biasing of concentrations occurred as a response by the least-squares minimizer to mitigate the larger systematic errors between 2000–$2250\,\text{cm}^{-1}$. Both CO and CO_2 emit strongly in this region. Unfortunately, the distribution of intensity in this spectral band cannot be adequately accounted for by this model without the introduction of systematic errors elsewhere in the spectrum. The RMS and standard errors were $36\,\text{W/sr/cm}^{-1}$ and 6.0, respectively. Relative errors where $\text{SNR} > 5$ and $T(\tilde{\nu}) > 0.05$ were 12% (RMS) and 5% (median magnitude).

Eliminating wavenumbers less than $2500\,\text{cm}^{-1}$ ($\lambda > 4\,\mu\text{m}$) during fitting dramatically improves the results at shorter wavelengths as demonstrated in Figure 21 (b). The systematic errors noted previously for the CO_2 and CO emission bands have disappeared. Comparing both sets of fit residuals on $\tilde{\nu} > 2500\,\text{cm}^{-1}$, the RMS error dropped from 22 to $13\,\text{W/sr/cm}^{-1}$ when excluding wavelengths greater than $4\,\mu\text{m}$. On the same region, the SE improved to 2.5 and the relative errors improved to 7.6% (RMS) and 3.4% (median magnitude). Some patterns in the residuals still remain, especially in the wings of the water absorption band centered at $3750\,\text{cm}^{-1}$.
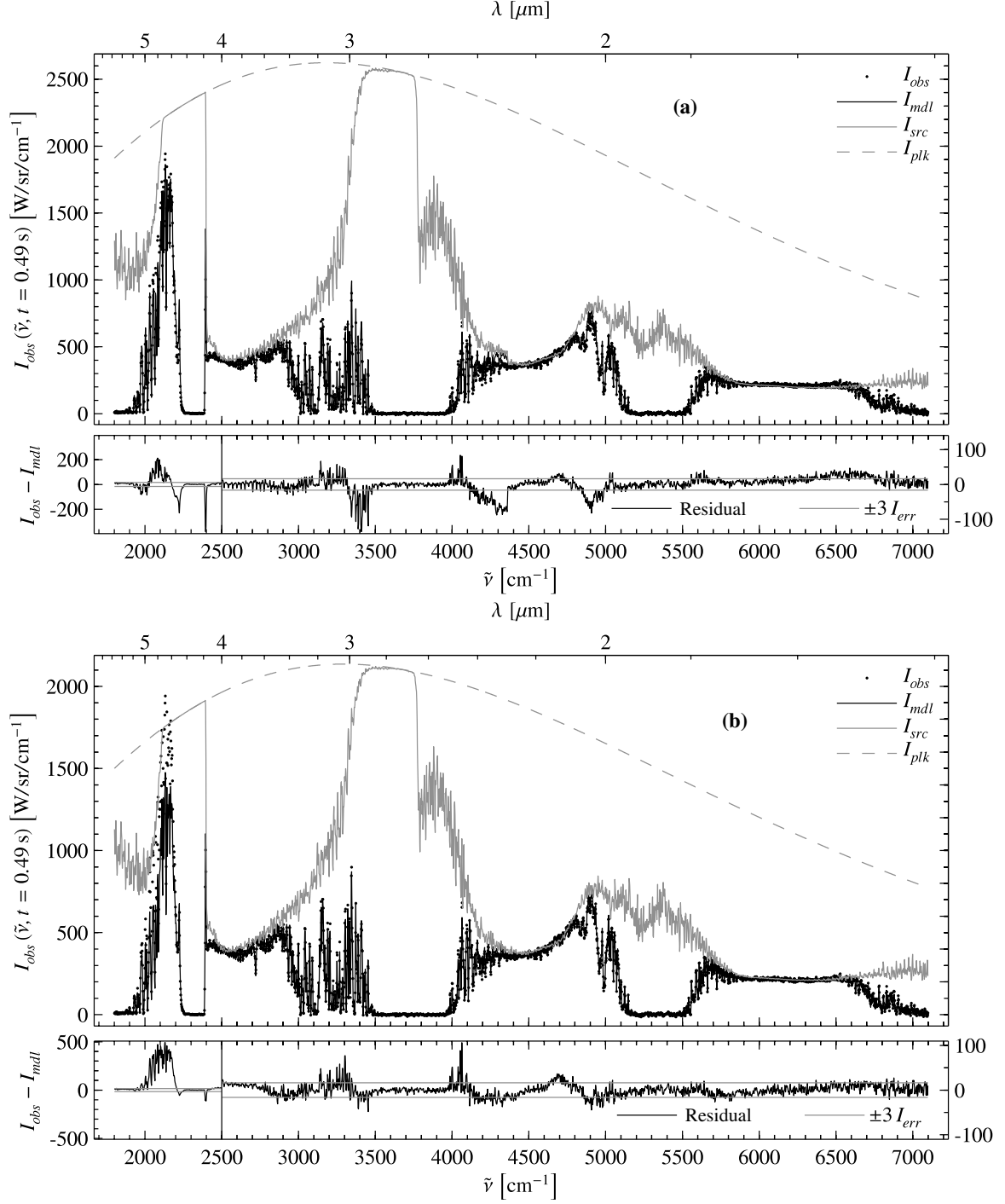
Figure 21: (a) *Top panel*: Observed fireball spectrum (·) at $t = 0.49\,\text{s}$ from a $50\,\text{kg}$ TNT detonation compared with the best fit model (solid black). The estimated at-source spectrum is provided (solid grey) along with the Planckian intensity distribution (dashed grey). *Bottom panel*: Fit residuals ($I_{obs} - I_{mdl}$, black) compared with I_{err} (grey), which is an estimate of the instrument noise level. The left ordinate is used for $\tilde{\nu} < 2500\,\text{cm}^{-1}$ and the right ordinate corresponds to $\tilde{\nu} \geq 2500\,\text{cm}^{-1}$. (b) Same observed data, but fit and residuals obtained when fitting only to wavenumbers greater than $2500\,\text{cm}^{-1}$.

62

For the $t = 0.49\,\text{s}$ fit, the optimum parameters and associated parameter uncertainties (95% confidence interval) are presented in Table 5. Each uncertainty value[4] provides a measure of the sensitivity of the data to the associated parameter, and also accounts for the effects of inter-parameter correlation. (In general, the less sensitive a model is to a particular parameter, a greater the amount of uncertainty will be associated with it. Likewise, when two parameters are highly correlated, i.e. a change in one parameter can be compensated by a change in another parameter, the uncertainty in both parameters will be larger.) Particular significance should not be attributed to the magnitude of the fit parameter uncertainties as they are computed under the assumption that the model accurately describes the data to within an unknown, but normally-distributed random variable. (If this were the case, there would be a 95% chance that the real value of the parameter p_i is contained in the interval $[p_i - \delta p_i,\ p_i + \delta p_i]$ where δp_i is the uncertainty just described.) The fit residuals, while small, indicate the presence of systematic errors and thus violate this normal error assumption. Nonetheless, the uncertainties do provide relative measure of confidence in the fit parameters. Temperature and fireball size are well-defined with low uncertainties, whereas only limited confidence in the CO and HCl concentrations is warranted. The parameter correlation matrix $\mathbf{C}$ is displayed in Table 6 to indicate in relative terms how correlated each pair of fit parameters are[5]. The parameters r and κ_p were moderately correlated, indicating that an increase in r could be partially compensated by a decrease in κ_p. This type of correlation was expected given the discussion in § 4.3.1.

Fitting each of the 50 kg TNT spectra resulted in the time-dependent parameters presented in Figure 22. Results from fitting to wavenumbers satisfying $\tilde{\nu} > 2500\,\text{cm}^{-1}$ are prominently displayed in black. Including $\lambda > 4\,\mu\text{m}$ changed the some parameters slightly and others considerably. For completeness, the time behavior of these fit parameters are displayed in grey. The large, systematic patterns in the fit residuals strongly

---

[4] Assuming normally-distributed errors, fit parameter uncertainties estimated in the following manner [68, 69]. Let $y_o(i)$ represent the ith observed data point (of N total points) and $y_c(i) = f(i; \{p_j\})$ represent the modeled value at that point, which is a function of the set of M parameters $\{p_j : j = 1...M\}$. Define J as the matrix of partial derivatives via $J_{i,k} = \frac{\partial y_c(i;\{p_j\})}{\partial p_k}$. The optimized parameters are those that minimize the standard error $\text{SE} = \sqrt{\chi^2/(N - M)}$ where $\chi^2 = \Sigma_{i=1}^{N}\left(\frac{y_o(i) - y_c(i;\{p_j\})}{\sigma_i}\right)$ and σ_i is the uncertainty associated with the ith data point. The parameter uncertainty is computed as $\delta p_i = f_{95}(N - M)\,\text{SE}\,\sqrt{V_{i,i}}$ where $f_{95}(N - M)$ is the 95% student t-value for $N - M$ degrees of freedom and V is the variance-covariance matrix, which can be expressed in terms of the partial derivative matrix $V_{i,i} = (J^t \times J)^{-1}$. Matlab's `nlinfit` provides a numerical approximation to the matrix J, from which the parameter uncertainties are then computed.

[5] The correlation matrix $\mathbf{C}$ is computed from the variance-covariance matrix as $C_{i,j} = V_{i,j}/\sqrt{V_{i,i}\,V_{j,j}}$ [68]. V is defined in the previous footnote.

Table 5:   Optimum fit parameters and associated uncertainties (95%) for the $\tilde{\nu} > 2500\,\mathrm{cm}^{-1}$ fit to a 50 kg TNT fireball spectrum at $t = 0.49\,\mathrm{s}$.

Param	Value	Error	% Error	Units
r	1008	15	1.5	cm
T	1680	9	0.5	K
κ_p	1.97E-04	7.70E-06	3.9	cm^{-1}
ξ_{H_2O}	3.45E+17	2.33E+16	6.8	molec / cm^3
ξ_{CO_2}	6.02E+17	3.78E+16	6.3	molec / cm^3
ξ_{CO}	2.81E+15	9.65E+14	34	molec / cm^3
ξ_{HCl}	4.92E+14	1.21E+14	25	molec / cm^3

Table 6:   Fit parameter correlation matrix **C** for the $\tilde{\nu} > 2500\,\mathrm{cm}^{-1}$ fit to a 50 kg TNT fireball spectrum at $t = 0.49\,\mathrm{s}$. Diagonals and elements with magnitudes less than 0.7 are displayed in grey.

	r	T	κ_p	ξ_{H_2O}	ξ_{CO_2}	ξ_{CO}	ξ_{HCl}
r	1	-0.568	-0.846	-0.744	-0.550	0.182	-0.104
T	-0.568	1	0.090	0.022	-0.237	-0.067	0.298
κ_p	-0.846	0.090	1	0.792	0.775	-0.173	-0.050
ξ_{H_2O}	-0.744	0.022	0.792	1	0.662	-0.116	-0.213
ξ_{CO_2}	-0.550	-0.237	0.775	0.662	1	-0.156	-0.098
ξ_{CO}	0.182	-0.067	-0.173	-0.116	-0.156	1	-0.314
ξ_{HCl}	-0.104	0.298	-0.050	-0.213	-0.098	-0.314	1

Table 7:   The magnitude of the largest correlation matrix value max (abs(**C**)) at each time step for the $\tilde{\nu} > 2500\,\mathrm{cm}^{-1}$ fits to the 50 kg TNT fireball spectra. For this data set, the correlation between r and κ_p was always the largest of any two-parameter pairs. At the first time step, the fireball was essentially an optically-trapped Planckian radiator (no apparent selective emission) and the numerical approximation to the Jacobian could not be inverted to estimate the correlation matrix.

t [s]	0.12	0.242	0.363	0.485	0.605	0.727	0.847	0.969
max (abs(**C**))	—	0.841	0.883	0.846	0.843	0.810	0.866	0.923

suggest that these parameters are biased by the model's inability to properly describe the longer wavelength regime. In other words, the temporal profiles of the fit parameters obtained by fitting to $\tilde{\nu} > 2500\,\mathrm{cm}^{-1}$ are preferred and are expected to better represent the state of the fireball. The following discussion will focus on the fits to the restricted spectral range unless otherwise specified. Error bars represent the statistical fit uncertainties associated with the parameters. For some spectra the CO and HCl concentrations could not be reliably estimated due to ill-conditioning of the Jacobian and is responsible for some gaps in the concentration profiles found in Figure 22.

Initial fireball size was approximately 9.7 m and, after some oscillation, increased to a peak value of 10.5 m with time. The uncertainty in r steadily grew with time. Including all wavelengths in the fits results size estimates roughly 1.5 m larger. For comparison, the square root of the peak area obtained from NIR imagery for this event was 10.5 m. The image from the NIR FPA corresponding to this peak area is provided in Figure 23. The reasonable agreement suggests that fireball size can be estimated from a well-calibrated, non-imaging FTS. A more thorough comparison of fireball sizes extracted from spectral fits and NIR imagery will be presented in § 4.5.1. Note that at later times, the degree of correlation between r and κ_p increased as indicated in Table 7.

The temperature approximately followed a linear decay from 1900 to 1200 K in 1 s. Slightly lower temperatures were obtained when including $\lambda > 4\,\mu$m in the fits. The initial temperature compares favorably with results from two optical pyrometry studies of TNT fireballs. Ogura *et al* [85] examined TNT charges spanning 1–100 kg and found that microseconds after detonation, temperatures were between 7000–10000 K. The fireballs rapidly cooled to between 1700–1900 K by ~5 ms and remained in this temperature range up to

65
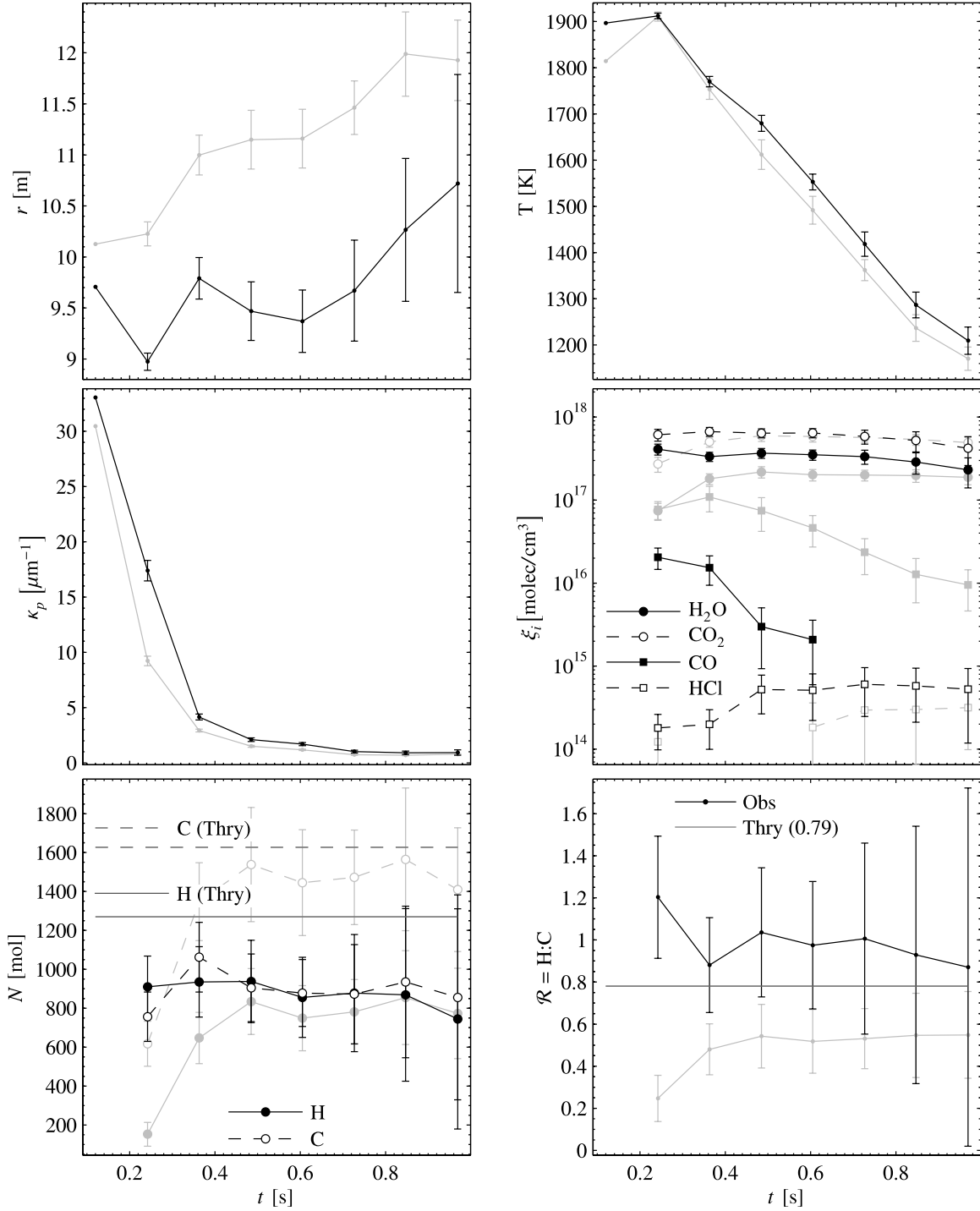
Figure 22: Time-resolved fit parameters and derived quantities extracted from a 50 kg TNT detonation fireball. Error bars represent fit parameter uncertainties at the 95% confidence level. Results from fits to $\tilde{\nu} > 2500\,\mathrm{cm}^{-1}$ are shown in black and results from fits to all spectral data are shown in grey. First spectrum was dominated by particulate emission and corresponding concentrations and derived quantities were unphysical and omitted. *Top panel*: fireball size (left) and temperature (right). *Middle panel*: particulate absorption coefficient (left) and gaseous concentrations (right). *Bottom panel*: total quantity of hydrogen and carbon compared with expected values (left) and the ratio of hydrogen and carbon amounts compared with theory (right). Gaps appearing in the plots indicate where model parameters could not be reliably determined.

Figure 23:   Image captured by the Alpha NIR FPA (320 × 256) during the detonation of 50 kg of TNT. The square root of the fireball area, defined by the number of saturated pixels, is approximately 10.5 m.

about 150 ms, which is approximately the timescals of a single scan of the FTS used in this study. Goroshin *et al* [45] recorded a temperature of 2150 ± 150 K for a 3.2 kg TNT charge between 10–50 ms.

The particulate absorption coefficient decays rapidly with time. The fireball size and absorption coefficient can be used to compute the particulate transmittance via $T_p = e^{-\kappa_p r}$. For this fireball, T_p monotonically increased from 0.04—nearly opaque—to 0.91—nearly transparent—over the observation time. The presence of particulate material is expected as TNT is underoxidized with a needed:available oxygen fraction of 0.37. Underoxidized hydrocarbon combustion typically results in soot taking the form of graphite and diamond [17]. The decay with time of κ_p is consistent with the possibility that soot oxidation is occurring as atmospheric oxygen is turbulently remixed with the fireball.

Concentrations of H_2O and CO_2 are fairly static during the observation time with mean values $\xi_{H_2O} \simeq 3 \times 10^{17}$ molec/cm^3 and $\xi_{CO_2} \simeq 5.5 \times 10^{17}$ molec/cm^3. Some fraction of the water concentration is due to atmospheric water vapor $\xi_{H_2O}^{atm}$ present in the volume of the fireball, and this value must be estimated so that the concentration attributable to the HE, $\xi_{H_2O}^{HE}$, can be determined. The atmospheric contribution is estimated using the ideal gas law with the fireball temperature, pressure, and water vapor mixing ratio (which is on the order of 10^3–10^4 ppm$_v$ during BF2). The fireball pressure is assumed to have returned to atmospheric pressure

by the observation time. For this event, the mean value of $\xi^{atm}_{H_2O} \simeq 0.4 \times 10^{17}$ molec/cm^3 so that $\xi^{HE}_{H_2O}$ is about 87% of the observed water concentration. A similar correction to the carbon dioxide concentration revealed that $\xi^{atm}_{CO_2}$ is ~0.2% of $\xi^{HE}_{CO_2}$. The correction is much smaller as the CO_2 concentration is about 380 ppm$_v$. Quantities derived from the extracted concentrations will use the corrected γ^{HE}_i values.

The initial concentration of CO is approximately 1/30 of the CO_2 concentration and rapidly decays below the limit of detectability, which is on the order of 10^{15} molec/cm^3 given the noise level of the spectra. This limit is also strongly influenced by fireball temperature. As the temperature drops, so does the thermal accessibility the overtone transition giving rise to the CO emission feature near 4000–4400 cm^{-1}. When wavelengths $\lambda < 4$ μm are excluded, this is the only CO band which can reasonably contribute to the emission spectra. The presence of CO is not strongly supported by the observed data and the estimated concentrations are low enough that the gas emissivity is not strongly influenced by its inclusion in the model. In most oxygen-rich hydrocarbon combustion systems (which the fireball would be upon turbulent remixing with atmospheric O_2), CO is often a short-lived intermediate which is quickly oxidized to form CO_2 [44]. As previously mentioned, inclusion of all wavelengths in the fits results in over-estimated CO concentrations which are not supported by the data in the overtone band 4000–4400 cm^{-1}.

HCl concentration grew slightly with time, but was approximately three orders of magnitude smaller than the H_2O concentration. Initially, HCl was not an expected combustion by-product. However, unlike CO, its presence was visually recognized[6] in structured fit residuals near 2700 cm^{-1}. This can be seen in Figure 24 which shows this residual pattern and its subsequent disappearance upon inclusion of HCl.

Two derived quantities are also presented in Figure 22. The number of the ith gaseous molecule can be computed from the volume and concentration via $N_i = r^3 \xi_i$. In the same fashon, the total number of hydrogen (H) and carbon (C) atoms can be accounted for, e.g. $N_H = r^3(2\xi^{HE}_{H_2O} + \xi_{HCl})$. N_H and N_C were computed and compared with expected values based on the weight and stoichiometry of the TNT charge. Both H and C are less than the theoretical maximum values. This could be a result of radiometric inaccuracy, or might indicate a non-trivial presence of carbonaceous soot which, in various combustion systems, can

---

[6]Thanks to John Selby of Northrop Grumman for recognizing this at the 9th Biennial HITRAN Conference in June 2006.
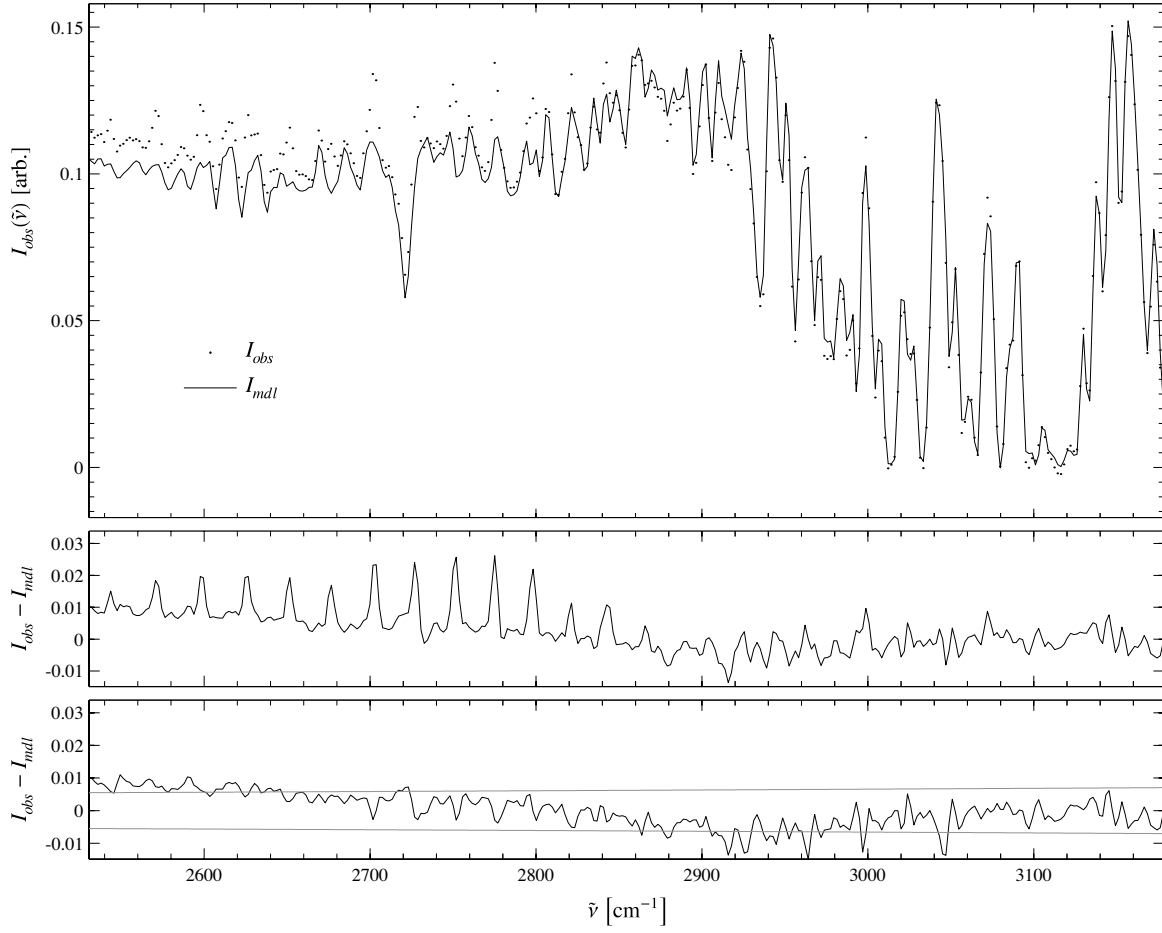
Figure 24: *Top panel*: Observed data and spectral fit before inclusion of HCl as a model parameter. Intensity is on an arbitrary scale. *Middle panel*: Fit residuals indicating structure which corresponds to the emission features of HCl. *Bottom panel*: Fit residuals after including HCl as a model parameter.
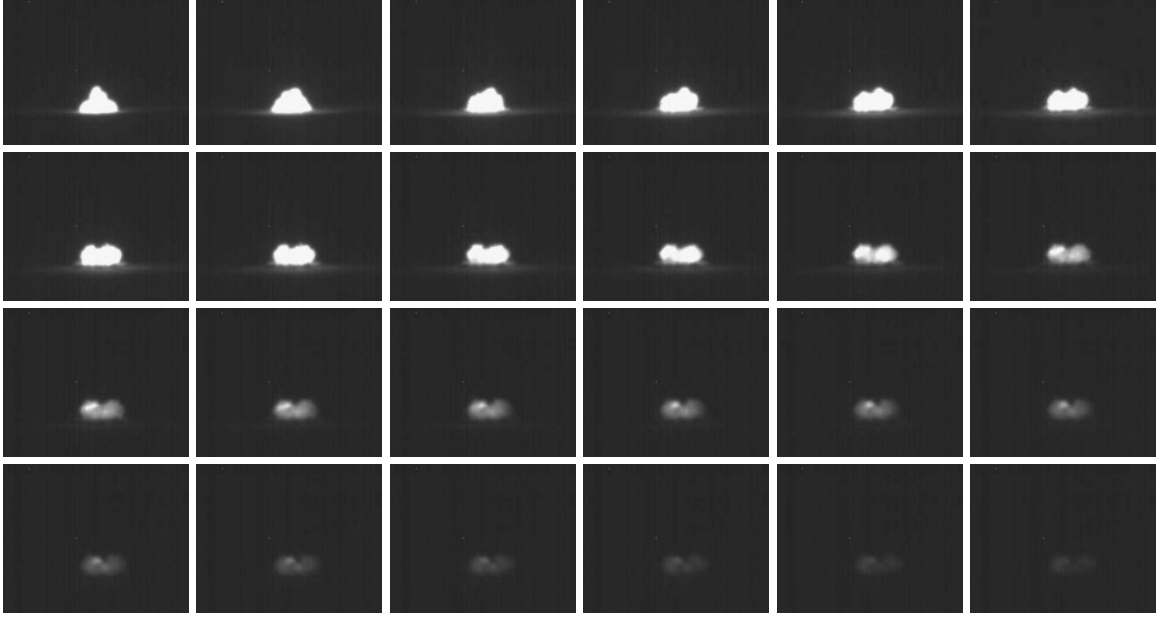
Figure 25:   30 Hz imagery sequence of a 50 kg TNT detonation fireball captured by the Alpha NIR FPA (320 × 256). Time increases from left to right and top to bottom.

contain up to 40% (by number) hydrogen [81]. Furthermore, the discrepency between the measured and fully-oxidized values of N_i suggest less efficiency for the carbon oxidation pathways. This behavior is expected given Cooper's [22] or the Kistiakowsky and Wilson's [2] empirical rules described in Appendix D: hydrogen is oxidized to H_2O before carbon is oxidized to CO_2 [22]. The behavior of N_H and N_C with time is fairly static. The ratio of these values, $\mathcal{R} = N_H/N_C$, also compares favorably with the expected value of 0.79. This indicates that fireball spectra can provide information about the HE starting material. Note that when all wavelengths are included in the fits, the behavior of $\mathcal{R}$ is substantially altered and suggests kinetic behavior which is no longer consistent with the empirical rules just mentioned.

4.5.1   Comparisons between NIR imagery and fireball model.   Sequential imagery captured at 30 Hz in the NIR of the 50 kg TNT detonation fireball described in the preceding section is provided in Figure 25. The pixel intensities corresponding to the fireball were well-separated from reflected light. As a result, simple thresholding can be used to estimate the fireball size [29]. Each pixel FOV is known, so the NIR fireball area A_{NIR} is simply the sum of individual fireball pixel areas. For comparison with the fireball model, the area is reduced to a linear dimension by taking its square root. For this event, the fireball saturated the detector and
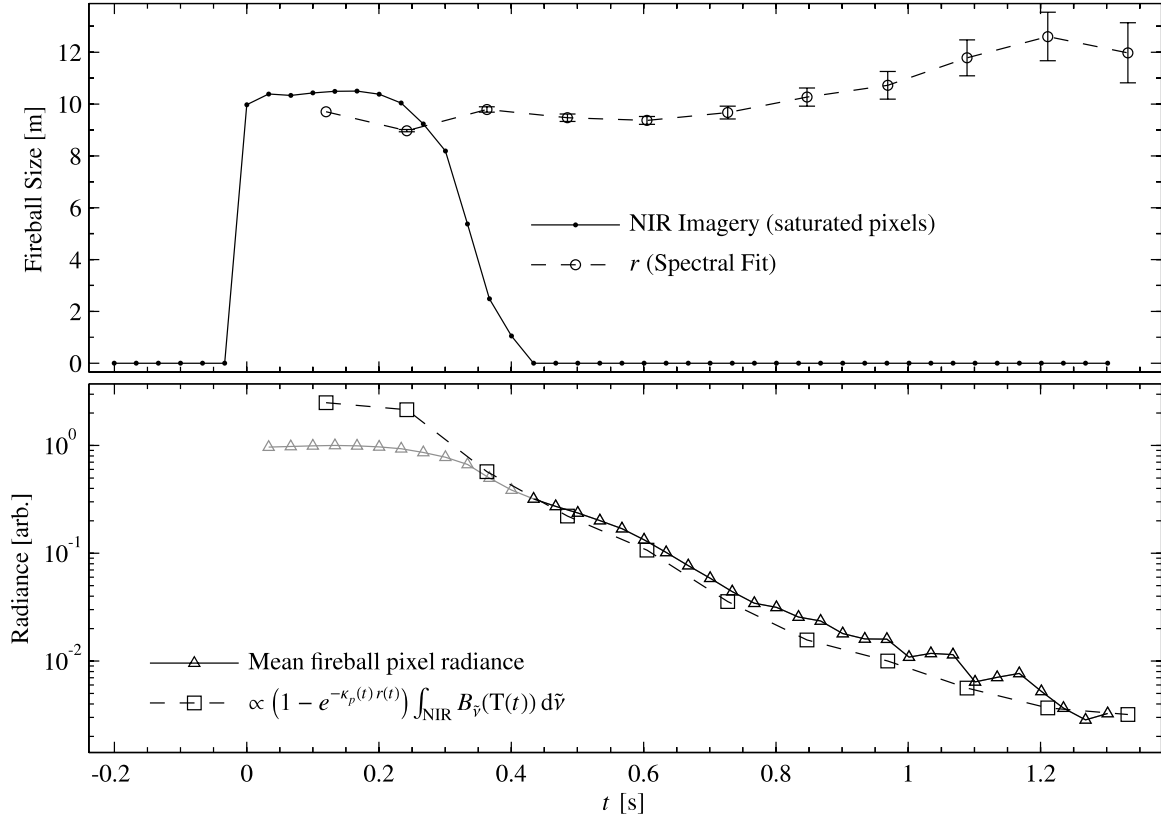
Figure 26: *Top panel*: 50 kg TNT detonation fireball size (square root of area) as captured by the Alpha NIR FPA (·) compared with the size estimated from fits to the corresponding MWIR spectra (○). Error bars associated with r represent its uncertainty at the 95% confidence level. *Bottom panel*: Comparison of mean pixel radiances estimated from the FPA (△) and computed using the fireball model (□). The radiance scale is arbitrary and the curves are scaled to match at $t = 0.43$ s, which is the point when fireball pixels no longer saturated the FPA.

pixel intensities greater than 95% of the FPA's dynamic range were attributed to the it. The temporal evolution of the fireball size is presented in Figure 26. The fireball reaches its peak size of 10.5 m instantaneously and maintains that size for approximately 0.25 s. Then the size appears to decay to 0 m by ~0.55 s. This is an artifact of the thresholding. The fireball has cooled and the pixel intensities have fallen below the cutoff value. Examination of the imagery sequence in Figure 25 confirms the fireball dims while the area remains approximately constant[7]. Prior to this dimming in the NIR, the spectrally determined fireball size r compares favorably with imagery.

---

[7] The dynamic range of the imagery is reduced upon printing making the claim appear unlikely. This approximately constant nature of the fireball is more apparent when viewing the electronic version of this document on a computer monitor.

Each pixel captured by the NIR FPA scales linearly with radiance provided the detector is not near saturation. Thus, to within a scale factor, mean fireball radiance can be estimated by averaging over pixel response values corresponding to the fireball[8]. Imagery reveals a non-homogeneous fireball, so an average radiance value enables comparison with the fireball model. As the fireball cools, systematically distinguishing fireball pixels from other above-ambient, non-fireball pixels is more difficult. To alleviate this problem, mean pixel radiance $\langle L_{pix} \rangle$ was computed for the set of pixels which initially saturated during the first frame.

The fireball model can predict pixel radiances using the extracted fit parameters. Ignoring the contribution from the selective emitters[9], $\langle L_{pix} \rangle$ is estimated via

$$\langle L_{pix} \rangle = \left(1 - e^{-\kappa_p(t)\, r(t)}\right) \int_{\text{NIR}} B_{\tilde{\nu}}\left(\text{T}(t)\right)\, d\tilde{\nu} \tag{26}$$

where NIR indicates integrating over the imaging detector's response curve. The Alpha NIR uses an InGaAs FPA with a response over $(0.9 \leq \lambda \leq 1.65\,\mu\text{m})$. For simplicity, the response was taken as unity over this bandpass.

Figure 26 provides the time-dependent, average pixel radiance measured by the NIR FPA and compares them with the radiance estimates from Equation 26. The scale is arbitrary as the FPA was not calibrated. Radiance levels are not accurate when the majority of fireball pixels are saturated—these points are shown in grey. Near $t = 0.43$ s, the number of saturated pixels comprising the fireball is less than 2%, so the subsequent decay in radiance is reliable. To facilitate comparison of the NIR and model radiances, both are scaled to match at $t = 0.43$ s. At all subsequent times, the experimentally estimated and theoretically computed radiance profiles are in excellent agreement. It is possible that the radiance profiles still differ by a constant scaling factor. Nonetheless, the predicted decay rate in mean pixel radiance remains in good agreement with observation.

---

[8]Although the NIR camera was not calibrated, a non-uniformity correction leveled individual pixel responses, preserving the ability to meaningfully average pixel values.

[9]Selective emission from gases could not be included as molecular cross-sections were not computed for the NIR.

4.5.2 Recommended Method of Fitting.   Improvements to fit quality and large reductions in systematic errors were observed when excluding $\tilde{\nu} < 2500\,\text{cm}^{-1}$ from fits to all fireball spectra collected during BF2. This illustrates a deficiency of the fireball model at longer wavelengths and suggests a practical method of avoiding it, namely omitting the longer wavelengths. All forthcoming results are derived from fits to $\tilde{\nu} \geq 2500\,\text{cm}^{-1}$. The underlying cause of the discrepancy at long wavelengths is unknown but certainly stems from the restrictive assumptions used to derive the fireball model. One possible explanation for the deficiency may be the assumption of a homogeneous temperature field. By including the effects of a cooler, above-ambient shell surrounding the hot fireball core, the long-wavelength region of the spectrum can be more accurately fit, a result which is briefly examined in Appendix C.

4.6 Analysis of 50 kg *ENE Fireball Spectra*

An abbreviated examination of fits to the detonation fireball spectra from a 50 kg detonation of ENE2B is now provided. The fits to the observed spectrum at $t = 0.24\,\text{s}$ are presented in Figure 27. The fit was restricted to $\tilde{\nu} > 2500\,\text{cm}^{-1}$, but the full spectrum and fit residuals are provided. The fit to this ENE spectrum was good with RMS and standard errors of $43\,\text{W/sr/cm}^{-1}$ and 6.3, respectively. In regions where SNR > 5 and $T_{atm}(\tilde{\nu}) > 0.05$, the relative error was 8% RMS and 5% median magnitude. Examination of the residuals reveals some systematic structure between 2800–3400 cm^{-1}, slight broadband curvature near 4700 cm^{-1}, and two narrow spikes at 6539 and 6592 cm^{-1}. The source of these two emission lines is presently unknown. It will be demonstrated in Chapter V to be a useful feature for distinguishing the "enhanced" explosives ENE1 and ENE2 from the baseline explosive ENE0.

The temporal evolution of the fit parameters are provided in Figure 28. The initial fireball size was about 9 m and grew to slightly less than 12 m after 1 s. The initial fireball size estimated from the MWIR spectrum was about 3 m smaller than the peak area from NIR imagery. Although the imagery and spectral estimates of the fireball size differ, the temporal behavior of the average pixel radiance from the NIR camera still compares favorably with the predicted $\langle L_{pix} \rangle$ trend. Figure 29 compares the size profiles and normalized radiance curves as estimated from the NIR FPA and predicted by the fireball model.

73
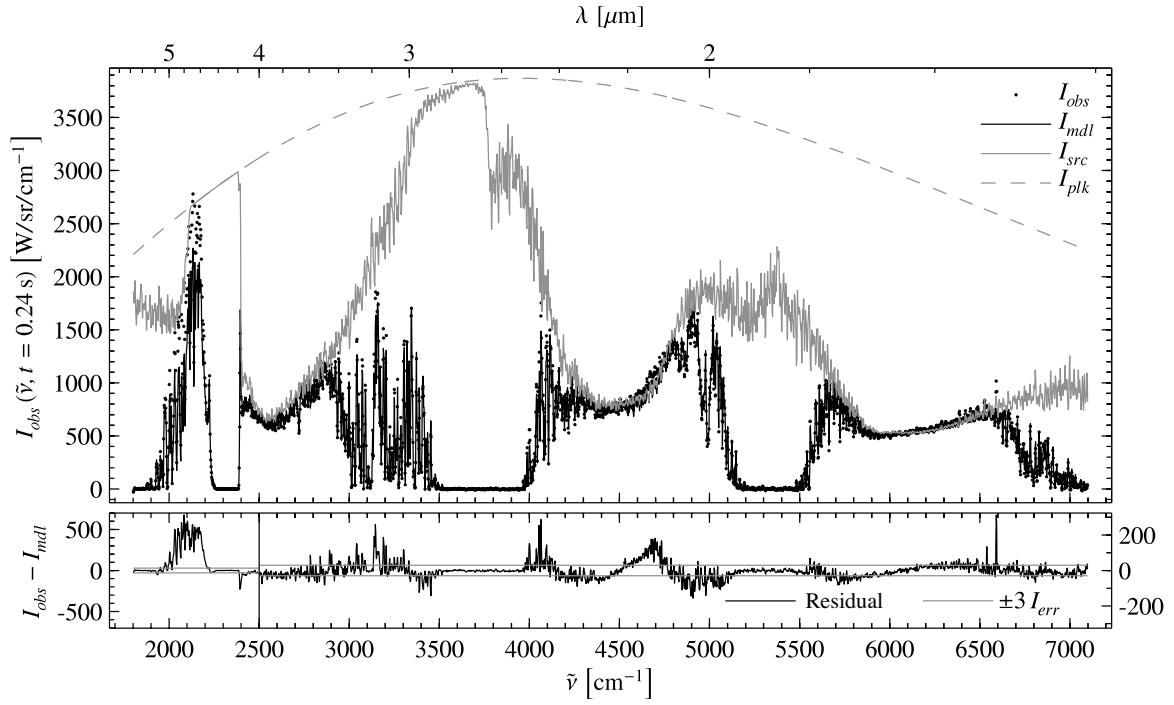
Figure 27: *Top panel*: Observed fireball spectrum ($\cdot$) at $t = 0.24\,\text{s}$ from a $50\,\text{kg}$ ENE2B detonation compared with the best fit of the fireball model to $\tilde{\nu} > 2500\,\text{cm}^{-1}$ (solid black). The estimated at-source spectrum is provided (solid grey) along with the Planckian intensity distribution (dashed grey). *Bottom panel*: Fit residuals ($I_{obs} - I_{mdl}$, black) compared with I_{err} (grey), which is an estimate of the instrument noise level. The left ordinate is used for $\tilde{\nu} < 2500\,\text{cm}^{-1}$ and the right ordinate corresponds to $\tilde{\nu} \geq 2500\,\text{cm}^{-1}$.
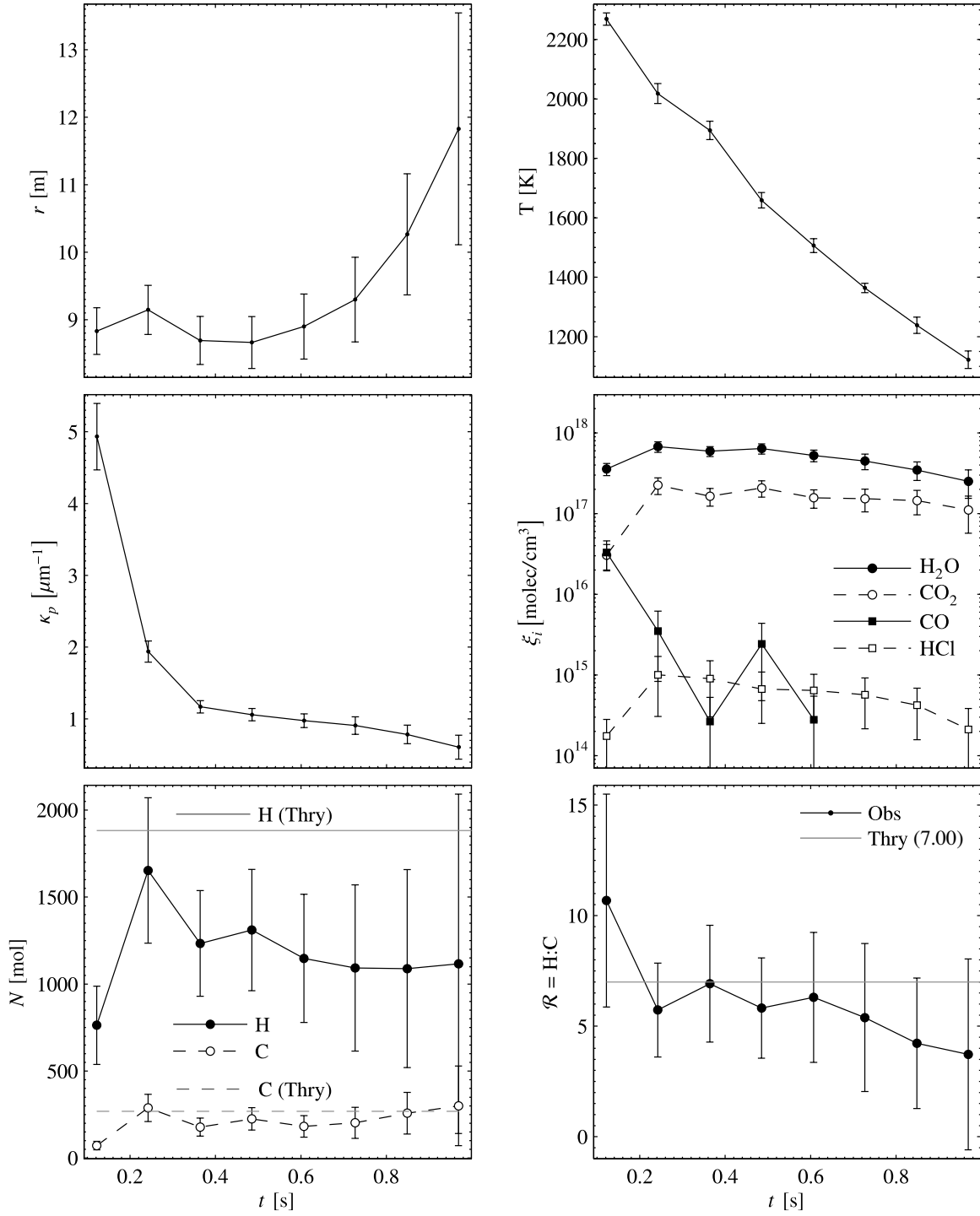
Figure 28: Time-resolved fit parameters and derived quantities extracted from a 50 kg ENE2B detonation fireball. Error bars represent fit parameter uncertainties at the 95% confidence level. *Top panel*: fireball size (left) and temperature (right). *Middle panel*: particulate absorption coefficient (left) and gaseous concentrations (right). *Bottom panel*: total quantity of hydrogen and carbon compared with expected values (left) and the ratio of hydrogen and carbon amounts compared with theory (right).

75
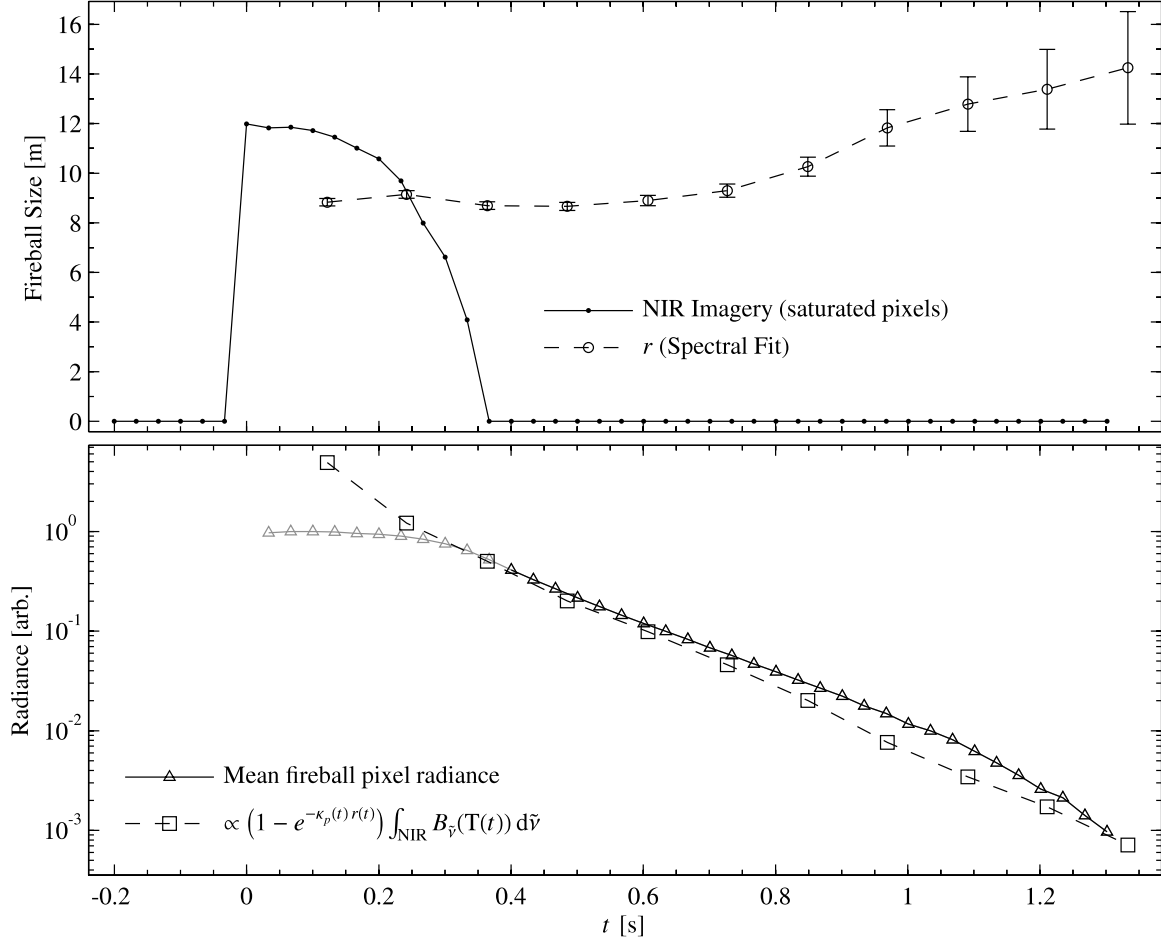
Figure 29: *Top panel*: 50 kg ENE2B detonation fireball size (square root of area) as captured by the Alpha NIR FPA (·) compared with the size estimated from fits to the corresponding MWIR spectra (○). Error bars associated with r represent its uncertainty at the 95% confidence level. *Bottom panel*: Comparison of mean pixel radiances estimated from the FPA (△) and computed using the fireball model (□). The radiance scale is arbitrary and the curves are scaled to match at $t = 0.37\,\text{s}$, which is the point when fireball pixels no longer saturated the FPA.

The initial temperature of the ENE2B fireball was 2270 K, much hotter than the initial TNT tempera-
ture. This is likely due to the presence of aluminum. Oxidation of aluminum is highly exothermic. It can be
oxidized to Al_2O_3 by reaction with the gaseous byproducts H_2O and CO_2. This has the effect of increasing
detonation temperatures, even when the explosive material is under-oxidized [2, pp. 94].

The ENE fireball was less optically thick with a particulate absorption coefficient that was much smaller
than that of TNT. κ_p quickly decreased with time, and the corresponding particulate transmittance monoton-
ically increased from 0.65 to 0.93. The smaller particulate absorption coefficients may reflect improved
combustion efficiency (relative to TNT) with more of the HE being fully oxidized to gaseous species in the
initial detonation reaction. This is consistent with the availability of more oxygen in the ENE2B starting
material relative to that in TNT. (See Table 3.) It may also be related to the much smaller fraction of carbon
in the HE compared with TNT.

Carbon dioxide concentrations were much smaller for the ENE fireball, consistent with the material's
stoichiometry. Initially, both the CO_2 and CO concentrations were the same (3×10^{16} molec/cm^3). Following
this, the CO_2 concentration increased to about 2×10^{17} molec/cm^3. The increase in CO_2 coincided with an
order-of-magnitude drop in CO concentration. The HCl concentration was between 2–10×10^{15} molec/cm^3.
Total gaseous hydrogen atoms N_H accounted for about 2/3 of the expected stoichiometric value, whereas
the measured and expected values for N_C were the same. This lead to $\mathcal{R}$ values that tended to somewhat
underestimate, yet agree to with within fit uncertainties, the expected value 7.0. This indicates $\mathcal{R}$ may be a
useful feature for the fireball classification problem: it is strongly correlated with the HE starting material
stoichiometry and clearly distinguishes the TNT and ENE2B fireballs.

4.7 Sensitivity Analysis of $\mathcal{R}$

Examples of fits to TNT and ENE spectra reveal that Equation 23 successfully describes the observed
MWIR emission features using a few physical parameters. Results from fitting all BF2 data will be more
thoroughly explored in Chapter V. As hinted at above, it will be demonstrated that $\mathcal{R}$ indeed correlates
strongly with the HE material. In anticipation of these key findings, it is important to explore measurement

factors which impact the estimation of $\mathcal{R}$. Three measurement factors are explored below which can adversely corrupt the estimation of $\mathcal{R}$ via spectral fits. They are (1) radiometric accuracy, (2) atmospheric water vapor concentration, and (3) spectral resolution. The first two factors represent possible sources of error with respect to the BF2 data set. Understanding the third factor might influence future field tests as the trade-off between spectral and temporal resolution will be understood in terms of key feature extraction. Furthermore, understanding all three factors might inform design trade-offs should an operational sensor for measuring $\mathcal{R}$ be pursued.

4.7.1 Radiometric Accuracy. Frequent calibrations were performed, but discrepancies existed between instruments collecting over identical spectral bands. Radiometric accuracy might best be considered good to within a factor of 2. As demonstrated in Equations 24, a radiometric scaling factor corrupts the fireball size and concentration terms. Since heated atmospheric water vapor can represents a sizable fraction of the measured water concentration, an accurate intensity scale is needed to ensure a good estimation of $\mathcal{R}$. In the presence of a multiplicative intensity scaling factor C, it can be shown that the estimate of $\mathcal{R}$ is affected as follows:

$$\mathcal{R} = \frac{2\xi_{H_2O} + \xi_{HCl} - 2\xi_{H_2O}^{atm}/\sqrt{C}}{2\xi_{CO_2} + \xi_{CO} - \xi_{CO_2}^{atm}/\sqrt{C}} \tag{27}$$

This form is encouraging as the presence of $\sqrt{C}$ lessens the degree to which radiometric accuracy affects $\mathcal{R}$. The impact on $\mathcal{R}$ is presented as a function of C in Figure 30 for three environments. The solid curve represents a 1% water mixing ratio (by volume) corresponding to the atmospheric state during BF2 testing. The two dashed curves demonstrate both extremes, an arid environment (0.25%) and a humid environment (2.5%). Note that the x-axis is logarithmic and spans two orders of magnitude. Not surprisingly, the more humid the environment, the more sensitive $\mathcal{R}$ is to radiometric accuracy. With the atmospheric conditions during BF2 the test conditions, a 200% error in the intensity scale ($0.5 \leq C \leq 2$) only introduces a maximum uncertainty in $\mathcal{R}$ of 5%. For comparison, in a humid environment, the uncertainty in $\mathcal{R}$ increases to 13%, and in an arid environment, the error drops to 1%.

78
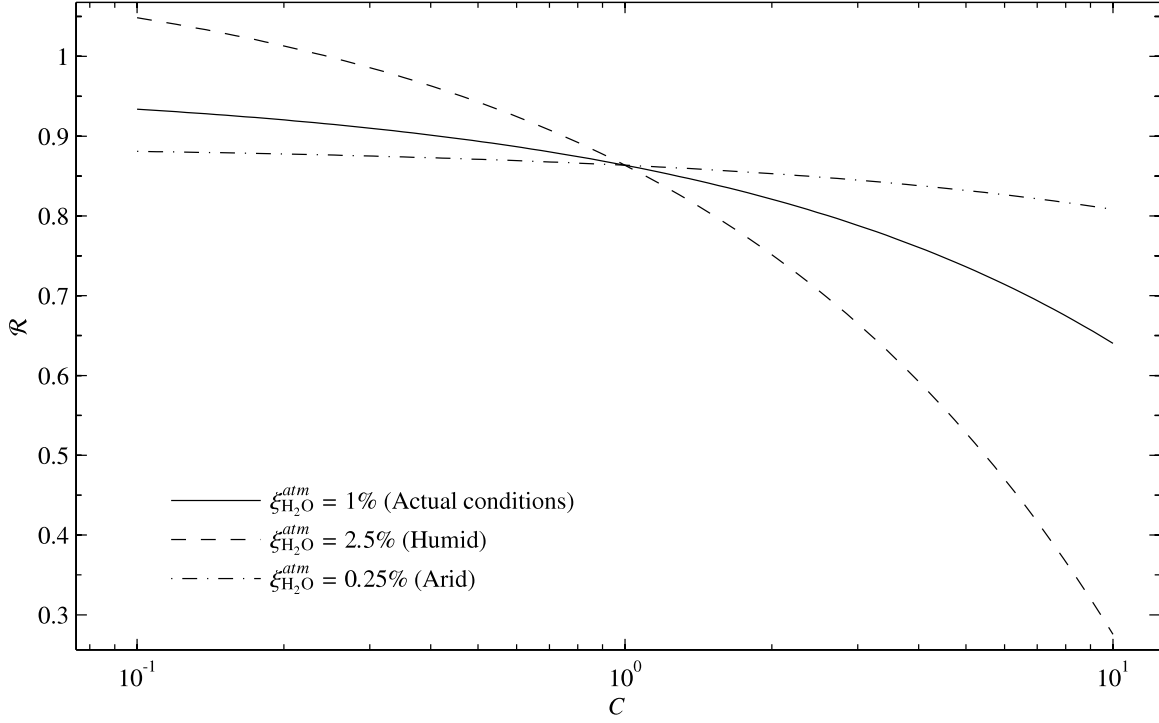
Figure 30: Sensitivity of $\mathcal{R}$ with respect to a multiplicative intensity scale factor error of C. The error in $\mathcal{R}$ depends on atmospheric water content. The solid curve represents BF2 test conditions ($1\%_v$), and the dashed lines represent extremely humid ($2.5\%_v$, — — —) and arid ($0.25\%_v$, — · — ·) conditions.

4.7.2 Atmospheric Water Vapor Concentration. Concentrations of most trace gases which absorb in the MWIR are well-known and vary slowly with time and geographical position [56]. As a result, their influence on the total atmospheric transmittance curve is easily estimate. However, water vapor can vary rapidly in both time and location. In the MWIR, it is a dominant absorber over moderate path lengths, so accurate estimates for $\xi_{H_2O}^{atm}$ are crucial for predicting T_{atm} and thus apparent intensity. $\xi_{H_2O}^{atm}$ was taken from meteorological instruments deployed during BF2 and was not a free parameter during the spectral fitting previously described. To assess the influence of atmospheric water vapor on $\mathcal{R}$, a sequence of fits to the 50 kg TNT spectrum described above were performed at several different values of $\xi_{H_2O}^{atm}$. Values for $\xi_{H_2O}^{atm}$ were taken between $\pm 50\%$ of the meteorological value. Trends were similar when $\xi_{H_2O}^{atm}$ was either under- or over-estimated. For brevity, only the over-estimation case will be presented.

Residuals from the fits to the $t = 0.24\,\mathrm{s}$ TNT spectrum are presented in Figure 31. The residual structure grows in magnitude as the water concentration is increasingly over-estimated. Also provided in
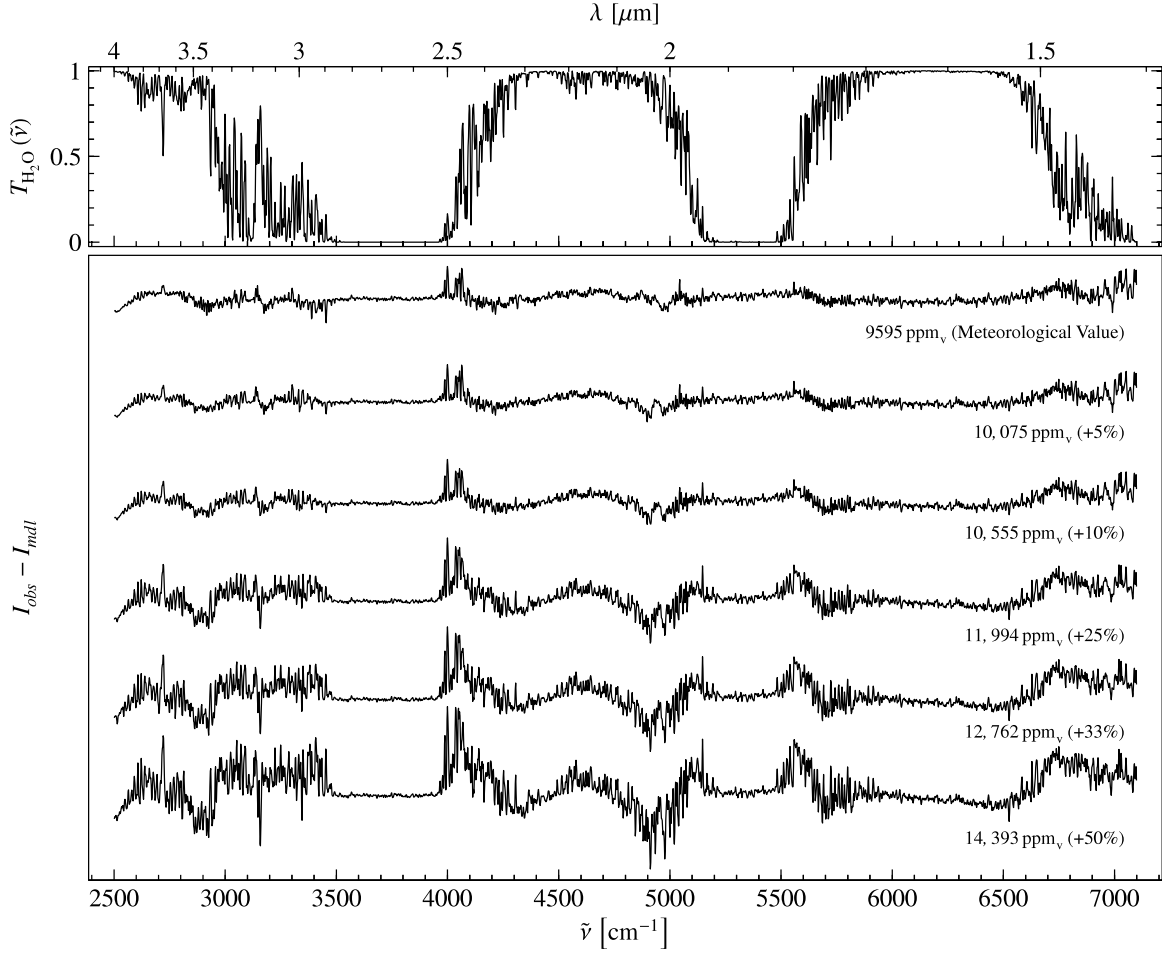
Figure 31: *Top panel*: Water transmittance profile over a 3.26 km pathlength and $\xi_{H_2O}^{atm} = 9595$ ppm$_v$. *Bottom panel*: Residuals resulting from fits to the $t = 0.24$ s spectrum of a TNT fireball where $\xi_{H_2O}^{atm}$ was varied up to a 50% over-estimation of the meteorological value.

Figure 31 is the water component of the atmospheric transmission curve T_{H_2O}. Many of the residual structures can be matched up with absorption features in T_{H_2O}. Thus, in cases when bad meteorological data leads to poor estimates of $\xi_{H_2O}^{atm}$, the fit residuals will suggest that a modification is needed.

When accurate meteorological data is unavailable, an understanding of the sensitivity of $\mathcal{R}$ to errors in atmospheric water vapor is appropriate. Figure 32 displays the dependence of $\mathcal{R}$ on $\xi_{H_2O}^{atm}$ for several time steps in the TNT data cube. Extracted $\mathcal{R}$ values were very sensitive to $\xi_{H_2O}^{atm}$ for the $t = 0.12$ s spectrum, over-estimating the true value by a factor of 10 with only a 25% over-estimation of the water vapor. Larger values of 11 and 150 (not shown) were obtained for the 33 and 50% over-estimations. This is not surprising; the first spectrum is dominated by particulate emission so that the gaseous emission appears small. Consequently, an
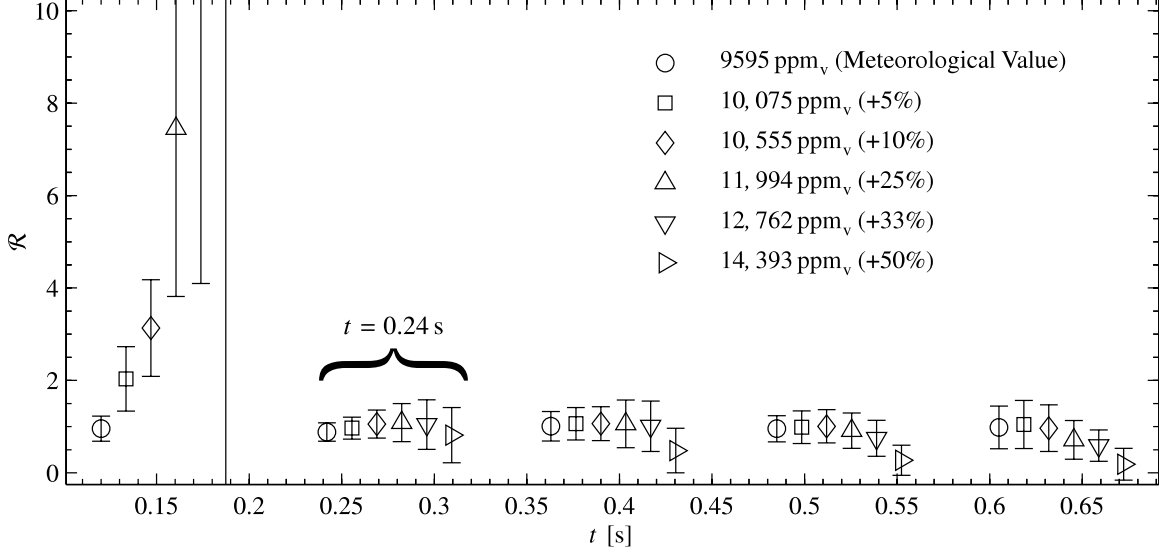
Figure 32: Sensitivity of $\mathcal{R}$ with respect to atmospheric water vapor concentration. An increasing time offset is applied to spectra fit with increasing water vapor concentrations. Error bars represent propagation of errors based on fit parameter uncertainties (95% confidence level).

accurate transmittance function is needed in order to extract reliable selective-emitter concentrations. Fortunately, the associated uncertainties grow as well, indicating that the $\mathcal{R}$ estimate is unreliable when the wrong atmospheric transmittance profile is used. Bad estimates of $\xi_{H_2O}^{atm}$ have a much smaller impact on $\mathcal{R}$ when selective emission begins to dominate the emission spectrum. For example, the average difference between the "true" $\mathcal{R}$ and that obtained with 25% over-estimation in $\xi_{H_2O}^{atm}$ was 20% for spectra satisfying $t \geq 0.24$ s.

In an operational setting, two important variables may be unknown. First, good meteorological data may be unavailable for estimating $\xi_{H_2O}^{atm}$. Furthermore, the range to the fireball may be unknown. Both of these factors influence T_{atm}. The range term is also important for scaling detector irradiance to intensity, and thus obtaining physically meaningful fit parameters. The attenuating effect of water vapor imparts a spectrally-varying fingerprint on the apparent intensity (or irradiance) reaching the detector. As a result, it is possible to treat $\xi_{H_2O}^{atm}$ as another fit parameter when meteorological data is unavailable. CO_2 also imparts a frequency-dependent absorption pattern in the MWIR. Since its concentration is, for the most part, temporally and geo-spatially stable at approximately 380 ppm$_v$, this information can be used to infer range to the target by allowing $\xi_{CO_2}^{atm}$ to be a fit parameter as well. For example, if $\xi_{CO_2}^{atm}$ represents the best fit parameter at a

81
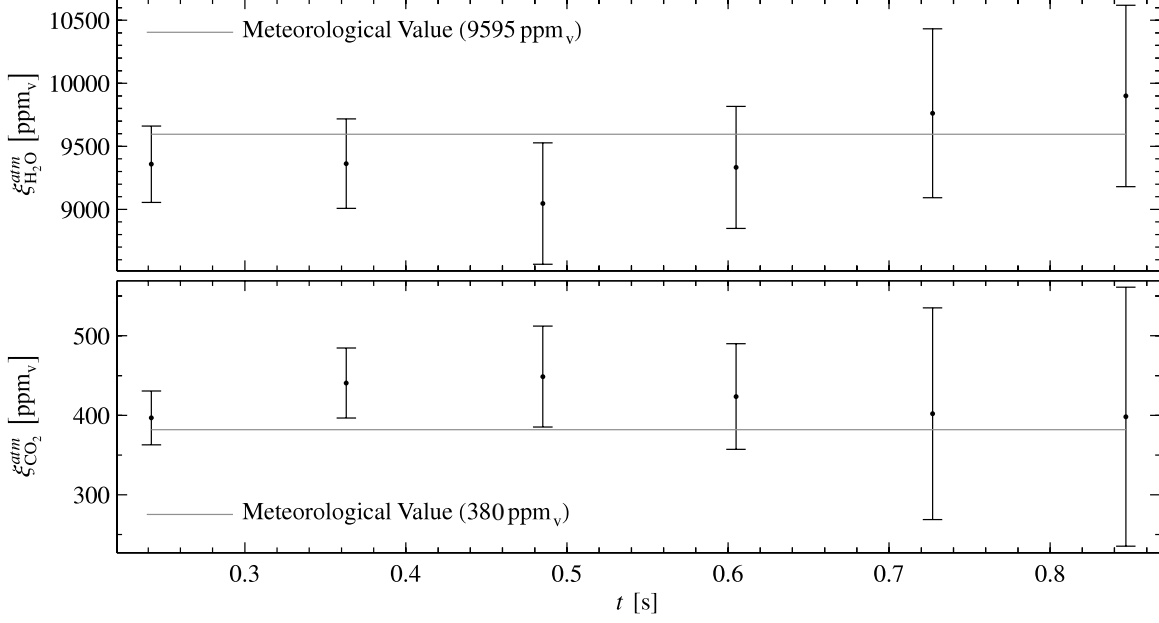
Figure 33: Comparison of meteorological and fitted parameters extracted from a 50 kg TNT fireball. *Top panel*: Results for $\xi_{H_2O}^{atm}$ compared with experimental value of 9595 ppm$_v$ from local weather station. *Bottom panel*: Results for $\xi_{CO_2}^{atm}$ compared with experimental value of 380 ppm$_v$ from La Jolla Pier CO_2 monitoring station. Error bars represent fit parameter uncertainty at the 95% confidence level.

guessed target range of R_g, the true range R_t can be inferred via

$$R_t = \frac{\xi_{CO_2}^{atm}}{380 \, \text{ppm}_v} R_g \tag{28}$$

For the 50 kg TNT fireball spectra, $\xi_{H_2O}^{atm}$ and $\xi_{CO_2}^{atm}$ were introduced as free parameters, bringing the total number of variables to 9. Figure 33 presents the fitted values of $\xi_{H_2O}^{atm}$ and $\xi_{CO_2}^{atm}$ for several spectra in this data set. In almost all cases, the fitted values agree with the meteorological values to within the parameter uncertainties. Mean values for $\xi_{H_2O}^{atm}$ and $\xi_{CO_2}^{atm}$ via fits were 9375 and 418 ppm$_v$, respectively. Meteorological values for water and carbon dioxide were 9595 and 380 ppm$_v$. Introducing these atmospheric parameters did not significantly alter the fireball parameters. If range to the target had not been known, the estimate based on $\xi_{CO_2}^{atm}$ would have been 3.57 km and the intensity would have been scaled up by a factor of 1.20. Viewing this as a radiometric scaling error, $\mathcal{R}$ would have been altered by only 1.1%.

These results demonstrate that both the atmospheric water vapor and range to target do not need to be known *a priori*. This information is encoded in the fireball spectra via T_{atm} and can be retrieved with accuracy sufficient enough for the reliable extraction of $\mathcal{R}$.

4.7.3 Spectral Resolution.   The trade-off between spectral and temporal resolution is common to nearly all spectral instrumentation. Increasing spectral resolution requires more acquisition time per spectrum thereby reducing the temporal resolution. In FTS, decreasing spectral resolution improves SNR and lessens the impact of scene-change artifacts. At the same time, multiple sharp emission features become broadened and may overlap, thereby reducing the ability to uniquely assign spectral features to particular emitters. For the present application, improved temporal resolution could enable a better understanding of event kinetics and lead to additional key features. Also, lesser demands on spectral resolution enables the development of a smaller, cheaper, and more readily deployed operational sensor for measuring $\mathcal{R}$, provided this key feature can still be robustly estimated.

The effects of decreased resolution on spectral estimates of $\mathcal{R}$ were studied by the truncation of inter-ferograms during post-processing. The 8192 pt. double-sided interferogram was symmetrically trimmed to lengths of 4096, 2048, and 1024 pts. for corresponding resolutions of $\Delta\tilde{\nu} = 3.9, 7.7$, and $15.4\,\text{cm}^{-1}$. The appropriate ILS was used to modify the fireball model (Equation 23) for fitting to the lower-resolution spectra. The effects of reducing resolution on the data and fit are presented in Figure 34 for the $t = 0.49\,\text{s}$ spectrum of the 50 kg TNT fireball. The top panel displays both the data and fit in black along with the fit residual, multiplied by 10, in grey. Panels below show the same data, fit and residual at subsequently reduced spectral resolutions. Each halving of spectral resolution would have been accompanied by nearly a doubling in the acquisition rate had the FTS system been so configured.

Examination of the fit residuals at decreased resolution reveals that many of the systematic errors are broadband in nature. As resolution is degraded, the apparent "white noise" disappears but the broadband systematic errors remain. This result is important for two reasons. First, this is strong evidence that SCAs are not responsible for any of the major sources of systematic error. In fact, if SCAs are at all present in the
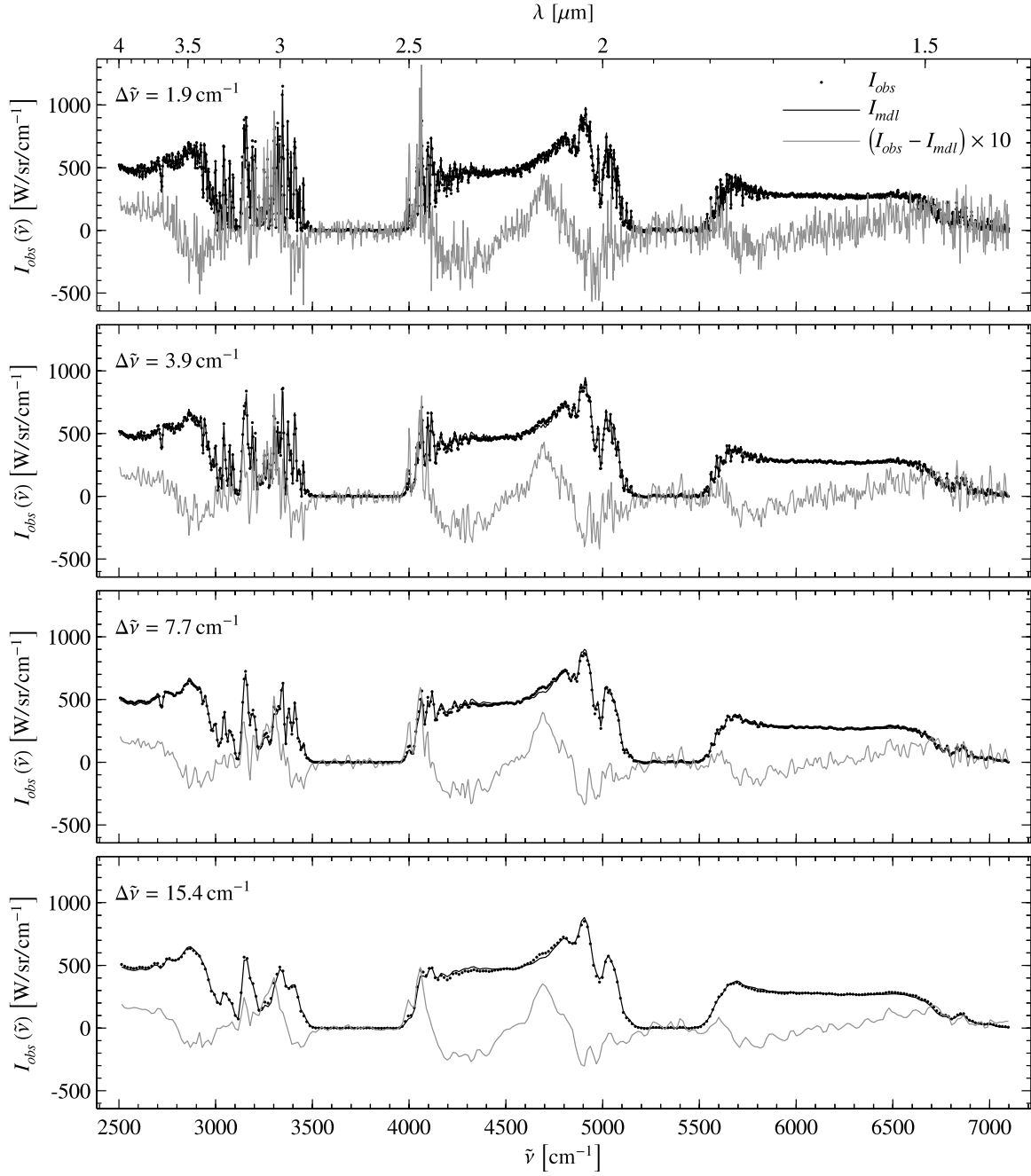
Figure 34: 50 kg TNT fireball spectrum ($\cdot$, $t = 0.49\,\mathrm{s}$) and fits (black line) at spectral resolutions of $\Delta\tilde{\nu} = 1.9, 3.9, 7.7, 15.4\,\mathrm{cm}^{-1}$. The corresponding fit residuals are shown in grey and are scaled up by a factor of 10 for clarity.

84

real component of the spectrum, their effect is difficult to distinguish from the high-frequency white noise. Secondly, the improved SNR with decreasing spectral resolution indicates that additional information content is still present in the fit residuals. At the original spectral resolution ($\Delta\tilde{\nu} = 1.9\,\mathrm{cm}^{-1}$), the standard error of the fit was 2.5. That is, the residuals were only about 2.5 larger than the instrument noise level, naively suggesting that most of the information content in the spectrum had been extracted by the fireball model. In fact, this is an artifact of the poorer SNRs accompanying single-scan, high-resolution spectra. The standard error, in order of decreasing resolution, increases to 3.5, 6.3, and 15.8. Thus, despite the surprisingly good agreement between the observed and fitted spectra, there is room for improvements to the fireball model.

Fitted concentrations changed by as much as 11% with variations in spectral resolution. Changes in temperature and size were less notable ($<$ 3%). Decreases in spectral resolution resulted in increased uncertainties for all fit parameters. For example, as resolution degraded from $\Delta\tilde{\nu} = 1.9$ to $15.4\,\mathrm{cm}^{-1}$, parameter uncertainties increased by a factor of 2–2.5. This means that the smearing and spectral mixing of the fitting "basis functions" imparted more uncertainty than was gained by an improved SNR. Fortunately, changes in the gaseous concentrations occurred in a manner which mostly preserved $\mathcal{R}$. This is seen in Figure 35, which illustrates the temporal changes in $\mathcal{R}$ as a function of resolution. Thus, while uncertainty in $\mathcal{R}$ grows as resolving power is reduced, the H:C ratio is still obtainable at moderate to low resolution. Increased concentration uncertainties might represent a worthy trade-off if increasing temporal resolution nets an improved understanding of fireball dynamics.

4.8 Conclusions

Midwave infrared emissions from several types of uncased, CHNOAl-based high explosives can be described by a basic physical model. The model enables high-fidelity dimensionality reduction of apparent intensity using seven physical parameters obtained by fitting. The fit parameters appear reasonable: fireball sizes estimated by fits to the (non-imaging) MWIR spectra agree favorably with NIR imagery and the initial TNT temperature is consistent with optical pyrometry studies. The extracted concentrations can be used to estimate the relative amounts of hydrogen and carbon ($\mathcal{R}$) within the HE starting material. For TNT and
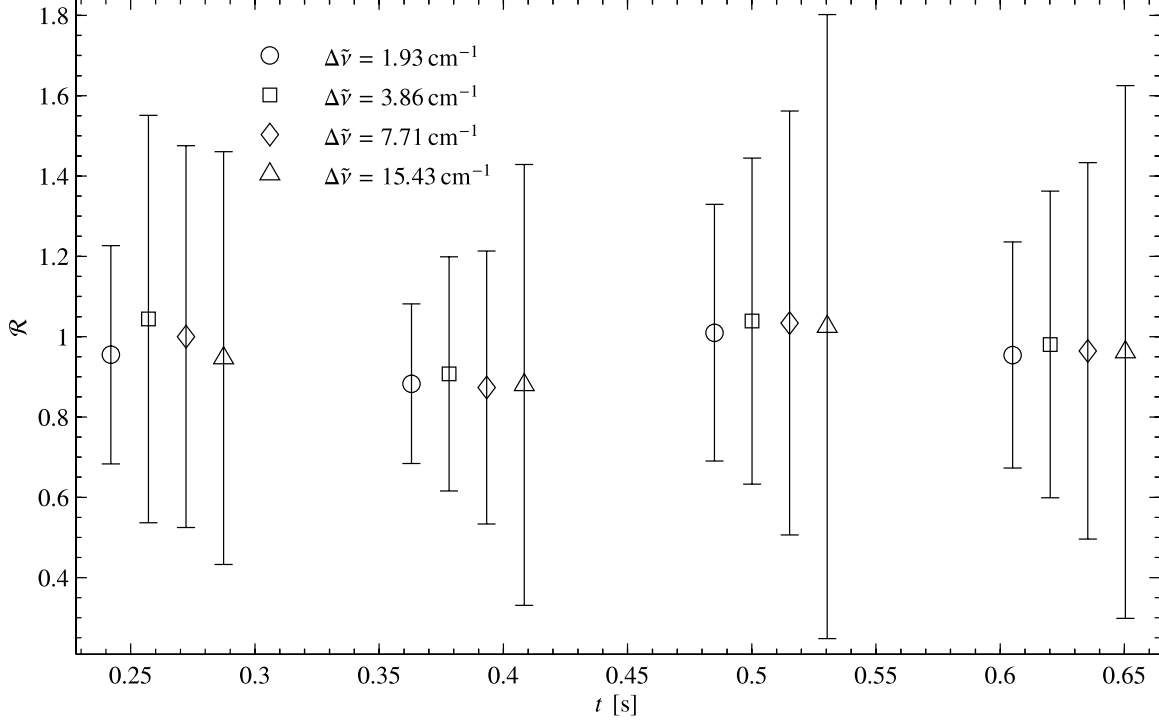
Figure 35: Temporal evolution of extracted $\mathcal{R}$ values at different spectral resolutions. An increasing time offset has been applied to $\mathcal{R}$ values extracted from increasingly degraded spectral resolutions. Error bars represent propagation of errors based on fit parameter uncertainties (95% confidence level).

ENE2B, the $\mathcal{R}$ agreed with the thermodynamically expected values to within the fit uncertainties, suggesting the utility of $\mathcal{R}$ to the HE classification problem. Because the model reduces dimensionality and produces key features which are connected to a physical fireball model, the prospect of remote HE identification from emission signatures has been substantially enhanced.

Since $\mathcal{R}$ is important to the HE identification problem, its sensitivities to radiometric accuracy, atmospheric state, and instrument resolution were examined. In general, radiometric errors have only a small impact on $\mathcal{R}$, and only become important in the most humid environments. When meteorological data and range-to-target are unknown, they can be treated as model parameters and estimated well and do not hamper the reliability of extracted $\mathcal{R}$ values. Finally, spectral resolution can be relaxed without substantially altering estimates of $\mathcal{R}$. Analysis of the fit residuals at various spectral resolutions also indicated that SCAs minimally impact the real component of the spectrum, demonstrating that FTS can be used to study detonation fireballs. These results may relax several design constraints of potential fieldable systems for measuring $\mathcal{R}$.

86

In the next chapter, fits to all spectra collected during BF2 will be examined and discussed in the context of phenomenological insight. The correlation between $\mathcal{R}$ and HE type will be made more explicit. Scaling relationships will be explored, and a radiometrically-invariant method of estimating the HE size will be presented. Thus, the development of the fireball model in this chapter brings closer the ability to answer the following question of fundamental importance in the battle space: "what kind and how big was that explosive?"

V. Fireball Phenomenology and Discrimination

In the previous chapter, a highly simplified physical treatment of fireball emissions resulted in a model which provides a high-fidelity representation of observed spectra via nonlinear regression. The primary purpose of dimensionality reduction had been achieved and the physics-based features showed promise for distinguishing high explosives. This chapter examines the results of fitting the fireball model to all Brilliant Flash II data to more carefully assess the potential utility of the extracted features to the HE classification problem. Specifically, type and size represent fundamental pieces of information about a high explosive. The ability to infer these key HE characteristics via the remote sensing of fireball emissions could significantly enhance battle space awareness and improve battle damage assessments. The results presented in this chapter demonstrate that the fireball model can reveal these key HE characteristics for the five classes of explosives examined during BF2. After summarizing the quality of the spectral fits to BF2 data, the temporal dynamics of each fit parameter will be discussed. Relationships to HE stoichiometry or weight will be explored as appropriate. It will be shown that $\mathcal{R} = $ H:C serves as a robust parameter to distinguish TNT explosives from the class of ENE explosives. Among the ENE explosives, an unknown emission feature can be used to distinguish the "boosted" ones (i.e. ENE1 and ENE2) from the baseline mixture (ENE0). Several parameters serve as valuable estimators of HE weight. The most useful of these is the temperature decay rate, since it provided the best discriminating ability and it has the additional advantage of being radiometrically invariant.

Before discussing the fitting results, however, it bears repeating some important limitations. First, the model used to extract the physical parameters to be discussed in this chapter was developed by making drastic simplifying assumptions about fireballs. Since it would be cumbersome to preface the discussion of each fit parameter with the necessary caveats, they will be discussed as if they are real properties of the fireball. The understanding is that the fit parameters are likely correlated with the physical phenomena they purport to describe. For example, the fitted water concentration ξ_{H_2O} represents some type of weighted average value, where the weighting accounts for the effects of spatial non-uniformity in both the matter and temperature fields. Of course, neglecting these effects also introduces some systematic error in ξ_{H_2O}. Despite this, ξ_{H_2O} will be described as "the" water concentration of the fireball. Second, only 44 high-explosives—spanning five HE types and four HE sizes—were detonated during the Brilliant Flash II field exercise. As a result, some

combinations of HE type and size were not tested and other combinations were tested only once. Empirical scaling relationships derived in this chapter will be affected by this and should only be considered as indicators of how HE size affects fireball dynamics.

In addition to examining the fit results for empirical relationships connected to bulk HE properties, some preliminary attempts will be made to infer a deeper phenomenological understanding of detonation fireballs. This is motivated by the operational need to further reduce data dimensionality, and in this case it will be across the time axis. Some of the efforts in this chapter indicate possible avenues to be taken towards this goal. For example, it will be demonstrated that radiative cooling is likely responsible for the observed temperature dynamics. It will also be shown that the temporal behavior of the particulate coefficient might be connected to soot oxidation kinetics. These observations lead to simple physical models which could eventually be used to fit the temporal behavior of $T(t)$ and $\kappa_p(t)$. However, the limitations mentioned above are compounded by relatively few observations in time. Due to the rapidly decaying signal, on average only about 10 observations in time could be fitted by the fireball model. It is stressed that the temporal phenomenology presented below is preliminary and only serves as a direction toward which future efforts might be focused.

Finally, a brief analysis on discriminating between TNT and the ENEs will be presented. This will serve as an illustration of how classification potential is quantified and will demonstrate utility of the key feature $\mathcal{R} = $ H:C in discriminating these two classes of high explosives.

5.1 Fit quality summary

In general, fits to all of the BF2 spectra were as good as the specific results presented in the preceding chapter. Table 8 summarizes key fit statistics for each class of high explosive. Each statistic represents the mean result for all spectra within a HE class, and the corresponding standard deviation is reported in parentheses. In general, TNT spectra were slightly better represented by the fireball model with the best relative fit errors and second best standard errors. Fits to ENE spectra exhibited slightly larger systematic errors and consequently had larger relative errors.

Table 8: Average fit statistics for each class of high explosive. SE is the standard fit error, RMS RE is the root-mean-squared relative error, med |RE| is the median magnitude of the relative error. Relative errors are expressed in per cent and were computed over spectral regions satisfying SNR > 5 and $T_{atm}(\tilde{v}) > 0.05$. Values are averaged (mean) for all fitted spectra within the HE class. Values in parentheses represent the standard deviation within the same HE class.

HE	SE	RMS RE (%)	med |RE| (%)
TNT	2.2 (1.1)	10.8 (3.9)	4.3 (2.4)
ENE0B	2.0 (1.1)	14.1 (2.5)	6.4 (2.1)
ENE1	3.2 (2.1)	13.2 (3.5)	5.7 (2.3)
ENE2A	2.7 (1.7)	14.1 (4.2)	6.0 (2.2)
ENE2B	2.6 (1.4)	10.9 (3.4)	5.3 (1.9)

5.1.1   Non-grey parameter.   Before discussing the results of fitting the BF2 spectra, a parameter will be introduced to help assess the uncertainty of the spectral fit parameters. The approximate Jacobian achieved via finite-differencing during nonlinear fitting can be used to estimate fit parameter uncertainties. While a helpful measure of confidence, these statistical uncertainties are not strictly valid due to the presence of systematic errors in the model. As a result, this method of uncertainty estimation does not always yield intuitive results. For example, parameter uncertainties are expected to increase with increasing optical depth in the observed fireballs. This trend is was typically not realized in the statistical uncertainties derived from the Jacobian. This is demonstrated in Figure 36 in which the relative errors in water concentrations $(\delta\xi_{H_2O}/\xi_{H_2O})$ are plotted against the minimum fireball emissivity. Water-concentration uncertainty tended to increased only slightly as the minimum emissivity approached 1. It is highly unlikely that the water concentration is known to within 20% when the minimum emissivity is greater than 0.95 as a few data points suggest.

A different measure of confidence in the fit parameters is proposed which is connected to the mathematical limitations discussed in § 4.3.1. For example, when the spectrum is nearly black ($\varepsilon \simeq 1$) or grey ($1 > \varepsilon \neq \varepsilon(\tilde{v})$), the extracted concentrations will not be seen as reliable. As selective emission becomes more dominant, concentration values will be more reliable. A metric might capture this behavior by comparing the difference between the full and particulate-only fireball models to the instrument noise level. Denoting this

90
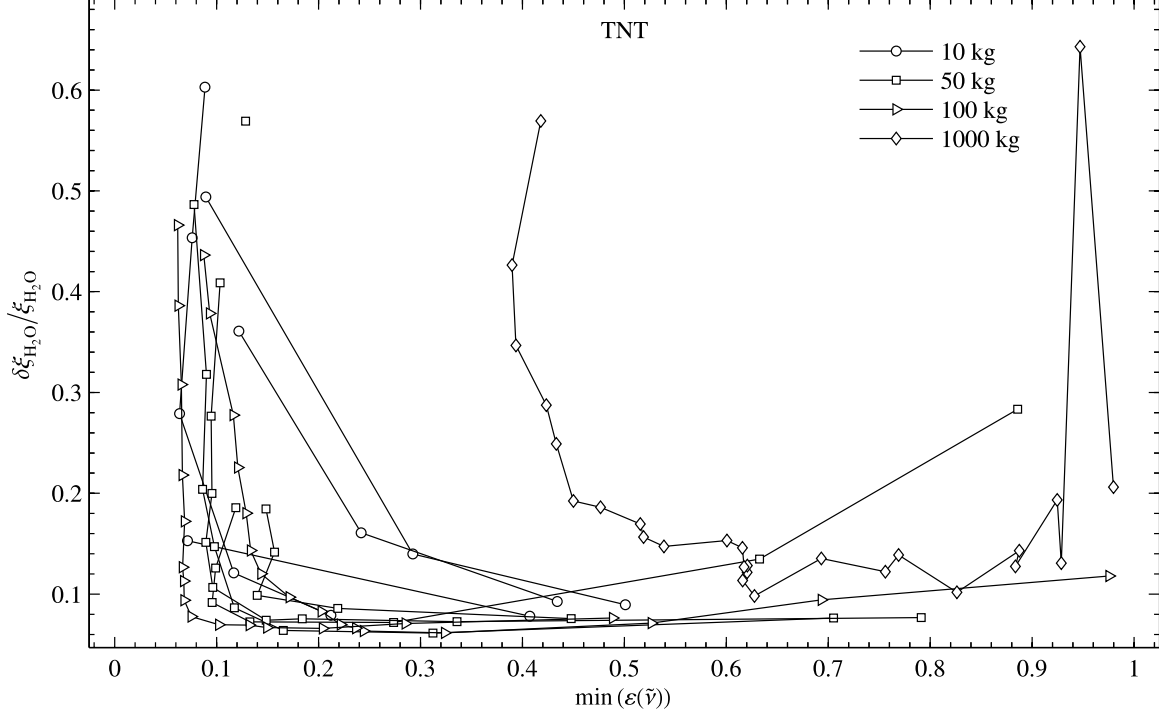
Figure 36: Relative fit uncertainty for water versus minimum fireball emissivity obtained by fitting to the TNT spectra collected during Brilliant Flash II field test. The results are categorized by weight.

metric G, it can be expressed as

$$G = \text{RMS}\left(\frac{T_{atm}(\tilde{\nu})\, r^2\, B_{\tilde{\nu}}(\text{T})\left(\varepsilon(\tilde{\nu}) - \varepsilon_p\right)}{I_{err}(\tilde{\nu})}\right) \tag{29}$$

where $\varepsilon(\tilde{\nu}) = 1 - T_p T_g(\tilde{\nu})$ is the total fireball emissivity, $T_p = e^{-\kappa_p r}$ is the particulate transmittance, $T_g(\tilde{\nu}) = e^{-r \Sigma_i \xi_i \sigma_i(\tilde{\nu})}$ is the selective emitter transmittance, and $\varepsilon_p = 1 - T_p$ accounts for the contribution of greybody particulates to emissivity. G might best be interpreted as the average "selective-emission signal-to-noise ratio" and for brevity it will be denoted as the non-grey parameter. Approaching either the black or grey case, $\varepsilon \rightarrow \varepsilon_p$ and $G \rightarrow 0$ and fitted concentrations would be unreliable. When a spectrum is dominated by selective emission and particulate contributions are minimal, the numerator becomes large and G increases. The degree to which G increases is tempered by the noise level of the spectrum. This is especially important when the effects of continuum and selective emission are comparable. For example, if the particulate emitters are such that $T_p \simeq 0.1$, the determination of gaseous concentrations is based on
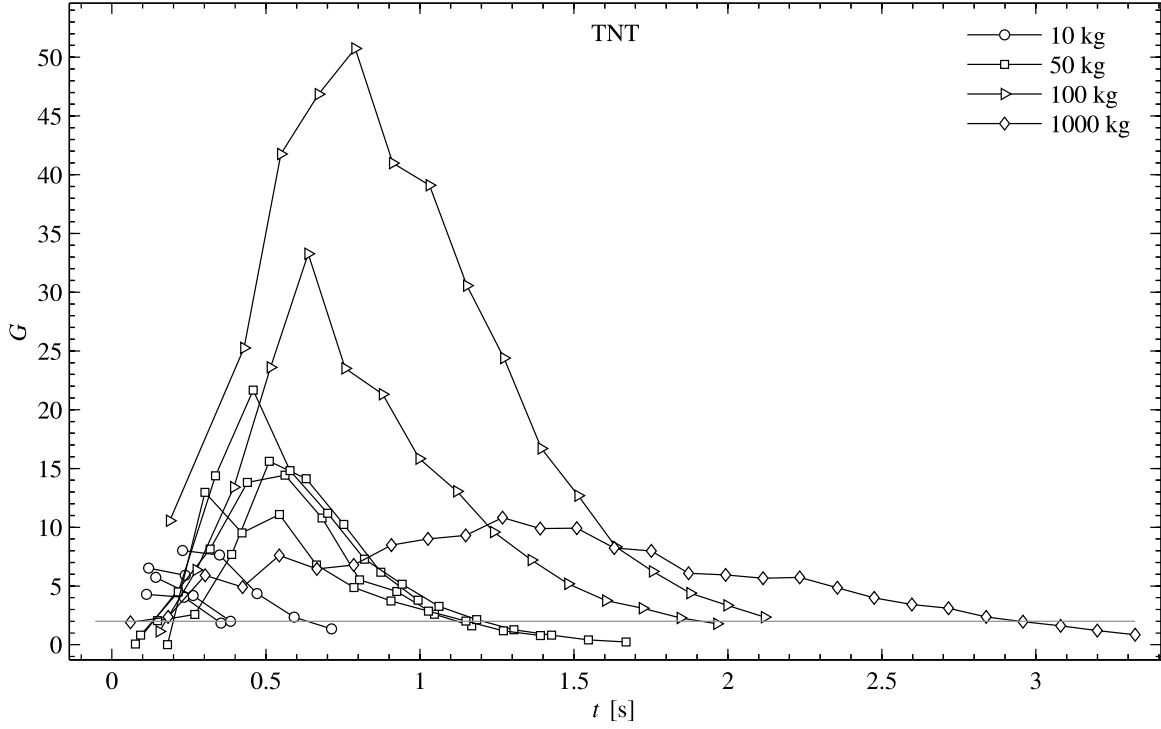
Figure 37: Non-grey parameter G for fits to the TNT spectra collected during BF2. Confidence in extracted gaseous concentrations increases with increasing G values.

spectral variations in emissivity between $0.9 \leq \varepsilon(\tilde{v}) \leq 1$. Thus, a good SNR is needed to establish accurate concentrations over this limited dynamic range. As the particulate emission subsides, confidence in gaseous concentrations is increased (or SNR requirements are relaxed).

The time-dependent behavior of G is presented in Figure 37 for all TNT fireball spectra collected during BF2. Initially, the spectra were dominated by continuum emission and G is small. As the continuum emission subsided, G increases suggesting improved reliability in the fitted concentrations. Finally, G tends to decrease with the decreasing SNR brought upon by the fireball cooling. The fireball resulting from the 1000 kg appeared nearly Planckian throughout its duration. This resulted in G values smaller than 12 despite excellent SNR for this event. When $G < 3$, concentrations will be viewed as unreliable and those corresponding data points will either be excluded or greyed out as necessary for visualization in several plots to be presented in subsequent sections.
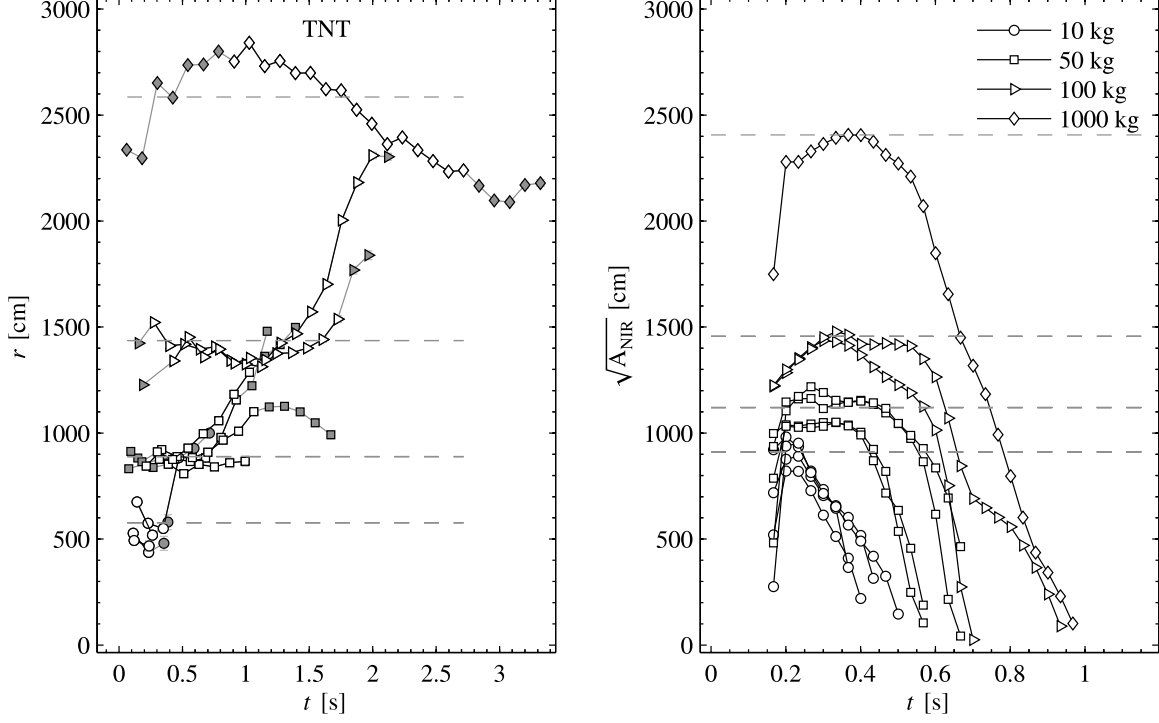
Figure 38: *Left panel*: Fireball size r obtained from fits to spectra collected from the detonation of 10 ($\circ$), 50 ($\square$), 100 ($\triangleright$), and 1000 kg ($\diamond$) charges of TNT. Dashed lines represent the weighted mean value of r for each weight class. Error bars indicate uncertainty in r but at early times are often smaller than the symbol size. *Right panel*: Corresponding sizes estimated from NIR imagery with dashed lines representing the mean peak sizes for each weight class.

5.2 Size (r)

The fireball sizes extracted from fits to the TNT spectra are provided in Figure 38, categorized by weight. The dashed lines represent the weighted arithmetic mean fireball size $\langle r \rangle$ within a weight class computed by

$$\langle r \rangle = \frac{\sum_i r_i w_i}{\sum_i w_i} \qquad (30)$$

Here, the sum over i accounts for all times of all individual events identical in HE weight and HE composition. The weight terms w_i are just the inverse of the statistical uncertainties in r_i, i.e. $w_i = \delta r_i^{-1}$. As expected, larger HE charges resulted in larger fireballs. For comparison, size estimates from NIR imagery ($\sqrt{A_{NIR}}$) are provided, and the dashed lines represent the average peak areas in each weight class. Agreement between $\langle r \rangle$ and NIR imagery was excellent for the larger fireballs, but $\langle r \rangle$ was almost 40% smaller than $\sqrt{A_{NIR}}$ for the 10 kg charges. In general, the agreement between fitted sizes and NIR imagery was poorer for the

Table 9: Comparison of MWIR spectral estimates of fireball size with NIR imagery. The values under the MWIR Fit columns represent the weighted average for each HE and weight class. The values under the NIR columns are the average peak area for each HE and weight class. Reported values are in cm.

HE	10 kg		50 kg		100 kg		1000 kg	
	MWIR Fit	NIR	MWIR Fit	NIR	MWIR Fit	NIR	MWIR Fit	NIR
TNT	577	911	889	1121	1436	1456	2585	2407
ENE0B	586	n/a	846	1043	n/a	1303	n/a	n/a
ENE1	557	n/a	875	1325	1164	1601	2400	2698
ENE2A	469	801	827	1390	1103	1627	1665	2390
ENE2B	n/a	n/a	860	1172	998	1403	1636	2197

ENE explosives. The same trend occurred, however, with better agreement at larger fireball sizes. Table 9 summarizes the results for $\langle r \rangle$ across HE class and weight, and those results are compared with NIR peak areas. The temporal trends for the 10, 50, and 100 kg fireballs were fairly similar for all types of high explosives. The fireball size was initially fairly static and then began to increase with time. The time at which the increase in r occurred varied with explosive weight; however, the increase in r typically began when the fireball had cooled to between 1200–1400 K. The size dynamics of the 1000 kg HEs were considerably different: r increased quickly to a local maximum and subsequently decreased with time. The 1000 kg ENE fireballs did exhibit a secondary increase in r upon reaching a temperature of about 1200 K. This trend was not observed for the TNT fireball. In general, early r values were in reasonable agreement with NIR imagery. The long-term behavior of r awaits confirmation with MWIR imagery. The intriguing temporal dynamics of r are connected to the fluid dynamical behavior of the fireball and warrant a deeper investigation beyond the scope of this effort.

The discrepancy between observed and fitted fireball sizes might be the result of the geometrically simplifying assumption of a cubic fireball. Imagery indicates that the fireballs are more spherical or dome-like. In a spherical homogeneous fireball, the optical depth will be larger through the middle of the sphere and decrease with distance from the center. Thus contributions to the apparent intensity will be lower from the periphery of the spherical fireball, and this will result in an under-estimation of r by assuming it is a cube.
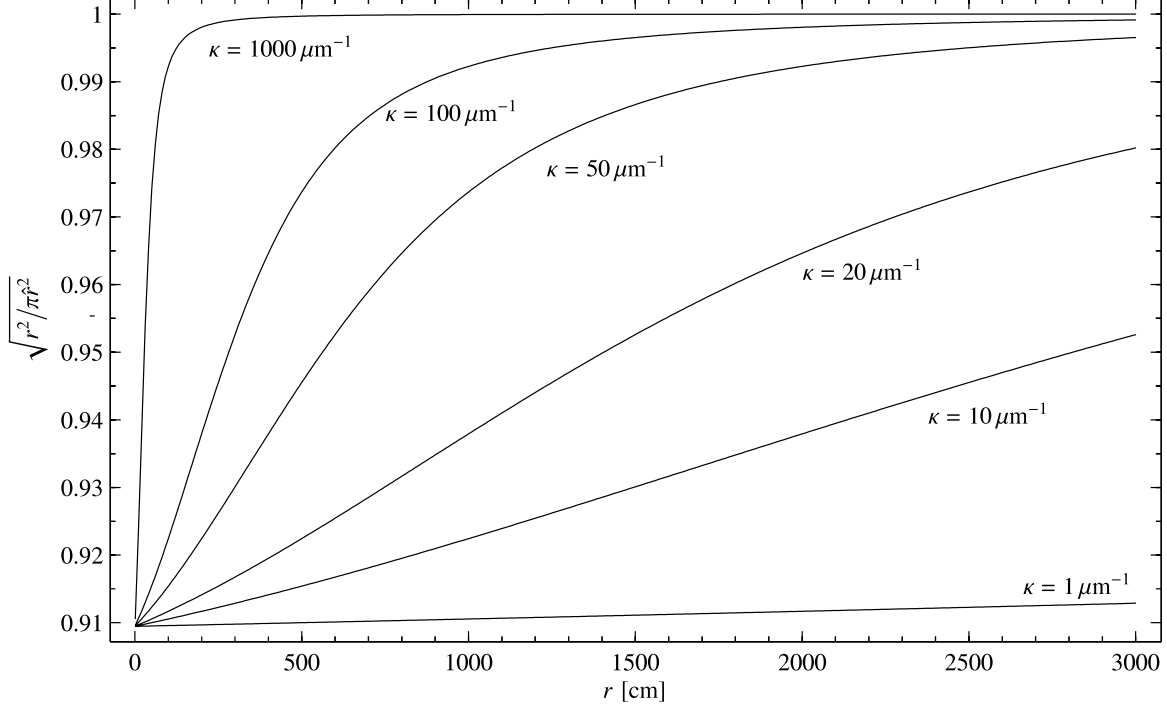
Figure 39: Ratio of fireball sizes (square root of projected areas) predicted by the cubic fireball model and the spherical fireball model plotted versus the cubic fireball model size r. Curves shown correspond to various absorption coefficients between 1 and 1000 μm^{-1}.

To assess the magnitude of this biasing, the radiative transfer solution for a spherical, homogeneous fireball of radius $\hat{r}$ derived in Appendix B will be used:

$$I_{sph} = \pi \hat{r}^2 \left(1 + \frac{e^{-2\kappa\hat{r}}}{\kappa\hat{r}} + \frac{e^{-2\kappa\hat{r}} - 1}{2\left(\kappa\hat{r}\right)^2} \right) B(\tilde{\nu}, \mathrm{T}) \qquad (31)$$

For a fixed κ, the value of $\hat{r}$ which makes I_{sph} equal to that predicted for a cubic fireball of size r via I_{mdl} will be computed. The results for several different values of κ are presented in terms of the ratio of the square roots of areas $\sqrt{r^2/\pi \hat{r}^2}$ in Figure 39. As κ increases, the edge effects become less important and both models will recover the same fireball projected area. While the observed fireballs are not perfect spheres, this analysis demonstrates that the cubic assumption leads to size estimates which can be too small by as much as 10%. This discrepancy is more pronounced for smaller fireballs or fireballs with smaller κ values due to the decreased optical depth. Furthermore, the observed trend of ENE fireball sizes having larger

95

discrepancies with NIR imagery is predicted by this analysis. ENE's have smaller initial κ_p values[1] than TNT. For example, average initial κ_p values for each explosive class are as follows: 28 ± 16 (TNT), 10 ± 3 (ENE0), 14 ± 1 (ENE1), and $20 \pm 12\ \mu\text{m}^{-1}$ (ENE2). However, the observed size differences between imagery and the spectral fits cannot be explained by this phenomena alone. For the 10 and 50 kg charges, the fitted r's were between 60–80% of the estimates from imagery. One highly speculative possibility is that κ_p takes on a radial dependence, decreasing with distance from the center. Such a radial dependence could be the result of the size distribution of soot generated during the detonation. Assuming each soot particle has an equal amount of kinetic energy imparted by the expansion wave, larger particles would be found closer to the center and smaller particles would be found nearer the edges. The result of such a scenario would be more significant edge effects than that predicted by a homogeneous fireball.

Fireball size r is the most intuitive indicator of the explosive's weight W. Larger HE charges are expected to produce larger fireballs and this trend was recognized in fits to the BF2 spectra. The uncertainty-weighted mean fireball size $\bar{r}$ was computed for each set of time-resolved spectra. $\bar{r}$ captures the early, static behavior of $r(t)$ as a result of the uncertainty weighting. The growth in $r(t)$ observed at later times was accompanied by much larger uncertainties. Note that $\bar{r}$ is different from $\langle r \rangle$: $\bar{r}$ represents an average for a single event whereas $\langle r \rangle$ represents an average for all events related by a common HE and weight. The relationship between $\bar{r}$ and the HE weight is presented in Figure 40 for the TNT events.

Both axes are logarithmic and the apparent linear behavior suggest a power-law relationship. To account for this, the following equation was fit to the data,

$$\bar{r} = aW^b \tag{32}$$

and the solid black curve represents the best fit with $a = 278 \pm 74\ \text{cm kg}^{-b}$ and $b = 0.33 \pm 0.05$. The number of points within each weight ranges from 1–4, so outliers could have a large influence. To examine

---

[1] Note that fireball area estimates from remote imagery are dependent on κ_p. There are spectral regions in which $\kappa(\tilde{\nu})$ is larger than κ_p because of selective emission from H_2O or CO_2. However, atmospheric attenuation by these same gases over several kilometers tends to strongly mitigate these contributions to the band-integrated intensity measured by an FPA. It turns out that the spectrally-averaged value weighted by the atmospheric transmittance function for $\kappa(\tilde{\nu})$ is typically only a few percent larger than κ_p.
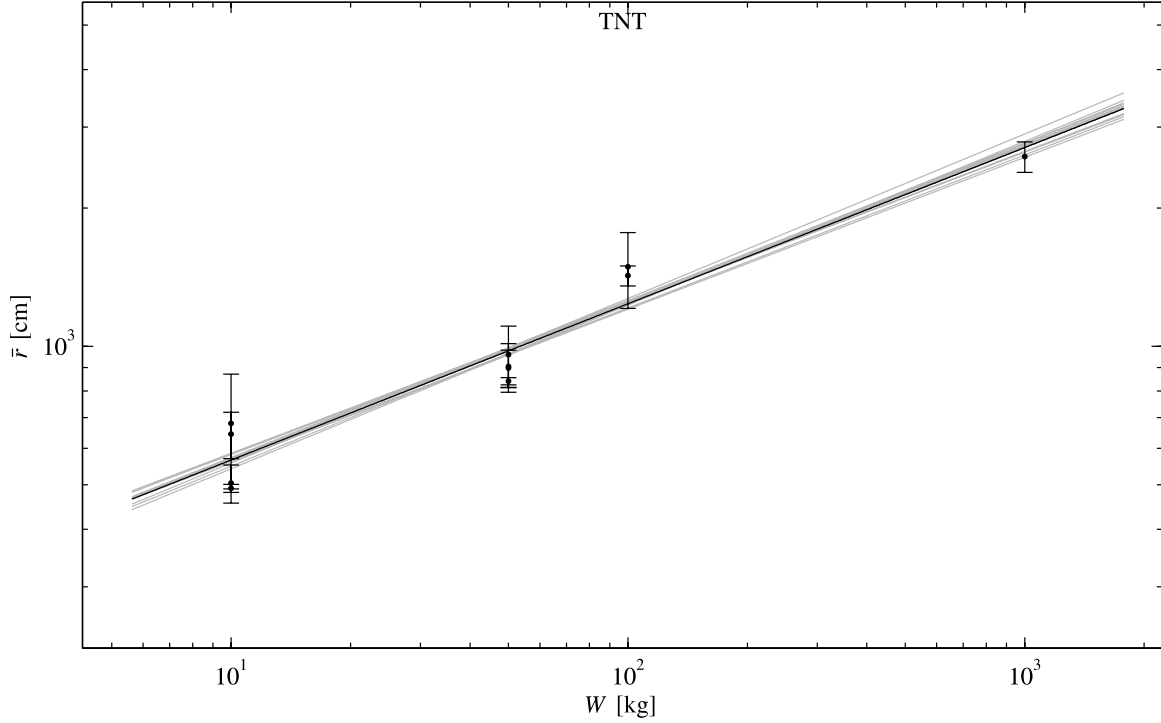
Figure 40: Uncertainty-weighted mean fireball size (·) versus high-explosive weight for the TNT detonations. Error bars indicate the standard deviation in r for each event. Solid black curve represents a power-law fit to the data. Grey curves are all possible power-law fits in which a single data point was excluded.

this possibility, the fits were performed on all subsets in which one point was excluded. The results, displayed in grey in Figure 40, were nearly identical except when the 1000 kg point was removed. Averaging over the leave-one-out fits resulted in $a = 272\,(24)\,\mathrm{cm\,kg^{-b}}$ and $b = 0.33\,(0.03)$ where the numbers in parentheses represent the standard deviation. Interestingly, the exponent $b \simeq 1/3$ might be expected under the conditions that the combustion chemistry and long-term fireball density are independent of the HE weight. If so, the total number of by-products N would scale linearly with weight, i.e. $N = r^3 \Sigma_i \xi_i \propto W$. Introducing a constant of proportionality a and solving for r, Equation 32 is recovered with $b = 1/3$. The same power-law analysis was performed for the ENE explosives and the scaling of $\bar{r}$ with weight is displayed in Figure 41. Fit results for TNT and the ENEs are summarized in Table 10. Fits to ENE1 were similar to TNT. However, both ENE2 mixtures featured a weaker weight dependence with b values near $1/4$. In ENE2A, the single 1000 kg data point has a large influence, and its removal results in a substantially different scaling relationship ($b = 0.42$
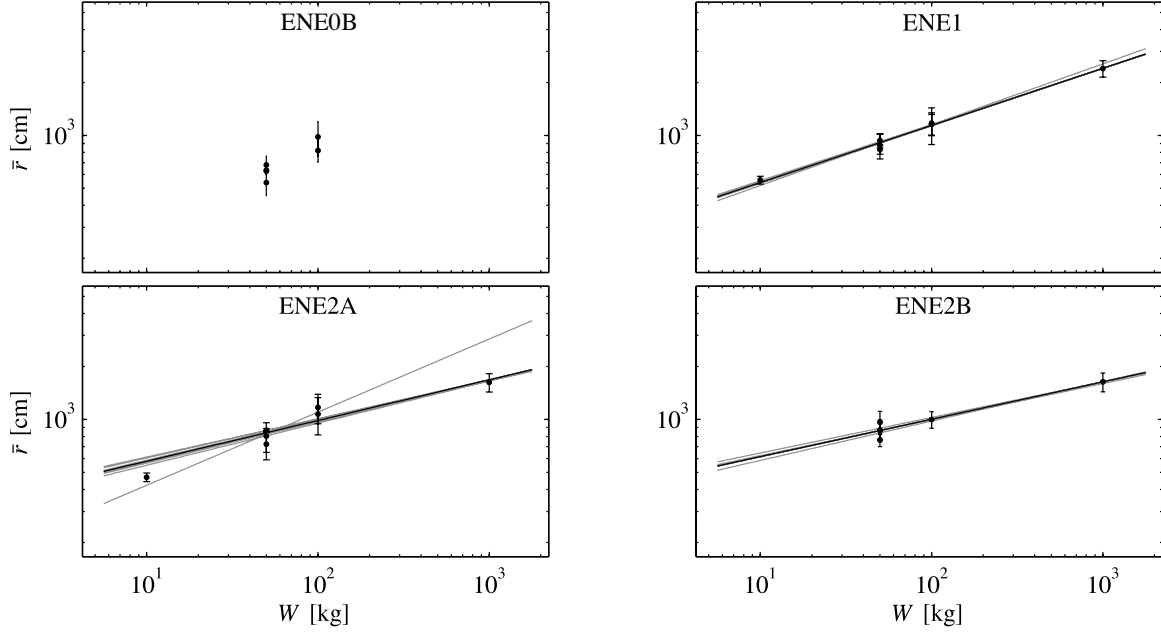
Figure 41: Uncertainty-weighted mean fireball size ($\overline{r}$, ·) versus high-explosive weight W for the different ENE detonations. Error bars indicate the standard deviation in r for each event. Solid black curve represents a power-law fit to the data. Grey curves are all possible power-law fits in which a single data point was excluded.

versus $b \simeq 0.23$). Substantially more data are needed to make this analysis statistically relevant and robust as well as to assess the validity of the power-law scaling description.

The power-law scaling relationship between fireball size and weight is interesting and is likely connected to the fluid dynamical processes which govern fireball growth. Understanding the physical basis for this relationship will not be pursued. However, with typical values of b ranging from 0.21 to 0.34, $\overline{r}$ enjoys only limited sensitivity with respect to HE weight. Thus, estimating HE weight from $\overline{r}$ demands low statistical uncertainties and good radiometric accuracy. Judging by the error bars in Figures 40 and 41, estimates of

Table 10: Results from fitting the power-law equation aW^b to $\overline{r}$. Fit parameter uncertainties are provided in parentheses. ENE0B was excluded as only two of the four weight classes were populated.

HE	$a \left[(cm/kg)^b\right]$	b
TNT	278 (74)	0.33 (0.05)
ENE0B	n/a	n/a
ENE1	255 (30)	0.32 (0.02)
ENE2A	340 (144)	0.23 (0.08)
ENE2B	377 (112)	0.21 (0.05)
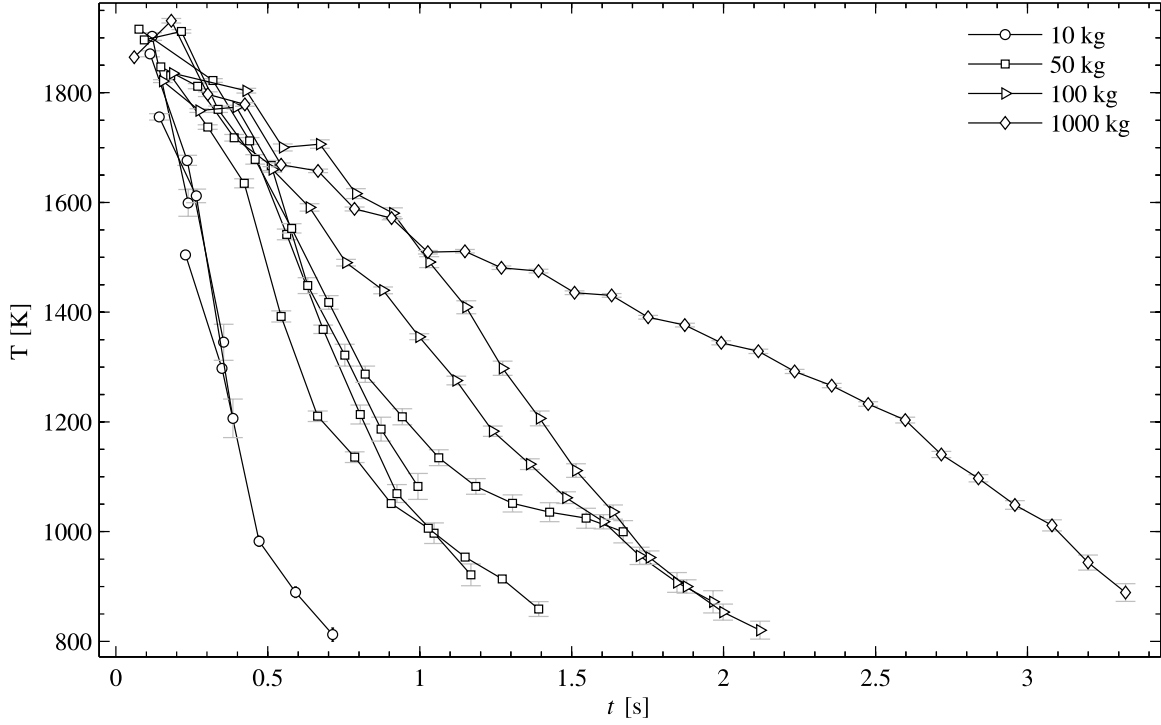
Figure 42: Temperature versus time curves obtained by fits to fireball spectra of 10 (○), 50 (□), 100 (▷), and 1000 kg (◇) charges of TNT. Error bars represent fit parameter uncertainties at the 95% confidence level.

HE weight from $\bar{r}$ would be highly uncertain. Nonetheless, the expected trend of increasing fireball size with

HE weight was captured by the spectral fits, building confidence in the fireball model.

5.3 Temperature (T)

The time-resolved temperatures extracted from the TNT fireball spectra are provided in Figure 42. The

mean initial temperature was 1850 K and this value was highly repeatable with a standard deviation of 50 K.

Temperatures collected at times satisfying $t < 200$ ms were considered initial temperatures. All initial TNT

temperatures were between 1756 and 1916 K. These results agree with the range of 1700–1900 K obtained

via optical pyrometry at comparable observation times [85]. Temperature decayed in an approximately linear

fashion, with moderate departures from linearity at the earliest and latest observation times. The tempera-

ture curves were all monotonically decreasing, which implies that the cooling processes (radiative emission,

expansion, etc.) dominate the effects of any exothermic chemistry that may be happening concurrently. Ac-
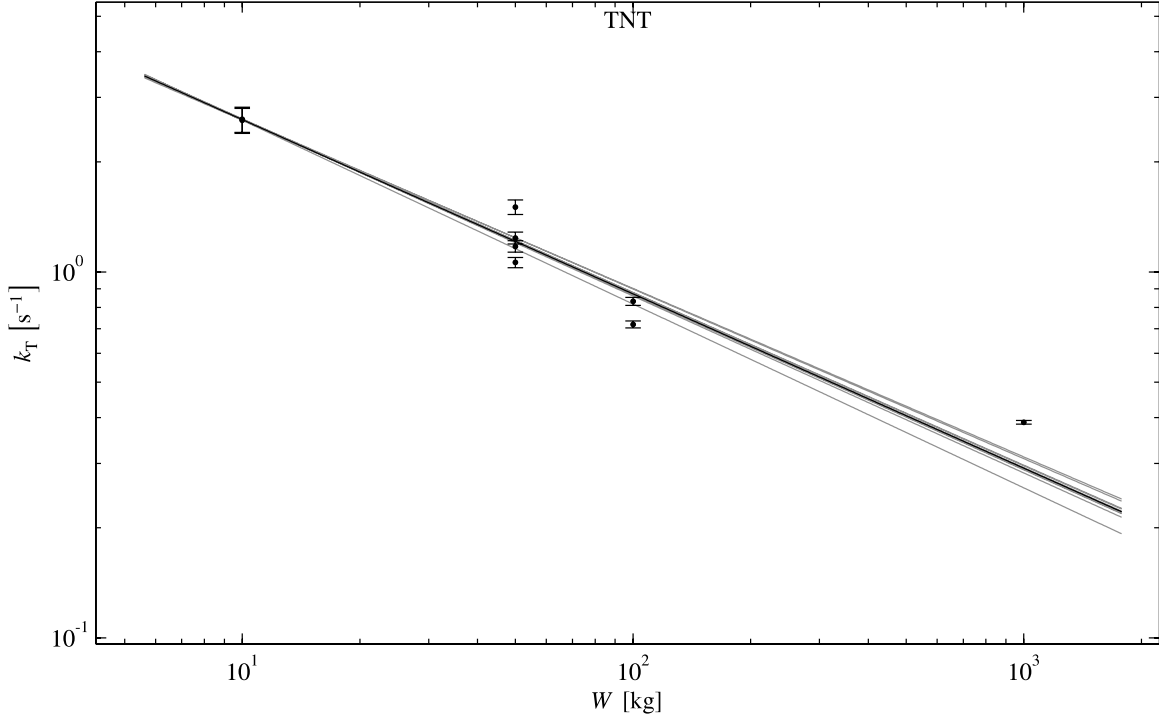
Figure 43: Linear temperature decay rate k_T versus HE weight for the TNT charges. Error bars represent uncertainties associated with observation time. Black line represents power-law fit to all points and individual grey curves represent leave-one-out power-law fits.

counting for some of these physical processes to understand and model the observed $T(t)$ curves will be postponed until § 5.3.1.

The rate of decay is highly dependent on the HE weight. To capture this weight dependency, the time $t_{1200\,K}$ at which $T = 1200\,K$ was recorded for each event[2]. A conservative estimate of the error associated with $t_{1200\,K}$ was taken as $1/4\,\Delta t$ where Δt is the time to acquire a single spectrum[3]. Taking the reciprocal provides one measure of the cooling rate and is denoted by $k_T = 1/t_{1200\,K}$. The weight-dependence of k_T is displayed on a log-log scale in Figure 43. Larger high-explosives produced fireballs that took much longer to cool than smaller HEs. The dependence appears linear on the logarithmic scale, again suggesting a power-law relationship with W. Fitting the following equation

$$k_T = aW^b \tag{33}$$

---

[2]A higher temperature could have been chosen, but less separation among different weights would be evident. Likewise, selecting a lower temperature would have resulted in greater separation of weights, but at the expense of 10 kg data points.

[3]Examination of the raw interferograms results in an improved estimation of the time at which the detonation occurred.
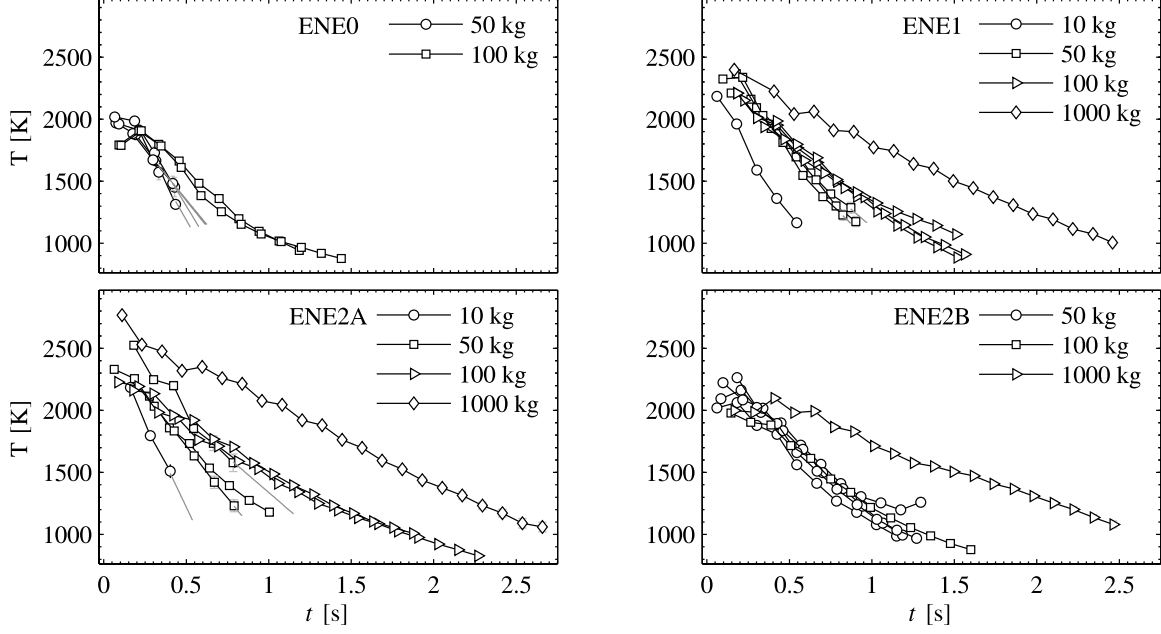
Figure 44: Temperature versus time curves obtained by fits to fireball spectra of 10 ($\circ$), 50 ($\square$), 100 ($\triangleright$), and 1000 kg ($\diamond$) charges of various ENEs. Not all HE sizes were represented in each class of explosive. Grey lines represent linear extrapolations to T = 1200 K for those events in which the final temperature was greater than T = 1200 K.

to the TNT temperature curves resulted in $a = 7.8 \pm 2.0\,\mathrm{s^{-1}kg^{-b}}$ and $b = -0.48 \pm 0.08$. Averaging over the leave-one-out results produced identical values for a and b to within the reported precision.

The temperature dynamics for the ENE fireballs is presented in Figure 44. In general, the ENE detonations resulted in higher fireball temperatures. Mean initial temperatures and associated standard deviations—in order of ENE0, ENE1, ENE2A, and ENE2B—were as follows: 1900 (100), 2260 (90), 2300 (240), and 2100 (120) K. The large standard deviation for ENE2A was the result of two initial temperatures in excess of 2500 K. The average ENE2A temperature, excluding those two events, is 2200 (80) K. Each of the "booster" ingredients is observed to increase initial fireball temperatures by 300–500 K above that obtained by the baseline ENE0 mixture. The ENE temperature profiles are more linear than the TNT profiles. This observation was used to extrapolate a few of the T(t) curves to T = 1200 K in order to compute k_T. This extrapolation was based on a linear fit to the last three recorded temperatures, and was only performed when the final recorded temperature was greater than 1200 K. The extrapolated curves are shown grey in Figure 44. The weight-dependence of k_T is provided in Figure 45. The results of power-law fits to each of the HEs are summarized

101
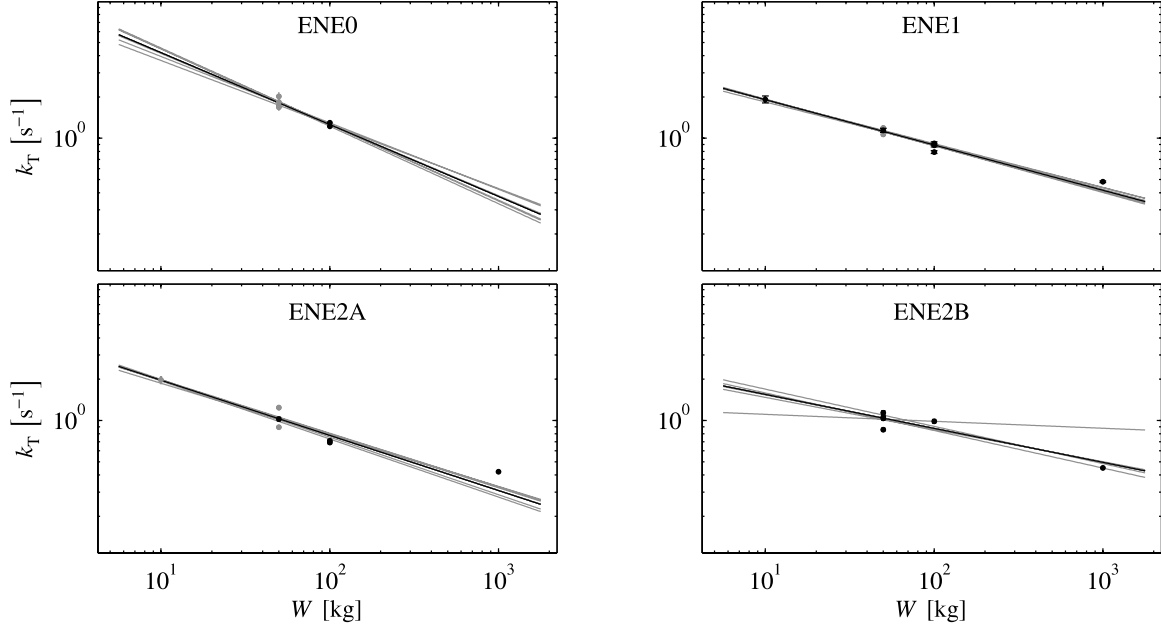
Figure 45: Linear temperature decay rate k_T versus HE weight for the TNT charges. Grey points correspond to k_T values estimated by linear extrapolations of $T(t)$. Error bars represent uncertainties associated with observation time. Black line represents power-law fit to all points and individual grey curves represent leave-one-out power-law fits.

in Table 11. In general, the behavior of ENE0B and ENE2A was similar to TNT, although the ENE0B result is highly uncertain as only two distinct weights were used. ENE1 exhibited the truest power-law relationship with the smallest relative fit errors. The behavior of ENE2B is difficult to judge as the 100 kg event appears anomalous with a k_T value commensurate with the 50 kg values. Interestingly, the fireball size for this event as measured by imagery and estimated by spectral fitting is also commensurate with the 50 kg values.

Table 11: Results from fitting the power-law equation aW^b to k_T. Fit parameter uncertainties are provided in parentheses.

HE	$a\ \left[(\mathrm{s}^{-1}/\mathrm{kg})^b\right]$	b
TNT	7.2 (1.8)	−0.46 (0.08)
ENE0B	14 (19)	−0.52 (0.34)
ENE1	4.1 (0.7)	−0.33 (0.05)
ENE2A	4.9 (2.0)	−0.40 (0.12)
ENE2B	2.7 (2.5)	−0.25 (0.22)

In terms of estimating HE weight, the decay rate as measured by k_T has some advantages over $\bar{r}$. First, radiometric accuracy is unimportant in measuring temperature[4]. Second, the only major sources of uncertainty in estimating k_T are the uncertainties in T and the measurement time axis t. Statistical uncertainties in temperature were the lowest of all fit parameters, on the order of 0.3–3%. The fit uncertainty is almost exclusively a function of instrumental SNR[5]. And third, the sensitivity of k_T, as captured by the exponent b, was larger in magnitude than the corresponding values obtained for $\bar{r}$. These characteristics improve the confidence in weight estimates obtained by k_T relative to the direct measure of fireball size via r. With more field tests, it might be possible to develop rules-of-thumb by which explosive size can be estimated from the observed temperature decay.

5.3.1   Temperature phenomenology.   The rate at which the fireball temperature changes with time reflects the balance between the production and dissipation of energy within the fireball. For example, processes which dissipate energy include expansion, non-radiative heat transfer (e.g., conduction, convection, turbulent mixing), and photon emission. Many HEs are under-oxidized so that their detonation results in residual fuels which can continue burn as atmospheric oxygen become available. This after-burning serves as a source of energy. At constant pressure, the balance between these sources and sinks of energy ($dq = q_{src} - q_{snk}$) represents the differential change in enthalpy H, and is related to the fireball temperature by its heat capacity C_p, i.e.

$$\mathrm{d}q = \mathrm{d}H = C_p \, \mathrm{dT} \tag{34}$$

It is both difficult and beyond the scope of this work to carefully estimate all contributions to $\mathrm{d}q$ for a turbulent fireball. The point of this section is to develop a reasonable (albeit purely heuristic at this point) physical explanation for the empirically observed scaling of the cooling rate with HE weight. In doing so, a simple, parametrized differential equation is found which affords dimensionality reduction of the temperature profiles.

---

[4]Of course, in a spectro-radiometer such as a FTS, relative calibration between frequency bins is critical.

[5]Highly accurate temperature measurements could be made at much higher temporal resolution by taking advantage of the improved SNR which accompanies reducing the spectral resolution. Likewise, a pair of radiometers with appropriately-chosen bandpass filters could provide high-SNR temperature measurements at a temporal resolution on the order of 100s of kilohertz.

Noting that the fireball is initially very hot ($1800 \leq T \leq 2800$ K), radiative cooling might be expected to dominate the q_{snk} term due to the variation in emitted radiant energy with T^4. Convective cooling will be proportional to the difference in fireball and ambient temperature $T - T_{bg}$, whereas radiative cooling will approximately vary with $T^4 - T_{bg}^4$. Turbulence will enhance the temperature decay as cool air is entrained via swirling eddies. Bhattacharjee and Grosshandler [13] in their analysis of flames define the radiation/convection parameter Φ as

$$\Phi = \frac{\sigma_{SB} \, \overline{\kappa} \, r}{\rho_i \, u_i \, C_{p,i}} \frac{T_f^4 - T_w^4}{T_f - T_i} \tag{35}$$

where σ_{SB} is the Stefan-Bolztmann constant, $\overline{\kappa}$ is the Planck mean absorption coefficient, r is the linear dimension of the flame (fireball), and the quantity $\rho_i \, u_i$ represents the mass flux of material with heat capacity $C_{p,i}$ brought into the flame. The three temperatures are the flame, wall, and inlet temperatures (T_f, T_w, T_i). For the present fireball case, the wall and inlet temperatures are both equal to the ambient background temperature of approximately 300 K. The quantity $\rho_i u_i C_{p,i}$ is difficult to estimate, but can be expected to increase with the amount of turbulent mixing. However, Grosshandler notes [50] note that large fires can have large ratios indicating the importance (and in some cases, dominance) radiative emission can have on the cooling process. It will be assumed that the HE detonation fireballs satisfy $\Phi \gg 1$ early in the cooling process. This will permit both a possible explanation for the observed scaling of cooling rate with HE weight and produce functional form that can be used to reduce the dimensionality of the temperature profile to a single fit parameter. However, an improved understanding of the fluid dynamics—in particular, the effects of turbulent mixing on temperature—will be needed to ascertain the degree to which the following development is valid.

So as a first step at understanding the observed temperature dynamics, it will be assumed that the fireball only radiatively cools and that the exothermic chemistry has completed so the source term can be neglected. Furthermore, the ambient temperature of approximately 300 K will be neglected since initially $T^4 \gg T_{bg}^4$. Finally, it is assumed that the fireball will instantaneously thermally equilibrate [6]. With these approximations,

---

[6]This assumption is needed to assume a single temperature. It is more likely that temperature gradients are introduced as the periphery of the fireball begins to cool.

Equation 34 can be recast as the following ordinary differential equation (ODE)

$$\frac{\mathrm{dT}}{\mathrm{d}t} = -\frac{\varepsilon_h S}{C_p} \sigma_{SB} \, \mathrm{T}^4 \tag{36}$$

where ε_h is the hemispherical emissivity, and S is the fireball surface area. In general, ε_h is a complicated function of the geometry and optical properties of the system. However, it can be shown [110, pp. 167] that the hemispherical emissivity behaves as $\varepsilon_h \sim l/r$ for an optically thick source with a photon mean free path of l. In an optically thick medium, l is small and photons emitted from the center participate less in radiative cooling than surface-born photons as a result of their increased chances of re-absorption. This effect becomes more pronounced as the geometrical fireball dimension becomes larger and the ratio l/r accounts for this. This limiting form is only valid when the photon mean-free path is much smaller than the linear dimension of the fireball, i.e. $l/r \ll 1$. Typically, this condition is satisfied at times less than 0.25–0.5 s for the HE fireballs examined in this work. Assuming all variables in Equation 36 are independent of time except $\mathrm{T}(t)$, it can be integrated obtaining

$$\mathrm{T}(t) = \left(\mathrm{T}(0)^{-1/3} + g \frac{l}{r} \frac{3 S \sigma_{SB}}{C_p} t \right)^{-1/3} \tag{37}$$

where $\mathrm{T}(0)$ is the initial temperature and g represents a geometry-dependent factor that would be present in the optically-thick limiting expression for the hemispherical emissivity $\varepsilon_h = g \, l/r$.

The effects of HE weight on the initial cooling rate can now be considered. Suppose that HE weight affects no fireball variables apart from the total number of particles and that the density is preserved. (The constant density assumption seems valid for TNT fireballs as it was discovered in § 5.2 that $r \propto W^{1/3}$). It follows that $S \propto r^2 \propto W^{2/3}$. The heat capacity will scale linearly with weight, i.e. $C_p \propto W$. Keeping mind of the l/r term, this can be expressed as

$$\mathrm{T}(t) = \left(\mathrm{T}(0)^{-1/3} + a \, W^{-2/3} \, t \right)^{-1/3} \tag{38}$$

with a being the collection of physical and proportionality constants. The expression above supports the observation that fireballs from larger HEs cool more slowly than smaller HEs. The time t_T required to decay to a temperature T can be solved for yielding

$$t_T = \frac{T(0)^3 - T^3}{a\, T(0)^3\, T^3} W^{2/3} \tag{39}$$

From the previous section, the decay rate $k_T = 1/t_T$ with $T = 1200\,\text{K}$ and this result suggests that exponent for the power-law relationship in Equation 33 should be $-2/3$. This value is somewhat larger in magnitude than the observed values reported in Table 11. Over much of the observation time, r is roughly constant, and the heat capacity isn't strongly influenced by temperature changes. However, l will be seen to vary with time in a manner that is weight-dependent (look ahead to Figure 46), so some variation from $-2/3$ is not unexpected. For example, in the case that l increases linearly with time starting from a small value, i.e. $l \simeq mt$, a similar analysis yields $k_T \propto W^{-1/3}$. Initially, the growth of l is approximately linear, coinciding with the rapid decrease in κ_p. Note that in most BF2 fireballs, l grows in time to values larger than r, so that the long-time behavior of the hemispherical emissivity does not trend as $\varepsilon_h \sim l/r$.

The photon mean free path represents the average distance traveled by a photon before being reabsorbed. Specifically, in a medium characterized by an absorption coefficient $\kappa(\tilde{\nu})$, on average only $1/e$ photons of frequency $\tilde{\nu}$ will not be absorbed after traveling a length $l_{\tilde{\nu}} = 1/\kappa(\tilde{\nu})$. In optically trapped media, the average photon mean free path is computed using Rosseland's weighting scheme [110, pp. 153] via

$$l = \int_0^\infty \frac{f(u)}{\kappa(u)}\, du \tag{40}$$

where the integration is performed over the dimensionless variable $u = hc_0\tilde{\nu}/k_B/T$. The weighting function f is the derivative of Planck's distribution with respect to temperature, and in terms of u is given by

$$f(u) = \frac{15}{4\pi^4} \frac{u^4 e^{-u}}{\left(1 - e^{-u}\right)^2} \tag{41}$$

106
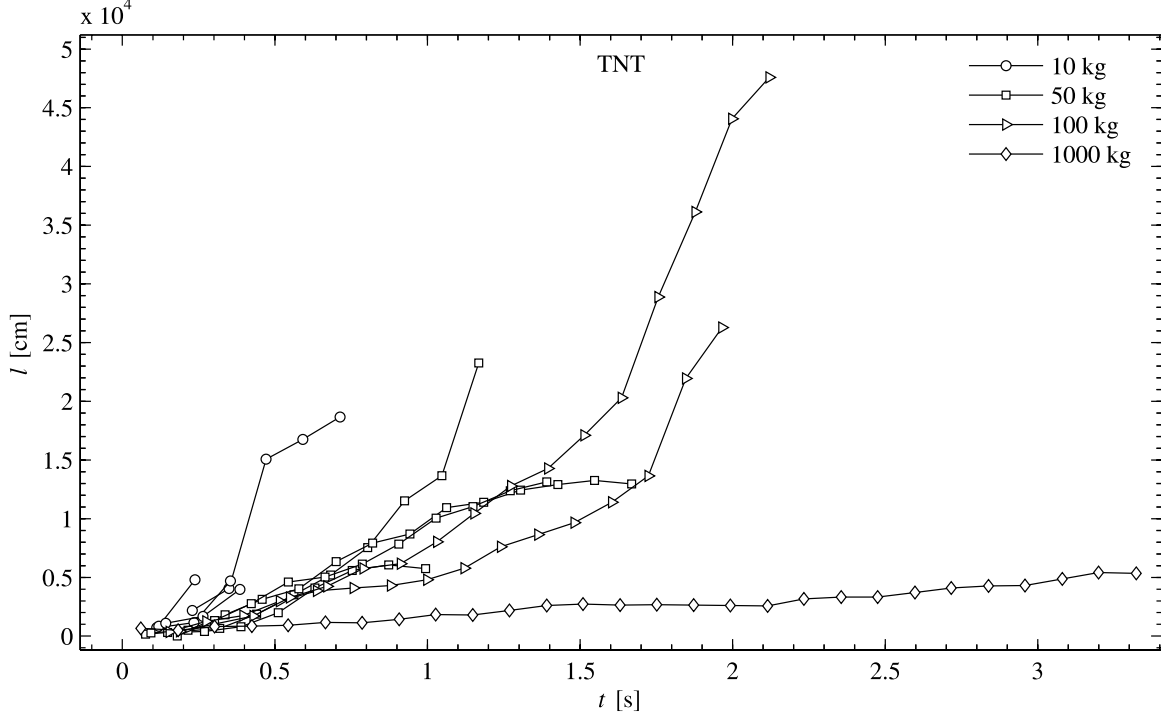
Figure 46: Photon mean free path l versus time for the TNT fireballs, grouped according to weight: 10 (○), 50 (□), 100 (▷), and 1000 kg (◇).

Larger absorption coefficients reduce the average length traveled by a photon before absorption. For each spectrum, the monochromatic absorption coefficient and fitted temperature was used to compute l. For the TNT events, the temporal dependence of l is provided in Figure 46. The mean free path increases with time at a rate that is dependent on HE weight, with smaller explosives featuring faster increases in l with time. The behavior of l is strongly influenced by the particulate absorption coefficient as will be discussed in § 5.4.

In the preceding discussion, a simplistic picture of fireball cooling leads to a plausible explanation for the observed dependence of the temperature decay rate with HE weight, namely that larger HEs have larger thermal mass and more optical trapping, and thus cool more slowly. Moreover, the differential equation (Equation 36) leads to a method of further dimensionality reduction. The temperature curves can be represented by an initial condition and a single fit parameter which is adjusted to minimize the squared differences between the observed $T(t)$ and the solution to the following equation:

$$\frac{dT}{dt} = -\hat{k}_T \, \sigma_{SB} \, T^4 \tag{42}$$

107
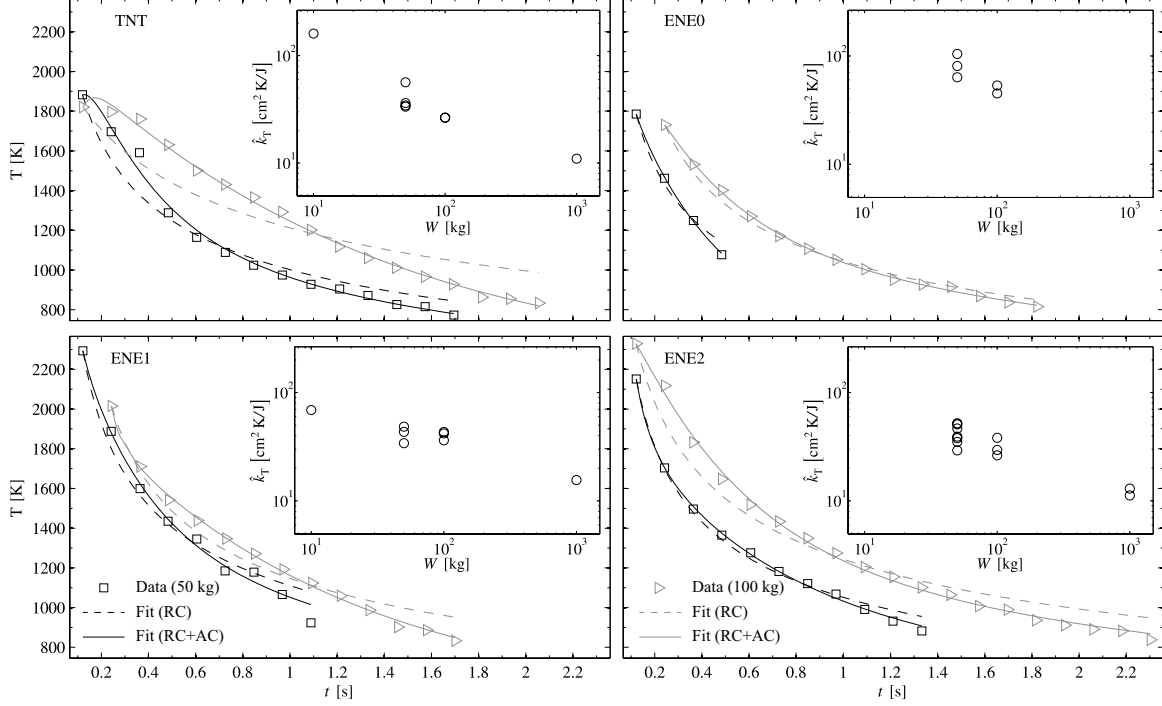
Figure 47: Spectrally estimated temperature profiles (·) from various BF2 fireballs compared with single-parameter fits to Equation 42 (– – –) based on radiative cooling (RC). The solid curves (—) represent the solution to a three-parameter differential equation (Equation 43) which includes an exponentially-decaying energy source term from additional combustion (RC+AC). Results from a 50 (black) and 100 kg (grey) detonation are shown for TNT, ENE0, ENE1 and ENE2. Each panel also features a log-log inset plot of $\hat{k}_T$ (from fitting to Equation 42) versus W demonstrating the expected scaling is preserved with the single-parameter fit to the temperature curves.

Here, $\hat{k}_T$ is a parameter representing the time-averaged contributions of the hemispherical emissivity, heat capacity, and surface area to the cooling rate. [7] Matlab's `ode45` solver[8] was used to numerically integrate Equation 42 for a given $\hat{k}_T$ with the initial condition matching that of the first observed temperature. A Nelder-Mead simplex method was used to find the $\hat{k}_T$ which minimized the sum of squared differences between the measured and predicted temperatures. Figure 47 compares the spectrally-estimated temperatures with the fitted solutions to Equation 36 for several BF2 fireballs.

---

[7]Accurately estimating these physical parameters for an arbitrary, unknown HE may not be possible from spectral measurements. For example, the fireball's heat capacity cannot be reliably estimated if the HE contains a large amount of nitrogen. Most nitrogen is converted to N_2 and its concentration cannot be estimated by emissive FTS due to its lack of a permanent electric dipole. Furthermore, turbulent mixing at the surface of the fireball, even if small enough not to invalidate the assumption that radiative emission dominates the cooling process, can increase the effective surface area of the fireball. In this case, estimating the surface area as $S = 6r^2$ for a cube or $S = 4\pi r^2$ for a sphere may lead to an underestimation of the radiative cooling rate. Finally, the hemispherical emissivity is strongly dependent on the geometry of the system, and analytic expressions can only be found for simple systems.

[8]While Equation 42 is analytically integrable, the numeric ODE solver was used in order to provide a framework for exploring other functional forms which have no analytic solution (see e.g. Equation 43).

The specific examples presented in Figure 47 are fairly representative of the results obtained in analyzing all BF2 fireballs. In general, the fitted temperatures based solely on radiative cooling compare favorably with the observed ENE temperature profiles. However, the TNT fireballs generally exhibited a less satisfactory agreement. For all ENE events, $\hat{k}_T$ ranged from 11–105 cm^2 K/J depending on weight and RMS fit errors were 64 K on average. The average relative error associated with $\hat{k}_T$ was 18%. For the TNT events, $\hat{k}_T$ ranged from 11–160 cm^2 K/J and RMS fit errors were larger at 114 K on average. Relative errors associated with $\hat{k}_T$ were 33% on average. While the ENE profiles are well-described by the fits, it is clear that Equation 42 cannot reproduce the TNT profiles with high fidelity. Also shown in Figure 47 are log-log plots of $\hat{k}_T$ versus HE weight. Note that fitting Equation 42 to the temperature curves results in a similar power-law relationship that was empirically observed in the previous section. And despite the mediocre fits to the TNT curves, the scaling relationship appears to be preserved for that class of HEs as well.

According to Equation 42, the initial decay rate will be the largest, i.e. the slope should be negative and largest in magnitude at early times. For many of TNT fireballs, the largest negative slope occurred in the third to fifth sample of the temperature profile, which is a temporal variation that cannot be modeled by Equation 42. There are possibly several reasons for this behavior. One plausible explanation is that at early times, the fireball is still combusting, adding energy to the system and initially slowing the net cooling rate. As a first approximation, the effects of possible combustion on the temperature profile are accounted for via an exponentially-decaying energy source term. Introducing two additional parameters a and b, the solution to the following modified differential equation was also fit to the observed temperature profiles:

$$\frac{dT}{dt} = ae^{-bt} - \hat{k}_T \, \sigma_{SB} \, T^4 \tag{43}$$

The best-fit solutions are also provided in Figure 47 as the dashed lines. The mean RMS fit errors were reduced to 16 and 30 K for ENE and TNT, respectively. However, parameter uncertainties were considerably larger (on average $\sim$ 87% for ENEs and $\sim$ 140% for TNT), and this is partially a consequence of having

only a few more data points than fit parameters[9]. Because of this, analysis of the fit parameters will not be explored. Instead, the improved fits demonstrate the possibility that a decaying energy source term may be responsible for the initially slow decay rate observed in the TNT temperature profiles.

Before continuing, it is important that the preceding results are put into a proper context. Equations 36 and 43 serve as useful dimensionality reduction tools which capture the observed weight scaling. The simplified physical picture ascribed to HE fireballs resulted in a model which enabled good fits, suggesting only that the model is consistent with the observed data. While this is a first step towards understanding the temperature dynamics of fireballs, the nature of the data precludes firm conclusions about the physical underpinnings of the empirical observations. The observed temperature profiles were sparsely sampled in time (typically only 3–15 points per HE) and exhibited a variation with time that could be represented by many simple mathematical forms. In other words, the observed temperature profiles do little to limit the scope of possible explanations. To improve the understanding of the temperature dynamics, future tests should incorporate instrumentation capable of capturing highly sampled temperature profiles (e.g. high-speed two- or three-color pyrometry).

With the above caveats aside, radiative emission may play a key role in the temperature dynamics of HE fireballs. Furthermore, it is possible that continued combustion may have a measurable effect on the decay rate as late as several hundred milliseconds after the detonation. It is interesting to note that the particulate absorption coefficient decays with time in an approximately exponential fashion. If κ_p is in fact connected with the optical properties of soot, its decay with time may be the result of oxidation. Such oxidation would serve as a source of energy, perhaps leading to a source term similar to the exponential form used in Equation 43. However, in this work no effort has been made to explicitly connect the two phenomena. Nonetheless, the temperature curves may provide one method of interrogating the phenomenology of this continued combustion. In the next section, the temporal behavior of κ_p will be discussed and its possible connection with soot oxidation will be explored.

---

[9]There were a few data sets in which only three temperatures were extracted via fitting. They were omitted from the three-parameter fits.

5.4 Particulate absorption coefficient (κ_p)

Particulate dynamics for the TNT events are presented in Figure 48. The grey points indicate when the non-grey parameter was less than 3. The circled points indicate when the fitted κ_p values resulted in minimum emissivities greater than 0.98, and should be viewed as highly uncertain. Overall, κ_p decreases with time. The rate of decay is initially large and becomes less pronounced at later times. Except for the largest HE charge, the decay rates are all similar. The 1000 kg charge only decreases slightly with time in a manner substantially different from the other HEs. The particulate material in the fireball is responsible for a significant portion of the optical trapping of light. This can be seen by comparing κ_p and $1/l$, which represents a weighted mean absorption coefficient[10]. This comparison is provided in Figure 46. Considering all data simultaneously, the correlation between κ_p and $1/l$ is 0.98, and their magnitudes are very similar. Given that the magnitude and temporal behavior of l is strongly influenced by κ_p, it appears that the dynamics of the particulate material is important in the radiative cooling of the fireball. κ_p is an important contributor to the average emissivity over the MWIR. The mean initial ($t < 0.2$ s) emissivity for the TNT fireballs was 0.85 with a standard deviation of 0.20.

For completeness, the κ_p curves are provided in Figure 49 for the ENE events. The $\kappa_p(t)$ curves were more reproducible for the ENE events, and no anomalous behavior was observed for the 1000 kg events. The combination of fireball sizes and particulate absorption coefficients resulted in initial emissivities that were less than the TNT events. Mean initial emissivities and corresponding standard deviations for ENE0, ENE1, ENE2A, and ENE2B are as follows: 0.60 ± 0.14, 0.74 ± 0.11, 0.81 ± 0.24, and 0.72 ± 0.15.

The fireball model enables time-resolved spectroscopy to be used as a tool to begin understanding the kinetics of the afterburning fireball. What follows is one possible interpretation of the kinetics of $\kappa_p(t)$ which is preliminary, speculative, and approximate in nature. The decay in κ_p appears consistent with the possibility that the particulate material is being consumed by oxidation. This view is adopted in Reference [85] to explain the optical pyrometry results. Apart from this study, however, soot oxidation in detonation fireballs has not been studied. To assess this possibility, the analogous oxidation process in a simple combustion system will

---

[10]Recall $l(\tilde{v}) = 1/\kappa(\tilde{v})$ and Equation 40.
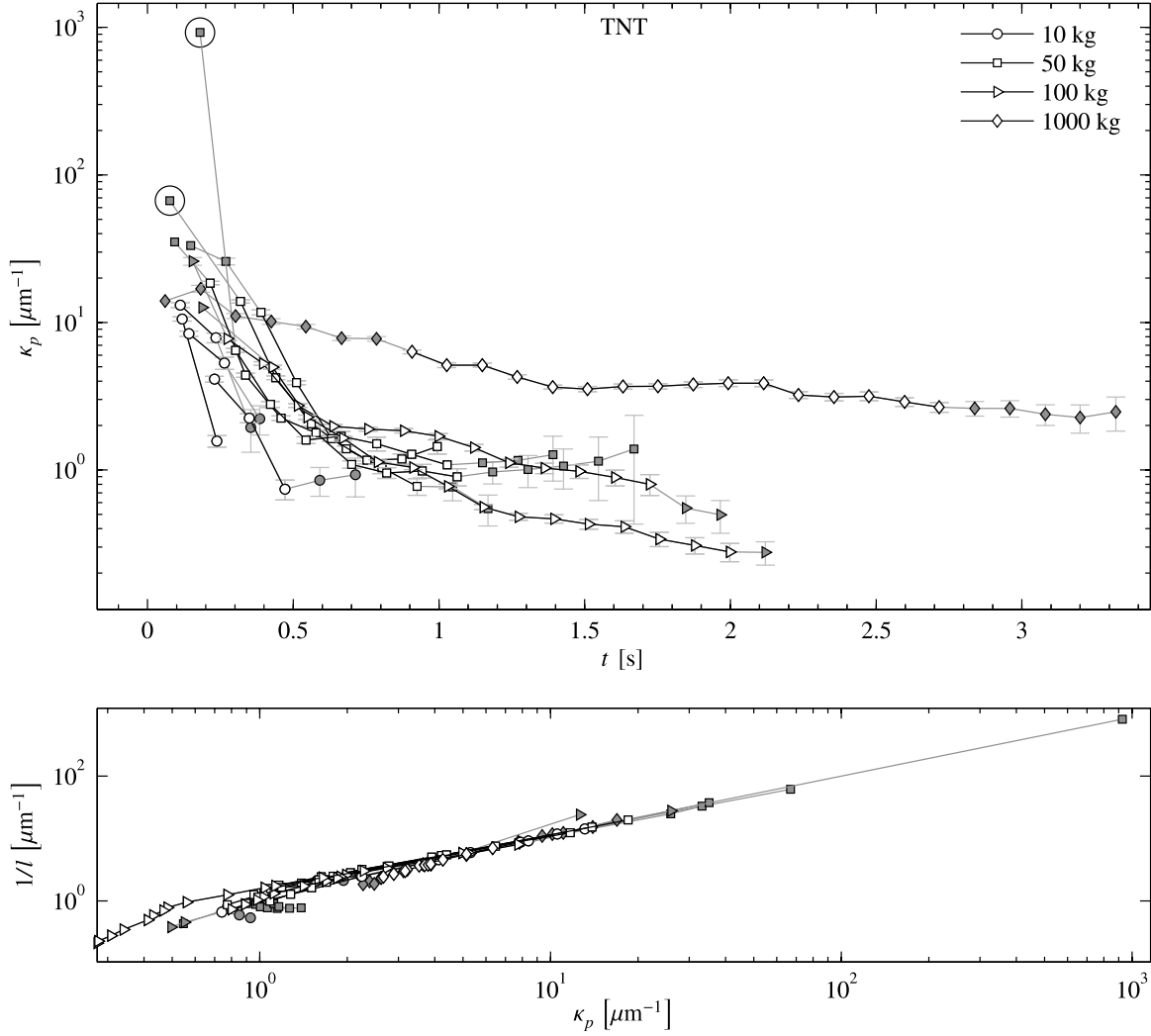
Figure 48: *Top panel*: Particulate absorption coefficient κ_p versus time for 10 ($\circ$), 50 ($\square$), 100 ($\triangleright$), and 1000 kg ($\diamond$) TNT detonation fireballs. Error bars represent fit parameter uncertainties (95% confidence level). *Bottom panel*: Particulate absorption coefficient versus the inverse Rosseland photon mean-free path, a measure of the average total absorption coefficient. Grey symbols denote spectra in which $G < 3$. Circled points indicate when the fitted κ_p resulted in a minimum emissivity of 0.98 and are thus highly uncertain.

112
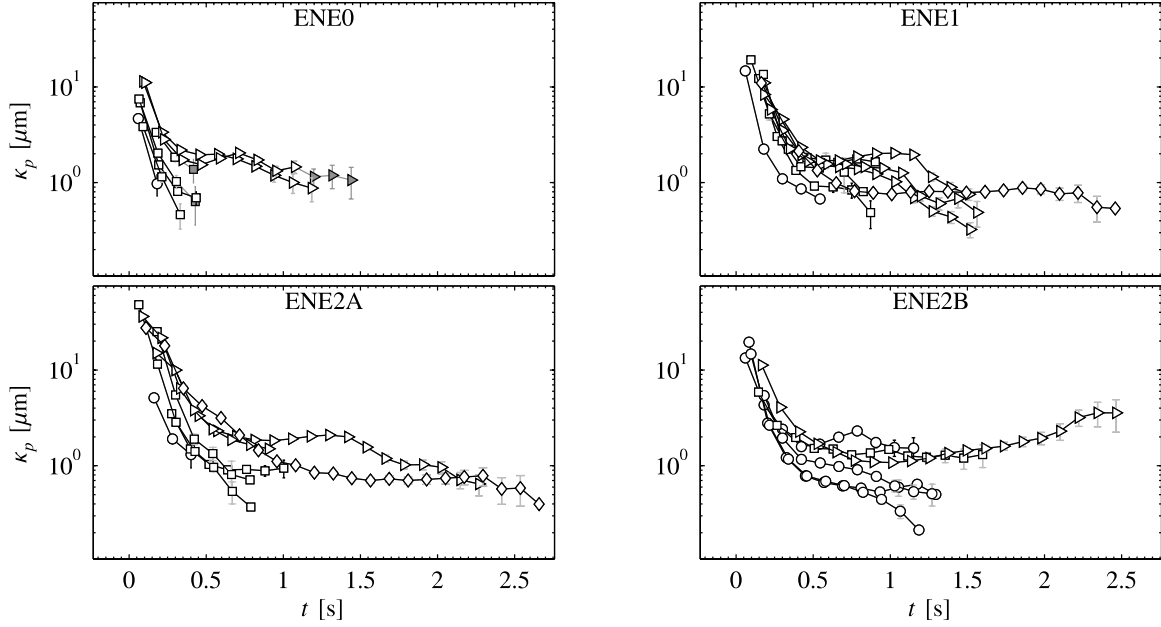
Figure 49: Particulate absorption coefficient κ_p versus time for 10 ($\circ$), 50 ($\square$), 100 ($\triangleright$), and 1000 kg ($\diamond$) ENE events, separated by HE type. Grey symbols denote spectra in which $G < 3$. Error bars represent fit parameter uncertainties (95% confidence level).

be considered. Recently, Roberts *et. al.* reported [55] an experimental technique to study the oxidation rates of soot produced in an ethylene diffusion flame. A differential mobility analyzer (DMA) was used to select monodisperse soot particles from the flame. Most soot particles were between 20 and 220 nm in diameter with 80–100 nm being the peak of the size distribution. Transmission electron microscopy revealed that the soot particles were agglomerates of spherical particles with diameters ranging between 20–30 nm. DMA was used to select three agglomerated soot particle sizes; in terms of diameter D they were 40, 93, and 130 nm. The soot particles were introduced into a high-temperature flow reactor, and a second DMA was used to monitor changes in particle size with time at various temperatures. The measured size decrease rate were described by the following modified Arrhenius expression

$$\frac{\mathrm{d}D}{\mathrm{d}t} = -a\sqrt{\mathrm{T}}e^{-\mathrm{E}_a/\mathrm{RT}} \qquad (44)$$

with a fitted activation energy $E_a = 164$ kJ and a pre-exponential factor a which depended on the initial particle size. Fitted values for a were 0.019, 0.026, and 0.032 cm $K^{-1/2} s^{-1}$ for the 40, 93, and 130 nm sized particles.

There are several complications which preclude assessing the applicability of Equation 44 to the temporal dynamics of κ_p. First, the chemical composition of the fireball soot likely differs from that produced in the ethylene flame, and differences in E_a are expected. Only the carbon-rich TNT explosives will be considered as they will better match the ethylene soot characteristics compared with the aluminized, carbon-lean ENE explosives. Second, the pre-exponential factor a depends on particle size and the soot size distribution in the fireball is unknown. Third, the concentration of the fireball particulate matter ξ_p is unknown. Finally, the fireball is a turbulent system whereas the oxidation study involved soot produced in a laminar flame. Nonetheless, some simplifying assumptions will be introduced to assess if the behavior of $\kappa_p(t)$ is in qualitative agreement with the dynamics predicted by Equation 44. First, the soot particles are assumed to be opaque and black so that their absorption cross-section is equal to their geometrical cross-section. With this, κ_p can be expressed as

$$\kappa_p = \xi_p \sigma_p = \xi_p \pi D^2 / 4 \tag{45}$$

Second, effects of the soot size distribution will be ignored and initial particulate sizes will be taken as 130 nm. Third, it will be assumed that sufficient atmospheric oxygen is available for soot oxidation. Otherwise, O_2 availability would influence the oxidation rate. Finally, it will be assumed that under the time scale of consideration, the concentration of agglomerated particulates is unchanging. This means that the decrease in κ_p with time is due entirely to reduction in surface area resulting from oxidation. Until a soot particle is completely oxidized, its contribution to ξ_p is constant. Under these assumptions, Equation 45 is solved for D and differentiated with respect to time yielding

$$\frac{\mathrm{d}D}{\mathrm{d}t} = \frac{1}{\sqrt{\pi \xi_p}} \frac{\mathrm{d}\kappa_p/\mathrm{d}t}{\sqrt{\kappa_p}} \tag{46}$$
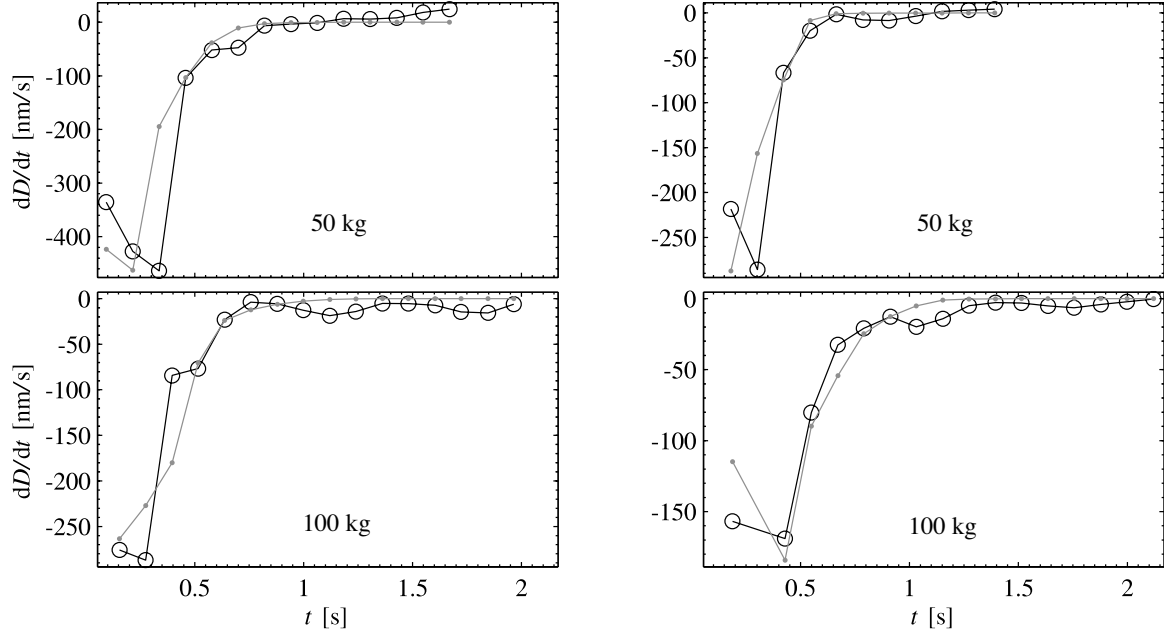
Figure 50: Soot oxidation rates as measured by the diameter rate-of-change for four TNT fireballs. Estimates from κ_p are denoted by $\circ$ and the grey points represent the theoretical prediction from a modified Arrhenius rate law.

So under the assumptions described above, the soot oxidation rate as measured by changes in particulate diameter can be compared with Equation 44 to within an unknown scale factor represented by ξ_p. Using extracted fireball temperatures, Equation 44 was used to estimate the particulate oxidation rate. This was compared with Equation 46 in which central differences were used to numerically approximate the time-derivative of κ_p. Since ξ_p is unknown, it was used to scale the result to match Equation 44. The results of this analysis for four TNT fireballs are presented in Figure 50. Qualitatively, the observed oxidation rate is in good agreement with the theoretical predictions for these four events. The initially large oxidation rate occurs at high temperature and as the fireball cools, the rate approaches zero. While ξ_p was a free parameter, it is worth noting that the shapes of the curves are in good agreement. By extension, the overall temporal behavior of the oxidation rates are in good agreement. Furthermore, the assumption was made that the initial soot particles were 130 nm in diameter. For the four events, the free parameter ξ_p was found to be on the order of 10^6. Plugging these values into Equation 45 give an initial absorption coefficient on the order of $10^{-4}\,cm^{-1}$. This is only one order of magnitude smaller than the observed initial κ_p values. Given the good agreement with the shape of the rate curves and absolute magnitudes consistent to within an order of magnitude, it is plausible

115
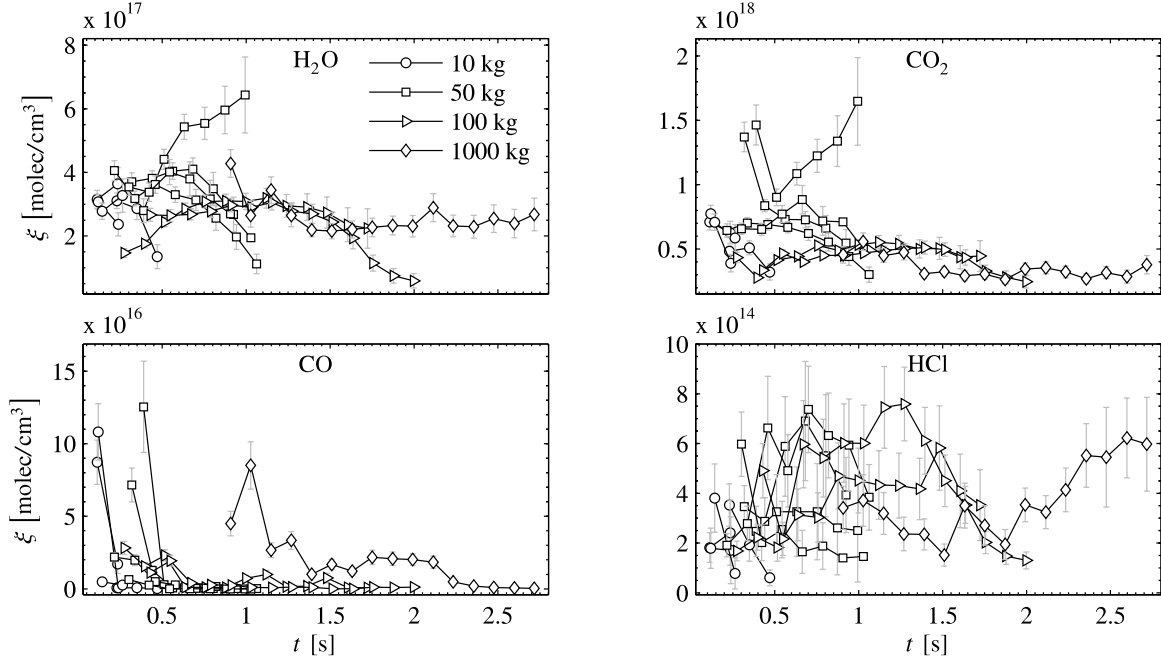
Figure 51: Concentration versus time profiles extracted from TNT fireballs for H_2O, CO_2, CO, and HCl. The different sized explosives are denoted in the following manner: 10 ($\circ$), 50 ($\square$), 100 ($\triangleright$), and 1000 kg ($\diamond$). The water and carbon dioxide values have been corrected for heated atmospheric contributions to the observed values. Concentrations extracted from spectra with the non-grey parameter satisfying $G < 3$ were omitted. Error bars represent fit parameter uncertainties (95% confidence level).

that the dynamics of κ_p are connected to soot oxidation with temperature-controlled kinetics described by familiar Arrhenius behavior. Active spectroscopic techniques such as laser-induced incandescence (LII) may be a useful tool to better monitor and understand the soot kinetics. While such an experimental set-up is likely impractical for field work, small scale laboratory experiments involving controlled micro-detonations might be possible which enable firmer conclusions to be drawn about the phenomenology underlying the temporal behavior of κ_p.

5.5 Molecular concentrations (ξ_i)

Time-resolved concentrations of four gaseous combustion by-products—H_2O, CO_2, CO, and HCl—are provided in Figure 51 for the TNT events. The concentrations have been corrected for contributions to emission from heated atmospheric gases. In general, the HE weight had no influence on the magnitude or shape of the extracted ξ_i's, supporting the notion that fireball density is independent of W as suggested in § 5.2. Both

116

the water and carbon dioxide concentration profiles are fairly static with some propensity to decrease with time. One 50 kg event displayed an increase in both concentrations with time. The carbon monoxide concentration rapidly decayed to below the detectability threshold typically within 1–2 scans of the instrument, i.e. within ~0.25 s. The 1000 kg event exhibited longer-lived CO concentrations. The observed behavior is consistent with the oxidation of carbon-rich soot. Glassman [44, pp. 463] points out that at temperatures above 1500 K, CO_2 is not found near the soot surface. Instead, only CO is made at the soot surface, and as it diffuses away from the particle, it may encounter additional oxygen and become fully oxidized to CO_2. Thus, on the basis of the kinetics of the soot oxidation, it is not unreasonable to expect emissions from CO in the fireball spectra when the temperatures are high. However, it should be stressed that only a single, small, and weak emission band—the $2 \rightarrow 0$ overtone—is used to establish the CO concentration. Furthermore, the necessity of CO for describing the observed fireball spectra is not as visually evident as for the other species included in the model. On the other hand, HCl emission was easily observed in the spectra, and this might appear counter-intuitive given the relatively large error bounds on the HCl concentrations. It is possible that HCl initially increases and subsequently decays, but the large parameter uncertainties caution such an interpretation. Apart from CO, the mostly static nature of these profiles may indicate that the bulk of the oxidative chemistry had completed prior to the observation times. If so, this would suggest higher temporal resolution is needed to interrogate the reactive kinetics of the gaseous species in TNT fireballs.

In general, the ENE concentration profiles exhibited interesting kinetic behavior, and were more suggestive of reactive chemistry occurring during the observation time[11]. The individual concentration profiles are provided in Figures 56–59 at the end of the chapter. Differences in the shapes of the $\xi_i(t)$ curves were evident both across HE type and HE weight. However, a substantially larger number of events would be required to assess whether this is the result of inherent variance in the data or due to differences in chemistry and weight. Nonetheless, the more interesting kinetic behavior at long time scales (0.5–2 s) might be expected since the ENEs are aluminized explosives. Miller points out [79] that the presence of aluminum in composite

---

[11] It is possible that the observed dynamics are the result of changes in fireball volume with time. However, the total number of water or carbon dioxide molecules also exhibited similar temporal trends, indicating that the $\xi_i(t)$ profiles were driven by something other than size dynamics.

explosive materials often results detonation reactions in which significant amounts of energy are released at much later times compared to non-aluminized, more ideal explosives such as TNT. This behavior is a result of the diffusion-limited process by which atomic aluminum and the oxidizer (O_2, CO_2, or H_2O) traverse the flame front surrounding the aluminum particle [2,7,79]. The diffusion rate is much slower compared with the reaction rates of the gas-phase oxidation of the non-metallic HE material. The net effect is a more sustained reaction period with higher temperatures due to the extremely exothermic oxidation of aluminum.

With an eye towards future field tests, a quick digression regarding aluminized explosives is in order. The oxidation of aluminum to form condensed Al_2O_3 is understood to proceed through AlO as an intermediary [7, 45]. At detonation temperatures, AlO gives off visible light via an electronic transition ($B^2\Sigma^+ \rightarrow X^2\Sigma^+$) between roughly 450–550 nm. This spectrum has been recorded in many aluminum combustion studies and has recently been observed in the detonation of aluminized nitromethane[12] [45]. Time-resolved visible spectra of the AlO B $\rightarrow$ X transition would reveal the time scale of the combustion process and help the interpretation of the concentration profiles for H_2O and CO_2. With sufficient spectral resolution ($\Delta\lambda \simeq 0.05$ nm), its temperature can be estimated from the spectrum, and would serve as a check of extracted temperatures from the MWIR spectrum. Furthermore, the presence or absence of this electronic transition in visible spectra would likely discriminate aluminized explosives from non-aluminized ones. Because of this, the deployment of visible spectrometers is strongly recommended for future field tests.

A sense of the general differences in gaseous concentrations among the HEs can be obtained in the form of group-averaged values. Weighted mean concentrations of the ith gaseous constituent were computed for each class of high explosive, irrespective of HE weight, in the same manner as in Equation 30. The individual contributions of $\xi_i(t)$ to the mean were weighted by $w = G/\delta\xi_i(t)$ where G accounts for the degree of selective emission in the corresponding spectrum and $\delta\xi_i(t)$ is the statistical uncertainty associated with the fitted $\xi_i(t)$ value. Weighted standard deviations were also computed to measure the degree of scatter about the mean among the better estimates of concentration. The mean concentrations and associated standard deviations, weighted as just described, are provided in Table 12. In general, gaseous concentrations were all

---

[12]The visible spectra presented in Reference [45] represent the only known detonation fireball spectra presented in the literature apart from articles by the AFIT remote sensing group.

Table 12: Group-averaged concentrations for each class of HE detonated during the Brilliant Flash II field test. The average value is the weighted mean where the weights are defined by $G/\delta\xi_i$. Weighted standard deviations are represented in parentheses. The weighted mean ratio of observed to theoretical carbon and hydrogen amounts, N_C/N_C^{th} and N_H/N_H^{th}, are also provided.

HE	$\xi_{CO_2}^{HE}/10^{17}\frac{\text{molec}}{\text{cm}^3}$	$\xi_{CO}/10^{15}\frac{\text{molec}}{\text{cm}^3}$	N_C/N_C^{th}	$\xi_{H_2O}^{HE}/10^{17}\frac{\text{molec}}{\text{cm}^3}$	$\xi_{HCl}/10^{14}\frac{\text{molec}}{\text{cm}^3}$	N_H/N_H^{th}
TNT	5.0 (1.8)	0.7 (2.5)	0.5 (0.2)	2.9 (0.8)	3.6 (1.8)	0.8 (0.2)
ENE0	1.9 (1.2)	0.4 (0.7)	1.0 (0.6)	9.2 (4.1)	10.8 (7.5)	0.5 (0.1)
ENE1	1.7 (1.2)	0.1 (0.8)	0.8 (0.5)	4.7 (2.0)	3.9 (3.2)	0.7 (0.2)
ENE2A	1.7 (1.6)	0.6 (4.1)	0.5 (0.4)	5.3 (2.9)	2.9 (4.1)	0.4 (0.3)
ENE2B	1.6 (0.6)	0.9 (1.8)	0.4 (0.2)	5.1 (1.8)	5.6 (2.5)	0.4 (0.2)

within the same order of magnitude—10^{17} molec/cm^3 for H_2O and CO_2, and 10^{14} molec/cm^3 for CO and HCl. TNT had relatively larger concentrations of CO_2 than any of the ENE's. Likewise, the ENE's exhibited larger water concentrations than that of TNT. Such behavior is not unexpected on the basis of the relative amounts of carbon and hydrogen in the high explosive starting materials. (See Table 3.)

Also provided in Table 12 are the total gaseous hydrogen (N_H) and carbon (N_C) values relative to the upper bounds fixed by the stoichiometry of the HE materials. These ratios speak to the efficiency in which the carbon and hydrogen in the HE are converted into gaseous molecules. ENE1 was the most efficient in this regard with ~80% of carbon and ~70% of hydrogen being converted to gaseous forms. Likewise, ENE2B appeared to be the least efficient with conversion factors of only ~40% for both carbon and hydrogen. It is reassuring to note that on average no unphysical efficiencies were obtained.

The concentration profiles contain a substantial amount of information about the combustion chemistry occurring in the fireball, and by extension, about the high-explosive precursor. Properly extracting this wealth of information awaits a chemical kinetics model for the detonation and afterburning processes, the development of which is beyond the scope of the present investigation. Nonetheless, the relative amounts of hydrogen and carbon may give clues about the underlying HE stoichiometry as suggested in Chapter IV and indicated in Table 12. The basic idea is that despite the temporally-evolving gaseous concentrations, the HE stoichiometry will influence in an overall sense the relative quantities of hydrogen- and carbon-containing species. Since the ENEs substantially differ from TNT in this regard, $\mathcal{R} = $ H:C may be a useful discriminant. To assess
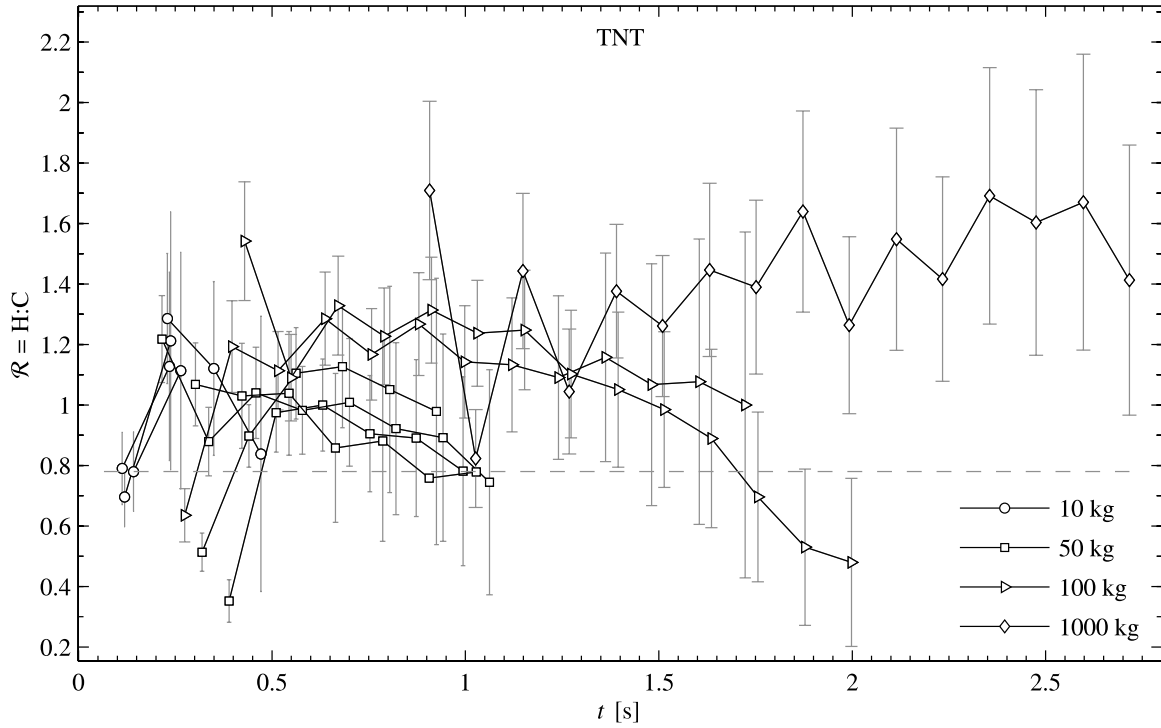
Figure 52: Time-resolved $\mathcal{R}$ values extracted from spectra of the TNT charges detonated during the Brilliant Flash II field test. The dashed grey line represents the hydrogen-to-carbon ratio in the high-explosive mixture. Points corresponding to $G < 3$ have been omitted. Error bars represent propagation of errors based on fit parameter uncertainties (95% confidence level).

this, the temporal dynamics of $\mathcal{R}$ are presented in Figure 52 for the TNT explosives and in Figure 53 for ENE compounds. For comparison, the hydrogen to carbon ratio from the HE starting material is provided.

For TNT, $\mathcal{R}(t)$ is fairly static with values typically slightly above the stoichiometric ratio of 0.79. This is consistent with some carbon taking the form of soot. ($\mathcal{R}$ only accounts for gaseous carbon in the form of CO_2 and CO, and gaseous hydrogen in the form of H_2O and HCl.) For TNT, the static nature of $\mathcal{R}$ agrees with the suspicion that most of chemistry has already occurred by the observation time scale of 0.5–2 s. Ogura *et. al.* [85] estimate via pyrometry that the after-burning in TNT detonations ranging from 1–100 kg is completed within 50–100 ms after the initial detonation. However, some chemistry appears evident in the decay of κ_p with time in the TNT system if it's attribution to soot oxidation presented above is correct. This appears to be at a small enough scale as to not strongly influence the $\mathcal{R}$ term.

The ENEs, in particular ENE2B, were more dynamic with initial values of $\mathcal{R}$ much larger than the stoichiometric ratio. This behavior is consistent with the Cooper [22] and Kistiakowsky-Wilson [2] empirical

120
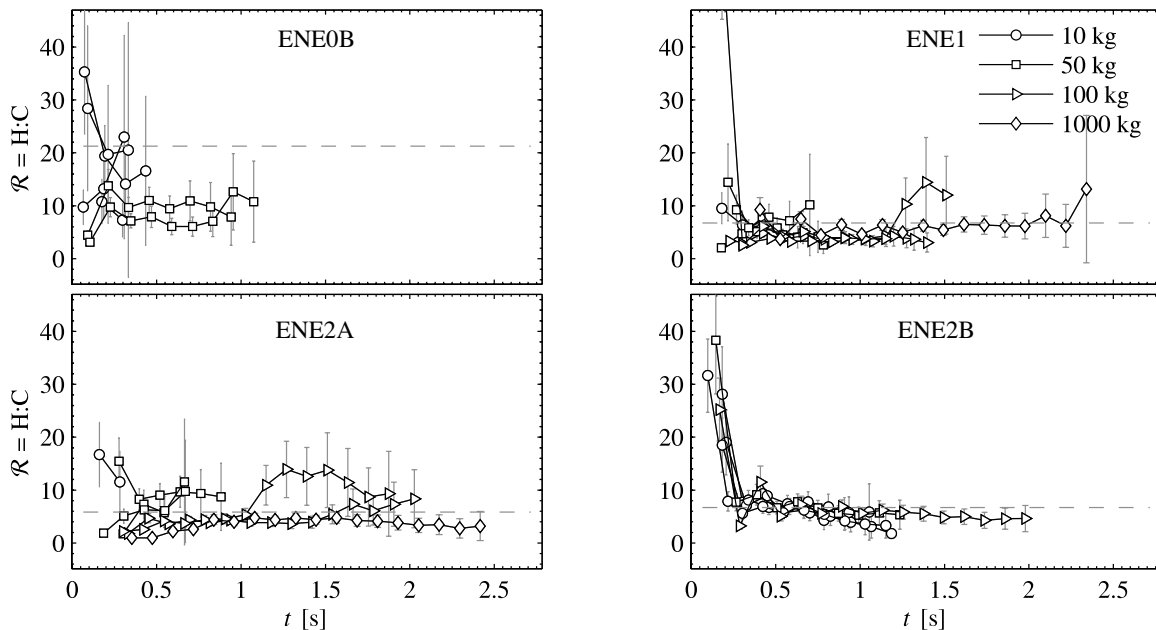
Figure 53:   Time-resolved $\mathcal{R}$ values extracted from spectra of the four types of ENEs detonated during the Brilliant Flash II field test. The dashed grey line represents the hydrogen-to-carbon ratio in the high-explosive mixture. Points corresponding to $G < 3$ have been omitted. Error bars represent propagation of errors based on fit parameter uncertainties (95% confidence level).

rules which predict formation of H_2O to precede the production of CO_2. Within about 0.35 s, $\mathcal{R}(t)$ had decayed to near the stoichiometric ratio. The only exception to this was ENE0B, which decayed to about half of the value predicted from the chemical composition. The ENE profiles of $\mathcal{R}$ indicate that the fireballs may be chemically reacting as late as 200–300 ms after detonation. After this time, it appears that the bulk of the reactive chemistry is finished. As suggested above, the observation of chemistry at long timescales is consistent with the non-ideal nature of the ENE explosives. ENE2B had the most reproducible $\mathcal{R}(t)$ curves. The long-term ($t > 0.35$ s) group averages for $\mathcal{R}$ are provided in Table 13, and it is clear that TNT is readily distinguished from the ENEs in this manner. Distinguishing among the different ENEs is more difficult as several have similar stoichiometries and all exhibit more spread about their mean $\mathcal{R}$ values. For all explosives examined, there is no discernible dependence of $\mathcal{R}$ on weight.

121

Table 13: Comparison of group-averaged $\mathcal{R}$ values with the H:C ratio in the HE starting material. Standard deviations are represented in parentheses. The average value is the weighted mean where the weights are defined by $G/\delta\mathcal{R}$, where G is the non-grey parameter and $\delta\mathcal{R}$ represents the uncertainty in $\mathcal{R}$. The average was performed for times satisfying $t > 0.35\,\text{s}$ to avoid influence by the initial dynamic behavior of $\mathcal{R}$.

HE	mean($\mathcal{R}(t)$)	Stoichiometry
TNT	1.13 (0.14)	0.79
ENE0B	9.2 (2.5)	21.3
ENE1	4.9 (1.5)	6.7
ENE2A	4.6 (2.6)	5.8
ENE2B	6.5 (1.5)	6.7

Alluded to in § 4.6 was the presence of an unknown emitter as evidenced by two emission lines[13] near 6539 and 6592 cm^{-1}. Figure 54 presents the time-resolved intensities integrated across the spectral bins containing the emission lines for all of the detonation events. These emission lines were strongly evident in early spectra obtained from ENE1 and ENE2 events. Conversely, there was no evidence for the unknown emitter in either the TNT or ENE0 fireballs. While the cause of this emission signature is unknown, the results may shed some light on possible explanations of the observed emission feature. Note that the unknown emitter was found only in the aluminized explosives with high initial temperatures (ENE1 and ENE2). The aluminum-containing ENE0 did not exhibit this emission feature, and the initial fireball temperatures were between 1790 and 2020 K, much lower than the "boosted" ENEs. (Of course, true initial temperatures are unknown given the limitations of the 8 Hz FTS scan rate.) Much higher temperatures (2900–3000 K) are needed to initiate aluminum combustion in air as the aluminum oxide shell must be softened and elemental aluminum vaporized [34]. One initial "boosted" ENE temperature was near this threshold at T = 2767 K, a few others were greater than 2400 K, and several ENE1 and ENE2 initial temperatures were above the $\sim$ 2325 K melting point of Al_2O_3. These results suggest an exploration of temperature-dependent, aluminum-based transient species may be worthwhile in an effort to assign the unknown emission feature.

In spite of the uncertainty regarding the cause of the emission signature, its presence in the spectrum is strongly indicative of whether or not the ENE contains either of the two "booster" ingredients. Determining

[13]Recall from Chapter II that an optical filter does not appear to be present in front of the InSb detector so that aliasing may be a problem at shorter wavelengths. It is therefor possible that the apparent emission doublet is in fact a pair of lines above the HeNe Nyquist limit of 7901 cm^{-1} near 9210 and 9263 cm^{-1}. These lines would have to be extremely bright since the response of the InSb detector would be very weak in this region.
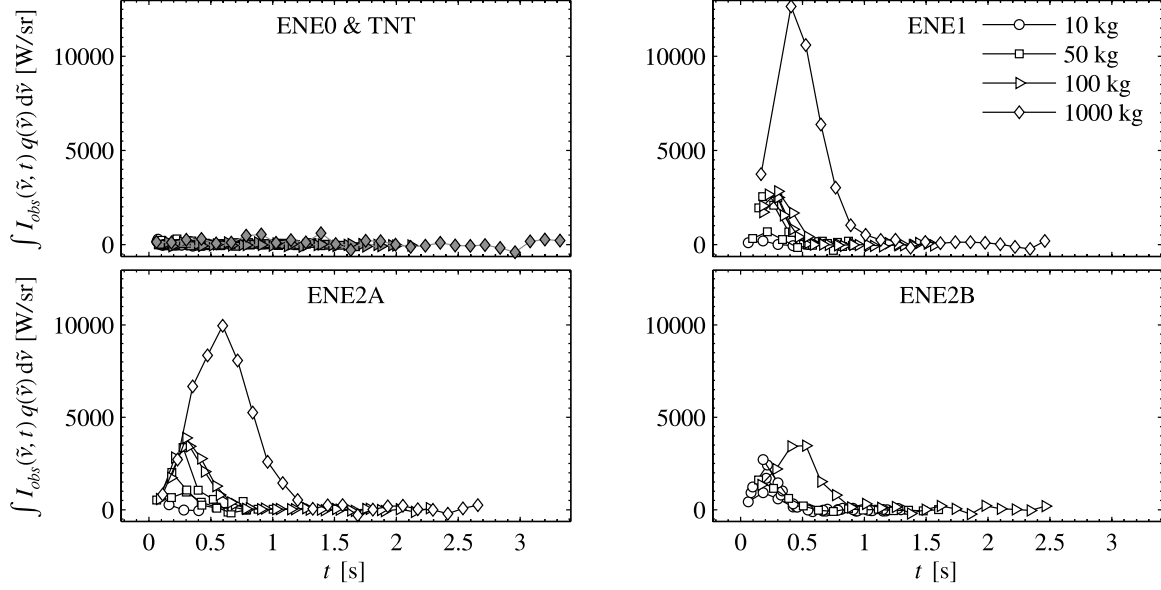
Figure 54: Time-resolved intensities at unknown emission frequencies for each HE type detonated during the Brilliant Flash II field test. The intensity was integrated over $q(\tilde{\nu})$ where $q = 1$ if $6535 \leq \tilde{\nu} \leq 6554\,\mathrm{cm}^{-1}$ or $6587 \leq \tilde{\nu} \leq 6598\,\mathrm{cm}^{-1}$ and $q = 0$ otherwise. Both the ENE0 (white) and TNT (grey) intensities are provided in the top left panel.

the cause of the emission will be an important next step. For example, it may be that the emission is connected to an impurity introduced during the mixing of ENE1, ENE2A, and ENE2B explosives. In this case, the emission may not be a signature which generalizes to the problem of distinguishing boosted from un-boosted ENE mixtures. However, if the observed emission can be related to the detonation chemistry of the bulk explosive, then this feature has the potential of being an extremely useful signature.

5.6 Distinguishing TNT from ENE

TNT and the various ENEs differ greatly in molecular composition, and the spectrally-determined $\mathcal{R} = \mathrm{H{:}C}$ captures this variation among the HEs examined in this study. While each of the ENEs are distinct in composition, collectively they contain a much larger fraction of hydrogen (relative to carbon) than TNT, and all of the ENEs contain a common baseline mixture. In some cases, it may be desirable to distinguish between TNT and ENE. There are a multitude of classification algorithms that can be applied to this problem. To demonstrate by example of how HE discrimination might be performed, the feature $\mathcal{R}$ will be used to make a statistical inference about which of the two classes (TNT or ENE) the event most likely belongs.

123

Bayesian decision theory is a common approach to feature-based classification. A brief summary based on *Pattern Classification* by Duda *et. al.* [35] is presented for the case of distinguishing between two classes, denoted $\{\omega_1, \omega_2\}$ using a single feature x. Taking x as a continuous random variable dependent on the state of nature ω_i (i.e., state of the fireball), let $p(x|\omega_i)$ represent its probability density (i.e., the distribution of x values all corresponding to ω_i). The *a priori* probabilities are denoted $P(\omega_i)$ and represent the prior knowledge about the likelihood of the event being ω_i known before the measurement. (In this case, the assumption is that TNT and ENE events are equally likely, implying $P(\omega_1) = P(\omega_2) = \frac{1}{2}$.) The *a posteriori* probability $P(\omega_i|x)$ represents the likelihood that the event was ω_i given the measurement x and is expressed by Bayes formula

$$P(\omega_i|x) = \frac{p(x|\omega_i)P(\omega_i)}{\Sigma_j p(x|\omega_j)P(\omega_i)} \tag{47}$$

For a given x, whenever $P(\omega_1|x) > P(\omega_2|x)$, Bayes decision rule is to choose ω_1; otherwise, ω_2 is chosen. An error occurs whenever ω_i is chosen instead of the true state ω_j where $i \neq j$. It can be shown that the Bayes decision minimizes the average probability of error, which can be written in the following form

$$P(error) = \int_{-\infty}^{\infty} \min \left[P(\omega_1|x), P(\omega_2|x) \right] \Sigma_i p(x|\omega_i)P(\omega_i) \, \mathrm{d}x \tag{48}$$

Assuming identical costs for a mis-classification into either class, no costs for proper classification, and equal *a priori* probabilities, the point(s) x at which the likelihood ratio $p(x|\omega_1) / p(x|\omega_2)$ is unity define the decision boundaries for classification.

This Bayesian analysis was applied to the BF2 data in the following way. Each of the ENE0B, ENE1, ENE2A and ENE2B events were collectively labeled ENE. Using the single feature $\mathcal{R}$, normal (gaussian) probability densities were estimated for both TNT and ENE. The probability densities include all explosive weights (10, 50, 100, and 1000 kg). Each spectral estimate of $\mathcal{R}$ was used as a separate observation. For example, a time-resolved data cube for a single TNT fireball may result in multiple $\mathcal{R}$ estimates, and each estimate is considered a separate observation. $\mathcal{R}$ values with uncertainties greater than 20% were excluded to minimize the effects of outliers, and $\mathcal{R}$ measured prior to $t = 0.35\,\mathrm{s}$ were excluded to minimize the influence

of initial kinetic behavior. Under these conditions, there were 27 individual TNT events with a mean and standard deviation of 1.17 ± 0.15. For the ENEs, there were 46 events with a mean and standard deviation of 4.81 ± 1.22. The additional spread in the ENEs is not unexpected given that several different explosives which differ in relative carbon and hydrogen amounts are considered a single group.

Figure 55 displays the probability distribution functions (PDF) for both the TNT and ENE classes. The actual $\mathcal{R}$ observations are projected onto each PDF. The *a posteriori* probabilities are also provided, and indicate the probability that the event belongs to a particular class. For example, the probability an event is TNT is near unity when $\mathcal{R} = 1.1$. Likewise, the probability an event is ENE is near unity when $\mathcal{R} = 5.0$. However, when $\mathcal{R} = 1.67$, the probabilities are equal that the event corresponds to TNT or ENE. This represents a decision boundary, i.e. whenever $\mathcal{R} > 1.67$, the event is more likely belongs to the ENE class. There is a second boundary at $\mathcal{R} = 0.56$, so that at values less than that, it is also more likely an ENE event. This is a result of the broad nature of the ENE PDF with a tail that, although miniscule in magnitude, is larger than the tail of the TNT PDF in that region.

An estimate of the mean probability of error is $P(error) = 0.28\%$. This was computed by performing the integration in Equation 48 over the finite limits of $\mathcal{R} \in [-9.9, 19.5]$. This domain represents a distance of 12 ENE standard deviations to the right of the ENE mean and to the left of the TNT mean. The low error probability indicates the excellent separation of TNT and ENE that $\mathcal{R}$ enables. Another way of examining the separation between these two classes is by considering the receiver operating characteristic (ROC) curve. The ROC curve captures the functional dependence of the detection probability (P_D) on the false-alarm probability (P_F). For the TNT vs. ENE case, the ROC curve (Figure 55, bottom panel) indicates that high-probability ENE detections are accompanied by extremely low false-alarm rates. For example, $> 99\%$ probability of ENE detection has an associated false-alarm probability of less than $10^{-4}\%$.

To put these detection results in perspective, they are compared with Dills' results [29] on distinguishing ENE from TNT events using features derived from imagery recorded on many of the same fireballs analyzed
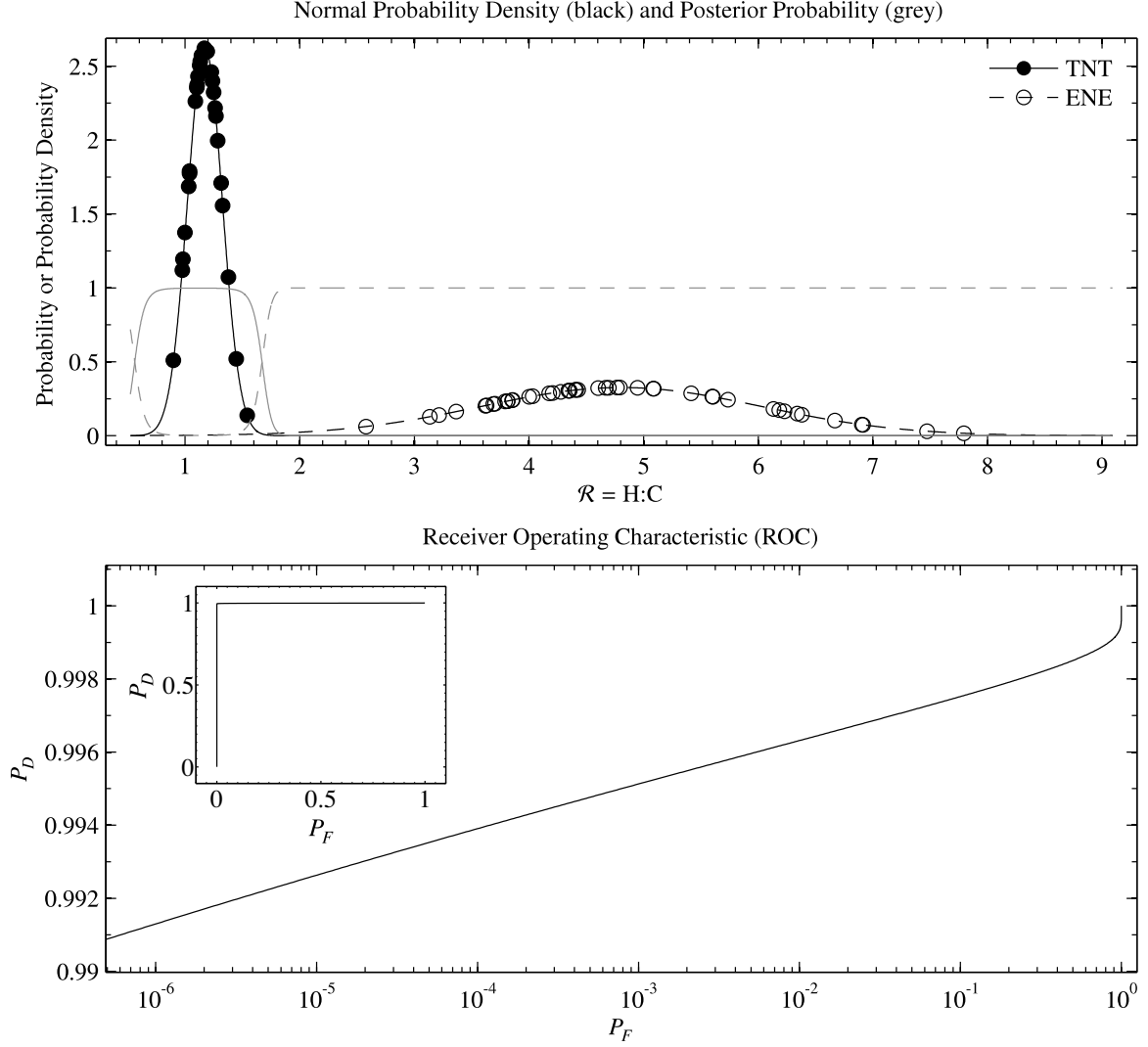
Figure 55:   *Top panel*: TNT (solid black) and ENE (dashed black) probability densities based on spectrally-extracted $\mathcal{R}$ values and assuming a normal distribution. $\mathcal{R}$ observations for TNT ($\bullet$) and ENE ($\circ$) are projected onto the corresponding curves. The solid and dashed grey lines correspond to *a posteriori* probabilities assuming TNT and ENE to be the only possible choices. *Bottom panel*: The receiver operating characteristic (ROC) curve displaying the detection probability P_D as a function of the false-alarm probability P_F for the discrimination of ENE from TNT using the normal distributions in the top panel.

in this work [14]. Dills performed Fisher linear discrimination [35, § 3.8.2], a technique in which some linear combination of features is chosen on the basis that it affords the best discrimination between multiple classes. The metric for selecting this combination of features is the Fisher ratio

$$\text{FR} = \frac{\frac{1}{D} \Sigma_{i \neq j} \left(\overline{x}_i - \overline{x}_j \right)^2}{\frac{1}{C} \Sigma_i \sigma_i^2} \tag{49}$$

where $\overline{x}_i$ and σ_i are the mean and standard deviation of the ith class, C is the total number of classes, and D is the number of unique between-class differences. The larger the Fisher ratio, the better the combination of features can be used to distinguish among the various classes. By maximizing FR, the between-class distances (numerator) are maximized as much as possible while concurrently minimizing the within-class spread (denominator) as much as possible.

Dills found that the time required for the fireball area to reach a maximum value (in NIR imagery) was the best single discriminant between TNT and ENE. TNT fireball areas peaked between 40–160 ms after detonation, whereas the ENE fireball areas peaked between 0–60 ms. With this single feature, Dills obtained a Fisher ratio of 2.5 indicating moderate discrimination capability of this feature. The single feature which provided the largest Fisher ratio was the peak of the "blue" area as measured by a visible-wavelengths RGB video camera with FR = 4.4. (While the maximum area in the blue offered a larger Fisher ratio, Dills discusses other factors which suggest the time-to-peak feature is a more robust predictor of ENE or TNT.) By comparison, in this work the Fisher ratio using $\mathcal{R}$ is FR = 17.4 indicating a much better separation of TNT and ENE events. In his work, Dills suggested phenomenology-based features would provide better separation between the TNT and ENE classes, and the present analysis confirms this suggestion.

This quick analysis confirms the intuitive expectation that $\mathcal{R}$ would serve as an excellent discriminant for TNT and ENE events. However, there are a few important caveats to be considered regarding this analysis. First, only a limited number of TNT and ENE events comprised the BF2 test and it is unclear if the natural variance of $\mathcal{R}$ was captured for each class. Second, this analysis only minimally demonstrates the utility

---

[14]Note that Dill's work includes imagery data from Brilliant Flash I. Recall that spectra from that field test were not analyzed in this dissertation due to the technical issues mentioned in § 2.3.

and good performance of phenomenologically-based features in the TNT vs. ENE classification problem. It is expected that the incorporation of additional features (e.g., initial temperatures, presence of the emission feature near $6600\,\mathrm{cm^{-1}}$, kinetic behavior of $\mathcal{R}$, etc.) along with the use of more sophisticated classification algorithms will significantly enhance the already promising prospect of HE classification.

5.7 Conclusions

This chapter presented the results of fitting all spectra collected during the Brilliant Flash II field test. Several important discoveries were reported. First, extracted $\mathcal{R}$ values from TNT fireballs are substantially different from those obtained from ENE fireballs, suggesting that this metric can be used to distinguish the engineered explosive from the improvised ones. Because $\mathcal{R}$ approached the stoichiometric H:C values of the known starting materials, this metric is an important key feature that connects observed infrared emissions to a fundamental property of the bulk HE. A Bayesian classification approach using $\mathcal{R}$ indicated a clear separation between TNT and all ENE events. To the extent that the estimated PDFs for TNT and ENE are representative of the true distribution of $\mathcal{R}$ values for each class, the mean probability of error in distinguishing between each class is $< 0.3\%$. The Fisher ratio, which provides measure of class separability, was FR $= 17.4$. It is expected that the hydrogen-to-carbon ratio will be useful for distinguishing between many types of CHNOAl explosives that differ in relative amounts of carbon and hydrogen. For the ENE fireballs, $\mathcal{R}$ exhibited interesting temporal behavior, suggesting that additional information possibly related to the underlying combustion kinetics can be extracted. $\mathcal{R}$ also appears useful in distinguishing ENE0 from the "boosted" ENE1, ENE2A, and ENE2B materials. However, there is enough variability in $\mathcal{R}$ values that the statistical confidence may not be high enough for classification purposes. Fortunately, the presence of an unknown emission feature near $\tilde{\nu} = 6539$ and $6592\,\mathrm{cm^{-1}}$ clearly distinguishes ENE0 from the boosted materials.

Initial temperatures of the TNT fireballs of 1756–1916 K were consistent with a previous optical pyrometry study. ENE0 (baseline ENE mixture) fireballs were slightly hotter on average. The presence of the "booster" materials substantially increased initial temperatures by 400–600 K. Thus, initial temperature also serves as an indicator of the type of high explosive material. The temperature decay rate was dependent on

the weight of the HE with larger HEs requiring more time to cool. Investigation of this phenomenon revealed that the dominant mode of cooling in fireballs appears to be through radiative emission, a conclusion drawn by the excellent agreement between the observed TNT temperature profiles and those predicted by the sole process of radiative cooling. If the HE type is known *a priori*, it may be possible to estimate HE weight from temperature decay, and this estimate will be independent of absolute radiometric accuracy.

Fireball size can be estimated by fits to the non-imaging FTS data. Comparison of estimated sizes with those from NIR imagery revealed an under-estimation of size for the smaller HE charges. Estimates improved with HE weight, and estimates were better for the TNT explosives. This behavior may be partially explained by the approximation of sphere-like fireballs as cubes. Fireball size scaled with HE weight that was dependent on the HE material. If the HE type is already known, it may be possible to estimate the HE weight provided r is estimated from high SNR spectra. This presumes that the intensity axis will be free from radiometric errors or other effects which alter the apparent intensity (e.g. an opaque object partially obscuring the instrument's view of the fireball.)

The particulate absorption coefficient decayed with time. The rate of decay was initially large and rapidly decreased with time. This phenomenon appeared connected with temperature in a manner suggesting Arrhenius-like kinetic behavior. One reasonable explanation is that κ_p is a measure of sooty particulate material and its disappearance in time is the result of oxidative chemistry reducing its surface area. Assuming this to be the case, nice agreement was observed between the time-derivative of $\kappa_p(t)$ and that predicted by the results from a recent study on the kinetics of soot oxidation.

Interpretations of the temporal behavior of T and κ_p are preliminary and other explanations may also be found which describe the observed behavior. However, the interpretations provided in this chapter are consistent with observation. Moreover, they illustrate how the spectral model for HE fireballs enables the underlying phenomenology to be remotely studied by techniques such as FTS.
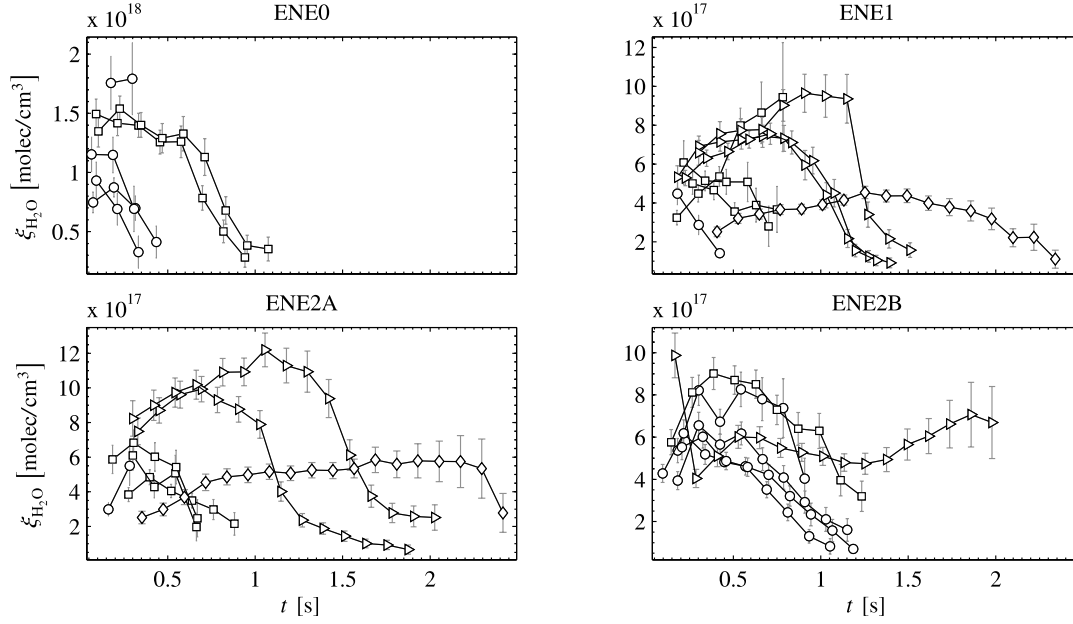
Figure 56:   H$_2$O concentration versus time profiles extracted from fireballs resulting from the detonation of the four types of ENE fireballs. The different sized explosives are denoted in the following manner: 10 (○), 50 (□), 100 (▷), and 1000 kg (◇). The concentration values have been corrected for contributions from the heated atmosphere. Concentrations extracted from spectra with the non-grey parameter satisfying $G < 3$ were omitted. Error bars indicate the fit parameter uncertainty (95% confidence level).
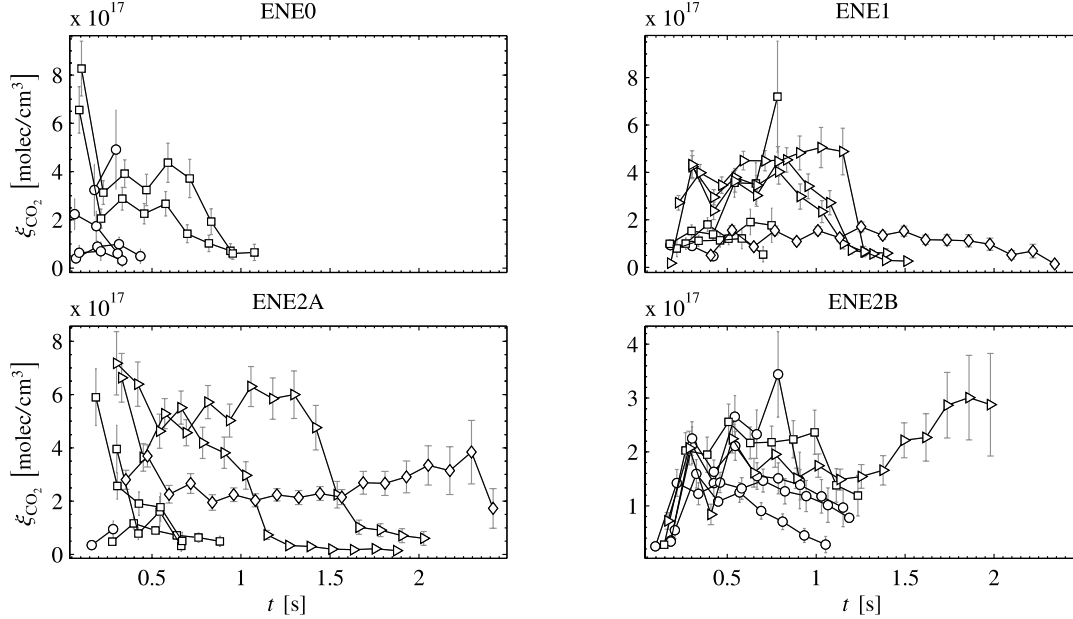
Figure 57:   CO$_2$ concentration versus time profiles extracted from fireballs resulting from the detonation of the four types of ENE fireballs. The different sized explosives are denoted in the following manner: 10 (○), 50 (□), 100 (▷), and 1000 kg (◇). The concentration values have been corrected for contributions from the heated atmosphere. Concentrations extracted from spectra with the non-grey parameter satisfying $G < 3$ were omitted. Error bars indicate the fit parameter uncertainty (95% confidence level).

130
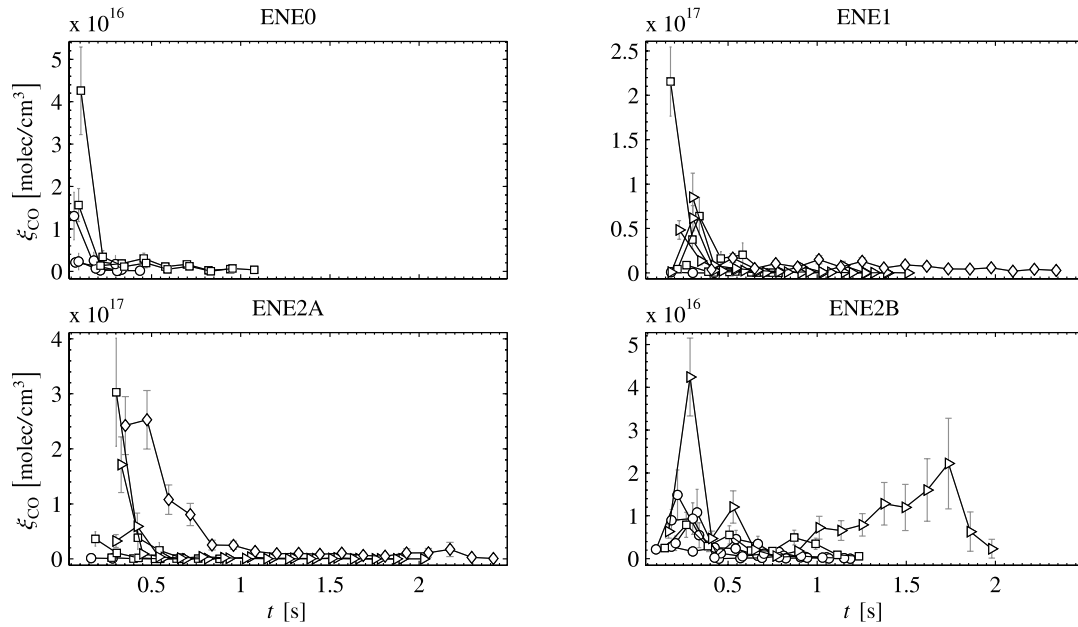
Figure 58: CO concentration versus time profiles extracted from fireballs resulting from the detonation of the four types of ENE fireballs. The different sized explosives are denoted in the following manner: 10 ($\circ$), 50 ($\square$), 100 ($\triangleright$), and 1000 kg ($\diamond$). Concentrations extracted from spectra with the non-grey parameter satisfying $G < 3$ were omitted. Error bars indicate the fit parameter uncertainty (95% confidence level).
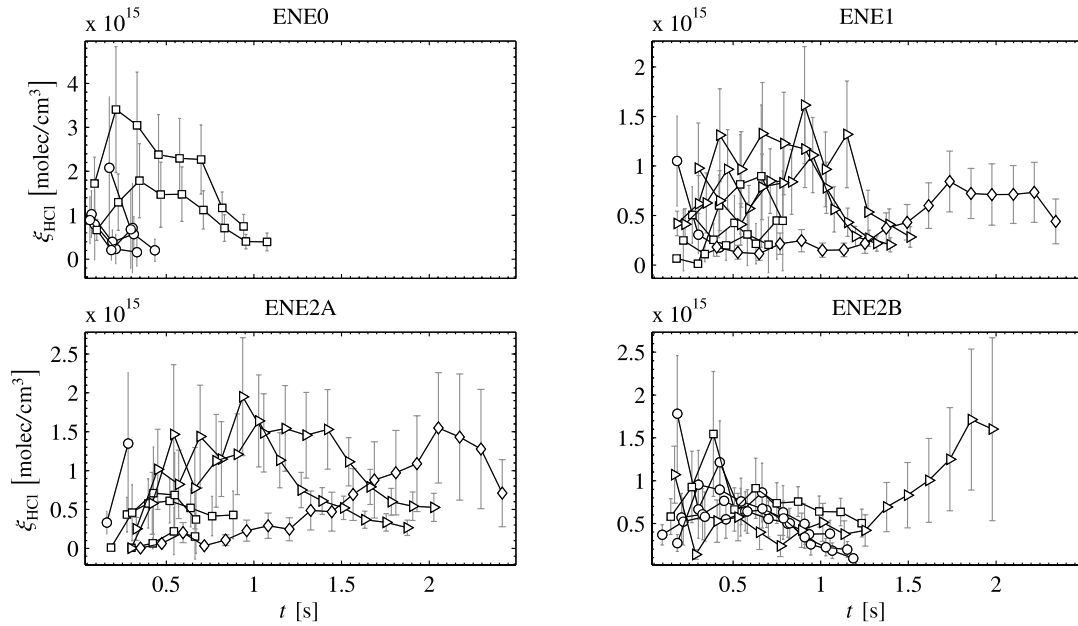
Figure 59: HCl concentration versus time profiles extracted from fireballs resulting from the detonation of the four types of ENE fireballs. The different sized explosives are denoted in the following manner: 10 ($\circ$), 50 ($\square$), 100 ($\triangleright$), and 1000 kg ($\diamond$). Concentrations extracted from spectra with the non-grey parameter satisfying $G < 3$ were omitted. Error bars indicate the fit parameter uncertainty (95% confidence level).

VI. Conclusions

6.1 Summary of Key Findings

Before discussing key findings of this research effort, the most salient results are briefly summarized.

1. A seven-parameter model was developed enabling MWIR spectra (2500–$7100 \, \mathrm{cm}^{-1}$) of HE detonation fireballs to be fit with residuals on the order of a few percent; model represents the radiative transfer in a homogeneous, non-scattering fireball in local thermodynamic equilibrium

2. Nonlinear regression enables a reduced dimensional representation of fireball spectra in terms of physical parameters that can be used to discriminate the type and size of HEs

   (a) The derived parameter $\mathcal{R} = \mathrm{H{:}C}$ distinguishes TNT and ENE fireballs; observed $\mathcal{R}$ values correspond to thermodynamic expectations based on known stoichiometry of starting materials: TNT 1.13 ± 0.14 meas. versus 0.79 expect., ENE0B 9.2 ± 2.5 versus 21.3, ENE1 4.9 ± 1.5 versus 6.7, ENE2A 4.6 ± 2.6 versus 5.8, and ENE2B 6.5 ± 1.5 versus 6.7.

   (b) Bayesian classification between TNT and ENE fireballs via $\mathcal{R}$ assuming normal distributions for each class resulted in well-separated PDFs. If estimated PDFs are representative of true TNT and ENE PDFs, the decision boundary of $\mathcal{R} = 1.67$ enables a mean probability of error of $P(error) < 0.3\%$. For a 99% probability of detecting ENE, the associated false-alarm probability is less than $10^{-4}\%$. Fisher ratio measuring the separability between these two classes was FR $= 17.4$.

   (c) Presence of an unknown spectral emission at 6539 and $6592 \, \mathrm{cm}^{-1}$ distinguishes the "boosted" ENE1 and ENE2 explosives from the non-"boosted" ENE0 explosive and TNT

   (d) The estimated temperature decay rate k_T and mean fireball size $\bar{r}$ correlate with HE weight W in a power-law form: $k_\mathrm{T} \propto W^b$ with $-0.52 \leq b \leq -0.25$ and $\bar{r} \propto W^b$ with $-0.33 \leq b \leq -0.21$

3. Interpreted spectral data reveals several aspects of fireball phenomenology

   (a) Uncased TNT and ENE charges between 10–$1000 \, \mathrm{kg}$ produce fireballs with a diameter between 450–$2600 \, \mathrm{cm}$

132

(b) Sizes determined from the non-imaging spectral data are consistent with NIR imagery (slight underestimation of imagery results observed for lower HE weight, an effect which may be partially attributed to representing a more spherical fireball by an idealized cubic geometry)

(c) Initial temperatures of TNT fireballs are between 1750–1950 K with a weight-dependent initial decay rate between 0.3–$3\,\mathrm{s}^{-1}$; initial temperatures agree well with reported pyrometry studies

(d) Temperature dynamics of the ENE fireballs can be fit to a single-parameter differential equation motivated by the consideration of only radiative losses. TNT fireballs appear to require both a radiative loss term and a decaying energy source term. The fitted $\hat{k}_{\mathrm{T}}$ capture the power-law weight dependence that was empirically observed.

(e) Average optical depth is dominated by continuum absorption; its decay with time may be the result of soot oxidation; this possible interpretation appears consistent with recently-published temperature-dependent Arrhenius soot oxidation rates

(f) TNT and ENE fireballs consist of H_2O and CO_2 concentrations on the order of $10^{17}\,\mathrm{molec/cm^3}$, HCl concentration near $10^{14}\,\mathrm{molec/cm^3}$, and possible CO concentration near $10^{14}\,\mathrm{molec/cm^3}$; concentrations appear independent of HE weight

(g) Cased conventional military munitions (CMM) spectra dominated by continuum emission

(h) CMM temperatures decay from about 1600–1800 K to ambient in 3–5 s

(i) Emissive area dynamics and apparent selective emission in CMMs provide limited discrimination capability

4. Moderate-resolution spectra ($4\,\mathrm{cm}^{-1}$ resolution) of detonation fireballs lasting 0.8–3 s can be captured by "slow" (8 Hz) FTS with scene-change artifacts that do not impact interpretation of the real component of the spectrum (evidence for SCAs are found in the imaginary component, but, if present in the real component, appear indistinguishable from white-noise and do not hamper the spectral fits)

5. Developed a general-purpose, robust method of decoupling effects of atmospheric attenuation from spectrally-smooth source emission; extracted water and trace-gas concentrations from CMM spectra

are within a few percent of measured and historical concentrations; for uncased TNT and ENE fireballs, absorption from H_2O and CO_2 can be treated as additional model parameters in the event that atmospheric conditions are unknown; comparison of the fitted and well-known CO_2 concentration provides a good estimate of range to fireball

6.2   Concluding Discussion of Key Findings

Prior to embarking upon this research project, the frequency-dependent emissive phenomenology of detonation fireballs was largely unstudied and, apart from the publications of the remote sensing group at AFIT, not reported upon in the literature. At the outset, it was unclear which physical attributes of the reacting fireball were most important in defining its emissive signature. This lack of understanding precluded the confident use of time-resolved spectroscopy as a robust forensic tool for the determination of the underlying HE starting material. As indicated in the introduction, such a forensic tool would be invaluable in aspects of homeland defense. Furthermore, such a capability could improve battle space awareness in both friendly and unfriendly theaters. Fortunately, the fruits of this effort demonstrate that key information about both the type and size of a HE is contained in the time-resolved infrared spectrum. More importantly, a method for extracting this critical information is a product of this work.

This project serves as an important first step towards understanding the key phenomenological aspects of infrared spectral emissions from high explosive detonations. A physically reasonable albeit highly simplified model of a HE fireball was developed. The low-dimensional model enables a high-fidelity description of a single MWIR spectrum in terms of seven physically meaningful parameters: size, temperature, particulate absorption, and four molecular concentrations. With nearly 2400 points between 2500–7100 cm^{-1}, much of the information in a raw fireball spectrum is either redundant or extraneous. The efficient dimensionality reduction afforded by the model is both necessary for and will substantially enhance classification efforts via pattern recognition tools. Moreover, some of the physically meaningful parameters which are extracted from the MWIR spectra are demonstrably useful discriminants. For example, the hydrogen-to-carbon ratio as estimated by fitted concentrations clearly separated TNT from the enhanced novel explosives, and among

134

the ENEs, could distinguish ENE0 from its "boosted" counterparts ENE1 and ENE2. Not only is $\mathcal{R} = $ H:C a useful discriminant, its ability to distinguish TNT from the ENEs is understood in terms of the stoichiometry of the bulk explosives. In addition to demonstrating the physical interpretability of the model parameters, this result builds confidence that the model might also distinguish between other CHNOAl-based HEs which differ in their relative amounts of carbon and hydrogen. Of course, such hopeful yet reasonable expectations should be tested with future field experiments.

Initial temperatures also served to separate the ENE explosives from TNT. ENE fireballs were hotter than TNT fireballs, and the "boosted" ENEs were much hotter than ENE0. Initial TNT temperatures were consistent with optical pyrometry studies, and the higher initial temperatures of the ENE fireballs were consistent with expectations given their aluminum content. The agreement with prior work and theoretical considerations builds confidence in the fireball model proposed in this work.

The most striking feature for distinguishing the "boosted" ENEs from the baseline mixture (ENE0) came in the form of an unidentified emission feature near 6539 and $6592 \, \mathrm{cm}^{-1}$. This feature should be the topic of future study as its understanding is crucial to determining is utility for the ENE classification problem. It is not yet clear whether this feature is due to the bulk properties of ENE1 and ENE2 or whether it indicates the presence of an impurity introduced during the on-site mixing of the HEs. It seems reasonable to expect that the unknown emission is in fact related to some property of the bulk HE. Neither the TNT nor ENE0 explosives featured the emission, and all HE charges were mixed on-sight under similar conditions.

In addition to being able to distinguish different classes of explosives based on extracted spectral information, some evidence has been found that estimating the size of explosives via spectral measurements is also possible. The size of the fireball is a natural fit parameter and was found to correlate with HE weight as expected: bigger HEs produce larger fireballs. In fact, for the larger HEs, the fitted sizes (r) agreed well with size estimates from NIR imagery. The smaller HEs resulted in fitted sizes which were too small, and suggest simple geometrical improvements in the fireball model that might afford improved size estimates. However, anything which leads to errors or unexpected deviations in the apparent intensity will impact the ability to estimate HE size from r. If the radiometry is off by a factor of two, the radius estimate will by wrong by a

factor of $\sqrt{2}$. Other effects which would reduce the apparent intensity measured by remote sensors include obstructions along the line-of-sight and scattering. In the midwave, scattering effects can be ignored. However, it would be both advantageous and straightforward to extend this model to the near infrared. In doing so, the effects of scattering will need to be carefully examined since the photon wavelengths will be on the order of the fireball particulates.

Fortunately, a radiometrically-invariant parameter was found which strongly correlates with HE weight. Fireball temperatures can be measured without a calibrated intensity scale in as few as two bands. The rate at which the fireball temperature decayed varied with HE weight (W). Larger explosives produced fireballs which took longer to cool. This decay rate roughly followed a power-law form of $k_T \propto W^b$ with $-0.52 \leq b \leq -0.25$. This weight scaling is consistent with the interpretation that the fireball cools predominantly by radiative emission at early times. Since temperature can be estimated with a low statistical uncertainty, this observed dependence should be useful in estimating HE weight provided the type of explosive can be ascertained *a priori*, for example via the behavior of $\mathcal{R}$.

The primary focus of this research effort was to develop a model which could be used to extract reproducible, discriminating information from MWIR fireball signatures. In this regard, this research effort has borne much fruit. However, in addition to providing key features for the classification problem, the successful development of a fireball model also yields significant insight into the dominant processes occurring in a detonation fireball. Exploring the physical significance of the temporal aspect of fireball phenomenology–for example, understanding the time-dependent temperature profile—was not a stated goal of this effort. However, a cursory analysis of the time-resolved fit parameters proved too tempting, and some initial thoughts regarding their interpretation are offered to begin a dialogue with the combustion and hydrodynamics communities.

The change in optical depth with time is driven almost entirely by a rapidly decreasing particulate absorption coefficient (κ_p). It is possible that κ_p is connected with the presence of carbonaceous soot in the fireball. In the case of TNT fireballs, the rate at which κ_p decays with time is remarkably consistent with what might be expected given published soot oxidation rates which follow an Arrhenius temperature dependence.

136

However, this conclusion is preliminary and based on a poorly-resolved time scale. It is entirely possible that other explanations exist which are both physically reasonable and consistent with the observed data.

6.3 Roadmap for future efforts

As with the completion of most research projects, a new and more expansive set of questions are uncovered. In the author's view, the two most pertinent and interesting questions are now discussed. First, the steps needed to transition the results of this research project into an operational forensic tool will be explored. Following this, an answer to the question of "how might phenomenological understanding of fireball emissions be improved?" will be discussed. The answer to this question will be provided in the form of an ideal (and incomplete) instrumentation suite along with the expected insight each sensor may provide. It is worth noting that there is a synergy between the avenues taken to answer each of these questions. As phenomenological understanding is improved, additional key features may be found which enable more robust HE classification. Likewise, as classification methodologies are developed, they will indicate which features are the most salient for the discrimination problem, thereby focusing the efforts to understand fireball phenomenology.

6.3.1 How can these results guide the transition to an operational forensic tool?

The purpose of this project was to learn how time-resolved infrared spectra could enable the discrimination of various high explosives, i.e. extracting the HE signature from the signal. Two key signatures are $\mathcal{R}$ for distinguishing HE type and k_{T} for estimating weight. The next step is to develop the operational capability to classify HE type and weight using these features. In this sense, classification is the process of feeding information into a decision-making algorithm (for example, a trained neural network, a Fisher linear discriminator, etc.). These systems are typically trained with truth data, and as new observations are collected, the algorithm can be used to estimate the probability that it was of a particular type. (For a relevant example, refer to Dill's dissertation [29] which discusses the problem of HE discrimination via features derived from imagery.) Of course, for this classification system to be useful dictates that a substantial number of HEs have been examined; if features from an unstudied HE are fed to the algorithm, the results will be, of course, meaningless. Furthermore, to get statistically meaningful confidence bounds from the decision algorithm requires that sample sizes in the truth

data are sufficient to span the natural variance of the individual event types. If an individual event's inherent variability is unknown, the algorithm's reported uncertainty will be of limited utility.

It should be evident from this discussion that a substantial number of future field tests will be needed to provide the appropriate data to train the decision-making algorithms. It should also be clear that a field test like BF2 is not sufficient for meeting these goals with the lack of reproducibility being its largest shortcoming. For reasons of economy, a test plan with carefully stated objectives will be needed. Important questions for developing such a plan include: (1) for which types of HEs is discrimination necessary; (2) what types of *a priori* information will be available; (3) what confidence level associated with the classification algorithm is needed; (4) how many repetitions of a given event type are needed to achieve the desired confidence level[1]; (5) which types of sensors will be or could be available in an operational setting.

The last question about sensors is an important one. The sensor suite used during the Brilliant Flash field tests are not tailored for operational deployment. They are heavy, bulky, and demand much in terms of support (liquid nitrogen, computers, operators and technicians, etc.). However, it is likely that the key features $\mathcal{R}$ and k_T could be extracted from a much simpler and more readily deployable sensor. As an example, consider a multi-channel radiometer, which with some engineering can be made quite small. Two bands in the region of continuum emission could be used to determine the temperature dynamics, and thus k_T. It is also possible that a small number of appropriately chosen bands could enable the determination of $\mathcal{R}$. The fireball model resulting from this project would be important in finding the optimum, minimal set of bandpass filters for this task. Of course, there are readily available spectral sensors with a smaller footprint than the ABB-Bomem system used in this project. As for how to optimally configure a spectral system, additional study could guide the selection of spectral and temporal resolutions since to enhance one the other must be degraded. In Chapter IV, it was found that reducing the spectral resolution increased the SNR, but not enough so that the uncertainty in $\mathcal{R}$ was reduced. However, with increased temporal resolution, additional features relating to the kinetic evolution of detonation fireballs may be found, and such a trade-off may pay off.

---

[1] This question is difficult to answer. As a start, a minimum of 10–15 repetitions should be considered a minimum.

6.3.2   How can the phenomenological understanding of detonation fireballs be improved?   With the development of the fireball model that accurately matches observed HE fireball data, it is natural to want to use this tool for more than its data reduction purposes. The physically meaningful and constrained parameters offer insight into the complex phenomena of the afterburning process. The results presented in Chapter V suggest interpretations of this process which are consistent with the observed data. Future tests are needed to validate these interpretations as well as expand upon them. With an appropriately chosen set of instruments, a rich data set which explores and explains HE fireball phenomena can be collected. Presented now is a "wish-list" of instruments along with a brief, informal list of phenomenological questions those instruments might help answer.

- Imaging FTS — AFIT's Remote Sensing laboratory will acquire the Telops FIRST MW-E imaging spectrometer in the Fall of 2007. This will be the world's fastest midwave imaging FTS built to date. For example, at a rate comparable to the non-imaging FTS used in BF2, the Telops instrument will be able to collect a 128×128 hyperspectral image, with each point consisting of a $16\,\text{cm}^{-1}$ resolution spectrum. This instrument will enable a number of questions to be answered, such as: How homogeneous are detonation fireballs? Is there an easily describable temperature and/or concentration gradient, for example one with a smooth radial dependence? Or are there stochastically-distributed regions with different temperatures and compositions? Are there important edge effects besides those already attributed to a difference in optical path length? For example, is there evidence of reactive chemistry occurring at the turbulent boundary layer? How do fluid dynamics issues affect the spectral signature? (This will be somewhat difficult to answer with this instrument because the frame rates are still slow compared to the fluids time scales.) Why does the highly-simplified homogeneous assumption result in a model which matches non-imaging FTS spectra so well?

- Visible spectrometer — Grating-based instruments are inexpensive and can provide adequate temporal and spectral resolution in the visible spectrum. Although more expensive, FTS instruments are now available which can collect high SNR spectra in the visible as well. Visible spectroscopy is important for answering the following questions. Can metalized and non-metalized explosives be distinguished

on the basis of metal oxide emissions in the visible regime? How does aluminum oxidation affect the kinetics of water and carbon-dioxide production in aluminized explosives such as the ENEs? Is there evidence for continuum emission in the visible? If so, how important is scattering in this spectral region? Does the visible temperature match the MWIR temperature?

- Faster non-imaging FTS — AFIT has acquired an ABB-Bomem MR-254 spectrometer. It is capable of collecting $4\,\mathrm{cm}^{-1}$ resolution spectra at $38\,\mathrm{Hz}$, a nearly $4\times$ improvement over the MR-154 used in the BF2 test. With faster acquisition rates, answers to following questions will likely be found in the data. What will the time-resolved fit parameters look like with improved temporal resolution, particularly early on? Can a reasonable mathematical model be developed for the observed kinetics of H_2O and CO_2?

- Banded radiometers — Simple radiometers can be operated at temporal rates of kilohertz to megahertz thereby providing a highly-resolved look at the initial kinetic behavior of detonation fireballs. Extremely high acquisition rates enable an investigation of the initial detonation process and also provide a method of testing filter combinations which enable $\mathcal{R}$ to be measured without spectral instrumentation. Examples of interesting questions to which radiometric data would help answer include: What are the timescales of combustion? At what point does combustion end and why? Can appropriately chosen bandpass filters be used to study the kinetics H_2O and CO_2? With a highly-resolved temperature profile, is it possible to infer the degree to which combustion processes are ongoing?

- High-speed visible and infrared imagery — the remote sensing lab has recently acquired two Phantom high-speed visible cameras which can frame at rates approaching $100,000$ pictures per second. The Telops imaging FTS can be run in an image-only mode with frame rates near $10,000$ pictures per second. Imagery serves as an important tool to understanding the fluid dynamics of fireballs and the hydrodynamic influences on remotely-sensed spectra. High-speed imagery in multiple bands will be beneficial in answering the following questions. What can be learned about the fluid dynamics? What is the "size" of the fireball as a function of observation wavelength? Is there a radial temperature dependence? When does the shock wave separate from the luminous fireball? What balancing forces

keep the fireball at the size that it is? How important is turbulent mixing on the reactive chemistry? What does the temperature field look like and why?

Reducing the data collected by these instruments is a formidable task, and the proper interpretation of this wealth of information could serve as the subject of several dissertations. In the author's opinion, continuing this research effort is worthwhile. First, this dissertation provides a framework for understanding of HE fireball emission thereby setting the stage for future scientific inquiry into this largely unstudied topic. And more pragmatically, the positive results of this work strongly suggest that the future efforts outlined above will pay dividends in the form of enhanced operational capabilities, impacting each of the homeland security, department of defense, and intelligence communities.

Appendix A. Atmospheric Correction Assuming a Smoothy Varying Source Spectrum

Many remote sensing problems pose the challenge of interpreting the spectral signature from an unknown or uncharacterized source when its signal has been attenuated by an atmosphere whose state is imprecisely known. In this appendix, a novel method is developed which decouples the atmospheric correction problem from the spectral and temporal characterization of the detonation fireball. Prior to beginning, however, it should be noted that the method has not been fully vetted by laboratory experiments nor has the algorithm been completely characterized. It was developed in response to initially not having access to weather data that was collected during the Radiant Brass III field test. In the end, this technique proved unnecessary as access to the atmospheric data was eventually provided. However, the ability to decouple the effects of atmospheric absorption from source emission is a general problem in remote sensing, and the method developed here may be desirable when accurate weather data is unavailable. An initial characterization of the detonation fireball spectra suggested that they were dominated by continuum-like emission. This in turn indicated that it may be possible to leverage this knowledge to de-tangle the effects of spectrally-sharp atmospheric absorption features from the spectrally-smooth source. The method assumes that the source intensity $I_{src}(\tilde{v}, t)$ is predominantly broadband in nature and its variation with $\tilde{v}$ is much more gradual than the atmospheric absorption features found in the observed spectrum $I_{obs}(\tilde{v}, t)$. It does not, however, assume a particular functional form for I_{src}.

The observed intensity is the convolution of the attenuated source with the instrument response,

$$I_{obs}(\tilde{v}, t) = \int_0^\infty \hat{T}_i(\tilde{v}') \prod_{j \neq i} \hat{T}_j(\tilde{v}') \, I_{src}(\tilde{v}', t) \, \text{ILS}(\tilde{v} - \tilde{v}') \, d\tilde{v}' \tag{50}$$

where $\hat{T}_i$ denotes the high-resolution transmittance function for the ith atmospheric constituent, the $\hat{T}_j$'s represent the high-resolution transmittance functions for the remaining atmospheric species, and ILS is the instrument lineshape function. With the assumption that $I_{src}(\tilde{v}, t)$ varies slowly with $\tilde{v}$, it can be pulled out of the integral. We can then express the observed intensity as

$$I_{obs}(\tilde{v}, t) = T_i(\tilde{v}) \, T_{j \neq i}(\tilde{v}) \, T_f(\tilde{v}) \, I_{src}(\tilde{v}, t) \tag{51}$$

where T_i is the low-resolution transmission function for constituent i (e.g. $i \Leftrightarrow H_2O$),

$$T_i(\tilde{\nu}) = \int_0^\infty \hat{T}(\tilde{\nu}') \, \text{ILS}(\tilde{\nu} - \tilde{\nu}') \, d\tilde{\nu}'$$

$T_{j \neq i}$ is the product of low-resolution transmission functions for the remaining constituents (e.g., $j \Leftrightarrow CO_2$, CH_4, N_2O, etc.),

$$T_{j \neq i}(\tilde{\nu}) = \int_0^\infty \prod_{j \neq i} \hat{T}_j(\tilde{\nu}') \, \text{ILS}(\tilde{\nu} - \tilde{\nu}') \, d\tilde{\nu}'$$

and T_f is a fix-up term given by

$$T_f(\tilde{\nu}) = \frac{T(\tilde{\nu})}{T_i(\tilde{\nu}) \, T_{j \neq i}(\tilde{\nu})}$$

with T representing the low-resolution transmittance function for the atmosphere (which includes attenuation from all absorbing species), i.e.,

$$T(\tilde{\nu}) = \int_0^\infty \prod_k \hat{T}_k(\tilde{\nu}') \, \text{ILS}(\tilde{\nu} - \tilde{\nu}') \, d\tilde{\nu}'$$

The fix-up term is needed because the convolution of a product of functions does not equal the product of individually-convolved functions. Typically, T_f is near one except in spectral regions in which substantial overlap of absorption lines exists between the ith and remaining species. Equation 51 is mathematically equivalent to $I_{obs}(\tilde{\nu}) = T(\tilde{\nu}) \, I_{src}(\tilde{\nu})$. For a pair of frequencies $(\tilde{\nu}_1, \tilde{\nu}_2)$, the ratio of Equation 51 can be expressed as

$$\overline{I}_{obs} = \overline{T}_i \, \overline{T}_{j \neq i} \, \overline{T}_f \, \overline{I}_{src} \tag{52}$$

where the bar denotes the ratio of terms, for example $\overline{I}_{obs} = I_{obs}(\tilde{\nu}_1, t) / I_{obs}(\tilde{\nu}_2, t)$.

An iterative method based on Equation 52 has been developed which allows for the estimation of atmospheric absorber concentrations from the observed spectrum. The method is based selecting closely-spaced frequency pairs associated with the peaks and valleys of sharp absorption features. For appropriately selected frequency pairs, the source ratio term $\overline{I}_{src}$ is near unity and concentration of the ith absorber can

be adjusted to minimize the error in Equation 52. Furthermore, while the influence of I_{src} on Equation 52 can be made small by the choice of frequency pairs, its effect can be estimated by defining $I_{src}(\tilde{\nu}, t) = \mathcal{F}\{I_{obs}(\tilde{\nu}, t)/T(\tilde{\nu})\}$, where $\mathcal{F}$ indicates the application of a smoothing filter. Starting from a guess of the atmospheric constituent concentrations, Equation 52 is used in conjunction with a large number of appropriate frequency pairs to estimate the concentration of the most prominent absorber, H_2O. With this improved estimate of the water concentration, Equation 52 is then reformulated for CO_2, the next most important absorber, and its concentration is estimated using appropriately chosen frequency pairs. In the same fashion, CH_4 and N_2O concentrations are also estimated. This process is then repeated until the relative change in concentrations between iterations is less than 10^{-3}. Typically only three iterations are needed. Details about the algorithm are now presented.

For the atmospheric constituent of interest, a set of all possible frequency pairs satisfying the following criteria was generated:

- $|\tilde{\nu}_2 - \tilde{\nu}_1| = n\,\delta\tilde{\nu}$, where $\delta\tilde{\nu}$ is half of the instrument resolution (usually $8\,\mathrm{cm}^{-1}$) and $n = 1, 2, ...5$

- $\left|1 - \overline{T}_i\right| > 10^{-2}$ to ensure that frequency pairs correspond to absorption features and not flat regions of the transmission spectrum

- $T(\tilde{\nu}_1) > 10^{-2}$ and $T(\tilde{\nu}_2) > 10^{-2}$ to remove opaque regions of the spectra from this analysis

- The SNR for both $I_{obs}(\tilde{\nu}_1, t)$ and $I_{obs}(\tilde{\nu}_2, t)$ is greater than 10

The $\overline{I}_{src}$ terms were based on an estimate of $I_{src}(\tilde{\nu}, t)$, which was computed by applying a robust LOESS algorithm [20] to $I_{obs}(\tilde{\nu}, t)/T(\tilde{\nu})$ in regions where $T(\tilde{\nu}) > 10^{-2}$ using a $500\,\mathrm{cm}^{-1}$ window. The ratios for each term in Equation 52 were computed using all detonation fireball spectra [1] so that a single concentration for H_2O, CO_2, CH_4, and N_2O was determined for each data cube. As discussed below, the detonation fireballs behaved as Planckian radiators with a small amount of structured non-Planckian emission. Frequency pairs picked from spectral regions containing this structured emission produced large outliers for Equation 52. Because the number of outliers was small, the concentration of each absorber was determined

---

[1] After about 100 frames, few frequency pairs could be found satisfying the SNR constraint.

using a robust fitting procedure. The difference between the left- and right-hand sides of Equation 52 were weighted according to the bisquare method. The sum-squared-error of this weighted difference was minimized by adjusting the concentration of the ith absorber. The transmittance functions were computed using the Line-by-Line Radiative Transfer Model [21]. The transmittance function used to start the iterative process was based on the Mid-latitude Winter standard atmosphere described in the Infrared Handbook [108].

Results from this atmospheric inversion method are provided in Table 14 for the RB3 conventional munitions detonations collected by the FTS at $16\,\text{cm}^{-1}$ resolution. As expected, water concentrations varied throughout each day. The remaining trace gases were stable with standard deviations about 2-3% of the average value. The extracted concentrations for the trace-gases were comparable to accepted values reported in the literature [56, 59, 61]. The measured water concentrations were estimated from the weather data collected on site. The station pressure (P), temperature (T), and wet-bulb temperature (Tw) were used to estimate the water-vapor mixing ratio. Spectrally-extracted water concentrations were always slightly higher than the values computed from P, T, and Tw.

Good agreement between extracted trace-gas concentrations (H_2O, CO_2, CH_4, and N_2O) and their historical averages was found. Spectral estimates of H_2O agreed well with meteorological data collected on-site. This reasonable agreement between expected and spectrally-derived concentrations suggests that the presented method can be used to decouple the effects of atmospheric attenuation from fireball source emissions. The only characteristic about the fireball source emissions used in this method was its observed variation with frequency that was much "slower" than the atmospheric transmittance function. Thus, this technique is expected to work with other spectrally smooth sources. In the event that the event distance is unknown, it is reasonable to expect that this technique might be used to estimate target range since trace-gas concentrations are stable and known.

Table 14: Concentrations of several species with prominent midwave infrared absorption profiles computed from the statically detonated fireball spectra. Mean and standard deviations were not computed for H_2O as it varied throughout the day. For comparison, recorded atmospheric variables (station pressure P, temperature T, and wet-bulb temperature Tw) were used to determine the water vapor content for comparison.

Time (GMT)	[H$_2$O] ppm	[CO$_2$] ppm	[CH$_4$] ppm	[N$_2$O] ppb	P (atm)	T (C)	Tw (C)	[H$_2$O][c] ppm	[H$_2$O][d] err
26-Oct-99 07:01	2338	372	1.63	302	0.873	6.0	0.0	2183	1860-2509
26-Oct-99 07:25	2479	368	1.61	288	0.873	6.0	-0.5	1550	1230-1872
26-Oct-99 08:15	2352	378	1.59	296	0.873	7.0	0.0	1395	1074-1722
26-Oct-99 08:37	2240	371	1.57	285	0.873	4.0	-2.0	1266	957-1580
26-Oct-99 09:00	2264	369	1.55	291	0.873	4.0	-2.0	1266	957-1580
26-Oct-99 09:20	3089	364	1.58	297	0.873	4.0	-2.0	1266	957-1580
26-Oct-99 09:40	4243	355	1.56	289	0.873	3.5	-2.0	1657	1347-1972
26-Oct-99 10:18	3885	362	1.54	283	0.873	3.5	-1.0	2886	2569-3206
30-Oct-99 05:00	4602	377	1.54	286	0.876	8.5	2.5	3487	3170-3855
30-Oct-99 07:47	4660	384	1.50	293	0.877	4.0	0.0	3725	3432-4082
30-Oct-99 09:39	4559	365	1.56	305	0.878	2.0	-1.0	4030	3745-4383
30-Oct-99 09:59	4593	370	1.57	298	0.878	1.5	-1.5	3803	3520-4152
30-Oct-99 10:32	4649	368	1.50	280	0.878	0.5	-2.0	3972	3693-4320
mean (stdev)	—	369 (8)	1.56 (0.04)	292 (8)	—	—	—	—	—
historical avg	0 - 2.5%	365[a]	1.75[b]	314[b]	—	—	—	0 - 2.5%	—

[a] Mean October 1999 value from Mauna Loa observatory in Hawaii

[b] 1998 values as reported in the 2001 IPCC Climate Change Report

[c] Value estimated from station pressure (P), temperature (T), and wet-bulb temperature (Tw)

[d] Error calculated assuming a ±0.25 C uncertainty in both T and Tw, each of which were reported in 0.5 C increments

Appendix B. Radiative Transfer in a Spherical, Homogeneous Fireball

Observed fireball spectra can be described surprisingly well as if the emission was from a homogeneous, non-scattering cube of combustion gases and particulates in local thermodynamic equilibrium (LTE). Not surprisingly, imagery indicates that real fireballs are more sphere-like in their geometrical appearance. It was found that size estimates from the cubic model tended to underestimate the imagery results for small HE charges. A possible explanation is that the tapering of optical depth near the fireball edges is reducing those regions net contribution to the apparent intensity. To account for this possibility, a highly simplified yet geometrically more accurate radiative transfer equation is developed. The temperature and matter fields are still taken to be homogeneous ($T \neq T(s)$ and $\kappa_{\tilde{\nu}} \neq \kappa_{\tilde{\nu}}(s)$), and scattering is still ignored ($\beta_{\tilde{\nu}} = 0$). However, now the fireball will be treated as a sphere. The integral appearing in the radiative transfer equation (Equation 18) is trivial in a homogeneous, non-scattering environment. Expressing the result here for convenience, the radiance along a line of sight s through an optical medium can be written as

$$L_{\tilde{\nu}}(s) = L_{\tilde{\nu}}(0) \, e^{-\kappa_{\tilde{\nu}} s} + \left(1 - e^{-\kappa_{\tilde{\nu}} s}\right) B_{\tilde{\nu}}(T) \tag{53}$$

where optical depth has been expanded, i.e. $\tau_{\tilde{\nu}} = \kappa_{\tilde{\nu}} s$.

The irradiance $F_{\tilde{\nu}}$ reaching the detector is determined by integrating L over the differential solid angle $d\Omega = dA/R^2$ of the spherical fireball. To do this, the differential area dA is expressed in terms of the impact parameter r', i.e. $dA = 2\pi r' dr'$ (see Figure 60), leading to

$$F_{\tilde{\nu}} = T_{atm}(\tilde{\nu}) \int L_{\tilde{\nu}} \, d\Omega \simeq T_{atm}(\tilde{\nu}) \frac{2\pi}{R^2} \int_0^r L_{\tilde{\nu}} \left(s(r')\right) \, r' \, dr' \tag{54}$$

Here r is the fireball radius and R is the distance between the fireball and instrument. (It is assumed that $r \ll R$, so the distance traversed by photons emitted from any part of the spherical surface is essentially just R, allowing it to be pulled out of the integral.) The pathlength s through the sphere at the impact parameter r' can be expressed in terms of the fireball radius as $s(r') = 2\sqrt{r^2 - r'^2}$. Assuming the background radiance is negligible ($L_{\tilde{\nu}}(0) \simeq 0$) and performing the integral in Equation 54 results in the following expression for

147

$$\theta = \sin^{-1}\left(r'/r\right)$$

$$\cos\left(\sin^{-1}(x)\right) = \sqrt{1 - x^2}$$

$$s = 2r\cos\theta$$

$$= 2\sqrt{r^2 - r'^2}$$
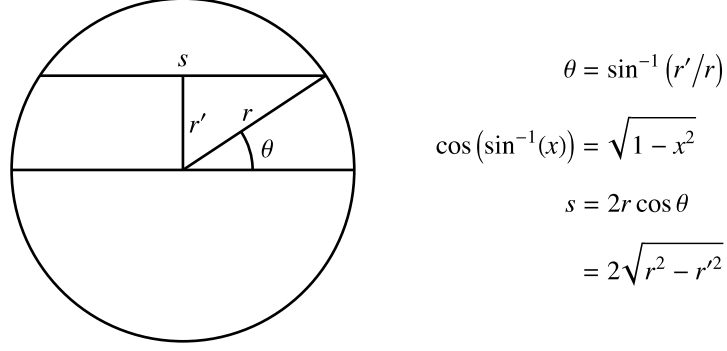
Figure 60:   Slice through an ideal spherical fireball of radius r. The impact parameter, r', is the perpendicular distance between the center of the fireball and the instantaneous line-of-sight being considered in the radiative transfer equation. At an impact parameter of r', the length of the instantaneous line-of-sight can be expressed as $s = 2\sqrt{r^2 - r'^2}$.

irradiance

$$F_{\tilde{v}} = T_{atm}(\tilde{v})\, \frac{A}{R^2}\varepsilon_{\tilde{v}}(r)\; B_{\tilde{v}}(\mathrm{T}) \tag{55}$$

where $A = \pi r^2$ is the projected area of the sphere and the effective emissivity $\varepsilon_{\tilde{v}}(r)$ has the form

$$\varepsilon_{\tilde{v}}(r) = 1 + \frac{e^{-2\kappa_{\tilde{v}}r}}{\kappa_{\tilde{v}}r} + \frac{e^{-2\kappa_{\tilde{v}}r} - 1}{2\left(\kappa_{\tilde{v}}r\right)^2} \tag{56}$$

For convenience, the fireball can be treated as a point source leading to an expression for intensity given by

$$I_{mdl} = R^2\, F_{\tilde{v}}.$$

148

Appendix C. Approximate Model for a Non-Homogeneous Fireball

Modeling detonation fireballs as perfectly homogeneous works surprisingly well considering the likelihood of heterogeneity in a real fireball. Systematic underestimation of the observed intensity at $\tilde{v} < 2500\,\mathrm{cm}^{-1}$ evidenced by large fit residuals was noted in Chapter IV. These errors may be the result of a distribution of temperatures across the fireball. In Chapter V, evidence is presented that fireball cooling is dominated by radiative emission, and the initially large optical depths indicate that early on, this cooling process will be near the surface of the fireball. (The center parts of the fireball don't participate in cooling because most photons emitted internally will be re-absorbed.) It is also possible that chemistry at the fireball edges is enhanced by its proximity to the surrounding cool, oxygen-rich environment, leading to a different composition of gaseous and particulate matter in this region. Assuming a spherical fireball which cools at the surface and ignoring turbulent effects, it is possible that the resultant temperature and matter fields would obtain a radial dependence as indicated in Figure 61. Keeping with the cubic geometry which greatly simplifies the radiative transfer, a two-zone approximation to this radial dependence is also provided. Working through the radiative transfer results in the following functional form for apparent intensity:

$$I_{mdl}(\tilde{v}) = T_{atm}(\tilde{v}) \left(A_1 L_1(\tilde{v}) + A_2 L_2(\tilde{v}) \right) \tag{57}$$

where the individual radiance L_1 and L_2 correspond to the two distinct pathways (parallel with the distant collection optic) through the cube, weighted by the projected area $A_1 = l_1^2$ and $A_2 = l_2^2 - l_1^2$. In terms of the distinct temperatures T_i, transmittances T_i, and emissivities $\varepsilon_i = 1 - T_i$, each radiance term is given by

$$L_1 = T_1 \left(T_1 \varepsilon_2 B(\mathrm{T}_2) + \varepsilon_1 B(\mathrm{T}_1) \right) + \varepsilon_2 B(\mathrm{T}_2) \tag{58}$$

$$L_2 = \varepsilon_3 B(\mathrm{T}_2) \tag{59}$$

This more complicated form enables the model to account for, in a highly approximate way, the effects of a temperature gradient. The effects of HCl were ignored leading to twelve distinct fit parameters: two

149
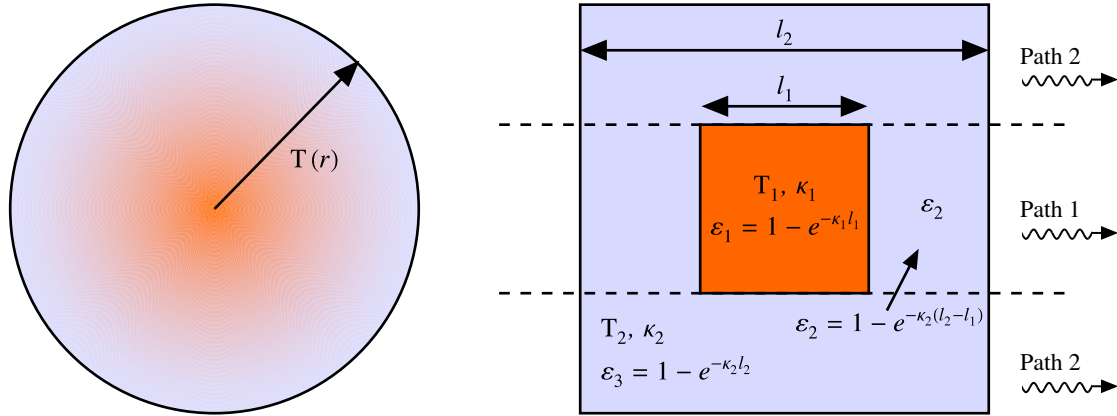
Figure 61:   Illustration of a radial temperature distribution in a spherical fireball and its approximation by two cubic regions. Solving the radiative transfer equation for a remote optic perpendicular to the right side of this cube requires the consideration of two distinct photon pathways denoted Path 1 and Path 2.

fireball dimensions, two temperatures, two particulate absorption coefficients, and individual H_2O, CO_2 and CO concentrations in each region. As demonstrated in Figure 62, fitting this model to all wavelengths of the same 50 kg TNT spectrum presented in Figure 21 of Chapter IV enables the longer wavelength region to be better represented. For comparison, the residuals from this fit are compared with the residuals obtained with the homogeneous model for fits to both all frequencies and those satisfying $\tilde{\nu} > 2500\,\mathrm{cm}^{-1}$. Considering wavenumbers greater than $2500\,\mathrm{cm}^{-1}$, this model performs slightly better than the homogeneous model fitted to $\tilde{\nu} > 2500\,\mathrm{cm}^{-1}$ (SE of 2.43 versus 2.49).

The dimensionality is increased by ~15% in going from $\tilde{\nu} > 2500$ to all frequencies. With the addition of four extra parameters, it is neither surprising that the fit quality is improved nor is it strong evidence that a spatial distribution in the temperature and matter fields are responsible for the long-wavelength behavior. Rather, the purpose of this exercise is to demonstrate that such a distribution *may* be responsible for the inability of the homogeneous model to perform well between 4–4.5 μm. A real test of this idea can be made when the BF2 data from the MCT detector is properly post-calibrated.

Now if there does exist a temperature and matter distribution by which Equation 57 is a reasonable approximation, then this analysis does indicate that the neglect of longer wavelengths in Chapter IV is some-what justified. This can be seen by considering ε_2 in the bottom panel of Figure 62. First, the emission from Path 2 only strongly contributes at the longer wavelengths. At wavenumbers greater than $2500\,\mathrm{cm}^{-1}$ and in
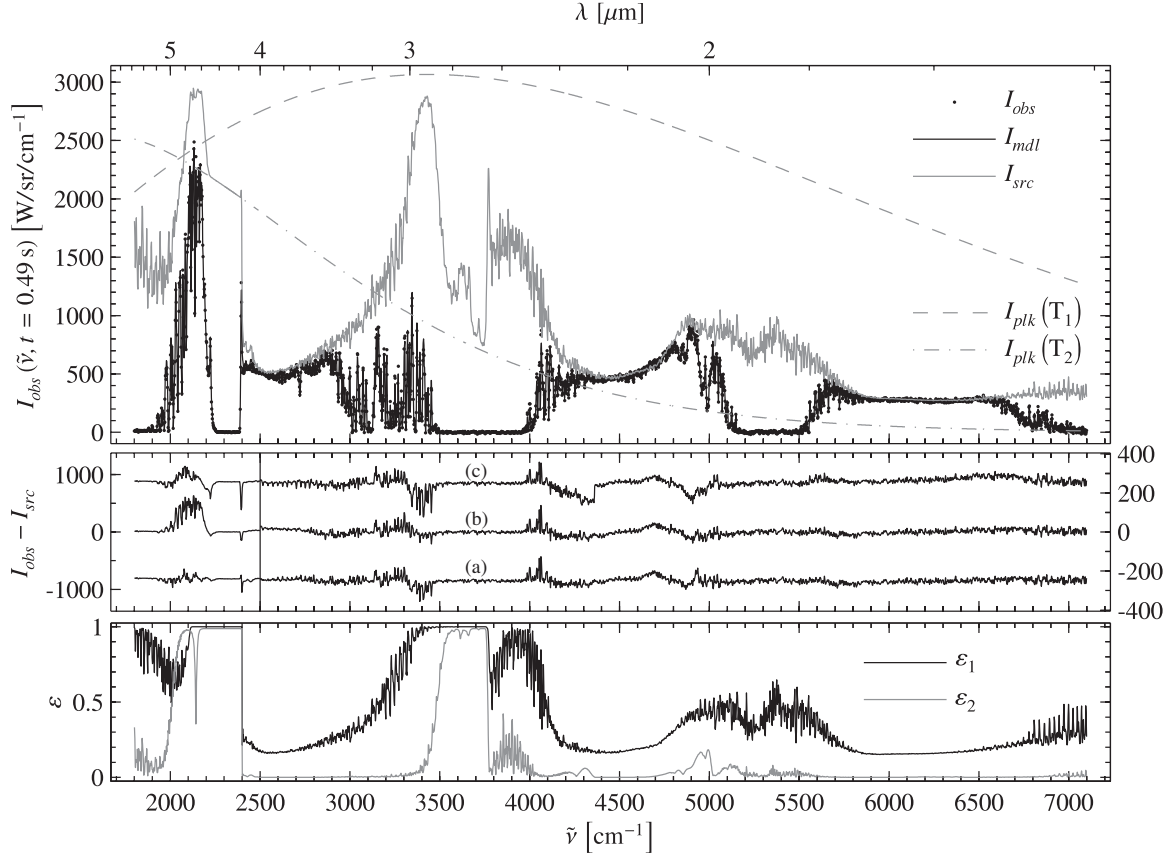
Figure 62: *Top panel*: Observed fireball spectrum (·) at $t = 0.49\,\text{s}$ from a 50 kg TNT detonation compared with the best two-temperature, eleven-parameter model (solid black). The estimated at-source spectrum is provided (solid grey) along with the Planckian intensity distribution for each temperature (dashed grey). *Middle panel*: Three sets of residuals from (a) this model, (b) the seven-parameter model fitted to $\tilde{\nu} > 2500\,\text{cm}^{-1}$, and (c) the seven-parameter model fitted to all frequencies. The left ordinate is used for $\tilde{\nu} < 2500\,\text{cm}^{-1}$ and the right ordinate corresponds to $\tilde{\nu} \geq 2500\,\text{cm}^{-1}$. *Bottom panel*: Estimated emissivity profiles for the distinct regions along Path 1.

the transparent regions of the atmosphere, ε_2 is small. The lower-temperature Planckian term is also rapidly decreasing with $\tilde{\nu}$ in this region. Furthermore, since the emissive term is small at shorter wavelengths, the effects of self-absorption—which are ignored in the homogeneous assumption—will also be small.

Since only one spectrum was fit with this model, it seems unwise to offer any interpretation of the optimized fit parameters. For completeness, they are recorded in the following table. However, it is worth noting that the CO concentration is negligible in the fireball core, and has a large presence in the cooler surrounding shell. This does seem puzzling given that oxygen availability is expected to be enhanced where the fireball meets the surrounding atmosphere. Perhaps it is an indicator that the CO parameter is serving as a proxy for another emitter in the 2000–2200 cm^{-1} region.

	l_i/m	T_i/K	$\kappa_{p,i}/\mu\mathrm{m}$	$\xi_{\mathrm{H_2O},i}/10^{17}\,\frac{\mathrm{molec}}{\mathrm{cm^3}}$	$\xi_{\mathrm{CO_2},i}/10^{17}\,\frac{\mathrm{molec}}{\mathrm{cm^3}}$	$\xi_{\mathrm{CO},i}/10^{15}\,\frac{\mathrm{molec}}{\mathrm{cm^3}}$
Inner cube	10.0	1752	161	2.5	4.9	3.5
Outer cube	28.9	813	14	0.1	4.5	86

Appendix D. Rules for Estimating Detonation By-Products

Given a particular high explosive, predicting the by-products of its detonation is a formidable task. The detonation conditions (pressure, temperature, charge geometry, etc.) all influence the reaction pathways taken in this extreme oxidative decomposition. During World War II, Kistiakowsky and Wilson (K-W) developed some rules-of-thumb to predict the detonation products of CHNO-explosives based on empirical observation and thermodynamic considerations [2]. The following K-W rules apply to explosives with an oxygen balance[1] of −40% or greater.

1. Carbon atoms are converted to carbon monoxide $C \rightarrow CO$

2. If any oxygen remains, then hydrogen is oxidized to water ($H \rightarrow H_2O$)

3. If any oxygen remains, then carbon monoxide is oxidized to carbon dioxide ($CO \rightarrow CO_2$)

4. All the nitrogen is converted to nitrogen gas (N_2)

For explosives with a larger negative oxygen balance (i.e., are more oxygen deficient), the modified K-W rules are to be used:

1. Hydrogen atoms are converted to water $H \rightarrow H_2O$

2. If any oxygen remains, then carbon is oxidized to carbon monoxide ($C \rightarrow CO$)

3. If any oxygen remains, then carbon monoxide is oxidized to carbon dioxide ($CO \rightarrow CO_2$)

4. All the nitrogen is converted to nitrogen gas (N_2)

Cooper [22] appends to the modified K-W rules that when the explosive contains nitrogen, a small amount of NO_x will be formed.

To illustrate with an example, the detonation decomposition of TNT with an oxygen balance of −74% would, according to the modified K-W rules proceed via

$$C_7H_5N_3O_6 \rightarrow 3.5\,CO + 3.5\,C + 2.5\,H_2O + 1.5\,N_2 \tag{60}$$

---

[1]Oxygen balance is the weight percent of oxygen liberated upon complete decomposition of the high explosive. For example, TNT ($C_7H_5N_3O_6$) has a molecular weight of 227 g/mol and an oxygen balance of −74%.

Bibliography

1. Adachi, Masayuki. "Emission measurement technique for advanced powertrains". *Measurement Science and Technology*, 11:R113–R129, 2000.

2. Akhavan, Jacqueline. *The Chemistry of Explosives*. Royal Society of Chemistry, Cambridge, UK, 1998.

3. Arrigone, Giovanni M. and Moira Hilton. "Theory and practice in using Fourier transform infrared spectroscopy to detect hydrocarbons in emissions from gas turbine engines". *Fuel*, 84:1052–1058, 2005.

4. Bagby, W. F. *Spectral and temporal characterization of high-temperature event*. Master's thesis, Air Force Institute of Technology, AFIT/GAP/ENP/01M-01, 2001.

5. Barlow, Robert S. "Laser diagnostics and their interplay with computations to understand turbulent combustion". *Proceedings of the Combustion Institute*, 31:49–71, 2007.

6. Baulch, D. L., C. J. Cobos, R. A. Cox, P. Frank, G. Hayman, T. Just, J. A. Kerr, T. Murrells, M. J. Pilling, J. Troe, R. W. Walker, and J. Warnatz. "Evaluated Kinetic Data For Combustion Modeling Supplement-I". *Journal Of Physical And Chemical Reference Data*, 23(6):847–1033, 1994.

7. Bazyn, Tim, Herman Krier, and Nick Glumac. "Evidence for the transition from the diffusion-limit in aluminum particle combustion". *Proceedings of the Combustion Institute*, 31:2021–2028, 2007.

8. Beckstead, Merrill W., Karthik Puduppakkam, Piyush Thakre, and Vigor Yang. "Modeling of combustion and ignition of solid-propellant ingredients". *Progress in Energy and Combustion Science*, in press (doi:10.1016/j.pecs.2007.02.003), 2007.

9. Beer, Reinhard. *Remote Sensing by Fourier Transform Spectrometry*. Wiley-Interscience, New York, 1992.

10. Bell, John R. *Introductory Fourier Transform Spectroscopy*. Academic Press, New York, 1972.

11. Bendtsen, Anders Broe, Peter Glarborg, and Kim Dam-Johansen. "Chemometric analysis of a detailed chemical reaction mechanism for methane oxidation". *Chemometrics and Intelligent Laboratory Systems*, 44:353–361, 1998.

12. Berden, Giel, Rudy Peeters, and Gerard Meijer. "Cavity ring-down spectroscopy: Experimental schemes and applications". *International Reviews in Physical Chemistry*, 19(4):565–607, 2000.

13. Bhattacharjee, S. and W. L. Grosshandler. "Effect Of Radiative Heat-Transfer on Combustion-Chamber Flows". *Combustion and Flame*, 3–4:347–357, 1989.

14. Bohm-Vitense, Erika. *Introduction to Stellar Astrophysics*. Cambridge University Press, 1989.

15. Chandrasekhar, S. *Radiative Transfer*. Oxford University Press, 1950.

16. Chase, M. W. (editor). *NIST-JANAF Thermochemical Tables (Journal of Physical and Chemical Reference Data)*. Springer-Verlag, New York, 2000.

17. Chen, P. W., F. L. Huang, and S. R. Yun. "Characterization of the condensed carbon in detonation soot". *Carbon*, 41(11):2093–2099, 2003.

18. Chung, T. J. *Computational Fluid Dynamics*. Cambridge University Press, 2002.

19. Clausen, Sønnik and Jimmy Bak. "Infrared low resolution emission spectroscopy of hot gases". *Proceedings of SPIE*, 3383:133–139, 1998.

20. Cleveland, W. S. "Robust Locally Weighted Regression and Smoothing Scatterplots". *Journal of the American Statistical Association*, 74:829–836, 1979.

21. Clough, S.A., M.W. Shephard, E.J. Mlawer, J.S. Delamere, M.J. Iacono, K. Cady-Pereira, S. Boukabara, and P.D. Brown. "Atmospheric radiative transfer modeling: A summary of the AER codes". *Journal of Quantitative Spectroscopy & Radiative Transfer*, 91(2):233–244, 2005.

22. Cooper, Paul W. *Explosives Engineering*. VCH Publishers, New York, New York, 1996.

23. Crow, Dennis, Charles Coker, and Wayne Keen. "Fast Line-of-sight Imagery for Target and Exhaust-plume Signatures (FLITES) scene generation program". *Proceedings of SPIE*, 6208, 2006.

24. Crow, Dennis, Fred Hawes, Matt Braunstein, Charles Coker, and Thomas Smith. "Scalable hardbody and plume optical signatures". *Proceedings of SPIE*, 5408:1–8, 2004.

25. Daily, John W. "Laser Induced Fluorescence Spectroscopy In Flames". *Progress in Energy and Combustion Science*, 23:133–199, 1997.

26. Dereniak, Eustace L. and Glenn D. Boreman. *Infrared Detectors and Systems*. Wiley-Interscience, 1996.

27. Derzy, Igor, Vladimir A. Lozovsky, and Sergey Cheskis. "Absolute CH concentration in flames measured by cavity ring-down spectroscopy". *Chemical Physics Letters*, 306:319–324, 1999.

28. Deshmukh, K. V., D. C. Haworth, and Michael F. Modest. "Direct numerical simulation of turbulence–radiation interactions in homogeneous nonpremixed combustion systems". *Proceedings of the Combustion Institute*, 31:1641–1648, 2007.

29. Dills, Anthony N. *Classification of battle space detonations from temporally-resolved multi-band imagery and mid-infrared spectra*. Ph. D. dissertation, AFIT/DS/ENP/04-2, Air Force Institute of Technology, 2005.

30. Dills, Anthony N., Kevin C. Gross, and Glen P. Perram. "Detonation discrimination techniques using a Fourier transform infrared spectrometer system and a near-infrared focal plane array". *Proceedings of SPIE*, 5075:208–216, 2003.

31. Dills, Anthony N. and Glen P. Perram. *Brilliant Flash II Preliminary Test Report: AFIT FTIR and Imaging Sensors*. Technical report, Air Force Institute of Technology, Wright-Patterson AFB, OH, 2003.

32. Dills, Anthony N., Glen P. Perram, and Steven C. Gustafson. "Detonation discrimination techniques using a near-infrared focal plane array and a visible CCD camera". *Proceedings of SPIE*, 5431:77–86, 2004.

33. Drake, M. C. and D. C. Haworth. "Advanced gasoline engine development using optical diagnostics and numerical modeling". *Proceedings of the Combustion Institute*, 31:99–124, 2007.

34. Dreizin, Edward L. "Experimental Study of Stages in Aluminum Particle Combustion in Air". *Combustion and Flame*, 105:541–556, 1996.

35. Duda, Richard O., Peter E. Hart, and David G. Stork. *Pattern Classification*. John Wiley & Sons, Inc., New York, 2001.

36. Ferioli, F., P. V. Puzinauskas, and S. G. Buckley. "Laser-Induced Breakdown Spectroscopy for On-Line Engine Equivalence Ratio Measurements". *Applied Spectroscopy*, 57:1183–1189, 2003.

37. Ferioli, Francesco and Steven G. Buckley. "Measurements of hydrocarbons using laser-induced breakdown spectroscopy". *Combustion and Flame*, 144:435–447, 2006.

38. Fickett, Wildon and William C. Davis. *Detonation: Theory and Experiment*. University of California Press, Berkley, California, 1979.

39. Fitch, Michael J., Megan R. Leahy-Hoppa, Edward W. Ott, and Robert Osiander. "Molecular absorption cross-section and absolute absorptivity in the THz frequency range for the explosives TNT, RDX, HMX, and PETN". *Chemical Physics Letters*, 443:284–288, 2007.

40. Fleckl, Thomas, Helmut Jäger, and Ingwald Obernberger. "Experimental verification of gas spectra calculated for high temperatures using the HITRAN/HITEMP database". *Journal of Physics D: Applied Physics*, 35:3138–3144, 2002.

41. Freeman, G. N., C. B. Ludwig, W. Malkmus, and R. Reed. *Development and validation of standardized infrared radiation model (SIRRM)*. Technical Report AFRPL-TR-79-55, Air Force Rocket Propulsion Laboratory, 1979.

42. Fried, Laurence E., W. Michael Howard, P. Clark Souers, and Peter A. Vitello. "CHEETAH 3.0 Users Manual", 2001.

43. Gamache, R. R. and L. S. Rothman. "Extension of the HITRAN database to non-LTE applications". *Journal of Quantitative Spectroscopy & Radiative Transfer*, 48(5):519–525, 1992.

44. Glassman, Irvin. *Combustion*. Academic Press, San Diego, California, 3rd edition, 1996.

45. Goroshin, Samuel, David L. Frost, Jeffrey Levine, Akio Yoshinaka, and Fan Zhang. "Optical Pyrometry of Fireballs of Metalized Explosives". *Propellants, Explosives, Pyrotechnics*, 31(3):1–13, 2006.

46. Griffiths, Peter R. and James A. de Haseth. *Fourier Transform Infrared Spectroscopy*, volume 83 of *Chemical Analysis*. Wiley-Interscience, 1986.

47. Grisch, Frédéric, Paul Bouchardy, and Walter Clauss. "CARS thermometry in high pressure rocket combustors". *Aerospace Science and Technology*, 7:317–330, 2003.

48. Gross, Kevin C., Anthony N. Dills, Glen P. Perram, and Ronald F. Tuttle. "Phenomenology of Exploding Ordnance Using Spectrally and Temporally Resolved Infrared Emissions". *Proceedings of SPIE*, 5075:217–227, 2003.

49. Gross, Kevin C., Glen P. Perram, and Ronald F. Tuttle. "Modeling infrared spectral intensity data from bomb detonations". *Proceedings of SPIE*, 5811:100–111, 2005.

50. Grosshandler, William L. *RADCAL: A Narrow-Band Model for Radiation Calculations in a Combustion Environment*. Technical report, National Institute for Standards and Technology, 1993.

51. Hahn, D. W., W. L. Flower, and K. R. Hencken. "Discrete Particle Detection and Metal Emissions Monitoring Using Laser-Induced Breakdown Spectroscopy". *Applied Optics*, 51(12):1836–1844, 1997.

52. Hall, Matthew J., Donald Lucas, and Catherine P. Koshland. "Measuring Chlorinated Hydrocarbons in Combustion by Fourier Transform Infrared Spectroscopy". *Environmental Science and Technology*, 25(2):260–267, 1991.

53. Heland, Jörg and Klaus Schäfer. "Analysis of aircraft exhausts with Fourier-transform infrared emission spectroscopy". *Applied Optics*, 36(21):4922–4931, 1997.

54. Heyberger, B., F. Battin-Leclerc, V. Warth, R. Fournet, G. M. Côme, and G. Scacchi. "Comprehensive Mechanism for the Gas-Phase Oxidation of Propene". *Combustion and Flame*, 126:1780–1802, 2001.

55. Higgins, Kelly J., Heejung Jung, David B. Kittelson, Jeffrey T. Roberts, and Michael R. Zachariah. "Size-selected Nanoparticle Chemistry: Kinetics of Soot Oxidation". *Journal of Physical Chemistry A*, 106(1):96–103, 2002.

56. Houghton, J. T., Y. Ding, D.J. Griggs, M. Noguer, P.J. van der Linden, X. Dai, K. Maskell, and C.A. Johnson (editors). *Climate Change 2001: The Scientific Basis. Contribution of Working Group I to the Third Assessment Report of the Intergovernmental Panel on Climate Change*. Cambridge University Press, Cambridge, United Kingdom, 2001.

57. Jacquinet-Husson, N., K. Garceran, N. A. Scott, R. Armante, and A. Chédin. "The 2003 Edition Of GEISA: A Spectroscopic Database System For The Second Generation Vertical Sounders Radiance Simulation". 13th *International TOVS Study Conference*. 2003. URL http://ara.lmd.polytechnique.fr.

58. Karpowicz, R. J. and T. B. Brill. "In Situ Characterization of the "Melt" Phase of RDX and HMX by Rapid-Scan FTIR Spectroscopy". *Combustion and Flame*, 56:317–325, 1984.

59. Keeling, C. D. and T. P. Whorf. *Atmospheric* CO_2 *Records from Sites in the SIO Air Sampling Network*. Federal government report, Carbon Dioxide Inf Analysis Center (CDIAC), 1994.

60. Keeling, C.D. and T.P. Whorf. "Atmospheric CO_2 concentrations (ppmv) derived from flask air samples collected at La Jolla Pier, California, USA.", May 2005. URL http://cdiac.ornl.gov/ftp/trends/co2/ljo.dat.

61. Keeling, C.D. and T.P. Whorf. "Atmospheric CO_2 concentrations (ppmv) derived from in situ air samples collected at Mauna Loa Observatory, Hawaii.", 2005. URL http://cdiac.esd.ornl.gov/ftp/trends/co2/maunaloa.co2.

62. Kick, Hermann, Volker Tank, and Erwin Lindermeir. "Impact of scene changes during data acquisition in Fourier spectroscopy". *Journal of Quantitative Spectroscopy & Radiative Transfer*, 92:447–455, 2004.

63. Kohse-Höinghaus, Katharina, Robert S. Barlow, Marcus Aldén, and Jürgen Wolfrum. "Combustion at the focus: laser diagnostics and control". *Proceedings of the Combustion Institute*, 30:89–123, 2005.

64. Kohsehoinghaus, K. "Laser techniques for the quantitative detection of reactive intermediates in combustion systems". *Progress in Energy and Combustion Science*, 20(3):203–279, 1994.

65. Kuhl, A. L., J. C. Leyer, and A. A. Borisov. *Dynamic Aspects of Detonations*, volume 153 of *Progress in astronautics and aeronautics*. American Institute of Aeronautics and Astronautics, 1993.

66. Kuhl, A. L., J. C. Leyer, and A. A. Borisov. *Dynamic Aspects of Explosion Phenomena*, volume 154 of *Progress in astronautics and aeronautics*. American Institute of Aeronautics and Astronautics, 1993.

67. Kuo, Kenneth K. *Principles of Combustion*. John Wiley & Sons, Inc., 1986.

68. Le Roy, R. J. *A Practical Guide to Least-Squares Fitting*. Technical Report CP-628, University of Waterloo, Waterloo, Ontario N2L 3G1, Canada, 1997.

69. Le Roy, R. J. "Uncertainty, Sensitivity, Convergence, and Rounding in Performing and Reporting Least-Squares Fits". *Journal of Molecular Spectroscopy*, 191:223–231, 1998.

70. Leahy-Hoppa, M. R., M. J. Fitch, X. Zheng, L. M. Hayden, and R. Osiander. "Wideband terahertz spectroscopy of explosives". *Chemical Physics Letters*, 434:227–230, 2007.

71. Lee, Tae-Woo and Nikhil Hegde. "Laser-induced breakdown spectroscopy for in situ diagnostics of combustion parameters including temperature". *Combustion and Flame*, 142:314–316, 2005.

72. Mader, Charles L. *Explosives and Propellants*. CRC Press, Boca Raton, Florida, 1998.

73. Marsi, A. R., R. W. Dibble, and R. S. Barlow. "The Structure Of Turbulent Nonpremixed Flames Revealed By Raman-Rayleigh-LIF Measurements". *Progress in Energy and Combustion Science*, 22:307–362, 1996.

74. McIlroy, Andrew. "Direct measurement of $^1CH_2$ in flames by cavity ringdown laser absorption spectroscopy". *Chemical Physics Letters*, 296:151–158, 1998.

75. McNesby, Kevin L. and Rose A. Pesce-Rodriguez. "Applications of Vibrational Spectroscopy in the Study of Explosives". J. M. Chalmers and P. R. Griffiths (editors), *Handbook of Vibrational Spectroscopy*, chapter 1, 1–17. John Wiley & Sons Ltd., Chichester, England, 2002.

76. Medwell, Paul R., Peter A.M. Kalt, and Bassam B. Dally. "Simultaneous imaging of OH, formaldehyde, and temperature of turbulent nonpremixed jet flames in a heated and diluted coflow". *Combustion and Flame*, 148:48–61, 2007.

77. Mertz, L. *Transformations in Optics*. Wiley, New York, 1965.

78. Mewes, B. and J. M. Seitzman. "Soot volume fraction and particle size measurements with laser-induced incandescence". *Applied Optics*, 36(3):709–717, 1997.

79. Miller, Philip J. "A Reactive Flow Model with Coupled Reaction Kinetics for Detonation and Combustion in Non-Ideal Explosives". Thomas B. Brill, Thomas P. Russell, William C. Tao, and Robert B. Wardle (editors), *Decomposition, Combustion, and Detonation Chemistry of Energetic Materials*, volume 418 of *Materials Research Society Symposium Proceedings*, 413–420. Materials Research Society, 1996.

80. Mitani, Tohru and Toshinori Kouchi. "Flame structures and combustion efficiency computed for a Mach 6 scramjet engine". *Combustion and Flame*, 142:187–196, 2005.

81. Modest, Michael F. *Radiative Heat Transfer*. McGraw-Hill, Inc., New York, New York, 1993.

82. Modest, Michael F. and Sudarshan P. Bharadwaj. "Medium resolution transmission measurements of CO_2 at high temperature". *Journal of Quantitative Spectroscopy & Radiative Transfer*, 73:329–338, 2002.

83. Najm, Habib N., Phillip H. Paul, Charles J. Mueller, and Peter S. Wyckoff. "On the Adequacy of Certain Experimental Observables as Measurements of Flame Burning Rate". *Combustion and Flame*, 113:312–332, 1998.

84. National Institute of Standards and Technology. "Chemical Kinetics Database on the Web, Standard Reference Database 17, Version 7.0 (Web version), Release 1.4", July 2007. URL http://kinetics.nist.gov/kinetics/index.jsp.

85. Ogura, Toshiyuki, Ken Okada, Takayuki Abe, Kunihiko Wakabayashi, Koki Ishikawa, Eishi Kuroda, Tomoharu Matsumura, Yoshio Nakayama, and Masatake Yoshida. *Pyrometry study on fireballs generated upon the explosion of TNT*, volume 18, 1–12. 34th International Annual Conference of ICT, Karlsrube, Germany, 2003.

86. Orson, J. A. *Collection of detonation signatures and characterization of spectral signatures*. Master's thesis, Air Force Institute of Technology, AFIT/GSO/ENP/00M-01, 2000.

87. Orson, J. A., W. F. Bagby, and G. P. Perram. "Infrared signatures from bomb detonations". *Infrared Physics and Technology*, 44:101–107, 2003.

88. Oyumi, Y. and T. B. Brill. "Thermal Decomposition of Energetic Materials 3. A High-Rate, In Situ, FTIR Study of the Thermolysis of RDX and HMX with Pressure and Heating Rate as Variables." *Combustion and Flame*, 62:213–224, 1985.

89. Reitz, R. D. and C. J. Rutland. "Development and testing of diesel engine CFD models". *Progress in Energy and Combustion Science*, 21:173–196, 1995.

90. Rothman, L. S., A. Barbe, D. Chris Benner, L. R. Brown, C. Camy-Peyret, M. R. Carleer, K. Chance, C. Clerbaux, V. Dana, V. M. Devi, A. Fayt, J.-M. Flaud, R. R. Gamache, A. Goldman, D. Jacquemart, K. W. Jucks, W. J. Lafferty, J.-Y. Mandin, S. T. Massie, V. Nemtchinov, D. A. Newnham, A. Perrin, C. P. Rinsland, J. Schroeder, K. M. Smith, M. A. H. Smith, K. Tang, R. A. Toth, J. Vander Auwera, P. Varanasi, and K. Yoshino. "The HITRAN molecular spectroscopic database: edition of 2000 including updates through 2001". *Journal of Quantitative Spectroscopy & Radiative Transfer*, 82:5–44, 2003.

91. Rothman, L. S., C. P. Rinsland, A. Goldman, S. T. Massie, D. P. Edwards, J.-M. Flaud, A. Perrin, C. Camy-Peyret, V. Dana, J.-Y. Mandin, J. Schroeder, A. Mccann, R. R. Gamache, R. B. Wattson, K. Yoshino, K. V. Chance, K. W. Jucks, L. R. Brown, V. Nemtchinov, and P. Varanasi. "THE HITRAN MOLECULAR SPECTROSCOPIC DATABASE AND HAWKS (HITRAN ATMOSPHERIC WORKSTATION): 1996 EDITION". *Journal of Quantitative Spectroscopy & Radiative Transfer*, 60(5):665–710, 1998.

92. Schäfer, Klaus, Jörg Heland, Dave H. Lister, Chris W. Wilson, Roger J. Howes, Robert S. Falk, Erwin Lindermeir, Manfred Birk, Georg Wagner, Peter Haschberger, Marc Bernard, Olivier Legras, Peter Wiesen, Ralf Kurtenbach, Klaus J. Brockmann, Volker Kriesche, Moira Hilton, Gary Bishop, Roy Clarke, John Workman, Michael Caola, Rachel Geatches, Roger Burrows, John D. Black, Philippe Hervé, and Johanna Vally. "Nonintrusive Optical Measurements of Aircraft Engine Exhaust Emissions and Comparison with Standard Intrusive Techniques". *Applied Optics*, 39(3):441–455, 2000.

93. Schroeder, M. A., R. A. Fifer, M. S. Miller, R. A. Pesce-Rodriguez, C. J. S. Mcnesby, and G. Singh. "Condensed-Phase Processes during Combustion of Solid Gun Propellants. I. Nitrate Ester Propellants". *Combustion and Flame*, 126:1569–1576, 2001.

94. Schroeder, M. A., R. A. Fifer, M. S. Miller, R. A. Pesce-Rodriguez, C. J. S. Mcnesby, G. Singh, and J. M. Widder. "Condensed-Phase Processes during Combustion of Solid Gun Propellants. II. Nitramine Composite Propellants". *Combustion and Flame*, 126:1577–1598, 2001.

95. Schulza, Christof and Volker Sick. "Tracer-LIF diagnostics: quantitative measurement of fuel concentration, temperature and fuel/air ratio in practical combustion systems". *Progress in Energy and Combustion Science*, 31:75–121, 2005.

96. Setchell, R. E. "Optical studies of chemical energy release during shock iniation of granular explosives". Bowen J. R., J.-C. Leyer, and R. I. Soloukhin (editors), *Progress in Astronautics and Aeronautics 106, Dynamics of Explosions*, 607–628. American Institute of Aeronautics and Astronautics, 1986.

97. Shaddix, Christopher R. and Kermit C. Smyth. "Laser-Induced Incandescence Measurements of Soot Production in Steady and Flickering Methane, Propane, and Ethylene Diffusion Flames". *Combustion and Flame*, 107:418–452, 1996.

98. Shen, Y. C., T. Lo, P. F. Taday, B. E. Cole, W. R. Tribe, and M. C. Kemp. "Detection and identification of explosives using terahertz pulsed spectroscopic imaging". *Applied Physics Letters*, 86:241116, 2005.

99. Soufiani, Anouar, Jean-Pierre Martin, Juan-Carlos Rolon, and Laurent Brenez. "Sensitivity of temperature and concentration measurements in hot gases from FTIR emission spectroscopy". *Journal of Quantitative Spectroscopy & Radiative Transfer*, 73:317–327, 2002.

100. Tashkun, S. A., V. I. Perevalov, J-L. Teffo, A. D. Bykov, and N. N. Lavrentieva. "CDSD-1000, the high-temperature carbon dioxide spectroscopic databank". *Journal of Quantitative Spectroscopy & Radiative Transfer*, 82:165–196, 2003.

101. Thiele, M., J. Warnatz, A. Dreizler, S. Lindenmaier, R. Schießl, U. Maas, A. Grant, and P. Ewart. "Spark Ignited Hydrogen/Air Mixtures: Two Dimensional Detailed Modeling and Laser Based Diagnostics". *Combustion and Flame*, 128:74–87, 2002.

102. Verbiezen, K., R. J. H. Klein-Douwel, A.P. van Vliet, A. J. Donkerbroek, W. L. Meerts, N.J. Dam, and J. J. ter Meulen. "Quantitative laser-induced fluorescence measurements of nitric oxide in a heavy-duty Diesel engine". *Proceedings of the Combustion Institute*, 31:765–773, 2007.

103. Vestin, Fredrik, Mikael Afzelius, and Per-Erik Bengtsson. "Development of rotational CARS for combustion diagnostics using a polarization approach". *Proceedings of the Combustion Institute*, 31:833–840, 2007.

104. Vestin, Fredrik, Mikael Afzelius, Christian Brackmann, and Per-Erik Bengtsson. "Dual-broadband rotational CARS thermometry in the product gas of hydrocarbon flames". *Proceedings of the Combustion Institute*, 30:1673–1680, 2005.

105. Von Holle, W. G. and C. M. Traver. "Temperature measurements of shocked explosives by time resolved infrared radiometry—a new technique to measure shock-induced reaction". *Proceedings of the International Symposium on Detonation*, 993–1003. Annapolis, Maryland, 1981.

106. Weiser, Volker and Norbert Eisenreich. "Fast Emission Spectroscopy for a Better Understanding of Pyrotechnic Combustion Behavior". *Propellants, Explosives, Pyrotechnics*, 30(1):67–78, 2005.

107. Widmann, John F. and Cary Presser. "A Benchmark Experimental Database for Multiphase Combustion Model Input and Validation". *Combustion and Flame*, 129:47–86, 2002.

108. Wolfe, William L. and George J. Zissis (editors). *The Infrared Handbook*. Environmental Research Institute of Michigan, 1978.

109. Xie, J., B. A. Paldus, E. H Wahl, J. Martin, T. G. Owano, C. H. Kruger, J. S. Harris, and R. N. Zare. "Near-infrared cavity ringdown spectroscopy of water vapor in an atmospheric flame". *Chemical Physics Letters*, 284:387–395, 1998.

110. Zel'dovich, Ya. B. and Yu. P. Raizer. *Physics of Shock Waves and High-Temperature Hydrodynamic Phenomena*. Dover, Mineola, New York, 2002.

111. Zhang, Zhengwei, Yan Zhang, Guozhong Zhao, and Cunlin Zhang. "Terahertz time-domain spectroscopy for explosive imaging". *Optik*, 118:325–329, 2007.

REPORT DOCUMENTATION PAGE

1. REPORT DATE *(DD–MM–YYYY)*	2. REPORT TYPE	3. DATES COVERED *(From — To)*
13–09–2007	Doctoral Dissertation	October 2001 — September 2007

4. TITLE AND SUBTITLE

Phenomenological Model for Infrared Emissions from High-Explosive Detonation Fireballs

5a. CONTRACT NUMBER

5b. GRANT NUMBER

5c. PROGRAM ELEMENT NUMBER

6. AUTHOR(S)

Gross, Kevin C.

5d. PROJECT NUMBER

5e. TASK NUMBER

5f. WORK UNIT NUMBER

7. PERFORMING ORGANIZATION NAME(S) AND ADDRESS(ES)

Air Force Institute of Technology
Graduate School of Engineering and Management (AFIT/EN)
2950 Hobson Way
WPAFB OH 45433-7765

8. PERFORMING ORGANIZATION REPORT NUMBER

AFIT/DS/ENP/07-03

9. SPONSORING / MONITORING AGENCY NAME(S) AND ADDRESS(ES)

N/A

10. SPONSOR/MONITOR'S ACRONYM(S)

11. SPONSOR/MONITOR'S REPORT NUMBER(S)

12. DISTRIBUTION / AVAILABILITY STATEMENT

APPROVED FOR PUBLIC RELEASE; DISTRIBUTION UNLIMITED

13. SUPPLEMENTARY NOTES

14. ABSTRACT

Time-resolved infrared spectra were recently collected via a Fourier-transform spectrometer (FTS) from the detonation fireballs of two types of conventional military munitions (CMM) as well as uncased TNT and four types of enhanced novel explosives (ENEs). The CMM spectra are dominated by continuum emission, and a single-temperature Planckian distribution, modified for atmospheric attenuation, captures most of the variation in the data. Some evidence of selective emission is identified by systematic patterns in the fit residuals. The behavior of these systematic residuals affords a distinction between the two types of CMMs studied. The uncased TNT and ENE spectra appear strongly influenced by both continuum and selective emission. A physics-based spectral model is developed consisting of seven parameters: size, temperature, particulate absorption coefficient, and gas concentrations for H_2O, CO_2, CO, and HCl. Fitting affords a high-fidelity representation with features that correlate with HE characteristics. The hydrogen-to-carbon ratio ($\mathcal{R}$) separates the TNT and ENE events and is consistent with stoichiometric expectations. Average values of $\mathcal{R}$ are compared with stoichiometry (in parenthesis): TNT 1.13 (0.79); ENE0B 9.2 (21.3); ENE1 4.9 (6.7); ENE2A 4.6 (5.8); ENE2B 6.5 (6.7). Bayesian discrimination boundary between TNT and ENE is $\mathcal{R} = 1.67$ and the mean probability of error is less than 0.3% for this two-class problem. The Fisher ratio is 17.4 and ENE can be distinguished from TNT with 99% detection rate with corresponding false-alarm rate of less than 10^{-4}%. Temperature decay rates k_T correlate with charge weights W, following a power-law dependence $k_T \propto W^b$ with $-0.52 \leq b \leq -0.25$ depending on explosive type.

15. SUBJECT TERMS

High Explosive, Improvised Explosive Device (IED), Combustion, Afterburning, Fireball, Fourier-Transform Spectroscopy, Radiative Transfer, Phenomenology, Dimensionality Reduction, Discriminant Analysis, Classification

16. SECURITY CLASSIFICATION OF:			17. LIMITATION OF ABSTRACT	18. NUMBER OF PAGES	19a. NAME OF RESPONSIBLE PERSON
a. REPORT	b. ABSTRACT	c. THIS PAGE			Dr. Glen P. Perram (AFIT/ENP)
U	U	U	UU	185	19b. TELEPHONE NUMBER *(include area code)* (937) 255–3636 ext. 4504; email: Glen.Perram@afit.edu